

CO₂ Profiling in the Lower Troposphere
using a High Spectral Resolution Infrared
Radiometer

Inaugural-Dissertation
zur
Erlangung des Doktorgrades
der Mathematisch-Naturwissenschaftlichen Fakultät
der Universität zu Köln

vorgelegt von
Kobra Khosravian Ghadikolaei
aus Ghaemshahr

Köln

2017

Berichterstatter:

PD. Dr. U. Löhnert
Prof. Dr. A. Wahner
Dr. D. D. Turner

Tag der mündlichen Prüfung:
16.10.2017

Abstract

The rapid increase of CO₂ concentration in the atmosphere due to the anthropogenic activities since the beginning of the industrial revolution in 1750 makes CO₂ the most important anthropogenic atmospheric trace gas. Improvements in space-based and ground-based instrumentation during the last decades provide a high potential to observe atmospheric CO₂ spatial and temporal variability in unprecedented details. The interaction of atmospheric CO₂ with the terrestrial ecosystem such as plant photosynthesis and soil respiration can produce a considerable diurnal change in the CO₂ concentration near the surface. The measurement of this diurnal evolution would provide a valuable tool to study the land-vegetation interaction with the atmospheric CO₂. Such a tool would also be useful to help evaluate the output of numerical models which predict the CO₂ flux near the surface. However, despite all improvements in the measurement capability, capturing this diurnal change in the boundary layer still remains a challenge.

One possibility to improve the observation of the diurnal CO₂ cycle is to use the Fourier Transform InfraRed (FTIR) spectrometer. One example of ground-based FTIR spectrometer is Atmospheric Emitted Radiance Interferometer (AERI). The AERI was installed in 2011, at Jülich ObservatorY for Cloud Evolution (JOYCE), in Germany. It measures the downwelling atmospheric radiation in the mid-infrared region from 520 cm⁻¹ (19 μm) to 3020 cm⁻¹ (3.3 μm). High temporal (less than 30 s) and spectral (better than 1 cm⁻¹) resolution as well as continuous measurements of the AERI give the opportunity to retrieve the atmospheric thermodynamic profiles and cloud properties. In addition, the AERI also observes the emission from several trace gas absorption bands, such as the 15 μm CO₂ band. These bands can be used to provide useful information about the atmospheric concentration of these trace gases. In the present work, the ability to retrieve profiles of CO₂ over the diurnal cycle from AERI-observed radiances is investigated. For this purpose, an algorithm, called AERIOe is utilized and modified to retrieve the CO₂ profile in the boundary layer.

Prior to applying the AERIOe to real AERI measurements, simulated radiances are used to evaluate the potential of retrieving atmospheric CO₂ concentration from AERI radiance observations. A line-by-line radiative transfer model (LBLRTM) using numerical model profiles as input are utilized to compute downwelling radiances, which are convolved with the instrument function and random noise added in order to simulate an AERI observation. In the first step, a constant atmospheric mixing ratio is considered for the atmospheric CO₂ profile. AERIOe results show about 2 ppm overestimation in retrieving the constant CO₂ mixing ratio. In order to improve the results, reduced noise, which can be interpreted as using temporally averaged AERI radiances, is added to the simulated radiances. These results show considerable improvement compared to the previous results where by ~ 70% of the retrieved values are within the expected uncertainty. However, a constant atmospheric profile can not provide any information related to the diurnal change of CO₂ concentration near the surface,

meaning that a profile which can represent the diurnal CO₂ variation needs to be retrieved. Due to the low numbers of degrees of freedom for signal in retrieving the CO₂ concentration, the CO₂ profile is parametrized using an exponential function. This exponential function gives the opportunity to calculate the CO₂ profile by retrieving 2 shape parameters, rather than retrieving whole profile.

In order to evaluate the modified AERIOe, simulated radiances with the reduced noise for one month are provided to the algorithm. The AERIOe is then run while temperature and humidity profiles are considered as known profiles. The CO₂ concentrations in different levels are captured quite accurately by the algorithm where the root mean square values between true and retrieved CO₂ concentrations are 6.8, 5.4, 4.0 and 1.9 ppm at the surface, 90 m, 200 m and 1 km respectively. The retrieved profiles improved the root mean square between true and prior profiles by $\sim 50\%$. The algorithm is then used to retrieve the temperature, humidity and CO₂ profiles simultaneously. These results show a significant reduction in the CO₂ degrees of freedom which causes poor retrieval results. Consequently, a second method is used wherein a principal component noise filter is applied to reduce the random error in the AERI observations. High temporal resolution simulated radiances are used to test the new method. The results of the AERIOe run with the noise-filtered radiances demonstrate considerable improvement in retrieving the CO₂ concentration near the surface.

The AERIOe is then applied to real AERI observations from two clear sky days at Jülich to retrieve profiles of CO₂. The tower in-situ measurements at Jülich are utilized to compare with the retrieved CO₂ concentration near the surface. It is shown that the AERI radiances have the potential to capture the diurnal variation of the CO₂ concentration near the surface. The retrieved values for the surface CO₂ concentration show between 5 to 10 ppm difference with the tower measurements during these two days, while the uncertainties in the retrieved values are between 4 to 7 ppm. The AERI radiances are also used to estimate the height where the CO₂ concentration deviates from its background value. The diurnal change of the derived heights for one of these two days are in good agreement with the expected diurnal change of the boundary layer for a sunny and clear sky day.

Zusammenfassung

Der schnelle Anstieg der CO_2 Konzentration in der Atmosphäre, der seit dem Beginn der industriellen Revolution ab 1750 durch anthropogene Aktivitäten hervorgerufen wird, macht CO_2 zum wichtigsten anthropogenen Spurengas der Atmosphäre. Fortschritte der satelliten- und bodengestützten Messtechnik in den letzten Jahrzehnten bieten ein hohes Potential, die räumliche und zeitliche Veränderung von atmosphärischem CO_2 in noch nie da gewesenem Detail zu erfassen. Das Zusammenspiel von atmosphärischem CO_2 und dem irdischen Ökosystem, zum Beispiel durch Pflanzenphotosynthese und Bodenatmung, kann einen erheblichen Tagesgang in der oberflächennahen CO_2 Konzentration verursachen. Messungen dieses Tagesgangs wären ein wertvolles Hilfsmittel zur Untersuchung des Zusammenspiels von Land und Vegetation mit dem atmosphärischen CO_2 . Ein solches Hilfsmittel könnte außerdem eine Beurteilung von numerischen Modellen, die den oberflächennahen CO_2 Fluss vorhersagen, ermöglichen. Trotz Verbesserung der Messungsmöglichkeiten ist die Messung dieses Tagesgangs in der Grenzschicht nach wie vor eine Herausforderung.

Eine Möglichkeit, die Beobachtung des CO_2 Tagesgangs zu verbessern, ist die Benutzung eines Fourier Transform InfraRot (FTIR) Spektrometers. Das Atmospheric Emitted Radiance Interferometer (AERI) ist ein Beispiel eines bodengestützten FTIR Spektrometers. AERI wurde 2011 am Jülich ObservatorY for Cloud Evolution (JOYCE) in Deutschland installiert. Es misst die einfallende atmosphärische Strahlung im mittleren Infrarotbereich von 520 cm^{-1} ($19 \mu\text{m}$) bis 3020 cm^{-1} ($3.3 \mu\text{m}$). Eine hohe zeitliche (weniger als 30s) und spektrale (besser als 1 cm^{-1}) Auflösung sowie kontinuierliche Messungen des AERI ermöglichen es, thermodynamische Atmosphärenprofile und Wolkeneigenschaften zu erfassen. Außerdem beobachtet AERI die Emission von mehreren Absorptionsbanden von Spurengasen, zum Beispiel die $15 \mu\text{m}$ CO_2 Bande. Diese Banden können benutzt werden, um Informationen über atmosphärische Spurengaskonzentration zu liefern. In der vorliegenden Arbeit wird die Möglichkeit untersucht, Profile von CO_2 im Tagesgang durch von AERI gemessene Strahldichten zu erfassen. Zu diesem Zweck wird ein AERIOe genannter Algorithmus benutzt und angepasst um CO_2 Profile in der Grenzschicht ableiten.

Bevor AERIOe auf reale AERI-Messungen angewandt wird, werden simulierte Strahldichten benutzt, um das Ableitungspotential atmosphärischer CO_2 -Konzentrationen aus der Strahldichtemessung von AERI zu evaluieren. Ein line-by-line radiative transfer model (LBLRTM), das Profile von numerischen Modellen als Eingabe benutzt, wird benutzt, um einfallende Strahldichten zu berechnen, welche mit der Sensorfunktion gefaltet werden und mit zufälligem Rauschen versehen werden, um Messungen von AERI zu simulieren. Im ersten Schritt wird ein konstantes Mischungsverhältnis des atmosphärischen CO_2 Profils angenommen. Ergebnisse von AERIOe überschätzen das konstante CO_2 Mischungsverhältnis um etwa 2 ppm. Um die Ergebnisse zu verbessern, wird ein reduziertes Rauschen zu der simulierten Strahldichte addiert. Dieses reduzierte Rauschen kann als zeitlich gemittelte AERI Strahldichte aufgefasst werden. Diese Ergebnisse zeigen eine erhebliche Verbesserung verglichen zu vorherigen

Ergebnissen: Etwa 70% der abgeleiteten Werte liegen innerhalb der erwarteten Unsicherheit. Jedoch kann ein konstantes atmosphärisches Profil keine Informationen über den Tagesgang der oberflächennahen CO₂ Konzentration liefern, sodass ein Profil, das den Tagesgang repräsentieren kann, abgeleitet werden muss. Auf Grund der geringen Anzahl an Freiheitsgraden für das Signal beim Ableiten der CO₂ Konzentration wird das CO₂ Profil mithilfe einer Exponentialfunktion parametrisiert. Diese Exponentialfunktion ermöglicht es, CO₂ Profile zu berechnen, indem 2 Parameter anstelle des ganzen Profiles abgeleitet werden.

Zur Evaluation des modifizierten AERIoe Algorithmus, wird er auf simulierte Strahldichten mit reduziertem Rauschen angewendet. AERIoe wird dabei mit bekannt angenommen Temperatur- und Feuchteprofilen ausgeführt. Die CO₂ Konzentrationen in unterschiedlichen Höhen werden von dem Algorithmus ziemlich genau erfasst: Die mittlere quadratische Abweichung zwischen wahren und erfassten Konzentrationen ist jeweils 6.8, 5.4, 4.0 und 1.9 ppm an der Oberfläche und in 90 m, 200 m und 1 km Höhe. Die abgeleiteten Profile verbessern die mittlere quadratische Abweichung zwischen wahren und a Priori Profilen um etwa 50%. Dann wird der Algorithmus benutzt, um die Temperatur-, Feuchte- und CO₂ Profile gleichzeitig abzuleiten. Die Ergebnisse zeigen eine signifikante Reduktion der Freiheitsgrade und damit einhergehend eine Verschlechterung der Ableitung von CO₂ Profilen. Infolgedessen wird eine zweite Methode benutzt, in der ein Hauptkomponenten-Rauschfilter angewandt wird, um den zufälligen Fehler in den AERI Messungen zu reduzieren. Um diese neue Methode zu testen, werden simulierte Strahldichten mit hoher zeitlicher Auflösung benutzt. Die Ergebnisse von AERIoe mit den gefilterten Strahldichten zeigen eine erhebliche Verbesserung in der Erfassung von oberflächennahen CO₂ Konzentrationen.

AERIoe wird letztlich auf reale AERI Messungen von zwei Strahlungstagen in Jülich angewandt, um CO₂ Profile abzuleiten. Die in-situ Messungen des Messmasts in Jülich werden mit den abgeleiteten oberflächennahen CO₂ Konzentrationen verglichen. Es wird gezeigt, dass die Strahldichten von AERI das Potential haben, den Tagesgang der oberflächennahen CO₂ Konzentration darzustellen. Die abgeleiteten oberflächennahen CO₂ Konzentration unterscheiden sich an diesen zwei Tage zwischen 5 und 10 ppm von den Messungen am Mast, während die Unsicherheiten in den abgeleiteten Konzentration zwischen 4 und 7 ppm liegen. Die AERI Strahldichten werden auch benutzt, um die Höhe abzuschätzen, ab der die CO₂ Konzentration vom Hintergrundwert abweicht. Der Tagesgang der abgeleiteten Höhen für einen dieser zwei Tage ist in Übereinstimmung mit dem erwarteten Tagesgang der Grenzschicht für einen Strahlungstag.

Contents

1	Introduction	1
1.1	Motivation	1
1.2	Carbon cycle	3
1.2.1	Terrestrial ecosystem	4
1.2.2	Ocean	5
1.3	Atmospheric CO ₂ measurement	6
1.3.1	In situ measurements	6
1.3.2	Space-based measurements	8
1.3.3	Ground-based measurements	9
1.4	Goal and structure of the thesis	10
2	Radiative transfer	13
2.1	Basic radiative transfer in clear sky	13
2.2	Radiative transfer in the infrared region for clear sky condition	15
2.2.1	Vibrational and rotational transition	16
2.2.2	Line broadening	17
2.2.3	Continuum absorption	17
2.2.4	Some important atmospheric gas absorbers in mid-infrared	18
2.2.5	Example of downwelling atmospheric infrared measurement	18
2.3	Weighting function	20
2.4	The line-by-line radiative calculation	21
2.5	Sensitivity study	23

3	Instrument and model data	27
3.1	AERI	27
3.1.1	Instrument design	28
3.1.2	Data acquisition	29
3.2	Microwave radiometer	32
3.3	GPS data	33
3.4	Tower measurement	34
3.5	COSMO_DE model	35
3.6	REMO model	36
4	Quality control and evaluation of AERI data	39
4.1	Flagging low-quality data	39
4.1.1	Imaginary part of observed radiances	39
4.1.2	Instrument responsivity	40
4.2	Finding clear sky cases	40
4.3	Finding the best measured IWV and surface temperature to scale COSMO_DE profiles	43
4.4	Spectral calibration	47
4.5	Radiometric calibration	49
4.5.1	Obstruction correction	50
4.5.2	Aft optic correction	52
5	Retrieval algorithm	55
5.1	Optimal Estimation theory	56
5.2	The AERIOe	58
6	CO₂ profile retrieval for simulated radiances	63
6.1	CO ₂ retrieval with fixed temperature and humidity	63
6.1.1	Retrieve the constant CO ₂ mixing ratio	65
6.1.2	Parametrization of the CO ₂ profile	67
6.1.3	Prior data of the three exponential function parameters	69
6.1.4	Case studies	72
6.1.5	Statistical assessment	76
6.2	Simultaneous retrieval of CO ₂ , temperature and humidity profiles	79
6.2.1	The prior data of temperature and humidity profile	79
6.2.2	Case studies	80
6.2.3	Fixed surface CO ₂ concentration	83
6.2.4	Noise filtering	86

7	CO₂ profile retrieval from real AERI measurements	91
7.1	Prior data of temperature and humidity profiles	91
7.2	Simultaneous retrieval of temperature, humidity and CO ₂ profile	93
7.2.1	Fixed the CO ₂ surface value	109
8	Summary and outlook	113
	Outlook	116
	Bibliography	119

Chapter 1

Introduction

Global warming, which is one of the main issues of the modern world, is a consequence of a rapid increase of atmospheric CO₂ (*Houghton, 2005*). Analyzing the Greenland and Antarctic ice cores revealed a significant correlation between climate change and the increase in concentration of some atmospheric trace gases where CO₂ was one of these trace gases (*Delmas et al., 1980; Neftel et al., 1982*). Therefore, during the last decades many studies focused on measuring and analyzing the atmospheric CO₂ variation. Near the surface, the atmospheric CO₂ concentration can have large diurnal variation due to interaction with the terrestrial ecosystem. Capturing this diurnal cycle can help characterize this interaction as one of the important parts of the natural carbon cycle. However, there is still a significant deficiency in the continuous measurement of the CO₂ diurnal cycle in the boundary layer. In the present study, we use continuous infrared measurements provided by a ground-based instrument to partially fill this gap.

1.1 Motivation

Thermal radiation emitted by the earth can be absorbed by several atmospheric trace gases such as H₂O, CO₂, O₃, CH₄ and N₂O which causes an increase in the temperature of the troposphere. The troposphere then emits thermal radiation which can be absorbed by the earth. Absorption of thermal radiation by the earth increases the earth temperature and leads to further thermal emission by the earth. This cycle, which is known as greenhouse effect, causes a change in the mean surface temperature of our planet from -18 °C to 15 °C (*Mitchell, 1989; Lorius et al., 1990; Mudge, 1997; Houghton, 2005*). CO₂ is the second most important atmospheric greenhouse gas after water vapor (*Lorius et al., 1990; Houghton, 2005*). However, the rapid increase of its emission due to human activities such as fossil fuel combustion and land use change makes it the most important anthropogenic greenhouse gas (*IPCC, 1990*). Since the industrial revolution at the beginning of 1750, 4000 million tons of anthropogenic carbon mainly in the form of CO₂ along with substantial amounts of other trace gases such as CH₄, N₂O and chlorofluorocarbons (CFCs) have been released to the atmosphere annually (*IPCC, 2013*). As a result, the CO₂ concentration in the atmosphere has increased by more than 40% since the industrial revolution (*IPCC, 2013*) and reached from 278 ppm (before 1750) to more than 400 ppm in 2016 (<http://cdiac.ornl.gov/>). If this growth rate continues during the 21st century, the CO₂ content can reach the level that is the highest level in the past 20 million years (*Houghton, 2005*).

The increase of the atmospheric CO₂ content causes strong positive feedbacks such as an increase in the water vapor amount of the atmosphere (*Manabe and Wetherald, 1967; Mitchell, 1989*). The increment mainly of these two trace gases, H₂O and CO₂, enhances the absorption of terrestrial radiation by the atmosphere. The consequence of this rise is an increase in the mean temperature of the earth surface as well as in the temperature of the atmosphere. The ice-core analysis in Vostok (East Antarctica) showed that there is a significant correlation ($r=0.79$) between atmospheric CO₂ level and the change in the earth temperature (*Barnola et al., 1987*). The increase of the atmospheric CO₂ and other trace gases also has some negative feedbacks such as the enhancement of low or middle clouds amount that can compensate the increase in the earth and atmosphere temperature (*Charney et al., 1979*). However, several studies showed that the overall effect is a substantial warming (*IPCC, 2001; IPCC, 2013*). By using a radiative–convective model, *Manabe and Wetherald (1967)* predicted the climate sensitivity, which is defined as the change in the global mean equilibrium temperature of near surface as a result of doubling the atmospheric CO₂, equals 2.2 K. Later in 1975, they derived an increase of 3 K using a three dimensional global circulation model (GCM). Further studies with more observational and reanalysis datasets support this overall substantial positive feedback and it was shown that the minimum increase is very unlikely to be below 1.5-2 K (*Knutti et al., 2006*). Finding an upper limit for climate sensitivity has been more challenging. *Annan and Hargreaves (2006)* proposed that the upper limit with very small probability (less than 5%) is more than 4.5 K. The range between 1.5 and 4.5 °C for the climate sensitivity is confirmed by other studies based on new observations and models during the last two decades. However, a small probability for an increase higher than 4.5 °C remains (*Hegerl et al., 2006; Rogelj et al., 2012; IPCC, 2013; Martínez-Botí et al., 2015*).

Accurate prediction of the future increase in global equilibrium temperature still suffers from different sources of uncertainty. One of them is the uncertainty in the carbon cycle measurement (*Knutti et al., 2006*). More accurate measurements of the atmospheric CO₂ as the main carbon carrier in the atmosphere can substantially reduce this uncertainty. Significant progress in space-borne CO₂ measurements in recent years has made considerable improvement in the accuracy of numerical model outputs. Besides, these measurements have also made a remarkable impact on providing a global view of carbon in the atmosphere (*Chédin et al., 2002; Crevoisier et al., 2004; Buchwitz et al., 2005*). However, satellite observations are usually quite poor in capturing the diurnal cycle of CO₂ in lower levels of the troposphere (*Crevoisier et al., 2004; Morino et al., 2011*). This problem can be solved by ground-based instruments since they can provide more accurate measurements in lower atmospheric levels compared to satellites. The Total Carbon Column Observing Network (TC-CON) is a good example of a ground-based network implemented to produce accurate measurements for studying the carbon cycle as well as validation of satellites data (*Wunch et al., 2011*). However, because of using sunlight radiances for measuring the CO₂, this network can only provide daytime measurements (*Wunch et al., 2011*) so that it does not have the ability to capture the diurnal variation of the atmospheric CO₂ profile. Terrestrial mechanisms such as photosynthesis and soil respiration as well as boundary layer processes can produce significant diurnal variation in the CO₂ profile of lower tropospheric levels. Capturing this diurnal cycle which is important for studying the effect of the terrestrial ecosystem on the atmospheric CO₂ profile is one of the main challenges for numerical models predicting the near surface CO₂ flux (*Tolk et al., 2009*). Therefore, continuous CO₂ measurements during daytime and nighttime are highly needed in order to improve these models and to validate their outputs as well as studying the CO₂ diurnal variation and its effect on the carbon cycle.

The Fourier Transform InfraRed (FTIR) emission spectroscopy is a well-known method

of remote sensing in different fields. In atmospheric research, for the first time in 1969, an Infrared Radiation Interferometer Spectrometer (IRIS) was used on-board the Nimbus-3 satellite (*Conrath et al., 1970*) and later an improved one used on-board the Nimbus-4 (*Hanel et al., 1972*). Afterwards, the request for more accurate measurements of atmospheric parameters lead to the design and installation of a new generation of FTIR spectrometers on-board several satellites (*Smith et al., 1983, 1990a; Revercomb et al., 1988; Clerboux et al., 2009*). For ground-based atmospheric measurements, the FTIR spectroscopy is applied with roughly 20 years delay compared to satellite measurements (*Smith et al., 1990b*). Since then, several FTIR spectrometers have been developed and installed around the world in different fields of atmospheric research such boundary layer studies, climate research and cloud studies (*Smith et al., 1993, 1999; Lubin, 1994; Spänkuch et al., 1996; Feltz et al., 2003; Löhnert et al., 2009; Turner and Löhnert, 2014*). One of these FTIR instruments which were designed to measure the atmospheric thermal emission with high spectral and temporal resolution is the Atmospheric Emitted Radiance Interferometer (AERI) (*Revercomb et al., 1994; Knuteson et al., 2004a*). The AERI is a ground-based instrument that measures downwelling atmospheric mid-infrared radiances continuously. It was designed and developed at the University of Wisconsin-Madison (*Knuteson et al., 2004a*). The AERI measurements have shown high ability to retrieve atmospheric parameters such as temperature and humidity profile as well as cloud properties (e.g. *Löhnert et al., 2009; Turner and Löhnert, 2014*). Its observations also showed sensitivity to the atmospheric CO₂ content (*Feldman et al., 2015*). In 2011, an AERI instrument was installed at Jülich ObservatorY for Cloud Evolution (JOYCE) (*Löhnert et al., 2015*), Germany and it has provided measurements since 2012. Continuous measurements of the AERI during nighttime and daytime provide a great opportunity for studying the diurnal CO₂ variation in the boundary layer. The aim of the present work is to use these highly spectrally and temporally resolving measurements to provide information about the CO₂ diurnal cycle in the lower atmosphere in order to partially improve deficiencies in carbon cycle studies.

This research has been supported by HITEC graduate school for energy and climate (www.hitec-graduate-school.de). HITEC is a graduate school at the Forschungszentrum Jülich that supports the PhD students working on energy and climate research. It is a partner of different universities such as Universität zu Köln, RWTH Aachen University and Heinrich-Heine-Universität Düsseldorf. The aim of HITEC is to provide an interdisciplinary communication between PhD students in order to enhance their scientific experiences as well as providing different opportunities to improve their professional skills and qualifications. HITEC is funded by the Helmholtz Initiative and Networking.

1.2 Carbon cycle

Carbon does not have a natural sink; it can only flow between three natural reservoirs consisting of land (the biggest one), ocean and atmosphere (the smallest one). This natural cycle is called the global carbon cycle (*IPCC, 1990*). For several thousands of years, before the industrialization, the concentration of CO₂ in the atmosphere was fluctuating roughly between 180 and 280 ppm (*Petit et al., 1999; Lüthi et al., 2008; Hönlisch et al., 2009*). Since the industrial era around 1750, anthropogenic activities such as extracting fossil fuels from geological pools and burning them along with deforestation in large areas released around $240 \pm 10 \text{ PgC}$ ($1 \text{ PgC} = 10^{15} \text{ gC}$) anthropogenic carbon into the atmosphere (*IPCC, 2013*). However, less than half of this amount remained in the atmosphere and the rest has been

uptaken by two other reservoirs. This extra anthropogenic carbon emission increased the CO₂ atmospheric concentration by more than 100 ppm (*IPCC*, 2013). Fig. 1.1 shows the global carbon cycle between the three natural reservoirs for the time period before and after the industrial revolution.

Carbon exchanges between atmosphere and other reservoirs can be divided into different classifications based on their time scale; carbon cycling from decade to centuries which can happen in the carbon exchange between plants, soils and the ocean surface with the atmosphere; centuries to millennia for exchanging carbon between deeper soils and the deep ocean with the atmosphere; and up to millions of years for transferring carbon between the atmosphere and geological pools e.g. carbonate sediments in deep sea (*IPCC*, 2013).

The atmospheric CO₂ is growing at about half of the rate of total CO₂ anthropogenic emissions into the atmosphere. The other half is uptaken either by the terrestrial ecosystems or dissolves in the sea water surface and the deep ocean (*IPCC*, 2001). Therefore, any small change in these two reservoirs can have a considerable effect on the atmospheric CO₂ content within years to a decade. Consequently, it is essential to learn about these reservoirs and their mechanism for uptaking or emitting the CO₂ in different conditions as well as the impact of the rapid increase of anthropogenic atmospheric carbon on them. In the next two subsections, these two reservoirs and their role in the global carbon cycle is briefly explained.

1.2.1 Terrestrial ecosystem

A terrestrial ecosystem can have different impacts on the atmospheric CO₂ content. While plant photosynthesis during daytime produces a sink for atmospheric CO₂, soil respiration and other oxidization processes such as decomposition or oxidation of organic materials generate a source of atmospheric CO₂.

The total amount of CO₂ uptaken by plants is known as gross primary production (GPP) (*IPCC*, 2001). The CO₂ interacts with water inside leaves and its oxygen isotope changes from ¹⁶O to ¹⁸O. Many of these CO₂ molecules participate in photosynthesis process and diffuse out again which make them measurable in the atmosphere (*Ciais et al.*, 1997). By measuring this CO₂ type, the contribution of plants in the uptake of the atmospheric CO₂ can be estimated. About half of the uptaken CO₂ amount, known as net primary production (NPP) remains in the plants and is consumed for growing new plant tissues such as leaves, roots and woods; the rest returns to the atmosphere by plant tissue respiration (*Lloyd and Farquhar*, 1996; *Waring et al.*, 1998). Ultimately, all the carbon which is used for growing plant tissues comes back to the atmospheric reservoir mainly by two processes; plant and soil respiration by bacteria, some fungi types and herbivores; and natural combustion or human-made fires (*IPCC*, 2001). The amount of carbon that is lost or gained by every ecosystem can be influenced by anthropogenic activities, perturbation in the natural ecosystem and climate variability (*IPCC*, 2001). However, currently, the terrestrial ecosystem acts as a global sink for atmospheric carbon (*IPCC*, 2013).

The growth of the human population and consequently the increase in the request for more food as well as wood products have caused deforestation in large areas and land use change mainly for growing more agricultural products. These activities have decreased the ability of the ecosystem for uptaking the atmospheric CO₂. However, reforestation in Europe and North America has compensated this effect in recent years (*IPCC*, 2013). Some other important anthropogenic factors which affect the amount of CO₂ that can be uptaken by the

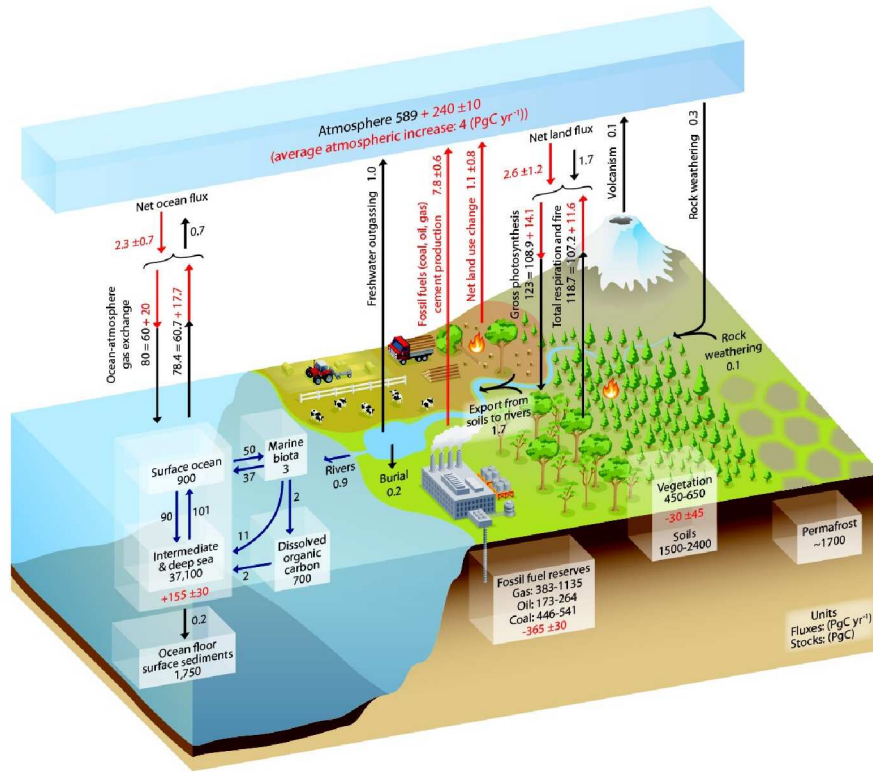


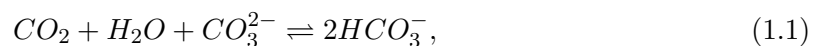
Figure 1.1: The carbon cycle between the 3 natural reservoirs, land, ocean and atmosphere. Black numbers and arrows show the estimated carbon mass in each reservoir and annual exchange fluxes between the three reservoirs for the time period before the industrial revolution. Red arrows represent the mean annual anthropogenic fluxes over time period between 2000 and 2009. Red numbers indicate the cumulative change of carbon in each reservoir due to the anthropogenic activities over the 1750-2011 industrial period (taken from *IPCC*, 2013).

terrestrial ecosystem are fire, drastic grazing and draining peatlands or wetlands for agricultural purposes (*IPCC*, 2001).

A significant amount of carbon is transported from soil to water through several ways. Carbon can be buried in the organic sediment of freshwater or it can go to the coastal ocean through rivers while parts of it may outgas as CO_2 and back to the atmosphere (*Tranvik et al.*, 2009). In the next subsection, the role of the ocean as the second most important natural reservoir in the global carbon cycle is presented.

1.2.2 Ocean

Higher solubility and chemical reactivity of CO_2 compared to other anthropogenic gases such as CH_4 and CFCs allows for a more efficient uptake by sea water (*IPCC*, 2001). The exchange of CO_2 between the ocean surface and the atmosphere can be shown as:



where CO_3^{2-} and HCO_3^- indicate the carbonate ion and bicarbonate ion (*IPCC*, 2013). This flux known as “*solubility pump*” is mainly due to the CO_2 partial pressure (pCO_2) difference

between ocean surface and the atmosphere as well as the solubility of CO_2 . The solubility by itself is a function of temperature and gas transfer coefficient (*IPCC*, 2001). The enhancement of the anthropogenic CO_2 in the atmosphere increases pCO_2 so that the uptake of atmospheric CO_2 by the surface ocean rises which is a superimposed uptake on the global natural transfer (*IPCC*, 2001; *IPCC*, 2013). The dissolved CO_2 in the ocean is known as Dissolved Inorganic Carbon (DIC). As Eq. 1.1 shows, the DIC is found in three main forms. The biggest part belongs to the bicarbonate ion (HCO_3^- , about 90%) where the carbonate ion (CO_3^{2-} , about 8%) and the dissolved CO_2 (non-ionic about 1%) are quite smaller parts (*IPCC*, 2001).

Another main source of carbon in the ocean is the Dissolved Organic Carbon (DOC) (*IPCC*, 2013). The DOC is a result of the gross primary production produced by phytoplanktons and other microorganisms in the ocean. The DOC together with dead organism and detritus transfer organic carbon vertically into the deeper ocean. Part of this production remains as the net primary production of the ocean (the main source of the DOC) while the other part is returned to the DIC through autotrophic respiration i.e. respiration by photosynthetic organisms. The sinking of a fraction of the DOC along with other particular organic carbon which is composed of dead organisms and detritus create a downward flux of organic carbon from upper ocean known as *export production* (*IPCC*, 2001). A very small fraction (less than 1%) of this export production remains in the ocean reservoir as sediments, mostly in the coastal ocean. The rest converts to the DIC. Without this mechanism which is known as *biological pump*, the atmospheric concentration would be about 200 ppm higher than its current concentration (*Sarmiento and Toggweiler*, 1984; *Maier-Reimer et al.*, 1996).

Conceptually, the ocean has enough capacity to uptake more than 70 to 80% of anthropogenic atmospheric CO_2 . However, the solubility rate of CO_2 in the ocean surface sets a considerable limit for this capacity meaning that the ocean needs several hundred years to reach this capacity (*Maier-Reimer and Hasselmann*, 1987; *Enting et al.*, 1994; *Archer et al.*, 1997). Since the atmosphere is the smallest reservoir of the carbon cycle, any slight change in the atmospheric carbon amount (particularly in the atmospheric CO_2 as a main carbon barrier in the atmosphere) can cause a significant effect on the global carbon cycle. This indicates the importance of tracking the atmospheric CO_2 content. Accurate measurements of the CO_2 content in the atmosphere can help to properly estimate the effect of rising the human-emitted CO_2 mainly on the future climate. In the next section the history of atmospheric CO_2 measurements, as well as recently-used methods and instruments in this field, are presented.

1.3 Atmospheric CO_2 measurement

Reliable prediction of future atmospheric CO_2 concentration and its impact on the earth climate need accurate measurements of its mean atmospheric concentration as well as its diurnal, seasonal and annual cycles in the atmosphere. In this section different kinds of atmospheric CO_2 measurements i.e. in-situ, space-based and ground-based measurements, together with their advantages and deficiencies, are introduced.

1.3.1 In situ measurements

Because of the long lifetime of the atmospheric CO_2 (*Archer et al.*, 1997), even a local measurement can represent approximately the CO_2 global trend. There are many in situ measurements of CO_2 around the world; the oldest one is the Mauna Loa observatory located in

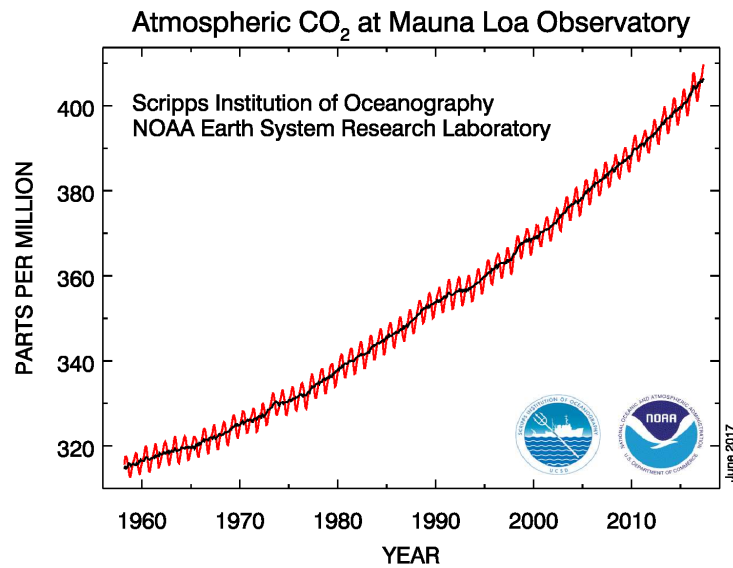


Figure 1.2: The CO₂ volume mixing ratio measured at the Mauna Loa Station in Hawaii. The data are presented from 1958 to June 2017 (taken from <http://esrl.noaa.gov/gmd/>).

the Hawaiian Islands (*Keeling et al., 1976*). The hourly collected air samples at the top of four 7-m towers are analyzed using a nondispersive infrared gas analyzer in order to determine the CO₂ concentration. Fig. 1.2 shows the long term observation of the CO₂ volume mixing ratio (VMR) provided by this site from 1958 to 2017. In addition to the seasonal cycle of CO₂ which can be seen clearly in the plot, it shows the significant increase of atmospheric CO₂ during last 60 years in a way that it reached up to 400 ppm in 2016.

In addition to the Mauna Loa station, the Scripps Institution of Oceanography (SIO) air sampling network has 11 observatory stations for recording the atmospheric CO₂ which are distributed mainly on the Pacific Ocean (<http://cdiac.ornl.gov>). Furthermore, the In-Situ Measurement Program of the Global Monitoring Division (GMD), belonging to the National Oceanic and Atmospheric Administration (NOAA)'s Earth System Research Laboratory (ESRL), monitors several greenhouse gases including CO₂ to analyze its short term and long term variations. These in situ measurements include 4 NOAA Baseline Observatories at Barrow, Mauna Loa, American Samoa and South Pole; and a tall tower network in US (e.g. *Thoning et al., 1989; 2000; www.esrl.noaa.gov*). These in-situ measurements mainly use the nondispersive infrared gas analyzer to determine the CO₂ concentration of the collected air samples at the towers. Besides, there are also some long term CO₂ observatory stations around the world such as the Amsterdam Island station that was located in the south Indian Ocean 5000 km off South Africa. It measured data from 1980 to 1995 (*Gaudry et al., 1983, 1991; Lambert et al., 1995*); The K-puszta air pollution monitoring station that was set in Hungarian Great Plain and provided CO₂ measurements between 1981-1997 (*Haszpra, 1995*); The Jubany Station on King George Island, Antarctic belongs to the Italian PNRA (National Research Program in Antarctica) and performed continuous CO₂ measurements recording from 1994 to 2009 (e.g. *Ciattaglia et al., 1997*) and the Baring Head station in New Zealand which provided data from 1970 to 1993 (e.g. *Manning and Pohl, 1986*).

In addition to the ground-based in-situ measurements, there are radiosonde-based in-situ

instruments such as AirCore (Karion et al., 2010) which is a stainless steel tube and can evacuate while ascending in order to collect the air samples while its descending. Moreover, the aircraft-based in-situ measurements collected during flight campaigns are used to validate and evaluate other measurements (Wunch et al., 2010, Messerschmidt et al., 2011). As an example, a flight campaign in 2009 over Europe which was used for calibration of ground-based CO₂ measurements (Messerschmidt et al., 2011).

1.3.2 Space-based measurements

Recent significant progress in satellite measurements had a considerable impact on the study of the chemical components of the earth atmosphere such as CO₂ and O₃. The big advantage of satellite measurements is to provide a global view of the atmospheric CO₂ which is a practical tool for studying CO₂ sinks and sources on the surface (Raven and Falkowski, 1999).

One of the first atmospheric CO₂ concentration retrievals from a space-borne instrument belongs to the Television and InfraRed Operational Satellite-Next generation (TIROS-N) Operational Vertical Sounder (TOVS) that was flown on-board the NOAA polar meteorological satellites (Chédin et al., 2002). Infrared and microwave observations from the High resolution Infrared Radiation Sounder (HIRS-2), the Microwave Sounding Unit (MSU) and the Stratospheric Sounding Unit (SSU) over the tropic [20S:20N] for the period of July 1987–June 1991 were used for retrieving the monthly mean mid-tropospheric CO₂ concentration. The results show good agreement with the present knowledge of the seasonal and annual atmospheric cycles (Chédin et al., 2002, 2003).

In March 2002, the European Space Agency (ESA) launched the environmental satellite ENVISAT carrying the SCanning Imaging Absorption spectroMeter for Atmospheric CHartography (SCIAMACHY) (Burrows et al., 1995, Bovensmann et al., 1999). SCIAMACHY measured the upwelling radiation in near-infrared region from 240 to 2400 nm. The derived dry air column averaged mixing ratios, X_{CO₂} from clear sky measurements over land showed good agreement with global model data. In addition, for the first time, a regional source/sink map of CO₂ on earth was detected from the space using the SCIAMACHY observation (Buchwitz et al., 2005).

In addition, NASA's Aqua satellite was also launched in May 2002. Thermal infrared radiation near the CO₂ absorption line at 15 μm has been measured by the Atmospheric Infrared Sounder (AIRS) on-board this satellite. Due to the strong absorption of this band, the instrument could not get any information about the CO₂ near surface layer. Therefore, the measurements are limited to the mid-tropospheric CO₂ concentration between 5 and 7 km (Crevoisier et al., 2004). A global map of the CO₂ amount in the upper troposphere at a resolution of 15°×15° is derived from monthly measurements over cloud-free condition (Crevoisier et al., 2004; Chevallier et al., 2005).

The Greenhouse gases Observing SATellite (GOSAT, IBUKI in Japanese) is the first satellite dedicated to measuring greenhouse gases (Kuze et al., 2009). GOSAT was a joint project of Japan Aerospace Exploration Agency (JAXA), the National Institute for Environmental Science (NIES) and the Ministry of the Environment (MOE), which was launched on 23 January 2009 (Kuze et al., 2009). One instrument on-board GOSAT is the Thermal And Near infrared Sensor for carbon Observation (TANSO) that is a Fourier Transform Spectrometer (FTS). The TANSO_FTS uses a Michelson interferometer with two sets of detectors. It can observe the solar radiation reflected from the earth only during the daytime as well as atmospheric thermal radiation during both daytime and nighttime (Kuze et al., 2009). The

shortwave radiance have been used to get information about CO₂ concentration near the earth surface while the thermal radiation has provided CO₂ concentration mainly above 2 km (*Saitoh et al., 2009*). Only observations of clear sky condition can be applied for retrieving the column averaged amount, X_{CO_2} (*Saitoh et al., 2009*). The first validation of its retrieved data was performed using measurements from a ground-based network. It showed a negative bias equal to 8.85 ± 4.75 ppm for X_{CO_2} . However, both data showed similar CO₂ seasonal cycle for the Northern Hemisphere (*Morino et al., 2011*).

Another satellite dedicated to studying atmospheric CO₂ is the Orbiting Carbon Observatory-2 (OCO₂, the first one lost during the launch in 2009) which was designed to capture regional CO₂ sinks and sources on the earth surface. The OCO₂ was launched on 2 July 2014. Its first data was sent on 6 September 2014 (*Crisp et al., 2017*). Same as GOSAT, OCO₂ also measures reflected sunlight from the earth surface to retrieve the X_{CO_2} . Around 7 to 12 % of its monthly measurements belonging to cloud free conditions, have been used to derive the monthly mean value of X_{CO_2} (*Crisp et al., 2017*). The analysis of its first 18 months of data revealed main features such as a considerable enhancement of X_{CO_2} from October until December over the eastern US and eastern China due to the strong fossil fuel combustion as well as enhanced X_{CO_2} in Amazon, central Africa and Indonesia because of biomass burning in this time period; a reduction of more than 10 ppm in the X_{CO_2} of Northern Hemisphere in May and June (compared to other months of year) due to the plant photosynthesis and a significant north-south gradient of X_{CO_2} in May and June (*Eldering et al., 2017*).

1.3.3 Ground-based measurements

Although satellite measurements can give a global view of the atmospheric CO₂ concentration, they are usually rather poor in capturing fine CO₂ variations near the earth surface. Besides, high-precision independent datasets are needed for validation of space-borne measurements. For these reasons, ground-base measurements are designed and developed. The Total Carbon Column Observing Network (TCCON) is one of the best example of the ground-based network which was established in 2004. The main purpose of this network is to provide accurate measurements of X_{CO_2} (0.25% or less than 1 ppm precision) for studying the global and regional carbon cycle, for data assimilation studies and linking satellite measurements to ground based measurements (*Wunch et al., 2011*). Currently, there are 18 sites affiliated with TCCON where 15 of them are operational (*Wunch et al., 2011*). TCCON instruments use near infrared measurements with sensitivity to the atmospheric CO₂. Two detectors cover the sensitivity of entire spectral region from 3900-15500 cm⁻¹ which is the same spectral region used by different satellites particularly SCIAMACHY, GOSAT and OCO₂. As auxiliary measurements, accurate surface temperature and pressure measurements are used at each site (*Wunch et al., 2011*).

A comparison between Park Falls TCCON data with SCIAMACHY measurements in lower tropospheric levels showed the accuracy of SCIAMACHY for capturing the seasonal cycle of the X_{CO_2} as a result of growing plants on monthly time scales (*Barkley et al., 2007*). Furthermore, comparing retrieved CO₂ column amounts from five European TCCON sites with CO₂ profiles derived from an aircraft campaign over these sites showed the suitability of TCCON data for calibration and validation of nadir viewing satellites (*Messerschmidt et al., 2011*).

The TCCON measurements are limited to daytime measurements therefore these data are useless for capturing diurnal variations of CO₂ concentration particularly in lower atmospheric levels where these variations due to the plant photosynthesis and respiration as well

as boundary layer mechanism can be quite significant. Thermal infrared radiation can be measured both in daytime and nighttime. The high spectral resolution measurements of thermal infrared radiation which have sensitivity to several atmospheric trace gases including CO₂ can help to study the diurnal cycle of CO₂ near the earth surface. The Atmospheric Emitted Radiance Interferometer (AERI) is a ground-based instrument that measures the downwelling atmospheric thermal radiation from 520 cm⁻¹ (19 μm) to 3020 cm⁻¹ (3.3 μm) with a spectral resolution of better than 1 cm⁻¹ (Knuteson et al., 2004a). AERI was designed to improve and evaluate the line-by-line radiation codes as well as to retrieve boundary layer properties such as temperature and humidity profile (e.g. Revercomb et al., 2003; Turner et al., 2004). Its highly temporally and spectrally resolving measurements have already been used for retrieving the temperature and humidity profile (e.g. Löhnert et al., 2009). However, there are just a few studies about using its measurements for studying atmospheric trace gases. In the present work, the sensitivity of AERI measurements to the atmospheric CO₂ is analyzed and is used to provide proper information about the diurnal variation of CO₂ near the surface. In the next section, the main goal of this study and the structure of the thesis are described.

1.4 Goal and structure of the thesis

The analysis of atmospheric CO₂ variations mainly in the boundary layer is a great tool for studying the impact of the terrestrial ecosystem as well as sea-water on the atmospheric CO₂ concentration. However, capturing these variations needs accurate measurements during daytime and nighttime. Thermal infrared radiation which includes the 15 μm CO₂ line and is measurable during daytime and nighttime has the potential to be used in this respect. The main focus of the present work is to exploit these radiances in order to provide the atmospheric CO₂ variations in the boundary layer. This information can be used for studying land vegetation mechanisms such as photosynthesis and soil respiration. Such data are also valuable for the validation of different numerical models which predict the near surface CO₂ flux.

For this purpose, observations of the AERI instrument in 2012 at JOYCE are used. First the sensitivity of AERI radiances to the atmospheric CO₂ profile is analyzed. Then an algorithm named AERIOe (Turner and Löhnert, 2014) is used to retrieve the CO₂ profile in the boundary layer. The AERIOe is a variational retrieval algorithm which applies the optimal estimation method for retrieving the temperature and humidity profile. In the present study, the AERIOe is modified to retrieve the CO₂ profile mainly in the boundary layer. In order to evaluate the theoretical potential of the algorithm in retrieving the atmospheric CO₂ profile, the AERIOe is applied to simulated AERI radiances which are provided by an accurate line-by-line radiative transfer model. After that, the real calibrated measurements of the AERI in clear sky cases are used for retrieving the diurnal cycle of the CO₂ concentration. Then retrieval results are compared with in-situ tower measurements in Jülich. In chapter 2, a general description of radiative transfer theory as well as short description of the line-by-line radiative transfer model LBLRTM are presented, followed by a section about studying the sensitivity of simulated AERI radiances to the variation of the atmospheric CO₂ profile. Different instruments as well as all measurements and data products related to this work are described in chapter 3. Chapter 4 deals with the calibration and the quality control of AERI measurements at JOYCE in 2012. The principal of optimal estimation method and the retrieval algorithm AERIOe which are used in the present work are given in chapter 5. The modification of the AERIOe in order to retrieve the atmospheric CO₂ profile is given in

chapter 6. Applying the simulated AERI radiances in the modified AERIOe as well as its results are also presented in this chapter. In chapter 7, real AERI observation radiances are used in the AERIOe and the results are compared with another observation provided by the tower measurements at JOYCE. In addition, a discussion on some issues related to the real AERI observation radiances at JOYCE is given in this chapter. Finally, the summary of this study as well as the outlook for future work are presented in chapter 8.

Chapter 2

Radiative transfer

Electromagnetic radiation of the sun known as solar radiation consists of different wavelengths from gamma rays with wavelengths less than 0.01 nm to radio waves with wavelengths larger than 1 m. The maximum intensity of solar radiation occurs around 0.5 μm . In addition, earth and atmosphere also emit electromagnetic radiation called terrestrial radiation with its maximum intensity around 10 μm . According to the wavelength of the maximum intensity, solar radiation is named shortwave radiation while earth-atmosphere radiation is named longwave radiation.

Longwave radiation can be absorbed by several atmospheric trace gases such as H₂O, CO₂ and O₃ due to the interaction between the electromagnetic radiation and these atmospheric trace gases. This interaction can be characterized by radiative transfer theory. The main focus of the present chapter is to shortly explain the Radiative Transfer Equation (RTE) specifically for the infrared region in clear sky conditions. In the first section, the basic RTE is derived. Then the possible solutions of this equation in the infrared region are investigated in section 2.2 followed by an overview of weighting functions that show the absorption weighting of a trace gas in terms of atmospheric altitude. In section 2.4, the line-by-line calculation of atmospheric radiation is explained and a pretty accurate numerical model for simulating atmospheric radiation is presented. Finally, in the last section, the sensitivity of thermal radiation to the change of CO₂ content in the atmosphere is discussed. Detailed information can be found in many textbooks such as *Petty* (2006) and *Liou* (2002).

2.1 Basic radiative transfer in clear sky

The intensity of light (electromagnetic wave) may change along a path through a medium. This change is due to the absorption or scattering of the light by different elements of the medium and can be characterized by the extinction coefficient β_e .

$$\beta_e = \beta_a + \beta_s, \quad (2.1)$$

where β_a and β_s refer to the absorption and the scattering coefficients respectively. These two coefficients β_a and β_s mainly depend on the wavelength as well as physical medium. While scattering by a particle can be negligible for a specific wavelength in a specific medium, it can be very significant for another wavelength in the same medium. The single scatter albedo

\tilde{w} is a ratio that shows the relative importance of scattering compared to absorption in a defined medium.

$$\tilde{w} = \frac{\beta_s}{\beta_e} = \frac{\beta_s}{\beta_s + \beta_a}. \quad (2.2)$$

When this ratio goes to 0, scattering is negligible. Conversely, for a purely scattering medium, this ratio goes to 1. From now on, all equations in this chapter are obtained for the non-scattering atmosphere where \tilde{w} and β_s are negligible. In the next section, it is shown that why this assumption is valid for the present work.

For the clear sky atmosphere, absorption coefficients of several trace gases need to be considered. Therefore, the total atmospheric gas absorption can be written as a sum of each trace gas absorption:

$$\beta_a = \sum_i \beta_{a,i}. \quad (2.3)$$

In addition, the absorption coefficient can be written in terms of mass absorption coefficient k_a :

$$\beta_a = \rho k_a, \quad (2.4)$$

where ρ shows the density of each trace gas. Consequently, we have:

$$\beta_a = \sum_i \beta_{a,i} = \sum_i \rho_i k_{a,i}. \quad (2.5)$$

When the light passes through a medium with the extinction coefficient of β_a , its depletion along a path ds can be written as:

$$dI_\lambda = I_\lambda(s + ds) - I_\lambda(s) = -I_\lambda(s)\beta_a(s)ds, \quad (2.6)$$

where s shows the geometric distance between two points, I indicates the intensity of light and λ refers to the wavelength of the light. Note that I is considered as monochromatic meaning that it has a single wavelength. By integrating this equation from s_1 to s_2 , we have:

$$I_\lambda(s_2) = I_\lambda(s_1) \exp\left[-\int_{s_1}^{s_2} \beta_a(s)ds\right]. \quad (2.7)$$

The term in the bracket is a dimensionless parameter which is called optical path τ :

$$\tau = \int_{s_1}^{s_2} \beta_a(s)ds. \quad (2.8)$$

If the path is considered as a vertical distance, this term is known as optical depth or optical thickness and can be used as a vertical coordinate in the radiative application. Another useful parameter is transmittance t which is defined by:

$$t(s_1, s_2) = \exp[-\tau(s_1, s_2)]. \quad (2.9)$$

Eq. (2.7) can be reformulated with this new parameter:

$$I_\lambda(s_2) = t(s_1, s_2)I_\lambda(s_1). \quad (2.10)$$

Another important interaction for radiative transfer is emission. Based on the Kirchhoff law, in the local thermodynamic equilibrium, the absorption of a specific matter is equal to its emission:

$$dI_{abs} = -\beta_a(s)I_\lambda ds = -dI_{emit} = -\beta_a(s)B_\lambda(T)ds, \quad (2.11)$$

where $B_\lambda(T)$ shows the Planck function for a specific wavelength and temperature. This function gives the electromagnetic emission of a blackbody at a given temperature T in the thermal equilibrium. A blackbody is considered as a theoretically perfect absorber of all electromagnetic radiation which has no reflect on.

In general, for a non-scattering medium, the change in the radiation intensity can be written as:

$$dI_\lambda = dI_{abs,\lambda} + dI_{emit,\lambda} = \beta_a(s)(B_\lambda(T) - I_\lambda)ds, \quad (2.12)$$

or

$$\frac{dI_\lambda}{ds} = \beta_a(s)(B_\lambda(T) - I_\lambda). \quad (2.13)$$

Eq. 2.13 is called Schwarzschild's equation. This equation is the basic form of the radiative transfer equation (RTE).

The real atmosphere is often considered as a plane parallel atmosphere. The plane parallel atmosphere is an atmosphere whose parameters vary in the vertical direction, while these parameters in the horizontal direction are assumed to be homogeneous. Therefore the variation in the z direction, dz , can be used instead of ds and thus we have:

$$ds = \frac{dz}{\cos\theta} = \frac{dz}{\mu}, \quad (2.14)$$

where θ is the zenith angle between the z and the s direction and $\mu = \cos\theta$. Substitution of Eq. (2.14) in Eq. (2.13) and using the mass absorption coefficient k_a gives:

$$-\mu \frac{dI_\lambda(z, \mu)}{k_a \rho dz} = I_\lambda(z, \mu) - B_\lambda(T(z)). \quad (2.15)$$

In the next section, possible solutions of this equation in the infrared region are investigated.

2.2 Radiative transfer in the infrared region for clear sky condition

In the previous section, the RTE for the non-scattering plane-parallel atmosphere has been derived. This equation is well-suited for the thermal infrared region in the clear sky since the scattering of air molecules or aerosols, i.e. the only particles in a non-cloudy atmosphere, is negligible in the thermal infrared region. Therefore, the RTE can be characterized by two interactions, absorption and emission. For solving Eq. (2.15), two boundary conditions need to be defined. In a clear sky condition, the surface and the top of the atmosphere (TOA) can be considered as two appropriate boundaries. Note that the earth surface acts like a black body for the thermal infrared radiation and thus $I_{\lambda(surface)} = B_{\lambda(T_{surface})}$. Besides, the total optical depth of the atmosphere needs to be calculated. The optical depth for a certain wavelength τ_λ can be calculated as:

$$\tau_\lambda = \int_z^{z_\infty} k_{a\lambda}(z')\rho(z')dz'. \quad (2.16)$$

Rewriting the Eq. (2.15) with τ gives:

$$\mu \frac{dI_\lambda(\tau, \mu)}{d\tau} = I_\lambda(\tau, \mu) - B_\lambda(T(\tau)). \quad (2.17)$$

Solving this equation gives the upward and downward components of the atmospheric radiation.

$$I_{\lambda}^{\uparrow}(\tau, \mu) = B_{\lambda}(T(\tau_*))e^{-\frac{(\tau_* - \tau)}{\mu}} + \int_{\tau}^{\tau_*} B_{\lambda}(T(\tau'))e^{-\frac{(\tau' - \tau)}{\mu}} \frac{d\tau'}{\mu}, \quad (2.18)$$

$$I_{\lambda}^{\downarrow}(\tau, -\mu) = \int_0^{\tau} B_{\lambda}(T(\tau'))e^{-\frac{(\tau - \tau')}{\mu}} \frac{d\tau'}{\mu}, \quad (2.19)$$

where $B_{\lambda}(T(\tau_*))$ in Eq. (2.18) shows the emission from the earth. For the downward radiation, the emission from the TOA is $B_{\lambda}(TOA) = 0$. With these considerations, in Eq. (2.18), the first term shows the emission from the earth surface multiplied by the transmittance between the earth and an arbitrary altitude above it (shown by τ) which represents the attenuated emitted radiation of the earth surface. The second term in this equation is the integrated emission from each point between the earth and the arbitrary altitude. The downward radiation shown in Eq. (2.19) can be interpreted same as the upward radiation. The derived term in this equation shows the integrated emission between TOA and an arbitrary altitude below it (shown by τ).

The most important atmospheric trace gases which lead to absorption and emission in the infrared region are H_2O , CO_2 and O_3 . The energy that is absorbed by a trace gas molecule can change into the different types of molecular energy such as translational kinetic energy, rotational kinetic energy, vibrational energy or it can change its electrical charge distribution. While the translational kinetic energy of a molecule can have any continuous amount, the values of other three types of molecular energy are quantized. The quantized energy level means that the molecule can not have any arbitrary amount of energy and thus the energy levels are discrete such as E_0, E_1, \dots, E_n . The electromagnetic radiation is also quantized. The quantized unit of electromagnetic energy is called photon. Based on quantum mechanics, the energy E of a single photon is proportional to its wavelength/frequency.

$$E = \frac{hc}{\lambda} = h\nu, \quad (2.20)$$

where h is the Planck constant and c shows the speed of light; ν and λ refer to wavelength and frequency of the photon respectively. A molecule can absorb/emit a photon, if the energy of the photon changes its molecular energy from one of its allowed state to another one meaning that only absorption/emission of a specified wavelength/frequency is allowed by a molecule. Before reviewing the absorption/emission lines of atmospheric trace gases in the thermal infrared region, some fundamental concepts and definitions related to this topic are shortly summarized.

2.2.1 Vibrational and rotational transition

While the energy related to the microwave and far-infrared spectral bands can only change the rotational energy levels of a molecule and is too low for changing the molecular vibrational energy, the mid-infrared and near-infrared spectral region can change both the rotational and vibrational energy levels of a molecule. For changing the molecular electrical energy levels, higher frequency or lower wavelength such as visible or UV bands are needed. The focus of this section is on the thermal infrared or mid-infrared region and the different types of the molecular energy transition related to this region.

A pure vibrational transition is a transition from one allowed vibrational level to another one. The spectral band related to the pure vibrational transition is called Q branch. For

example, a linear triatomic molecule such as CO_2 has three different types of vibrational modes consisting of ν_1 , ν_2 and ν_3 corresponding to the symmetric stretch, bending and asymmetric stretch respectively. However, in reality, the vibrational and rotational transition may happen together. Consequently, the rotational levels which are shown by quantum number J can split the vibrational levels into finer ones. The Q branch is related to the $\Delta J = 0$ and the spectral bands corresponding to $\Delta J = -1$ and $\Delta J = +1$ are called P and R branch respectively. The P and R branches present the vibrational-rotational transitions that are related to the emission or absorption lines slightly lower/higher than a pure vibrational line.

2.2.2 Line broadening

From the previous explanation given in section 2.2.1, one might assume that the absorption or emission lines have an exact frequency and thus should have a zero line width. However, in reality, they have a finite width. There are several reasons behind this physical phenomenon. Some important ones, i.e. natural, pressure and Doppler broadening are summarized in the following.

The Heisenberg uncertainty principal is the fundamental reason for the line width which is called natural broadening. However, compared to other reasons, natural broadening is relatively small. In addition, in the troposphere and stratosphere with higher pressure and thus higher density of air molecules compared to the upper atmosphere, collision between air molecules disturb the basic absorption/emission molecular lines which is called pressure broadening. In the upper atmospheric levels such as the mesosphere and above it where the air molecules can move without restriction, the Doppler broadening is more significant. The Doppler effect due to the speed of air molecules can cause the Doppler-shift in the absorption/emission wavelength of the molecules.

2.2.3 Continuum absorption

As it is mentioned in the previous subsection, in reality an absorption/emission line has a finite width meaning that the line needs to be characterized with a line shape. The Lorentz line shape is the one which is used widely. This line shape is derived based on the instantaneous interaction between two molecules. This assumption agrees well for the weak interaction; however, the close-range interaction deviates significantly from the Lorentz shape. For simplicity, an absorption/emission line is separated into two contribution, local line contribution and continuum contribution. The local line contribution can be considered as the spectral absorption up to some fixed distance from the line center (typically 25 cm^{-1}) and any deviation from the Lorentz shape within the line cutoff considered as continuum absorption (*Turner and Mlawer, 2010*).

The most important continuum absorption in the troposphere is water vapor continuum. Although there is not any strong absorption line in 800 to 1200 cm^{-1} , due to the water vapor continuum absorption, there is considerable thermal energy in this region. It has been shown that the optical depth of water vapor continuum absorption in this region varies with the square of the atmospheric water vapor amount which implies that these continuum bands are due to the interaction of two water vapor molecules known as “self-continuum”. In addition, the interaction of water vapor molecules with different types of molecules can produce the continuum absorption known as foreign water vapor continuum. *Clough et al.*

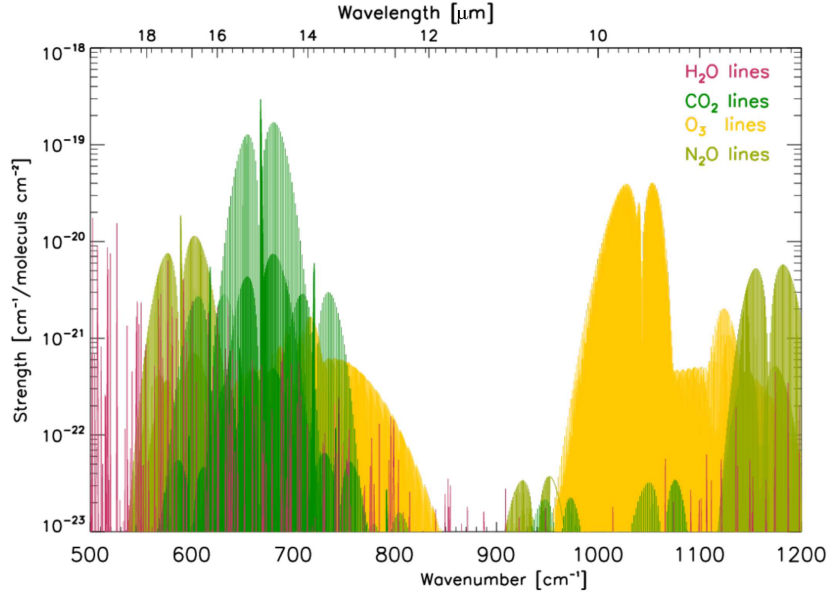


Figure 2.1: Absorption lines of different atmospheric trace gases in the mid-infrared region. The absorption lines are based on the HITRAN database.

(1989) using a generalized line shape and semi-empirical parameters modeled the observed self-continuum absorption and showed that water vapor continuum absorption due to the far wings of resonant lines can be hundred of wavenumbers (cm^{-1}) away from the center of resonant lines.

2.2.4 Some important atmospheric gas absorbers in mid-infrared

Fig. 2.1 shows the absorption lines of some important atmospheric gas absorbers in the infrared region from 500 to 1200 cm^{-1} . These lines are taken from the high-resolution transmission molecular absorption (HITRAN) database (*Rothman et al., 2013*) which is a widely-used database and provides absorption lines of several trace gases with high accuracy. One important absorber in this region is CO_2 which has the resonant line at the line center of $15 \mu\text{m}$ which is spread from 600 to 800 cm^{-1} . This line is a ν_2 line and composed of finer rotational lines with three branches, P, Q and R. Another feature in this region is strong absorption of H_2O molecules at the wavelength longer than $15 \mu\text{m}$. In addition, the water vapor continuum absorption due to the far wings of the resonant lines are spread from 800 to 1200 cm^{-1} . The other important trace gas in this region is O_3 which has the resonant line at the center of $9.6 \mu\text{m}$. However, the O_3 is not the subject of this work since its absorption occurs mainly in the stratosphere. Moreover, the contribution of the N_2O in the spectral band from 510 to 610 cm^{-1} ($17 \mu\text{m}$) as well as in the spectral band higher than 1100 cm^{-1} ($7.9 \mu\text{m}$) can be seen in the plot.

2.2.5 Example of downwelling atmospheric infrared measurement

Fig. 2.2 shows the high resolution downwelling atmospheric radiation in the mid-infrared region measured by a ground-based infrared spectrometer called Atmospheric Emitted Radiative Interferometer (AERI) in Jülich, Germany. The data have been taken during a clear

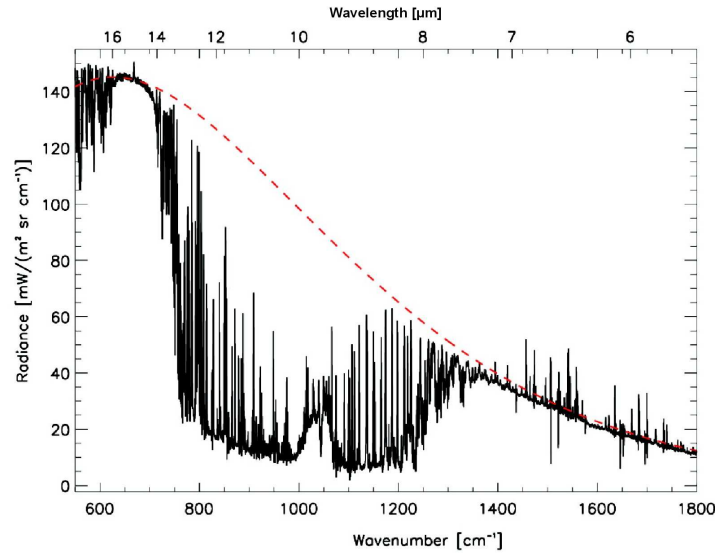


Figure 2.2: Downwelling atmospheric radiation in the mid-infrared region measured by the AERI in Jülich, Germany. Dashed red line shows the Planck curve at the temperature equal to 300 K.

sky hour on 25 of May, 2012. The dashed red line shows the calculated Planck function at a temperature of 300 K representing the near surface air temperature. As the plot shows, in two regions, i.e. in $1400\text{--}1800\text{ cm}^{-1}$ and in $550\text{--}700\text{ cm}^{-1}$, the downwelling radiances are very close to the Planck curve. This implies that the atmosphere in these regions is relatively opaque and radiation comes from the nearest levels close to the surface. In the region with wavelength $\lambda > 14\text{ }\mu\text{m}$ ($\nu < 730\text{ cm}^{-1}$) two important features are strong absorption by the CO_2 molecules in the vicinity of $15\text{ }\mu\text{m}$ and strong absorption by the H_2O molecules at the wavelength longer than $15\text{ }\mu\text{m}$. The peak in the center of the CO_2 band shows the pure vibrational line (Q branch) with the strongest absorption. Therefore, the emitted radiation comes from the levels close to the surface e.g. a few couple of meters above the surface. The right side of the CO_2 Q branch belongs to the vibrational-rotational band (R branch) with quantum number $\Delta j = +1$ and the left side belongs to vibrational-rotational band (P branch) with quantum number, $\Delta j = -1$. The second region which is close to the Planck curve belongs to the $\lambda < 8\text{ }\mu\text{m}$ ($\nu > 1270\text{ cm}^{-1}$) which is also related to the strong absorption of H_2O molecules. The plot clearly shows that the atmosphere is also quite opaque in this region. The spectral band from $8\text{--}13\text{ }\mu\text{m}$ shows the radiation far below the Planck curve which means this radiation should be originating from higher atmospheric altitude. This spectral band is regarded as a window region. In the window region, the atmosphere is quite transparent in cloud-free scenes since there is no strong absorption line in the window region. However, this window region ($8\text{--}13\text{ }\mu\text{m}$) is divided into many micro windows due to individual weak water vapor continuum absorption. Another exception in this window region is the O_3 line at $9.6\text{ }\mu\text{m}$. Since the O_3 molecules are mainly in the stratosphere, the radiation at this line comes from higher atmospheric levels compared to the CO_2 and water vapor where the density of O_3 molecules are much higher.

As it is mentioned in section 1.4, the aim of the present study is to get information about the CO_2 concentration in the boundary layer. Therefore it should be known in which altitude the main absorption of CO_2 (or generally each trace gas) occurs. This helps to know how much information comes from which atmospheric level which makes the retrieval of atmospheric

CO₂ profile from a ground-based measurements possible. Answering this question leads to definition of the absorption weighting of each trace gas in terms of the atmospheric altitude.

2.3 Weighting function

An important question in calculating the atmospheric radiation from the perspective of a sensor is to find the altitude where the maximum absorption rate of an individual line occurs. For answering this question, the absorption rate of a wavelength in terms of atmospheric altitude should be determined. Eq. (2.9) gives the transmittance between two arbitrary points. If a vertical distance between an arbitrary altitude z and TOA is considered, the transmittance can be written as:

$$t(z) = \exp \left[-\frac{\tau(z)}{\mu} \right]. \quad (2.21)$$

And thus for the absorption, we have:

$$a(z) = 1 - t(z). \quad (2.22)$$

Consequently, the absorption between two altitudes z_1 and z_2 (refer to Eqs. 2.9 and 2.14) can be written as:

$$a(z_1, z_2) = t(z_1) - t(z_2). \quad (2.23)$$

If the distance between these two altitudes goes to an infinitely small distance, the local absorption related to this particular altitude is defined as:

$$W(z) = \lim_{\Delta z \rightarrow 0} \left[\frac{a(z, z + \Delta z)}{\Delta z} = \frac{t(z + \Delta z) - t(z)}{\Delta z} \right], \quad (2.24)$$

or

$$W(z) = \frac{dt(z)}{dz}, \quad (2.25)$$

where $W(z)$, known as weighting function relates the local absorption rate to the local rate of the transmittance change. Weighting function can be also written in terms of optical depth and absorption coefficient:

$$W(z) = \frac{\beta_a(z)}{\mu} e^{-\frac{\tau(z)}{\mu}} = \frac{\beta_a(z)}{\mu} t(z). \quad (2.26)$$

This relation shows the transmittance from an arbitrary altitude to the TOA which is multiplied by the absorption coefficient. As it has been mentioned, the altitude with the strongest absorption needs to be calculated. Consequently, the derivative of Eq. (2.26) with respect to z needs to be taken and set to zero.

$$\frac{dW(z)}{dz} = 0 \quad (2.27)$$

The details relates of solving this equation is not shown here (more details can be found in chapter 7, *Petty (2006)*). However, the final solution for the altitude with highest absorption can be written as:

$$\frac{\tau(z)}{\mu} = 1. \quad (2.28)$$

This formula states that the maximum absorption occurs where the optical depth in the direction of radiation from the TOA is equated to one.

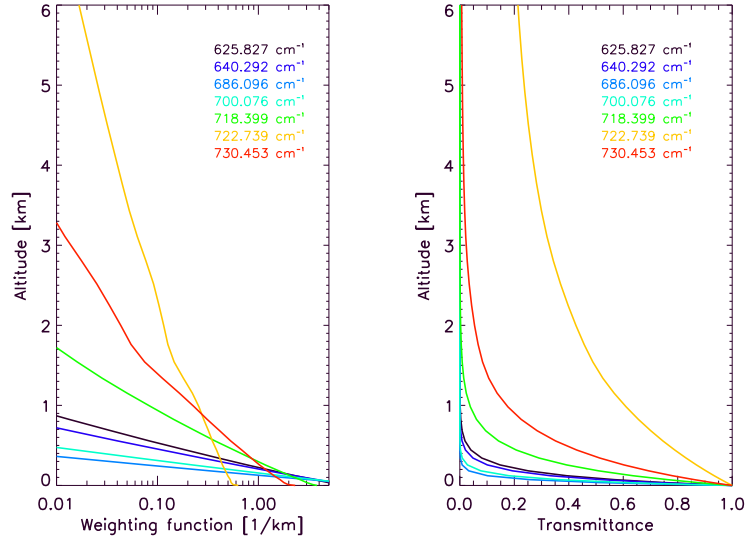


Figure 2.3: Weighting function (left plot) and the transmittance (right plot) of the downwelling atmospheric radiation (upward looking for a ground-based sensor) for 6 channels in the $15 \mu m$ CO_2 spectral band.

Fig. 2.3 shows the weighting function (left) and the transmittance (right) of the downwelling atmospheric radiation (can be derived from an upward looking ground-based sensor). Both plots are shown for 7 channels in the $15 \mu m$ CO_2 spectral band. While the transmittance for all channels is 1 at the surface, it goes rapidly to zero for the channels near the center of the $15 \mu m$, i.e. 625.827 , 640.292 , 686.096 and 700.076 cm^{-1} . Conversely, the transmittance of the channels at the edge of the line, i.e. 722.739 and 730.453 cm^{-1} goes to zero in relatively higher altitudes. Similarly, the weighting function shows that the channels at the center of the $15 \mu m$ band have strong absorption near the surface and all of them are nearly saturated below 1 km. These channels can mainly provide CO_2 information near the surface. On the other hand, the channels at the edge of the CO_2 band can provide information related to the CO_2 concentration in upper atmospheric levels.

2.4 The line-by-line radiative calculation

In section 2.2, the upward and the downward radiation for the non-scattering atmosphere has been shown. Alternatively, these equations can be written in terms of atmospheric levels, z and weighting function:

$$I_{\nu}^{\downarrow}(z) = \int_z^{\infty} B_{\nu}[T(z')]W_{\nu}(z', z)dz', \quad (2.29)$$

$$I_{\nu}^{\uparrow}(z) = B_{\nu}(T_s)t_{\nu}(0, z) + \int_0^z B_{\nu}[T(z')]W_{\nu}(z', z)dz', \quad (2.30)$$

In order to expand this equation, $\beta_{\nu}(z)$ needs to be written as a sum over all trace gas absorption coefficients of the specific atmospheric level:

$$\beta_{a,\nu}(z) = \sum_{i=1}^N \rho_i(z)k_{a,i}(z), \quad (2.31)$$

where ρ_i presents the density of each atmospheric absorber in the specific atmospheric level, $k_{a,i}$ is the mass absorption coefficient of each N atmospheric trace gas absorbers. In other words, if radiation over the thermal infrared region is considered, information about the absorption coefficients of all atmospheric absorbers in this region is needed. As it is shown in Fig. 2.1, some of the main atmospheric absorbers in the thermal infrared region are H₂O, CO₂, O₃. In order to calculate k_a for each of these absorbers, accurate information about the shape, width and positions of the absorption lines of these absorbers including continuum and resonant lines are needed. Some of this information can be found in a line absorption database such as HITRAN database. Similarly, for calculating the monochromatic intensity at a specific atmospheric level, this procedure should be repeated for all atmospheric layers dz' in the integral of Eq. 2.29 or Eq. 2.30. This procedure for calculating the radiant intensity at an arbitrary level z is known as line-by-line calculation. The line-by-line calculation of downwelling or upwelling atmospheric radiation coincident with a satellite or ground-based measurements can help the comparison between calculated and measured radiances for validation or calibration of the measurements. In the following section, a powerful model which is used the line-by-line method for calculating the atmospheric radiation is shortly introduced.

The Line-By-Line Radiative Transfer Model (LBLRTM) (*Clough et al., 1992; Clough and J., 1995; Clough et al., 2005*) is an accurate radiative transfer model capable of performing monochromatic radiative transfer. It has been used to evaluate both ground-based, and space-based spectral radiance observations. It is also utilized to build radiative transfer model parameterizations that can be used in numerical weather prediction and climate models. The LBLRTM is originally based on the FASTCODE (*Clough et al., 1981*). In order to calculate the atmospheric radiation in the clear sky case, the model needs the input profiles of temperature and humidity as well as atmospheric trace gases such as CO₂, CH₄, N₂O and O₃. The first step is the calculation of the spectral optical depth. Note that the atmosphere is considered as a quasi-homogeneous in the horizontal direction. Then the radiance is calculated from the optical depth by a discrete radiative transfer equation. In order to use the LBLRTM simulated radiances to evaluate the real measurements, monochromatic radiances simulated by the LBLRTM need to be convolved with response functions to mimic realistic instruments. The code used the Clough-Kneizys-Daies (CDK) water vapor continuum model (*Clough et al., 1989*); however, in the early 2000s this model was modified and renamed the MT_CDK model (*Mlawer et al., 2012*). It also uses the HITRAN data base for its line base core. The details about the core of the LBLRTM including line shape, width, position and line coupling continuum model for different trace gases can be found in *Clough et al. (2015)*.

The Atmospheric Radiation Measurement (ARM) Program performed several campaigns in order to evaluate and improve the radiative transfer model while the LBLRTM was one of the important ones. One of the first evaluations of the LBLRTM radiances was a comparison of the LBLRTM radiances with the AERI radiances. However, the large uncertainty in the water vapor profile measurements as an input profile to the LBLRTM was the significant limitation in improving the LBLRTM model (*Revercomb et al., 2003*). In 1993, during the Pilot Radiation Observation Experiment (PROBE), the observations of Fourier transform infrared (FTIR) spectrometer from the National Oceanic and Atmospheric Administration (NOAA) was used to compare with the LBLRTM radiances. This comparison showed a large bias in the spectral band from 800 to 1000 cm⁻¹ for the moist tropical condition (*Mlawer and Turner, 2016*). Later analysis of this comparison showed that this large bias was due to the deficiency in the CDK continuum model of the LBLRTM. This result was also demonstrated, in 1996, using the new generation of the AERI as well as NOAA FTIR observations on the research

ship *Discoverer* (Han et al., 1997). Moreover, improving the accuracy of the measured integrated water vapor (IWV), between early 1990s and early 2000s, which reduced the measured IWV uncertainty from 15% to 3% (Turner et al., 2016), helped the further improvement in the CDK model of the LBLRTM, particularly in the accuracy of the spectral band 800-1300 cm^{-1} (Turner et al., 2004). The ARM program also performed the Surface Heat Budget of the Arctic Ocean (SHEBA) (Uttal et al., 2002) in order to improve the strong water vapor absorption band for wavenumbers less than 600 cm^{-1} . In this campaign an extended range of the AERI which measures the wavenumbers from 400 cm^{-1} was used. The result of this campaign demonstrated that the CDK continuum model in the far-infrared was approximately by a factor of 3 too strong (Tobin et al., 1999) and led to a significant improvement in the CDK model in this region. Further studies in this region as well as more observations from other campaigns provided useful information on the strength of the pure rotational water vapor band in 400-650 cm^{-1} region (Delamere et al., 2010).

Furthermore, in 2002, the AERI observation radiances as well as observations from High-resolution Interferometer Sounder (HIS) and Scanning HIS (S-HIS) were used to evaluate and modify the CO_2 line shape and CO_2 continuum band from 500 to 900 cm^{-1} in the LBLRTM (Mlawer and Turner, 2016).

In this work, the LBLRTM version 12.1 with the core of HITRAN 2008 (Rothman et al., 2009) data base is used. The calculated radiances in the thermal infrared region, from 650 cm^{-1} to 2760 cm^{-1} using this LBLRTM version were validated against the observed radiances provided by IASI satellite measurements for 120 nighttime clear sky cases (Alvarado et al., 2013). The comparison between calculated and observed radiances as well as comparison between the retrieved temperature profiles from both calculated and measured radiances showed a remarkable improvement in spectroscopy of the ν_2 and ν_3 bands of the CO_2 lines compared to the older version of the LBLRTM. This progress is due to several improvements in the HITRAN code such as the inclusion of the P- and R-branches CO_2 line coupling (Lamouroux et al., 2010) and improvement in the CO_2 and the water vapor continuum model. However, it was shown that still some residuals between observed and calculated radiances exist e.g. a residual around -0.5 K at 720 cm^{-1} , around 0.2 K between 755 and 770 cm^{-1} and also a small residual near the ν_3 band of CO_2 (Alvarado et al., 2013).

In the next section, the LBLRTM is used for calculating the downwelling atmospheric radiances in the thermal infrared region in order to determine the sensitivity of 15 μm CO_2 line to the change in the atmospheric CO_2 concentration near the surface during daytime and nighttime.

2.5 Sensitivity study

In order to find the sensitivity of the 15 μm CO_2 line to the diurnal variation of atmospheric CO_2 concentration mainly in the boundary layer, a sensitivity study is performed that is presented in this section.

The LBLRTM is used to calculate the downwelling atmospheric radiances at 15 μm CO_2 line (from 600 to 750 cm^{-1}). The input temperature and humidity profiles are taken from a regional numerical model called REMO (it is introduced in more details in section 3.6). The input atmospheric absorbers profiles such as O_3 , CH_4 and N_2O are considered as a constant

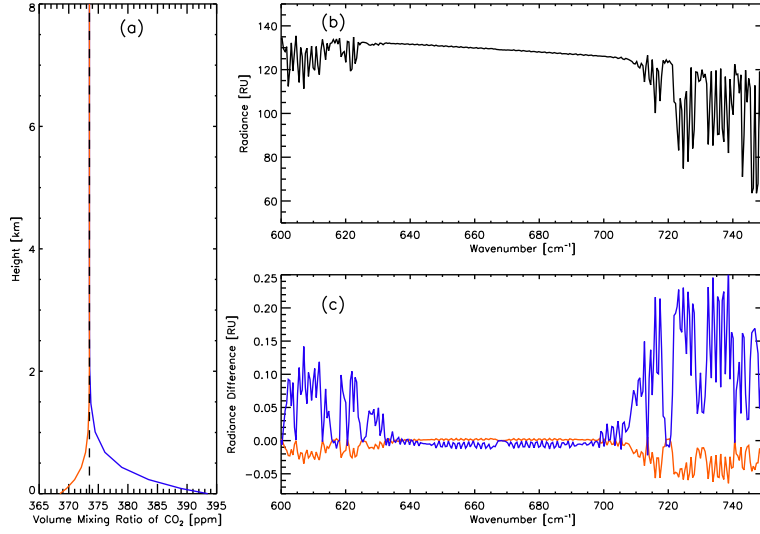


Figure 2.4: Calculated downwelling atmospheric radiances from 600 to 750 cm^{-1} using the LBLRTM. (a) A nighttime (blue) and a daytime (red) CO_2 profile for 25 of May, 2012. The dashed black line shows the constant CO_2 profile equal to 372 ppm. (b) The downwelling atmospheric radiation in CO_2 15 μm band using the dashed black CO_2 profile as an input profile for LBLRTM. (c) The radiance differences between the calculated radiance using the constant CO_2 input profile and the daytime CO_2 input profile (red) and; the same radiance difference for the nighttime CO_2 input profile (blue).

atmospheric profile where their constant mixing ratio are equated to a value close to their mean atmospheric concentration.

In the first run the input CO_2 profile is considered a constant profile of 373.5 ppm. The calculated radiances of this run are shown in Fig. 2.4b. In order to calculate the sensitivity of 15 μm CO_2 line to the diurnal change of the CO_2 profile, a typical daytime and nighttime CO_2 profile are considered which are shown in Fig. 2.4a. The constant CO_2 profile is also shown in this plot. The LBLRTM is then run using each of these CO_2 profiles (same temperature and humidity profiles). The radiance differences between the calculated radiances using the daytime CO_2 profile and the constant CO_2 profile as well as the radiance differences between the calculated radiances using the nighttime CO_2 profile and the constant profile are shown in Fig. 2.4c.

As the plot shows, in the spectral band between 625 and 710 cm^{-1} , the radiance differences for both runs with the nighttime and the daytime CO_2 profiles are relatively close to zero, which is an expected consequence of strong absorption in the Q-branch. As it is shown in Fig. 2.3, the spectral band in the center of 15 μm line has the strong absorption near the surface meaning that the atmosphere is quite opaque close to the center of 15 μm . Therefore, this spectral band does not have a significant sensitivity to the change in the CO_2 input profile. Conversely, the spectral bands at the edge of 15 μm line, i.e. 710-750 cm^{-1} and 600-625 cm^{-1} show relatively higher sensitivity to the change in the input CO_2 profiles. Since the nighttime CO_2 profile has an increase in the CO_2 concentration near the surface compared to the constant CO_2 profile, the simulated radiances using the nighttime profile minus the simulated radiances using the constant profile show a positive differences. Conversely, the simulated radiances using the daytime CO_2 profile minus the simulated radiances using the

constant CO₂ profile show a negative differences which is due to the decrease in the daytime CO₂ concentration near the surface compared to the constant CO₂ profile. These sensitivities can be used to get the information about the change in CO₂ concentration in the boundary layer, and thus they may be used to retrieve the CO₂ profile in the boundary layer.

In conclusion, this study illustrates that 15 μm CO₂ spectral band has valuable information related to the atmospheric CO₂ profile. However, in chapter 6, it is shown that the sensitivity of 15 μm CO₂ spectral band can be used to retrieve the CO₂ profile, if the noise characteristic of the instrument would be lower than this sensitivity.

Chapter 3

Instrument and model data

In this chapter, instruments as well as model data which are used in the present work, either for comparison to the retrieved results or taking as input data in the radiative transfer model, are shortly introduced. The main instrument that is used in the present study is a high spectral resolution ground-based spectrometer called AERI which was installed at Jülich Observatory for Cloud Evolution (JOYCE) (Löhnert et al., 2015). The AERI is introduced in the first section. In section 3.2, a brief explanation about the microwave radiometer which is another ground-based instrument at JOYCE is presented. Then the GPS data and the tower measurements are introduced in section 3.3 and 3.4 respectively. These measurements are also taken at JOYCE. Finally, two regional numerical models, COSMO_DE and REMO are described in the last two sections.

3.1 AERI

In the 1980s, the significant uncertainties in the radiative transfer parameterizations used in climate models forced the scientists to start a program in order to measure the highly spectrally resolved atmospheric radiation (Ellingson and Fouquart, 1991). This program initiated the Atmospheric Radiation Measurements (ARM) program by the Department of Energy (DOE) (DOE, 1990; Turner and Ellingson, 2016). In the mid-1980s, the University of Wisconsin-Madison space Science and Engineering Center (UW-SSEC) developed an airborne infrared interferometer that is called High-Resolution Interferometer Sounder (HIS) (Revercomb et al., 1988). HIS was built in order to retrieve temperature and humidity profiles with improved vertical resolution from space-based instrument (Revercomb et al., 1988). In addition, the success of the HIS during the Ground-Based Atmospheric Profiling Experiment (GAPEX; Smith et al., 1990b) led to a ground-based HIS (GB-HIS) design (Knuteson et al., 2004a). The development and operation of GB-HIS as well as funding support by ARM led to the first AERI system design called AERI-00 in 1992 (Knuteson et al., 2004a). The experience of deployment of the AERI-00 during a campaign led to first operational AERI (AERI-01) design by the UW-SSEC. AERI-01 was deployed at the Southern Great Plains (SGP) site in summer of 1995. The experiment of operating the AERI-01 on the SGP site led to the development of AERI_v2 system that was operated later on different ARM sites (Turner et al., 2016). Fig. 3.1 shows the AERI at JOYCE, Germany. The AERI at JOYCE was built by ABB/BOMEN Inc and was installed at JOYCE in 2011.



Figure 3.1: The AERI at Jülich Observatory for the Cloud Evolution (JOYCE), Germany. The photo was taken in 2013.

The AERI measurements showed good potential to analyze the water vapor continuum as well as high potential for validation of infrared radiative transfer models in clear sky cases (*Revercomb et al., 2003; Turner et al., 2004*); to study the cloud radiative and micro-physical properties in cloudy cases (*Collard et al., 1995; Mace et al., 1998; DeSlover et al., 1999; Turner et al., 2003*) and to provide the real time temperature and humidity profiles (*Feltz et al., 1998; Turner et al., 2000; Löhnert et al., 2009; Turner and Löhnert, 2014*). In the following section, first the AERI instrument design is presented. Then, in subsection 3.1.2, the processes in order to obtain radiometrically and spectrally calibrated AERI radiance from real observation as well as short explanation about the AERI noise are given. The main information for this section is taken from *Knuteson et al. (2004a)* and *Knuteson et al. (2004b)*.

3.1.1 Instrument design

The AERI is an automated ground-based spectrometer for measuring the downwelling atmospheric mid-infrared radiation with high temporal and spectral resolution. It measures the infrared radiation from 520 cm^{-1} ($19\text{ }\mu\text{m}$) to 3020 cm^{-1} ($3.3\text{ }\mu\text{m}$) in the zenith view with a spectral resolution of better than 1 cm^{-1} . The temporal resolution of the AERI can change from 8 min in the slow sample mode to 20 s in the rapid sample mode. While the slow sample mode is more appropriate for retrieving the temperature and humidity profiles, the rapid sample mode is well-suited to provide the information related to cloud properties.

The AERI is composed of two major parts, the optics bench assembly and the electronics support equipment. The main pieces of the optics bench assembly are an interferometer, two black bodies and two detectors. One AERI detector is responsible for longwave infrared band and is made of mercury cadmium telluride (HgCdTe), while the other one is responsible for the shortwave infrared band and is made of indiumantimonide (InSb). The optical part is thermally isolated from the ambient temperature by a thermal isolated box. The AERI interferometer consists of a helium-neon laser, a fixed mirror, a moving mirror and a beam splitter. The blackbodies that are utilized to calibrate the measured radiances, are called hot blackbody (HBB) and cold blackbody (CBB). The blackbodies are identical but they operate at two different temperatures. The CBB operates at the temperature near the ambient

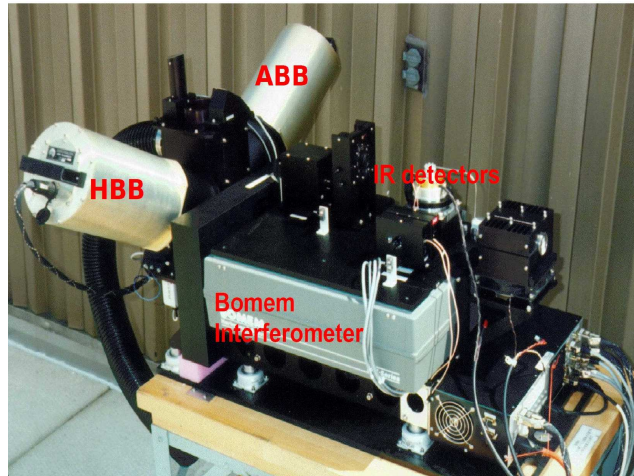


Figure 3.2: The optic part of the AERI. The hot blackbody (HBB), the ambient blackbody (ABB), the interferometer and detectors are shown in the picture (taken from *Knuteson et al. (2004a)*).

temperature while the HBB operates at a constant temperature near 60° C. The emissivity of the blackbodies are greater than 0.999 with an uncertainty better than $\pm 0.1\%$. Fig. 3.2 shows the optical part of the AERI.

The electronic support equipment consists of different parts where the most important ones are the blackbody temperature controller, a housekeeping system, a Sterling cooler and a control computer. The HBB temperature is controlled by the blackbody temperature controller in order to keep it at a certain temperature with a defined uncertainty. The Sterling cooler keeps the detectors at cryogenic temperatures (~ 77 K) to improve the signal-to-noise ratio of the observations. The housekeeping system measures temperatures and voltages at different parts of AERI in order to control the instrument performance. The control computer is used to control different processes inside the AERI such as working the housekeeping system, continuously receiving the data and the performance of the interferometer.

3.1.2 Data acquisition

As it has been mentioned in the previous subsection, the optics bench assembly of AERI includes an interferometer which is used to produce an interferogram. The atmospheric radiation which goes to the interferometer is divided into two parts using the beamsplitter. One part goes to the fixed mirror while the other one goes to the moving mirror. The moving mirror has continuous forward and backward movement. The reflected beams from two mirrors are combined together while the difference in their path cause a phase difference between two beams. Consequently, the combined beam produce an interference pattern which is called interferogram. The Fourier transform is then used to convert the raw interferogram to the radiance spectra. Note that the raw interferograms are real numbers but they are not necessarily symmetric around zero path delay (i.e., the part of the interferogram where the distance between the moving mirror and the beamsplitter is the same as the distance between the fixed mirror and the beamsplitter). At zero path delay, there is no destructive interference at any wavelength, and effectively the detector is sensing the spectrally integrated contribution from all wavelengths. Fig. 3.3 shows an example of the raw interferogram and the

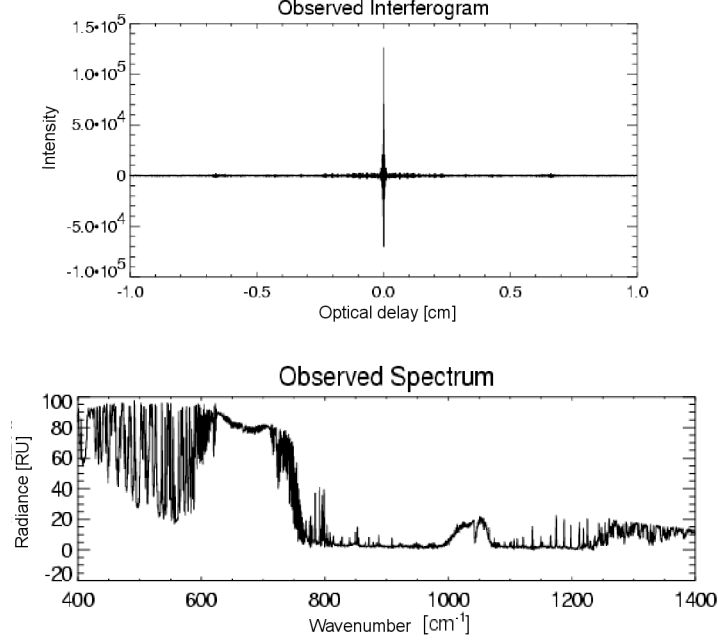


Figure 3.3: The raw interferogram derived from an AERI interferometer (upper plot) and the AERI radiances which are computed by applying the FT on the raw interferogram (lower plot). Source: *personal communication with D. D. Turner*.

calculated radiances. The high peak in the center of the interferogram shows the integrated contribution for the zero path delay where there is no destruction.

Two black bodies of the AERI are used to derive the radiometric calibrated radiances. For this reason, one or multiple sky views (depending on the instrument configuration) are sandwiched between looking to the black bodies of the form HASAHS, where H and A represent looking to the HBB and CBB respectively; and S represents the sky view. A gold mirror is used to select the scene being viewed, i.e., the sky view, ABB view or HBB view. The calibrated radiance for a specific wavenumber ν that is given by N_ν , is calculated using the radiometric calibration (Revercomb et al., 1988) as:

$$N_\nu = \text{Re}\left\{\frac{I_\nu^S - I_\nu^C}{I_\nu^H - I_\nu^C}\right\}(\hat{B}_\nu^H - \hat{B}_\nu^C) + \hat{B}_\nu^C, \quad (3.1)$$

$$\hat{B}_\nu^H = e_\nu^H B_\nu(T^H) + (1 - e_\nu^H)B_\nu(T^R), \quad (3.2)$$

$$\hat{B}_\nu^C = e_\nu^C B_\nu(T^C) + (1 - e_\nu^C)B_\nu(T^R), \quad (3.3)$$

where $\text{Re}\{\}$ refers to the real part of the argument; I_ν is the complex spectra derived from the observed interferogram; B_ν is the Planck function radiance at the observed temperature; and e_ν is the blackbody emissivity. T^R shows the reflected temperature that is the temperature of the environmental radiance that enters the blackbody and is reflected back to the detector. Note that the H, C and S refer to HBB, CBB and sky view respectively.

The imaginary part of the complex radiance, D_ν , is an estimation of each observed scene noise and computed as:

$$D_\nu = \text{Im}\left\{\frac{I_\nu^S - I_\nu^C}{I_\nu^H - I_\nu^C}\right\}(\hat{B}_\nu^H - \hat{B}_\nu^C), \quad (3.4)$$

where $\text{Im}\{\}$ refer to the imaginary part of the radiance. The variation of D_ν over different spectral bands can be used to evaluate the quality of the observed radiances and it gives an estimation of observed radiance noise.

Another important factor that provides a quality assessment of the instrument performance is the instrument responsivity, H_ν defined as:

$$H_\nu = \frac{I_\nu^H - I_\nu^C}{\hat{B}_\nu^H - \hat{B}_\nu^C}. \quad (3.5)$$

Comparing this equation with Eqs. 3.1 shows that the responsivity is the inverse of the radiometric calibration equation slope. The responsivity of the system depends on different factors where the important one is the instrument optical transmission and this factor in particular depends on the state of the gold scene mirror. The stability of the responsivity over the time can be used as a valuable test to find the noisy data in order to remove them.

As mentioned, the AERI uses the interferometer to produce the interferogram for each sky view and the interferogram is converted to the AERI spectrum using the Fourier transform. In a Fourier transform spectrometer, the interferogram sampling interval corresponding to the optical path delay is used for the spectral calibration. In the AERI interferometer, the laser fringe is used to provide this sampling. For each AERI detector, the wavenumber scale is given by:

$$\nu = (i - 1)\Delta\nu, \quad (3.6)$$

where i changes from 1 to N_{DS} and $\Delta\nu = \nu_{eff}/N_{DS}$. ν_{eff} refers to the effective sampling frequency and N_{DS} presents the number of points in a produced interferogram that is equal to 32768 in the AERI system. The effective sampling frequency is determined by:

$$\nu_{eff} \cong \nu_{laser}(1 + b^2/4), \quad (3.7)$$

where b shows the half-angle of the AERI field of view that is equal to the interferometer field of view. The nominal ν_{eff} of an AERI is known by design and is called true or reference frequency. For the AERI at JOYCE, with $b=16$ mrad and HeNe laser frequency= 15798.02 cm^{-1} , the effective laser frequency is 15799.0 cm^{-1} . However, after deployment of the instrument in the field, any misalignment between laser optical paths and the infrared paths can change this reference frequency and cause an inconsistency in the wavenumber calibration. Therefore, after deployment, the data needs to be spectrally evaluated. This is shown in section 4.4 for the AERI radiance observations at JOYCE.

The AERI noise can be calculated by several ways such as computing the square root of the variance of magnitude radiances derived from hot black body observation over 25 cm^{-1} (e.g. *Knuteson et al., 2004b*). However, operationally, the standard deviation of the calibrated imaginary radiances derived from complex observed radiances, D_ν over 25 cm^{-1} are used as an estimation of the observed radiances noise (e.g. *Knuteson et al., 2004b*). Previous studies showed that the random AERI noise between any two spectral channels can be considered independent (e.g. *Turner, 2005*). This was confirmed by using a well-characterized blackbody which was placed in the sky port of the AERI. Analyzing observation of the blackbody for a long time series of data confirmed a correlation coefficient with absolute values of 0.3 between any two spectral channels. This study showed that the AERI noise can be considered as uncorrelated random noise.

The AERI at JOYCE works in rapid sample mode which has a temporal resolution of around 30 s, while the sky view is around 12 s (the rest is used to look at the HBB and CBB).

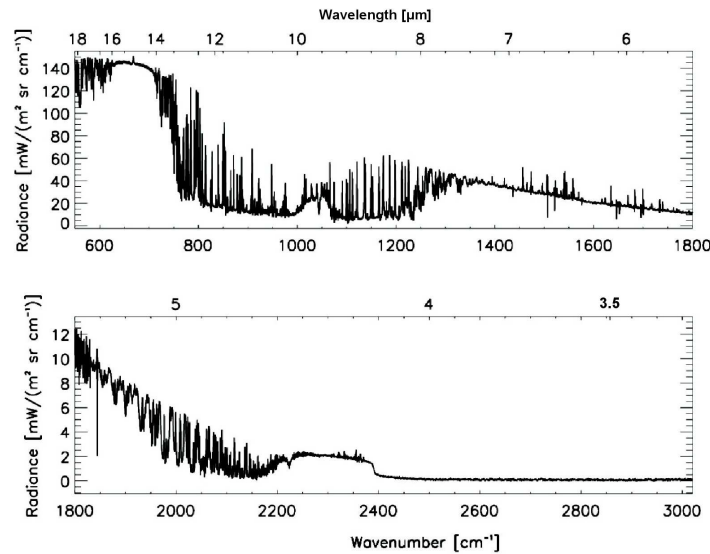


Figure 3.4: The AERI radiance observation that was taken during a clear sky scene on 25 of May 2012 at Jülich, Germany. The upper plot shows the AERI longwave infrared band and the lower plot shows the AERI shortwave infrared band.

This short sky view produces high noise in the AERI observation radiances (particularly compared to slow sample mode). In order to reduce the noise and increase the signal-to-noise ratio, different methods can be applied such as temporally averaging radiances or using the objective technique to determine the number of principal components of the AERI radiances with eigenvalues higher than the noise level to reconstruct the AERI observation radiances. The second method which is called Principal Component Analyze (PCA) is described in more detail in section 6.2.4.

The calibrated AERI radiances are saved in two separate files as channel one and channel two corresponding to the longwave and the shortwave detectors. The channel one includes the spectral band from 500 to 1800 cm^{-1} and the channel two includes the spectral band from 1800 to 3000 cm^{-1} . The data related to the quality control and housekeeping values are also saved in a file known as summary file. Fig. 3.4 shows an example of the AERI observation radiance for both channels. The data was taken during a clear sky scene at JOYCE on 25 of May, 2012.

3.2 Microwave radiometer

The microwave radiometer is a passive instrument that measures atmospheric radiation in the microwave region. The first studies showed that a dual-channel microwave radiometer with one channel at the water vapor line and one at the window region has the ability for observing liquid water path (LWP) and integrated water vapor (IWV) (*Westwater, 1978*). In addition, the microwave radiometers can be used for retrieving temperature and humidity profiles using the band measurements at the wings of water vapor or oxygen absorption lines (*Solheim et al., 1998; Crewell et al., 2001*). Further studies showed that elevation scans can improve the vertical resolution of the temperature profile in the boundary layer (*Westwater et al., 1999*). *Crewell and Löhnert (2007)* demonstrated that elevation scans of relatively opaque channels can improve the vertical resolution of the retrieved temperature profile in the boundary layer

compared to a retrieval using only zenith measurements. A comparison to radiosonde data showed that the standard deviation of the retrieved temperature profile is better than 1 K (for the atmospheric levels below 1.5 km).

In the present study, the data of a microwave radiometer called Humidity And Temperature PROfiler (HATPRO) is used (Rose et al., 2005). The HATPRO is a microwave radiometer built by Radiometer Physics GmbH, Germany (RPG).

The HATPRO has 7 channels in the vicinity of rotational transitions of O₂ at 60 GHz (V-band from 51 to 58 GHz) and can be used for retrieving the temperature profile and 7 channels in the vicinity of water vapor absorption line at 22.235 GHz (K-band from 22 to 31.4 GHz) and can be used for determining the humidity profile as well as LWP (Rose et al., 2005). Several studies showed the high ability of HATPRO for retrieving the temperature and humidity profiles as well as observing the LWP with the temporal resolution of 1 s. Besides, it was shown that the accuracy of retrieved IWV using the HATPRO is better than 0.5-1 kg/m² (Steinke et al., 2015).

The HATPRO also has some additional sensors for measuring the surface temperature, humidity and pressure as well as one sensor for detecting the rain onset and a GPS sensor for providing the UTC time.

The accuracy of the microwave radiometer measured data, among other parameters, significantly rely on calibration accuracy (Solheim et al., 1998). The calibration is periodically needed since the measured voltage by the microwave radiometer needs to equivalently convert to the brightness (radiative) temperature. The microwave radiometer ideally needs two reference points for calibration which are derived using a cold and a hot blackbody. An internal ambient target is used typically as hot blackbody (at ~ 300 K). For the cold blackbody, either a liquid nitrogen (LN₂) cooled blackbody of approximately 77 K (Ulaby et al., 1981), or a clear sky zenith measurement known as Tipping Curve Calibration (TCC) (Han and Westwater, 2000) can be used. Maschwitz et al. (2013) determined an uncertainty of 0.5 K for the TCC method, whereas it was demonstrated that the absolute uncertainty in the blackbody brightness temperature at the LN₂ boiling point for all frequencies is ± 0.5 K (Maschwitz et al., 2013; K uchler et al., 2016).

In this study, the retrieved temperature profiles and the retrieved IWV amounts as well as the in-situ surface temperatures (measured by the HATPRO sensor) from HATPRO measurements at JOYCE on clear sky days in 2012 are used.

3.3 GPS data

Bevis et al. (1992) presented a new approach to calculate the atmospheric IWV using the Global Navigation Satellite System (GNSS). It was shown that the signal propagating from a navigation satellite has a time delay which depends, amongst other things, on the atmospheric water vapor. Therefore, by calculating this delay, the atmospheric IWV can be estimated. The signal transmitted from a GNSS satellite can be received by a Low Earth Orbit (LEO) satellite or by a ground-based receiver. The signal received by a ground-based receiver can be used to estimate the integrated parameters such as IWV. In this study, the IWV derived from a ground-based receiver at JOYCE is used. In the rest of this section, the principle of deriving the IWV from a ground-based GPS receiver and the approach that is used for the ground-based receivers in Germany includes JOYCE receiver is summarized.

The ground-based GPS station consists of a receiver and an antenna. Each GPS station can receive signals at 12 different channels. However, receiving the signal of 4 satellites is enough for a station to make its measurements applicable. In addition the signal needs to be received in an elevation which is typically considered higher than 7° (Ning and Elgered, 2012). The data of a GPS station is scientifically usable, once these two criteria are fulfilled.

In order to calculate the tropospheric delay in a network approach, a low computational cost method is the Precise Point Positioning (PPP) (Zumberge et al., 1997). The IWV is then calculated by determining the dry and the wet tropospheric delay and mapping them to zenith. The Zenith Total Delay (ZTD) can be written as:

$$ZTD = ZHD + ZWD, \quad (3.8)$$

where ZHD and ZWD refer to the Zenith Hydrostatic Delay and Zenith Wet Delay. The ZHD can be approximated by:

$$ZHD = 10^{-6} k_1 R_d \int_z \rho dz \approx k'_1 p_s, \quad (3.9)$$

where $R_d = 287.05 \text{ Jkg}^{-1}\text{K}^{-1}$ is the specific gas constant for dry air; ρ is the air density; k_1 is an empirical constant and k'_1 refers to a constant that mainly depends on the k_1 , height and the receiver latitude. The integral is calculated from the earth surface to the top of the atmosphere. Furthermore, ZWD can be calculated using:

$$ZWD = k'(T_m) \int_z \rho_w dz, \quad (3.10)$$

where ρ_w is the atmospheric water vapor density and $k'(T_m)$ is a function of weighted mean temperature. Substituting Eqs. 3.9 and 3.10 in Eq. 3.8 gives:

$$IWV = \int_z \rho_w dz = \frac{1}{k(T_s)(ZTD - ZHD)}. \quad (3.11)$$

There is a network of GPS stations consisting of approximately 300 stations in Germany and some of its neighboring countries in order to retrieve the IWV that is called GFZ network. The ZTD is calculated using the PPP method. In this approach, a system of equations including 40-50 equations is solved which leads to calculate the ZTD as well as its standard deviation with relatively high temporal resolution of 15 min (Gendt et al., 2004).

However there are still some unsolved issues in the measured GFZ data such as a large break between the calculated IWV at 23:45 UTC and 00:00 UTC of the following day (Steinke et al., 2015) and the calculated IWV in this network has an uncertainty the order of 1-2 kg/m^{-2} (Gendt et al., 2004). In the present study, the IWVs derived at JOYCE on clear sky days in 2012 are used.

3.4 Tower measurement

The meteorological tower in Jülich, Germany is placed in a rural and predominately flat area. It measures the concentration of trace gases such as CO_2 , CH_4 , CO and H_2O as well as meteorological data such as temperature, pressure, relative humidity, wind-direction and wind-speed in a temporal resolution of 10 min. The tower was built in 1963 and 1964. The

trace gases have been measured at two different altitudes, at 20 m since March 2011 and at 100 m since May 2009. There is a coal fired power plant in Weisweiler (wind-direction cir. 218 ° south-west, at the distance of about 9 km) which is expected to have a rather significant effect on the trace gas measurements of the tower.

The trace gas concentration are measured using Off-Axis Integrated-Cavity-Output-Spectroscopy (ICOS) which is developed by Los Gatos Inc (www.lgrinc.com/analyzers). The measurements are based on trace gas absorption spectroscopy (*Schrade, 2011*). A light source is passed through a gas sample cylinder. Then the intensity of the incoming light is compared with the intensity of the outgoing light. According to the trace gas absorption lines of incoming light, the light can be absorbed by the trace gases inside the gas cylinder so that its intensity changes. By measuring the intensity of the outgoing light the concentration of the trace gases inside the cylinder can be estimated (*Schrade, 2011*). The attenuation of the incoming light due to passing through the gas cylinder is computed using Beer-Lambert-Law as:

$$\frac{I_\nu}{I_0} = e^{-(\epsilon_\lambda cL)}, \quad (3.12)$$

where I_0 shows the intensity of the incoming light and I_ν shows the intensity of the outgoing light. ϵ is the molar absorption coefficient, c is the concentration of the probe and L is the pathlength.

The tunable diode lasers and Quantum Cascade (QC) lasers in the mid-infrared region (3-5 μm) can be used as input light since there are several trace gas absorption lines in this region. The ICOS-instrument uses a cavity with 50 cm pathlength and the QC laser at 4.9 μm (www.lgrinc.com).

The CO_2 measurement data which were collected in 2012 were not calibrated. However, the accuracy of the CO_2 measurements are probably better than about 5 ppm. In addition, if there would be an offset in the data, it should be constant over several days meaning that the diurnal variation of the measurements should be rather accurate. Moreover, the precision of the CO_2 measurements in 2012 are about 1 ppm (*personal communication with M. V. Hobe*).

In this study the CO_2 measurements at 100 m on two clear sky days in 2012 as well as the temperature measurements at 100 m on all clear sky days in 2012 are used.

3.5 COSMO_DE model

The Consortium for Small scale MOdelling (COSMO) (<http://www.cosmo-model.org>) is a cooperation between meteorological services of different countries in order to develop regional numerical models. COSMO_DE is the operational numerical weather prediction model of the Deutscher WetterDienst (DWD; German weather service) since 2007. It has been mainly developed to improve the short term forecast of severe weather (*Baldauf et al., 2011*). The COSMO_DE is a non-hydrostatic, fully compressible model with 51 levels from the surface up to 22 km. The model thickness range changes from 20 m close to the surface to 400 m at 5 km height and 1000 m at 20 km height. The horizontal resolution of the model is 2.8 km with the $1200 \times 1300 \text{ km}^2$ domain covering Germany, the Netherlands, Belgium, Switzerland, Austria and some parts of adjoint countries as well as a large part of the Alps (*Baldauf et al., 2011*). It runs 8 times per day (at 00, 03, 06, 09, 12, 15, 18 and 21 UTC). The model output are available in an hourly resolution (*Baldauf et al., 2011*).

The input data as well as boundary conditions are provided using the interpolated data of a 7-km regional model COSMO_EU which uses the input data provided by the 30-km global model GME (*Majewski et al., 2002*). The COSMO_DE boundary conditions are updated using the COSMO_EU data of 3 h behind (e.g. the COSMO_DE at 00 UTC uses the data at 21 UTC of the COSMO_EU). The COSMO_DE input data is adjusted using four-dimensional data assimilation based on the nudging approach. For this purpose, the temperature, relative humidity, pressure, geopotential height, two-dimensional horizontal wind vector and precipitation observations from several measurements such as observation at synoptic stations, radiosondes data, the data of radar network and the data of ground-based wind profilers (*Stephan et al., 2008; Schraff and Hess, 2012*) are used.

In this study the hourly temperature and humidity profiles of the COSMO_DE from the closest column output to the JOYCE on clear sky days in 2012 are used.

3.6 REMO model

The REgional MOdel (REMO) is an on-line atmosphere-chemistry model that uses tracer transport modules as well as modules for tropospheric chemical quantities to simulate CO₂ and some other atmospheric trace gases variation (*Langmann, 2000; Chevillard et al., 2002*). The model uses the physical parametrization package of the EuropaModell (EM). It has 20 vertical levels from the surface up to 20 km with 7 levels below 1500 m. The horizontal resolution of the model is 0.5° in a rotated spherical coordinate that is roughly 55 km over Europe. It forecasts 30 hours with hourly resolution (*Chevillard et al., 2002*). The initial and the boundary condition values are updated every 6 h using the European Center for Medium-Range Weather Forecasts (ECMWF) model data. In the present section the REMO configuration for simulating the CO₂ transport is roughly summarized.

In order to simulate the CO₂ profile, three different components, i.e. the biosphere, the oceanic and the anthropogenic factors are considered. These components can be generated by sources inside the model domain as well as external sources once the emission of external sources enters into the domain through model boundaries. The biosphere component which describes the exchange of CO₂ between the atmosphere and the terrestrial vegetation is provided by the Terrestrial Uptake and Release of Carbon (TURC) model (*Lafont et al., 2002; Ruimy et al., 1996*). The TURC model simulates the terrestrial photosynthesis and the respiration by plants and soil using meteorological data and satellite observations. The daily estimation of the biosphere component provided by the TURC model is converted to hourly biosphere fluxes in REMO. The oceanic component is computed based on the *Takahashi et al. (2002)* approach. In this approach, the measurements of CO₂ partial pressure difference of sea minus air is assembled and interpolated in order to estimate the mean net fluxes with monthly resolution (*Wanninkhof, 1992*). The anthropogenic component is determined according to the Emission Database for Global Atmosphere Research (EDGAR; *Olivier et al., 1996*). This database provides global emission maps with 1° × 1° resolution. Emissions due to industrial activities, heating processes, transportation and cement production are taken into account. The REMO model uses the global transport model TM3 (*Heimann, 1995*) for CO₂ initial data and boundary conditions. However, the TM3 model data does not provide absolute concentration of CO₂ and hence the REMO model uses an offset correction value about 360.5 ppm that is constant in time and space and makes the REMO data comparable with the real CO₂ measurements.

In the present work, the data of the Hegyhatsal station in Hungary is used. The station is located in a rural area so that it has the lowest contribution of CO₂ fossil fuel. This station also shows the best agreement with the observation compared to other stations that were analyzed in *Chevillard et al. (2002)* study. The CO₂ profiles as well as the temperature and humidity profiles of November in 2012 and 2013 provided by REMO for this station are used in this study.

Chapter 4

Quality control and evaluation of AERI data

In section 3.1, the AERI is shortly introduced. In this chapter, the methods for evaluating and calibrating the AERI data are presented. Between 2012 and 2017, there are several epochs of AERI data due to occasional instrument malfunctions; in this study, only the AERI measurements in 2012 are used. Consequently, in the following chapter, the quality control and the calibration of AERI measurements in 2012 are explained. In the first section, the methods for finding and removing the low-quality data are presented. In order to do the spectral and radiometric calibration, the LBLRTM are used to simulate the AERI radiances using the COSMO_DE profiles. Due to the limitation of the LBLRTM simulation to the clear sky conditions, a method is used to find the clear sky cases in 2012 which is explained in section 4.2. In addition, the COSMO_DE temperature and humidity profiles are scaled using observations in Jülich for a better representation of the real temperature and humidity profiles, and thus provide the AERI simulated radiances with higher accuracy. The methods for selecting the best surface temperature and IWV observations are explained in section 4.3. The simulated radiances are then used for spectral and radiometric calibration which are demonstrated in sections 4.4 and 4.5 respectively.

4.1 Flagging low-quality data

Before evaluating and calibration of the AERI data, the measurements with low-quality are detected and flagged. The procedure for finding this data is summarized in this section.

4.1.1 Imaginary part of observed radiances

In section 3.1, it is shown that the asymmetric interferogram around the zero path delay cause complex observed radiances. The radiometric calibration uses the real part of the complex observed spectra to compute the calibrated radiances while the imaginary part D_ν which gives an estimation of the observation noise, can be used to assess the quality of the observed radiances. D_ν needs to be zero within the instrument noise. However, analyzing the AERI data shows some jumps in the D_ν values. These jumps refer to noisy data that need to be removed.

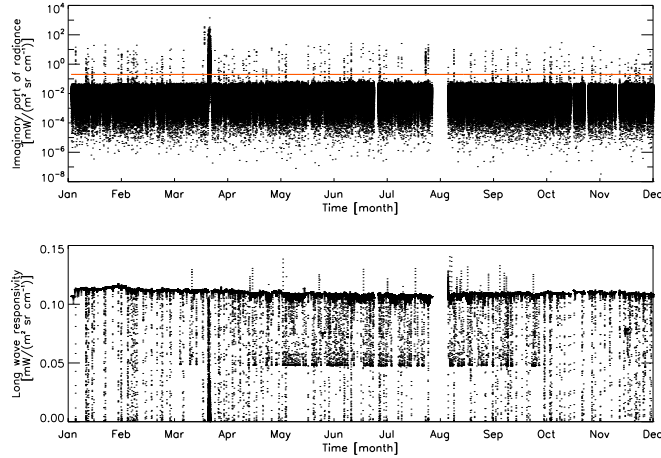


Figure 4.1: The averaged imaginary part of observed radiance in the $2510\text{--}2515\text{ cm}^{-1}$ region for each AERI sample from 2012 (top) and the longwave detector responsivity (bottom) in 2012. The red line in the imaginary plot (top) shows the threshold equal to 0.2 RU that is used to flag the noisy data.

In the real-time AERI implementation, the D_ν is calculated over different spectral bands and its value for each sky view is saved in the summary file. In this study, the sky view imaginary radiance between 2510 and 2515 cm^{-1} was used for filtering the noisy data. This variable is saved with the name of “*skyViewImaginaryRadiance2510 – 2515*” for each sky view during the AERI measurements. The upper plot in Fig. 4.1 shows this variable for all sky views in 2012. The red line in this plot shows the threshold that is used for filtering the data. All measurements with the value higher than this threshold are flagged.

4.1.2 Instrument responsivity

Another important factor which can be used to find the low-quality data is the instrument responsivity H_ν , which is introduced in section 3.1. Any issues, particularly when the gold scene mirror becomes dirty by dust or precipitation, can significantly reduce the responsivity of the instrument, and thus can produce the data with low-quality. Therefore, the measurements with low responsivity need to be found and flagged.

Operationally, the responsivity of the shortwave and the longwave detectors are saved separately for each sky view in the daily summary file. The lower plot in Fig. 4.1 shows the AERI longwave detector responsivity for measurements in 2012. In order to filter the data that was obtained with the low detector responsivity, the mean responsivity of each month is calculated and the data with responsivity less than 90 % of the mean calculated responsivity are flagged.

4.2 Finding clear sky cases

After flagging poor quality and noisy measurements, the remains of measurements need to be validated by reference radiances. In this study, these radiances were calculated using an accurate radiative transfer model. As described in section 2.4, the LBLRTM is an accurate

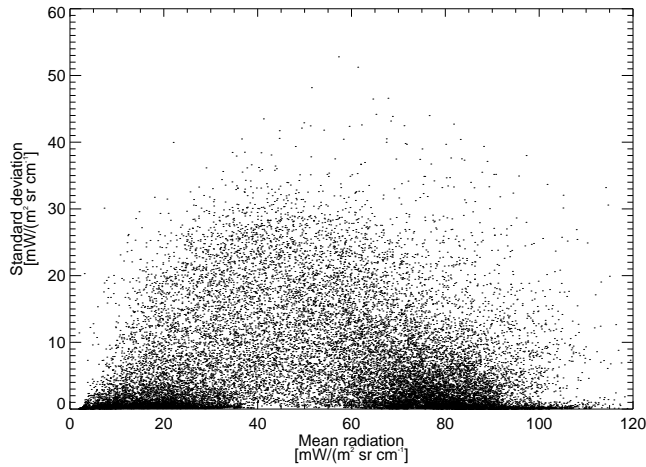


Figure 4.2: Scatter plot of mean radiation of the spectral band between 898 and 904 cm^{-1} in terms of its standard deviation for 10 min time intervals of AERI measurements in 2012.

radiative transfer model which has been used to evaluate and calibrate the space-based or ground-based observations. It is also used in the present study to evaluate the AERI measurements and to determine if there is any systematic bias in the data. The LBLRTM does not include clouds, and thus is limited to clear sky calculations. The accuracy of the LBLRTM calculation is limited not only by its spectroscopy (which has been well validated by other observations; see chapter 2) but also by the accuracy of the input temperature and humidity profiles used to drive the LBLRTM. Therefore, in the present section, first the clear sky cases in 2012 are determined. Then the best observation data in Jülich are selected to scale the model profiles which are used as input data in the LBLRTM.

There are several ways using different instruments to find clouds but many of them are not accurate enough for the infrared measurement. For example, the ceilometer backscatter is pretty useful for capturing the low- and mid-level clouds, however, it is poor in capturing the high and thin ice clouds while the AERI has sensitivity to both ice clouds and thin clouds with small amounts of LWP (e.g. *Turner et al., 2007; Comstock et al., 2007*). Another example is using the window channels in the microwave region but it is not applicable in the present work since the sensitivity of this radiation to various types of clouds are different from the infrared radiation; that means a clear sky for the microwave radiation may not be totally clear and non-cloudy for the infrared radiation. As a result, the method applied in this study is using the window channels of the AERI in order to filter the cloudy cases. As it is mentioned in section 2.2.4, the spectral region from 8 to $13 \mu\text{m}$ is a window region in the mid-infrared radiation that is divided into several micro-window bands due to water vapor absorption lines in this area. One of these micro-window bands is 898 to 904 cm^{-1} with the high sensitivity to the cloud (*Turner et al., 2007*) that is highly suitable for this purpose and is used to find clear sky cases in the present work.

In a clear sky condition, the radiation of a window channel may come from the top of the atmosphere so that its radiance should have quite small value. On the other hand, in the 8 - $13 \mu\text{m}$ band, and especially the 898 - 904 cm^{-1} region, the main absorbers are water vapor and clouds. Water vapor is pretty uniform over time, but clouds can change more quickly. Therefore, the temporal standard deviation of this band can be used to separate the cloudy cases from clear ones. While for the clear sky conditions, the temporal standard deviations are small, the cloudy conditions can produce larger standard deviation over this band.

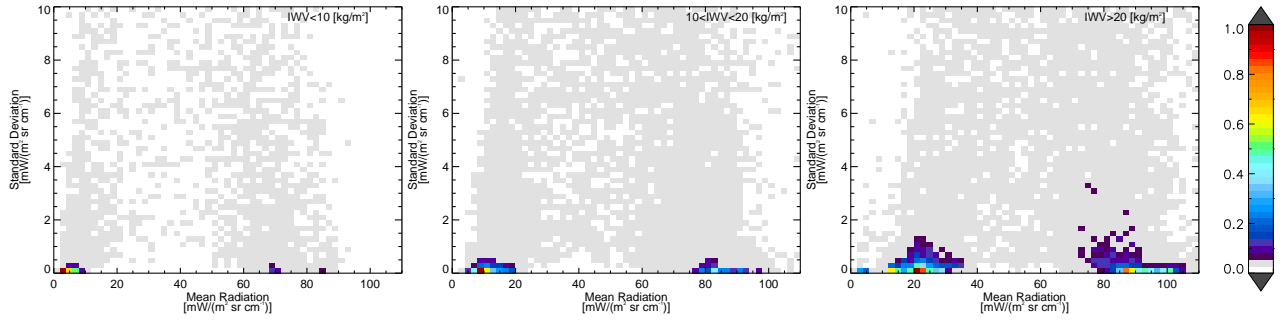


Figure 4.3: The three histograms show the mean radiation in the micro-window between 898 and 904 cm^{-1} in terms of its standard deviation in 10 min time intervals for AERI observations in 2012. The left plot belongs to the atmospheric condition with the IWV lower than 10 kg/m^2 , the middle one belongs to the IWV from 10 to 20 kg/m^2 and the right one belongs to IWV higher than 20 kg/m^2 . Based on these plots, the thresholds for filtering the clear sky cases is determined.

Consequently, in the first step, the mean radiance of this micro-window and its standard deviation over a small time interval that is chosen 10 min here, is calculated. Fig. 4.2 shows the scatter plot of the mean radiation for the mentioned spectral band, 898-904 cm^{-1} , in terms of its standard deviation, for AERI measurements in 2012. The plot shows two dense areas with low standard deviation. From the left side, as it is expected, the first region with the smaller mean values between 5 and 30 radiance unit (RU; here is $\text{mW/m}^2 \text{ sr cm}^{-1}$) belongs to clear sky condition. The second dense region with mean radiation higher than 70 RU belongs to the clouds which are opaque for the infrared radiation. This kind of cloud can block all the infrared radiation and cause that the radiance comes from the cloud bottom that means it gets higher mean value due to the radiation from the lower atmospheric level as well as the infrared radiation of the cloud by itself. Besides, it has small standard deviation because of emitting from the certain level.

The smallness of window channel radiances mainly depend on the atmospheric water vapor content. While in a dry and cold atmosphere, the radiances can have very small amounts, in a hot and humid condition, due to the increase in the optical depth of the water vapor layer, and thus more emission, the observed radiances can have larger amounts. Consequently, AERI measurements in 2012 are divided into the 3 different categories based on the atmospheric IWV amounts that are calculated using the zenith observation of the microwave radiometer HATPRO at JOYCE.

In order to define accurate thresholds to separate clear sky cases from the cloudy ones, the histogram of the mean radiation in terms of its standard deviation for each of these categories are plotted. Fig. 4.3 shows 3 histograms for 3 different IWV contents of the atmosphere. The left plot shows the histogram for the IWV lower than 10 kg/m^2 , the middle one plotted for the IWV between 10 and 20 kg/m^2 and the right histogram belongs to measurements with the IWV higher than 20 kg/m^2 . As it can be seen, in all 3 plots, the regions belonging clear sky conditions and thick clouds are clearly separated from each other which make determining thresholds for clear sky cases easier. According to these 3 plots, the threshold for the clear sky standard deviation is chosen to be less than 0.2 RU. In addition, the threshold for the mean radiation is chosen between 2 and 6; 8 and 12; and 20 and 24, for the left plot with low IWV, middle plot with the moderate IWV and right plot with the high IWV respectively.

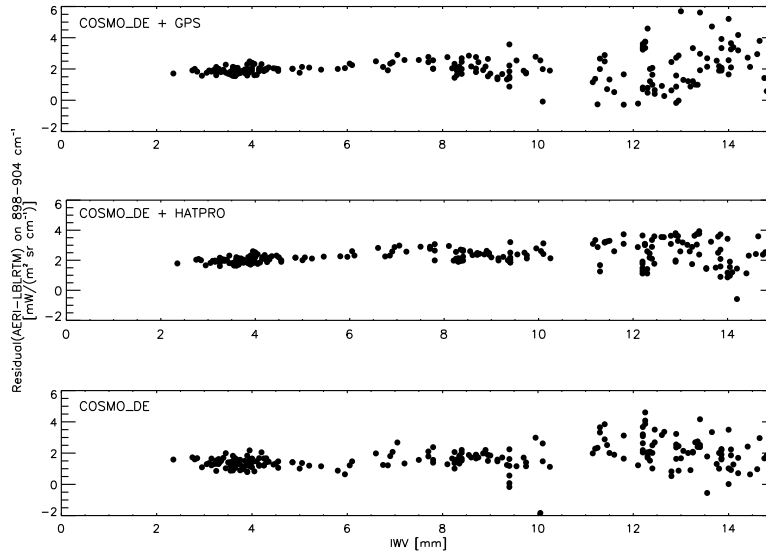


Figure 4.4: Residuals between AERI and LBLRTM radiances for the micro-window spectral band from 898 to 904 cm^{-1} . For the upper plot, the LBLRTM is run using the humidity profile scaled with the IWV measured by GPS station. In the middle plot, input humidity profiles of the LBLRTM are scaled with the HATPRO retrieved IWV and in the lower one, the original humidity profiles of the COSMO_DE are used in LBLRTM runs.

Based on these thresholds, clear sky time intervals in 2012 are selected. Since these cases are needed for running the LBLRTM using the COSMO_DE profiles and these profiles have hourly resolution, the clear sky time intervals are selected in a way to be suitable for using in the LBLRTM; i.e. each 30 min clear sky duration with 15 min before and after a specific hour for which COSMO_DE profiles are available, is selected for this analysis. In this way, 221 clear sky cases are selected that are spanned from 15 January to 15 October 2012. Most of these cases belong to cold months, January and February, while there are only few cases in warm months such as Jun, July and August. One important reason is for many days in these 3 months, the AERI data is missing. In addition, there is not any case in November and December because of missing the AERI data in these two months.

4.3 Finding the best measured IWV and surface temperature to scale COSMO_DE profiles

In the previous section, clear sky cases which can be used to run the LBLRTM are found. The LBLRTM is run using temperature and humidity profiles as well as profiles of atmospheric absorber gases such as CO_2 , CH_4 and O_3 . In the present study, temperature and humidity profiles are taken from the COSMO_DE data and for each atmospheric absorber gas, a constant profile is considered with a value close to its mean atmospheric content. The uncertainty in these profiles, particularly in temperature and humidity profiles, can reduce the accuracy of calculated radiances by the LBLRTM and thus it can affect the accuracy of the calibration process. In order to reduce the uncertainty in model temperature and humidity profiles, some of the real observations of the JOYCE site are used as an auxiliary data to scale these profiles. Two important parameters that are used in this study to correct the model

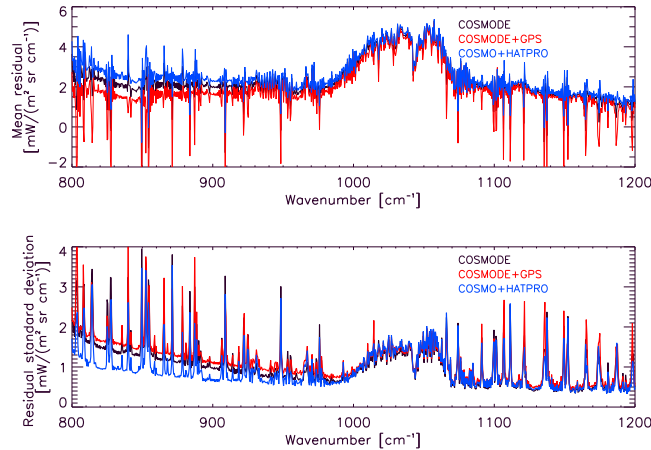


Figure 4.5: The mean difference (upper plot) and the standard deviation (lower plot) between AERI and LBLRTM radiances for 221 clear sky cases. The LBLRTM is run using the COSMO_DE profiles where the humidity profiles are scaled with HATPRO retrieved IWVs (blue line), with the GPS measured IWVs (red line) as well as using original COSMO_DE humidity profiles (black line).

profiles are the IWV and the surface temperature. Using the IWV for scaling the humidity profiles has been used in several studies (*Turner et al., 2003; Turner et al., 2004*). In this section, the procedure for selecting the best option among all observations and measurements at JOYCE for each of these parameters is explained.

The IWV is measured by two different instruments at JOYCE, the retrieved IWV by the microwave radiometer HATPRO and the measured IWV by the ground-based GPS receiver. Both IWVs are analyzed to find the more appropriate one for scaling model humidity profiles. Note that IWV is a height-independent scale factor. In order to compare the accuracy of these IWVs, the LBLRTM is run with three different settings, one for scaled humidity profile with GPS measured IWV, one for scaled humidity with HATPRO retrieved IWV and one for original COSMO_DE profiles. The humidity profile q is scaled as:

$$q_{input} = q_{COSMO_DE} \times \frac{IWV_{observation}}{IWV_{COSMO_DE}}, \quad (4.1)$$

where q_{input} refers to the input humidity profile in the LBLRTM and $IWV_{observation}$ are replaced by the retrieved IWV by HATPRO and measured IWV by the GPS. The temperature profiles and other trace gas profiles are considered the same for all 3 settings. The LBLRTM is then run for all 221 clear sky cases. Calculated radiances by the LBLRTM are compared with coincidence AERI measurements. The micro-window region between 896 to 904 cm^{-1} which has not any strong absorption lines, is selected for this comparison. The AERI minus LBLRTM residuals in this spectral band are calculated for all clear sky cases. Fig. 4.4 shows these residuals in terms of IWV for each of LBLRTM runs. As the plot shows, residuals in all three plots are clearly lower for lower IWVs while they get higher values as the IWV increasing. This can relate to the fact that in higher IWVs the deficiency in humidity profiles of the COSMO_DE model is more significant. However, it is known that only part of this residual is due to the uncertainty in the input humidity profile and other reasons such as calibration issue which is discussed more in this section or spectroscopy issue in the LBLRTM are also important. The middle plot also shows that scaling the humidity profile with the

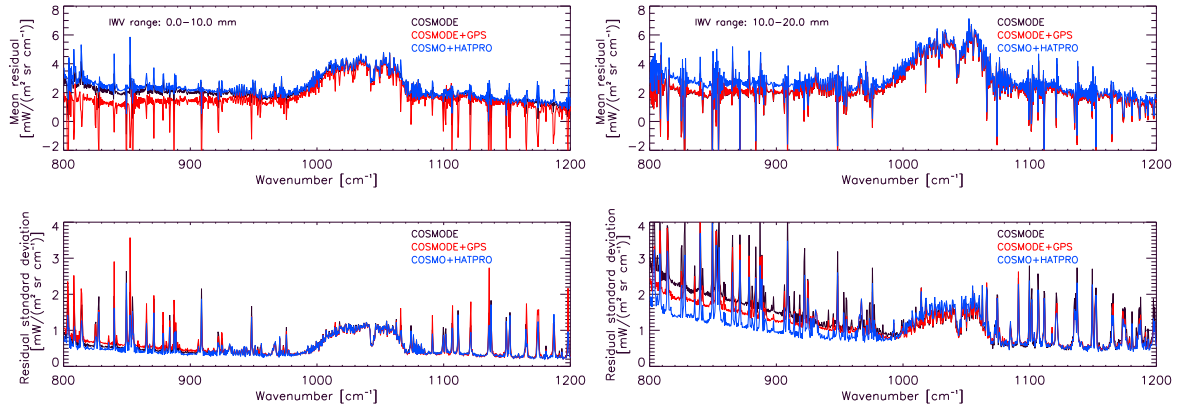


Figure 4.6: The mean difference (upper plots) and the standard deviation (lower plots) between AERI and LBLRTM radiances. The left panel shows the mean and the standard deviation for 135 clear sky cases with IWVs lower than 10 kg/m^2 and the right panel shows the same for 85 cases with IWVs between 10 and 20 kg/m^2 . The LBLRTM is run using the COSMO_DE profiles where the humidity profiles are scaled with HATPRO retrieved IWVs (blue line), with the GPS measured IWVs (red line) as well as using original COSMO_DE humidity profiles (black line).

IWV retrieved by the HATPRO cause that residuals in higher IWVs are improved compared to other two runs.

The mean difference between AERI and LBLRTM radiance spectra over all clear sky cases as well as its standard deviation for these cases are calculated. Fig. 4.5 shows the mean residual radiance spectra and its standard deviation for the window region from 800 to 1200 cm^{-1} . The upper plot shows that calculated radiances using scaled humidity profiles with the IWVs measured by GPS has the lowest mean residual, however, it has the highest standard deviation. Calculated radiances using the scaled humidity profile with the HATPRO retrieved IWV shows the highest mean residual with the lowest standard deviation. The lowest standard deviation implies that the residual is relatively constant for all cases and it is independent of the IWV amount.

In order to analyze the mean residual and the standard deviation of AERI minus LBLRTM radiances more precisely, the clear sky cases are divided into two groups based on their IWV amounts. Fig. 4.6 shows the mean difference between AERI and LBLRTM calculated radiance spectra as well as its standard deviation for 135 cases with the IWV lower than 10 kg/m^2 and 85 cases with the IWV from 10 to 20 kg/m^2 . There was only 1 clear sky case with the IWV higher than 20 kg/m^2 which is ignored in this analysis. In both panels, LBLRTM radiances calculated using the scaled humidity profiles with the HATPRO retrieved IWV shows the highest mean residual with the lowest standard deviation. In addition, the standard deviation shows a significant decrease for the cases with the lower IWV which makes the HATPRO retrieved IWV even more reliable for these cases. According to this analysis, the HATPRO retrieved IWV is selected as the appropriate one for scaling the COSMO_DE humidity profiles.

Another important parameter in the LBLRTM run is the surface temperature. Particularly, the radiances in the CO_2 line, $15 \mu\text{m}$, that is the focus of this work, are mainly affected by the temperature near the surface, therefore, finding the best surface temperature in order to use in the LBLRTM run is essential for this work. Several surface temperature measurements are

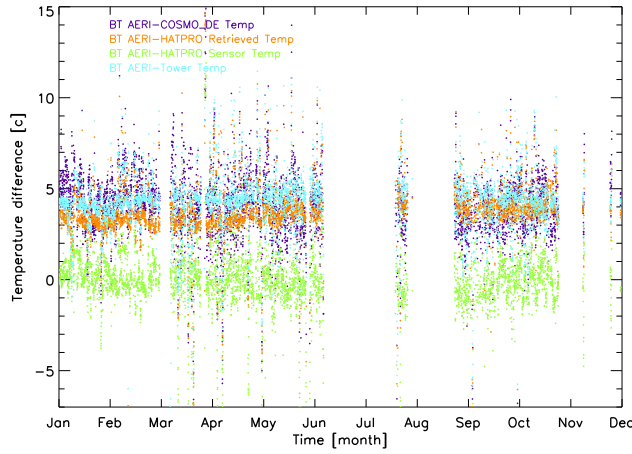


Figure 4.7: The difference between saturated AERI brightness temperature (BT) with other near surface temperatures observed at JOYCE site for measurements in 2012.

available in the JOYCE site. In the first step, for comparing these temperatures with each other, the difference between these temperatures with the radiative temperature measured by the AERI is calculated for whole AERI measurements in 2012. The radiative or the brightness temperature (BT) is calculated using the inverse of the Planck function.

$$BT_{\nu} = \frac{c_2 \nu}{\ln(c_1 \nu^3 / R + 1)}, \quad (4.2)$$

where $c_1=1.191042e-5$ [$\text{mW}/\text{m}^2 \text{ sr cm}^{-4}$] and $c_2=1.4387752$ [K cm] are two constant factors, ν is the wavenumber and R represents the AERI measured radiance for each wavenumber. The AERI BT at the surface can be calculated using the spectral band between 673 and 680 cm^{-1} . Note that the calculated BT can only provide an estimation of the surface temperature since due to the opacity of the absorption line, the calculated BT may show the temperature of slightly higher altitude above the ground. The median of calculated temperatures for this spectral band is considered as the radiative surface temperature measured by the AERI. The temperatures that are used for comparing with the AERI BT are the HATPRO retrieved surface temperature, the surface temperature measured by the HATPRO in-situ sensor and the temperature measured by the tower at 100 m as well as the COSMO.DE temperature at 2 m. Fig. 4.7 shows the hourly differences between each of these temperatures and the AERI BT. As it can be seen, tower temperatures show the highest difference with the AERI BTs that is between 4 and 5 °C. This large difference can be due to the difference in the altitude where the tower temperature has been measured which is at 100 m and the altitude of the AERI which is 111 m. The differences between HATPRO retrieved temperatures and the AERI BTs are slightly lower, between 3 and 4 °C. Temperatures measured by the HATPRO in-situ sensor are the closest ones to the AERI BTs with the differences between -1 and 1 °C. COSMO.DE temperatures show very unsteady behavior during the year which make them unreliable.

The same analysis as it is done for selecting the best IWV, is done for selecting the best surface temperature among all available ones at JOYCE. In this analysis, the LBLRTM is run using the same humidity profile provided by the COSMO.DE model and scaled with the HATPRO retrieved IWV and different surface temperatures as the input surface temperature in the LBLRTM. The mean residual of AERI minus LBLRTM radiances as well as its standard

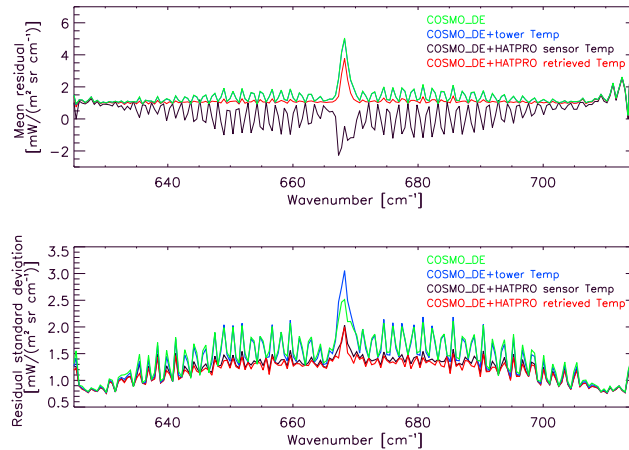


Figure 4.8: The mean difference between AERI and LBLRTM radiances for 214 clear sky cases in 2012. The LBLRTM is run using the COSMO_DE profiles where the surface temperature is replaced by HATPRO retrieved surface temperatures (red line), by HATPRO in-situ sensor measured temperature (black line) and by tower temperature measurements at 100 m above ground (blue line) as well as using the original COSMO_DE temperatures at 2 m above ground (green line).

deviation for 214 clear sky cases are calculated. Fig. 4.8 shows the mean residual and its standard deviation for the spectral band from 625 to 715 cm^{-1} (the center of the 15 μm CO_2 line which has the highest sensitivity to the surface temperature). As the plot shows, calculated radiances using HATPRO retrieved temperatures has the mean difference around 1 RU while this difference for radiances calculated with tower temperatures and COSMO_DE temperatures are higher than 1 RU. Furthermore, the HATPRO in-situ sensor gives the mean difference between -1 and 1 RU. The standard deviation for COSMO_DE and tower temperatures are relatively higher than two other surface temperatures meaning that these two temperatures are not appropriate to use in the LBLRTM run. In addition, HATRPO in-situ sensor and HATPRO retrieved temperature show the lowest standard deviations, while, the standard deviation of HATPRO retrieved surface temperature is slightly lower than the HATRPO in-situ surface temperature. Therefore, the HATPRO retrieved surface temperature is selected as input surface temperature in the LBLRTM run. In the next two sections, radiances calculated by the LBLRTM using scaled humidity profiles and HATPRO retrieved surface temperatures are applied to use for spectral and radiometric calibration of the AERI observation radiances.

4.4 Spectral calibration

In section 3.1, the acquisition of spectrally calibrated AERI radiances is shown. The laser fringe of the AERI interferometer is used to provide the interferogram interval sampling which is used in the spectral calibration (Knuteson et al., 2004b). The effective laser frequency known as true or reference frequency for each AERI instrument is known by design. However, any misalignment between AERI laser optical paths and the infrared paths can change this frequency and produce an inconsistency in the AERI spectral calibration. In order to avoid this problem, after deployment of AERI at site, the ν_{eff} of each AERI detector can be

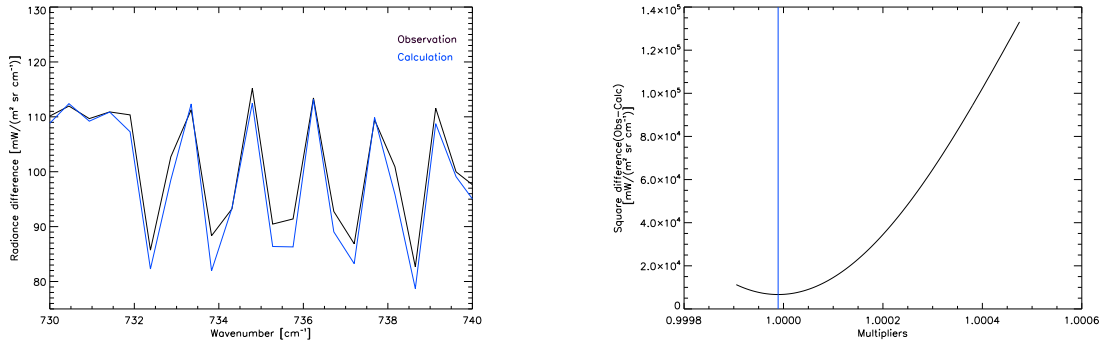


Figure 4.9: The difference between observed AERI radiances and calculated radiances using the LBLRTM for a clear sky cases at 0600 UTC 30 October 2012 (left plot). The square difference between calculated and observed radiances in terms of a series of multipliers used for changing the longwave reference frequency (right plot). The blue line shows the minimum of the curve or the best multiplier for changing the reference frequency.

determined empirically to compare with its reference frequency and to find the accuracy of the AERI spectral calibration. If the reference frequency is found to be different that what was assumed, the data need to be spectrally reassembled (i.e., to achieve a spectral calibration). In the rest of this section, the evaluation of the AERI spectral calibration after operating at JOYCE for measurements in 2012 is described.

In order to determine the ν_{eff} empirically, AERI observations need to be compared with high accurate calculated radiances. The CO_2 absorption band from $730\text{-}740\text{ cm}^{-1}$ which has regularly spaced CO_2 absorption lines and the spectral position of the centers of these absorption lines are well-known based on the laboratory measurements (*Rothman et al., 1992*) is selected to use in the longwave spectral calibration. By minimizing the differences between calculated and observed radiances as the reference sampling frequency is varied, the ν_{eff} used in AERI observations is figured out. An example of comparing calculated and observed radiances is shown in the left plot of Fig. 4.9. The radiances belong to a clear sky case at 0600 UTC 30 of October 2012. The calculated radiances are simulated with the LBLRTM using the COSMO_DE profiles. Part of the difference between calculated and observed radiances in this plot is due to the uncertainty in the input temperature and humidity profiles used the LBLRTM run. The right plot of Fig. 4.9 shows the square difference between observed and calculated radiances in terms of a series of multipliers utilized for changing the reference sampling frequency. The minimum point of this curve which is shown by the blue line is the best multiplier for changing the reference frequency. It can be seen that the blue line is relatively close to 1 in this case that means the ν_{eff} used for the longwave spectral calibration is nearly close to the reference frequency. For this case, the difference between ν_{eff} and ν_{ref} is 0.17 cm^{-1} .

The approach for finding the difference between the reference frequency and the empirically derived effective frequency for the longwave detector is repeated for 218 clear sky cases in 2012. The LBLRTM is run for all of these cases using the COSMO_DE profiles. As it is mentioned, in order to reduce the uncertainty of model profiles, humidity profiles are scaled with HATPRO retrieved IWVs and model surface temperatures are replaced by HATPRO retrieved surface temperatures. The left plot in Fig. 4.10 shows the difference between calculated effective frequencies and the reference frequency which is considered 15799.0 cm^{-1} during the AERI measurements in 2012. The plot shows that this difference is nearly less

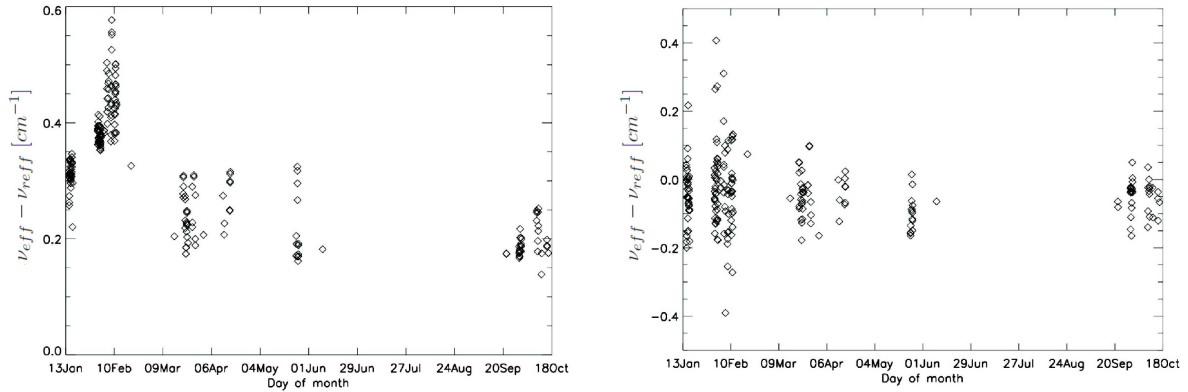


Figure 4.10: Time series of the difference between reference frequency and empirically calculated frequency for the longwave (left plot) and shortwave (right plot) AERI detector for clear sky cases in 2012. The reference frequency for this year is 15799.0 cm^{-1} .

than 0.35 cm^{-1} for whole 2012 with an exception for clear sky cases in first days of February. Since there was not any change in the laser setting or any other part of the AERI in this time period, this increment can be related to the weather condition which was quite cold and dry in these days. The gap in warm months is mainly due to the missing AERI data for many days in these months; however, there are only few clear sky cases in these months. The mean difference between the reference frequency and empirically derived frequencies for the longwave detector in 2012 is 0.31 cm^{-1} with the standard deviation of 0.10 cm^{-1} . This is an acceptable uncertainty in the effective frequency for the AERI spectral calibration. Therefore, we did not any further spectral calibration for measurements in 2012. The right plot in Fig. 4.10 shows the distribution of these differences for the shortwave detector. The same procedure is done for the shortwave detector using the radiances between 2207 and 2220 cm^{-1} . The sudden change in the laser frequency can be also seen for this detector, in first days of February; however, it seems for the rest of the year, the laser frequency is more stable. The mean difference for the shortwave infrared radiation is -0.07 cm^{-1} with the standard deviation of 0.482 cm^{-1} .

4.5 Radiometric calibration

A radiometric calibration in the laboratory was performed for the first generation of the AERI prior to the deployment of them in the field (*Knuteson et al., 2004b*). This calibration used two extra blackbodies where one of them operated at an intermediate temperature, 318 K and another one was kept at very cold temperature equals 217 K . Radiometric temperatures of these two extra blackbodies were calculated and considered as reference temperatures in order to compare with observed radiances by the instrument. It was shown that uncertainties in the measured radiances of both blackbodies were close to the predicted uncertainties (*Knuteson et al., 2004b*). After operating an AERI instrument in the field, several issues such as an obstacle or dust in the AERI field of view or an unexpected increment or reduction of the temperature inside the interferometer cavity can affect the accuracy of measured radiances. Consequently, an assessment of the systematic error in the AERI radiance observations is essential before the data are used.

In order to do this assessment, first, AERI measurements are compared with highly accurate

simulated radiances to find the difference between its measurements and simulated radiances. Same as spectral calibration, the LBLRTM is applied for simulating these radiances using the COSMO_DE profiles of temperature and humidity while humidity profiles are scaled with HATPRO retrieved IWVs and COSMO_DE surface temperatures are replaced by retrieved HATPRO surface temperatures. Fig. 4.11 shows the AERI minus LBLRTM mean residual and its standard deviation for 218 clear sky cases in 2012. As it can be seen, in the upper plot, there is a mean residual around 1 RU in the spectral band from 620 to 715 cm^{-1} with relatively high standard deviation around 1.5 RU. The main contribution of the residual in this area is due to the calibration issue in AERI measurements; however, relatively high standard deviation implies that uncertainties in the input temperature profiles particularly in temperatures near the surface have also contribution on this residual. Another important area in this plot is window region from 800 to 1200 cm^{-1} that shows quite large mean residual from 1.5 to 3 RU with the standard deviation between 0.5 and 1.5 RU. Similarly, the calibration issue has a significant impact on the residual in this area while same as the center of the 15 μm CO_2 line, the high standard deviation in this region shows the problem both in the shape and in the content of the input humidity profiles. Note that the extremely high residual in the spectral band between 970-1070 cm^{-1} is due to the high uncertainty in the input O_3 profile, notably in the stratosphere, that is not the subject of this work. Furthermore, another large residual in the region from 715 to 800 cm^{-1} is mainly due to the uncertainty of input CO_2 profiles in upper levels and thus it is ignored in the calibration analysis.

As it is mentioned, two important regions that are needed to be evaluated are the center of the 15 μm CO_2 line and the window region. In order to reduce the effect of the uncertainty of the input humidity profiles, only clear sky cases with quite low IWV are used in this analysis. For this purpose, 65 cases with the IWV amounts lower than 2.5 kg/m^2 are selected (that are found in the first 10 days of February). These cases are used to calculate the mean residual and standard deviation of AERI minus simulated radiances again. Fig. 4.12 shows the mean residual as well as the standard deviation for these cases. As the plot shows, the mean residual in the window region reduces compared to Fig. 4.11 and reaches nearly less than 2 RU. There is also a significant reduction in the standard deviation in this region compared to Fig. 4.11 that is around 0.2 RU. This very low standard deviation gives high certainty that there is a constant bias in AERI measurements (and most probably is not due to the uncertainty in the input profiles of LBLRTM run). Because AERI measurements are higher than simulated radiances, this bias which has been seen in measurements of other operational AERIs (*Turner, 2003; Delamere et al., 2010*) is known as warm bias. A series of tests were performed during a series of field experiments the Radiative Heating in Underexplored Bands Campaigns (RHUBC) that are organized by ARM which showed that the warm bias is due to the calibrational issue in the AERI and is not related to the accuracy of the LBLRTM (*Delamere et al., 2010*). This warm bias can be also seen in the spectral band 620-715 cm^{-1} ; however, the standard deviation in this region is only slightly reduced compared to Fig. 4.11 meaning that that there are still some uncertainties in the input temperatures of LBLRTM, particularly in temperatures near the surface. The investigation about this bias in the AERI measurement led to two ideas behind this problem which are explained in the rest of this section.

4.5.1 Obstruction correction

The first reason which was found for the warm bias in the AERI measurement was a probable warm obstruction in the AERI field of view (*Delamere et al., 2010*). This obstruction can

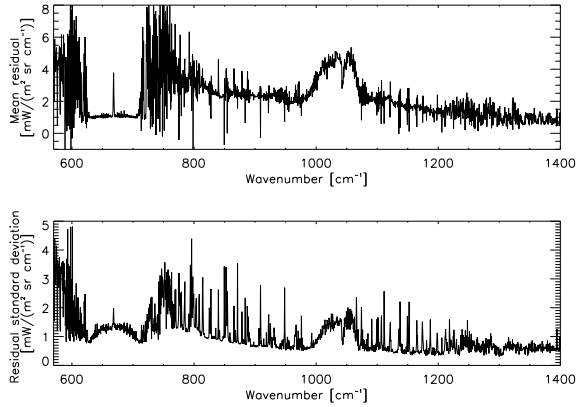


Figure 4.11: The mean residual (upper plot) and the standard deviation (lower plot) of AERI minus LBLRTM radiances for 218 clear sky cases in 2012. The LBLRTM input humidity profiles are scaled with HATPRO retrieved IWVs and retrieved surface temperatures of HATPRO are used for the input temperature profile.

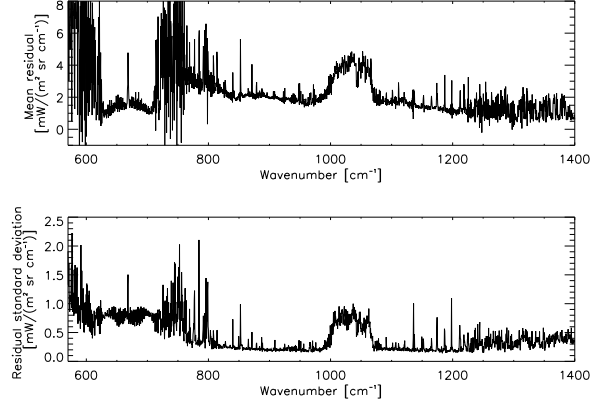


Figure 4.12: The mean residual (upper plot) and the standard deviation (lower plot) of AERI minus LBLRTM radiances for 65 clear sky cases with IWVs lower than 2.5 kg/m² in 2012. The LBLRTM input humidity profiles are scaled with HATPRO retrieved IWVs and retrieved surface temperatures of HATPRO are used for the input temperature profile.

change the true sky view radiance R_{sky}^{truth} to the AERI observed radiance \tilde{R}_{sky} as:

$$\tilde{R}_{sky} = (1 - f_v)R_{sky}^{truth} + f_v B(T_{effective-obstruction}), \quad (4.3)$$

where B is the Planck function and $T_{effective-obstruction}$ is assumed to be equal to the blackbody support structure temperature which is a temperature measured at the support structure holding the blackbodies in place and saved with the name of “*BBsupportStructureTempe*” in the AERI file for each sky view. Using Eq. 4.3, the f_v can be calculated as:

$$f_v = \frac{\tilde{R}_{sky} - R_{sky}^{truth}}{B(T_{effective-obstruction}) - R_{sky}^{truth}} \quad (4.4)$$

In order to solve this equation, clear sky cases with very low IWV are considered for simulating the R_{sky}^{truth} using the LBLRTM. The micro-window region between 898-904 cm⁻¹ is again used to estimate the difference between R_{sky}^{truth} and \tilde{R}_{sky} and to calculate the f_v for each case. Fig. 4.13 shows the bar plot of calculated obstruction factors for 65 clear sky cases with the IWV lower than 2.5 kg/m². The mean f_v is considered as the fractional obstruction factor of the AERI measurements at JOYCE in 2012. The mean f_v equal to 0.0256 is shown by the black solid line in the plot. Two dashed solid lines in the plot show the standard deviation of f_v equals 0.0021. This value is twice the size that was seen in previous studies (Delamere et al., 2010) and might relate to the centering of the AERI within its hatch.

After calculation of f_v , AERI measurements can be calibrated using this factor. The calibrated AERI radiances, R^{cal} is calculated as:

$$R^{cal} = \frac{\tilde{R}_{sky} - \tilde{f}_v B(T_{effective-obstruction})}{1 - \tilde{f}_v}, \quad (4.5)$$

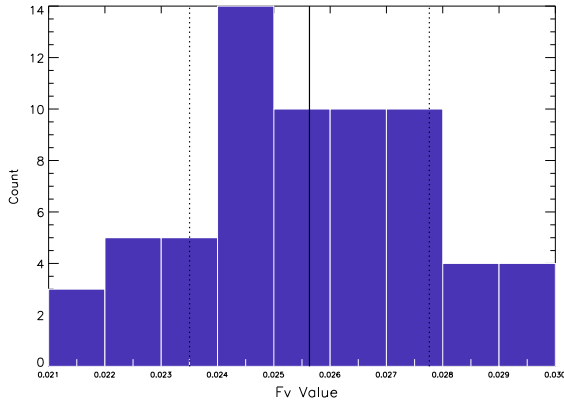


Figure 4.13: The distribution of calculated f_v obstruction correction factors for 65 clear sky cases with low IWV for measurements in 2012. The solid and dashed black lines shows the mean and the standard deviation of f_v respectively.

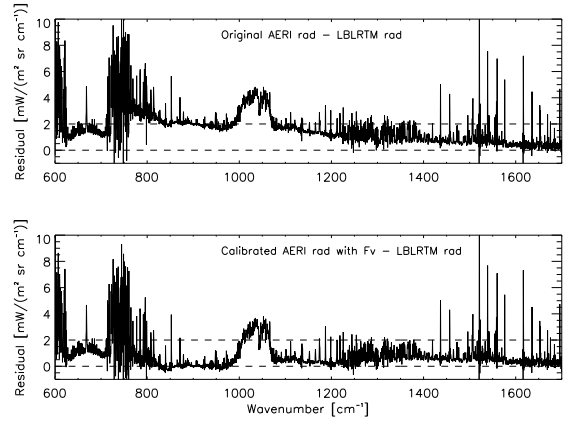


Figure 4.14: The mean residual of AERI minus LBLRTM radiances for 65 clear sky cases with low IWV. The upper plot shows the AERI original radiances - LBLRTM and the lower plot shows AERI calibrated radiances using median f_v - LBLRTM.

where \bar{f}_v is the calculated mean value of f_v . AERI measurements for 65 clear sky cases with low IWV are calibrated using this factor and compared with simulated LBLRTM radiances again. Fig. 4.14 shows the mean difference between AERI and simulated radiances for these 65 cases, before and after calibration. The dashed black lines in the plot are hint lines to make the comparison between two plots easier. As it can be seen, applying this factor has a significant effect on the window region and make the residual in this region close to zero. However it changes slightly the residual in the CO₂ band between 620-715 cm⁻¹. Its effect on water vapor lines from 1200 to 1700 cm⁻¹ is also quite negligible. According to this analysis, the obstruction correction can remove the warm bias in the window region but it has nearly no effect on the warm bias in the CO₂ and water vapor lines, therefore another reason for this bias was found which is discussed in the next subsection.

4.5.2 Aft optic correction

The second reason that was found behind the warm bias of AERI measurements was the aft optic contribution in the blackbody radiances that was not considered properly in the radiometric calibration equation of the AERI (*personal communication with D. D. Turner, 2014*). The radiance comes from inside the interferometer shelter cause a small error in the radiometric calibration equation. This contribution makes the hot blackbody slightly cooler and most probably the ambient blackbody slightly warmer. The assumed blackbody radiance, \tilde{B} with the aft optic contribution can be written as:

$$\tilde{B}_x = (1 - f_a)\hat{B}_x + f_a B(T_{aft}), \quad (4.6)$$

where x refer to the hot or ambient blackbody and \hat{B} is the blackbody radiance calculated by Eqs. 3.3 and 3.2. Besides, The AERI measures a temperature near the interferometer for each sky view that is saved in the AERI channel one and channel two file with the name of “*airNearInterferometerTemp*”. This temperature is considered in this analysis as T_{aft} .

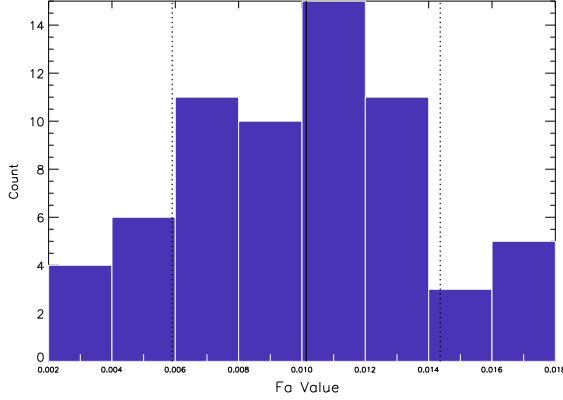


Figure 4.15: The distribution of calculated f_a at optic correction factors for 65 clear sky cases with low IWVs lower for measurements in 2012. The solid and dashed black lines shows the mean and the standard deviation of f_a respectively.

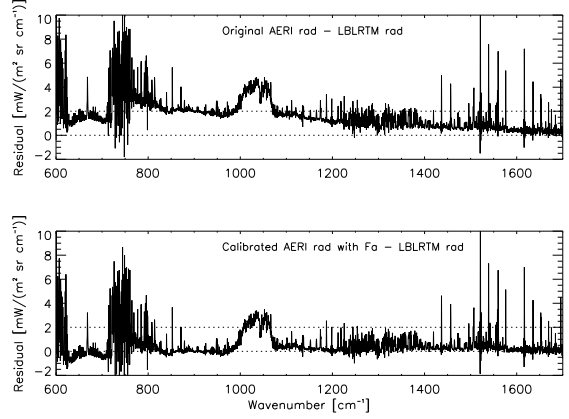


Figure 4.16: The mean residual of AERI minus LBLRTM radiances for 65 clear sky cases with low IWVs. The upper plot shows AERI original radiances - LBLRTM and the lower plot shows AERI calibrated radiances using median f_a - LBLRTM.

Based on this assumed bias in the blackbody radiance, the AERI measured radiance, \tilde{R}_{sky} can be written as:

$$\tilde{R}_{sky} = \left(\frac{C_S - C_A}{C_H - C_A}\right)(\tilde{B}_H - \tilde{B}_A) + \tilde{B}_A = \left(\frac{C_S - C_A}{C_H - C_A}\right)(1 - f_a)(\hat{B}_H - \hat{B}_A) + \hat{B}_A + f_a B(T_{aft}), \quad (4.7)$$

where C_S , C_A and C_H refer to the complex spectra observed from sky view, ambient blackbody and hot blackbody respectively. Combining Eqs. 4.7 and 3.1 and solving for f_a , gives:

$$f_a = \frac{\tilde{R}_{sky} - R_{sky}^{truth}}{B(T_{aft} - (R_{sky}^{truth} - \hat{B}_A))}, \quad (4.8)$$

with the approximation of:

$$\left(\frac{C_S - C_A}{C_H - C_A}\right)(\hat{B}_H - \hat{B}_A) \approx R_{sky}^{truth} - \hat{B}_A. \quad (4.9)$$

The LBLRTM simulated radiance is considered as true radiance, R_{sky}^{truth} . The model is run using COSMO_DE scaled profiles. f_a is then calculated using the spectral band 673-680 cm^{-1} that has the highest sensitivity to the surface temperature. Fig. 4.15 shows the bar plot of calculated f_a for 65 low IWV cases. The mean of calculated f_a for these cases is equal to 0.0101 with the standard deviation of 0.0042. The mean value and the standard deviation are shown in the plot by the black solid line and black dashed lines respectively. The calibrated radiance, R^{cal} , using this factor can be written as:

$$R^{cal} = \tilde{R}_{sky} - \bar{f}_a B(T_{aft}) + \bar{f}_a (\tilde{R}_{sky} - \hat{B}_A) \quad (4.10)$$

Note that this equation is also used the approximation in Eq. 4.9. The calibrated AERI radiance is calculated using this equation for 65 low IWV cases. Fig. 4.16 shows the mean residual of original AERI radiances minus LBLRTM radiances as well as the mean residual of calibrated AERI radiances minus LBLRTM radiances for these cases. The plot shows that

calibration by this factor has a considerable impact on the residual in the window region and make it quite close to zero. It has also reduced the residual in water vapor band between 1200-1700 cm^{-1} down to zero. The mean residual in the spectral band, 673-680 cm^{-1} that is used in this analysis for determining the f_a reaches also close to zero. However, on the right side of the band, 680-715 cm^{-1} and the left side of it, 625-650 cm^{-1} , a negative residual can be seen. The possible reason for this negative residual can be due to the fact that there is an overestimation in calculating the aft optic factor. This overestimation most probably relies on the uncertainty in the HATPRO retrieved temperatures used as surface temperatures in the LBLRTM run. However, the HATPRO temperatures reduce the uncertainty in the COSMO_DE surface temperatures, they are not absolutely accurate and thus small bias on these temperatures affect the calibration result. According to this analysis, the aft optic factor has more improvement in AERI measurements compared to obstruction factor; however, finding the absolute value of this factor is a challenge that needs quite absolute surface temperatures.

Chapter 5

Retrieval algorithm

New observations and thus new instruments are essential tools to develop improved scientific understanding of atmospheric phenomena. Atmospheric measurements can be divided into two main groups: in-situ and remote sensing. While in-situ measurements can only provide data about subjects which are in direct contact with them, remote sensing instruments can observe objects a long distance away. These instruments often do not directly measure the desired parameters. In fact, they take advantage of radiative interaction that relate the desired parameter to their measurements. The inverse method for exploiting desired parameters from this kind of measurements is called retrieval.

Retrieval methods can be classified into two groups: regression-based and variational-based. The regression-based algorithms use an empirical relationship between atmospheric states and observations such as linear or polynomial regression relationship. These algorithms are strongly sensitive to statistical properties of background information, i.e. if the desired parameter which is needed to be retrieved, is appropriately represented by the background dataset, the algorithm can retrieve the desired parameter with an acceptable accuracy, otherwise these algorithms are poor in providing an accurate result. Examples of regression-based retrieval can be found in (*Nakajima and King, 1990; Conner and Petty, 1998; Adler et al., 2003; Protat et al., 2007*).

Variational-based retrieval algorithms mainly use Bayes theorem (*Rodgers, 2000*). In this approach, the probability density function (*pdf*) of measurements are related to the *pdf* of atmospheric states to provide a *pdf* of the desired parameters, rather than provide an exact solution. The main advantage of the variational-based algorithm is to provide simultaneously the uncertainty of the retrieved parameter. In fact the *pdf* of the desired parameter is considered as its uncertainty. However, these algorithms are usually more computationally expensive compared to regression-based algorithms.

In the present work, a variational-based retrieval algorithm, called AERIOe (*Turner and Löhnert, 2014*) is applied. The AERIOe is based on the optimal estimation method which is a specific application of Bayes theorem. In this chapter, first, the optimal estimation method is generally explained. Then, in section 5.2, specifications of AERIOe are described. More details about inverse methods and optimal estimation theory can be found in *Rodgers (2000)*.

5.1 Optimal Estimation theory

The inverse method is setting up and solving a number of linear or non-linear equations. These equations describe relations between measurements and parameters that are needed to be retrieved. The measurement vector is usually represented by Y that has a dimension of m . Measurements always suffer from uncertainties that are inherent in any real observation. These uncertainties can be due to systematic errors such as calibration issues or random errors caused by instrument noise. Consequently, in the presence of uncertainty (ϵ) it is better to show the measurement with a *pdf* of ϵ .

In addition, parameters that are being retrieved, are shown by the state vector X , which has a dimension of n . The state vector can be temperature, humidity, trace gas concentration, cloud properties or any combination of these parameters. The state vector also needs to be expressed with its uncertainty defined by a *pdf*.

While the inverse method or the retrieval algorithm maps the *pdf* of Y vector into the *pdf* of X vector, the physical law of the measurement procedure which is called forward model, $F(X)$, is used to map the state vector into the measurement space. In many problems, the forward model is considered as a perfect model. However, it may suffer from several deficiencies such as incomplete physical basis. This means that there is also uncertainty in the forward model. Thus, the relation between the measurement, Y , and the forward model can be written as:

$$Y = F(X, b) + \epsilon, \quad (5.1)$$

where ϵ shows the noise or any systematic error in the measurement as well as the forward model uncertainty and b that is called model parameter, indicates parameters that have an impact on the forward model simulation but considered to be known to some extent. The uncertainty in the b parameters need to be also considered in the retrieval uncertainty.

Furthermore, there can be some background information about the state vector. This information called prior information and is given by X_a . The prior data that are used to constrain the state vector, also define by a *pdf* of their uncertainty. The prior uncertainty is usually high (for example compared to the uncertainty in the measurements). The background information can be provided using the climatological or long-term model data.

A helpful approach for relating the *pdf* of the measurement vector to the *pdf* of the state vector in the presence of the prior data is the Bayesian method, in which the background information of the state vector is updated using the measurement as:

$$P(X|Y) = \frac{P(Y|X)P(X)}{P(Y)}, \quad (5.2)$$

where $P(X)$ shows the *pdf* of the prior information of X which is normalized to 1; the $P(Y|X)$ is the conditional *pdf* of Y for a given X that indicates the act of the forward model; $P(X|Y)$ is the posterior *pdf* of X for a given Y or the desired quantity; and the $P(Y)$ which can be interpreted as a priori information of the measurement, is a dominator and in practice considered as 1. The Eq. 5.2 or in general the Bayesian approach characterizes all possible states for a given problem and assigns a *pdf* to each of them. However, the desired state is the best or the optimal solution. The optimal solution can be regarded as the most probable state with minimum uncertainty.

Before finding the most probable state, an appropriate distribution needs to be assigned to different *pdfs*. A useful distribution that can well present many *pdf* in real problems and is

algebraically convenient is the Gaussian distribution. Using the Gaussian distribution for the *pdf* of both the measurement and the prior vector, the Eq. 5.2 can be written as:

$$-2\ln P(x|y) = [y - F(x)]^T S_\epsilon^{-1} [y - F(x)] + [x - x_a]^T S_a^{-1} [x - x_a] + c_3, \quad (5.3)$$

where S_ϵ and S_a refer to the measurement error covariance matrix and the prior covariance matrix respectively. A covariance matrix is a symmetric matrix where each of its diagonal elements shows the variance of that element and non-diagonal elements indicate the covariance between different elements. The covariance matrix is used to show the uncertainty of a vector. In order to find the most probable state, the derivative of Eq. 5.3 need to be equated zero:

$$\nabla_x \{-2\ln P(X|Y)\} = -[\nabla_X F(X)]^T S_\epsilon^{-1} [Y - F(X)] + S_a^{-1} [X - X_a] = 0. \quad (5.4)$$

If the *pdf* of the prior and the measurement are considered as a Gaussian distribution, Eq. 5.4 can be regarded as a general solution for both linear and non-linear forward model. However, in real problems such as the problem in the present work, many forward models are non-linear which lead to a non-linear retrieval problem. In *Rodgers* (2000), the linearity or non-linearity of inverse problems are qualitatively categorized where many of real inverse problems belong to the moderately non-linear category. The moderately non-linear inverse problem means that this problem can be regarded as a linear problem in order to analyze its error, but for finding the solution, the problem needs to be considered as a non-linear problem. For these kinds of problems, Eq. 5.4 can be solved numerically using the Gauss-Newton method (*Rodgers*, 2000). Using this method, the solution of Eq. 5.4 can be written in two forms as:

$$X_{i+1} = X_i + (S_a^{-1} + K_i^T S_\epsilon^{-1} K_i)^{-1} K_i^T S_\epsilon^{-1} [Y - F(X_i) + K_i(X_i - X_a)] \quad (5.5)$$

$$= X_i + S_a K_i^T (K_i S_a K_i^T + S_\epsilon)^{-1} [y - F(X_i) + K_i(X_i - X_a)], \quad (5.6)$$

where K that is called Jacobian, defined as $K = \nabla_X F$. The Jacobian is an important parameter in the retrieval problem which shows the sensitivity of the forward model to a change in each state vector element. The first guess in the iterative retrieval is usually X_a , but this is not required. Note that i shows the number of iteration.

In a numerical method which produces iterative solution, criteria should be defined to stop the algorithm. The criteria stops the retrieval when the change in the state vector (either in X -space or in Y -space) is small, i.e., within the error of the X - or Y -space uncertainty, respectively. There are different ways for testing the convergence of the retrieval algorithm. A popular one is to check the size of the step between two iterations in the measurement space or in the state space that need to be smaller than the estimated error. This test in the measurement space can be written as:

$$d_i^2 = [F(X_{i+1}) - F(X_i)]^T (S_\epsilon (K S_a K^T + S_\epsilon)^{-1} S_\epsilon)^{-1} [F(X_{i+1}) - F(X_i)] \ll m, \quad (5.7)$$

where m is the dimension of measurement vector. And in the state space, it can be written as:

$$d_i^2 = (X_i - X_{i+1})^T (S_a^{-1} + K_i^T S_\epsilon^{-1} K_i)^{-1} (X_i - X_{i+1}) \ll n, \quad (5.8)$$

where n is the dimension of space vector.

An important parameter that needs to be determined after finding the retrieval solution is the uncertainty of the optimal solution known as a posteriori covariance matrix. This covariance matrix can be calculated as:

$$S_{opt} = (K_{opt}^T S_\epsilon^{-1} K_{opt} + S_a^{-1})^{-1}, \quad (5.9)$$

Table 5.1: Primary spectral bands as well as their primary sensitivity used in the AERIOe algorithm.

spectral band wavenumber (cm ⁻¹)	primary sensitivity
538-588	Water vapor
612-618	Temperature
624-660	Temperature
674-713	Temperature
828-835	Cloud properties
843-848	Cloud properties
860-865	Cloud properties
872-877	Cloud properties
898-905	Cloud properties

where K_{opt} is the Jacobian of the forward model with respect to the retrieval solution.

Another useful parameter that can be calculated after finding the optimal solution, is degrees of freedom for signal (DFS). The DFS shows the number of independent piece of information in the measurement state. The DFS is defined as:

$$DFS = tr([K^T S_\epsilon^{-1} K + S_a^{-1}]^{-1} K^T S_\epsilon^{-1} K), \quad (5.10)$$

where tr denotes the trace of the matrix.

5.2 The AERIOe

The AERIOe is a variational-based retrieval algorithm based on the optimal estimation method (*Turner and Löhnert, 2014*). The algorithm uses the AERI observation as a Y vector, while the X vector includes temperature and humidity profile as well as cloud properties consisting of liquid water path (LWP) and cloud droplet effective radius (Reff). In the present study, the AERIOe was modified to include the retrieval of atmospheric CO₂ profile.

The AERIOe algorithm has a range of options that could be applied that affect how it runs. For example, in section 4.5, it has been discussed how corrections could be applied to the AERI data to account for a partial obscuration (i.e., the f_a of f_v parameters). Additionally, AERI radiance data could be averaged over many minutes to improve the signal-to-noise ratio and hence the accuracy of the retrieval. These options are controlled via the variable input parameter (VIP) file (hereafter VIP file). A flow chart that shows the input data streams in the AERIOe is shown in Fig. 5.1.

The spectral bands used in the retrieval algorithm are also defined in the VIP file. In the present AERIOe version, these spectral bands need to be selected from either the AERI channel one or the channel two file (see section 3.1), i.e. they can not be selected from both channel one and two, simultaneously. The primary selected spectral bands to retrieve the temperature, humidity and cloud properties are listed in Table 5.1. These are the spectral bands that were used in the previous AERI studies (*Smith et al., 1999; Turner and Löhnert, 2014*). However, in order to retrieve the CO₂ concentration these spectral bands are slightly modified. The modification is described in more details in chapter 6.

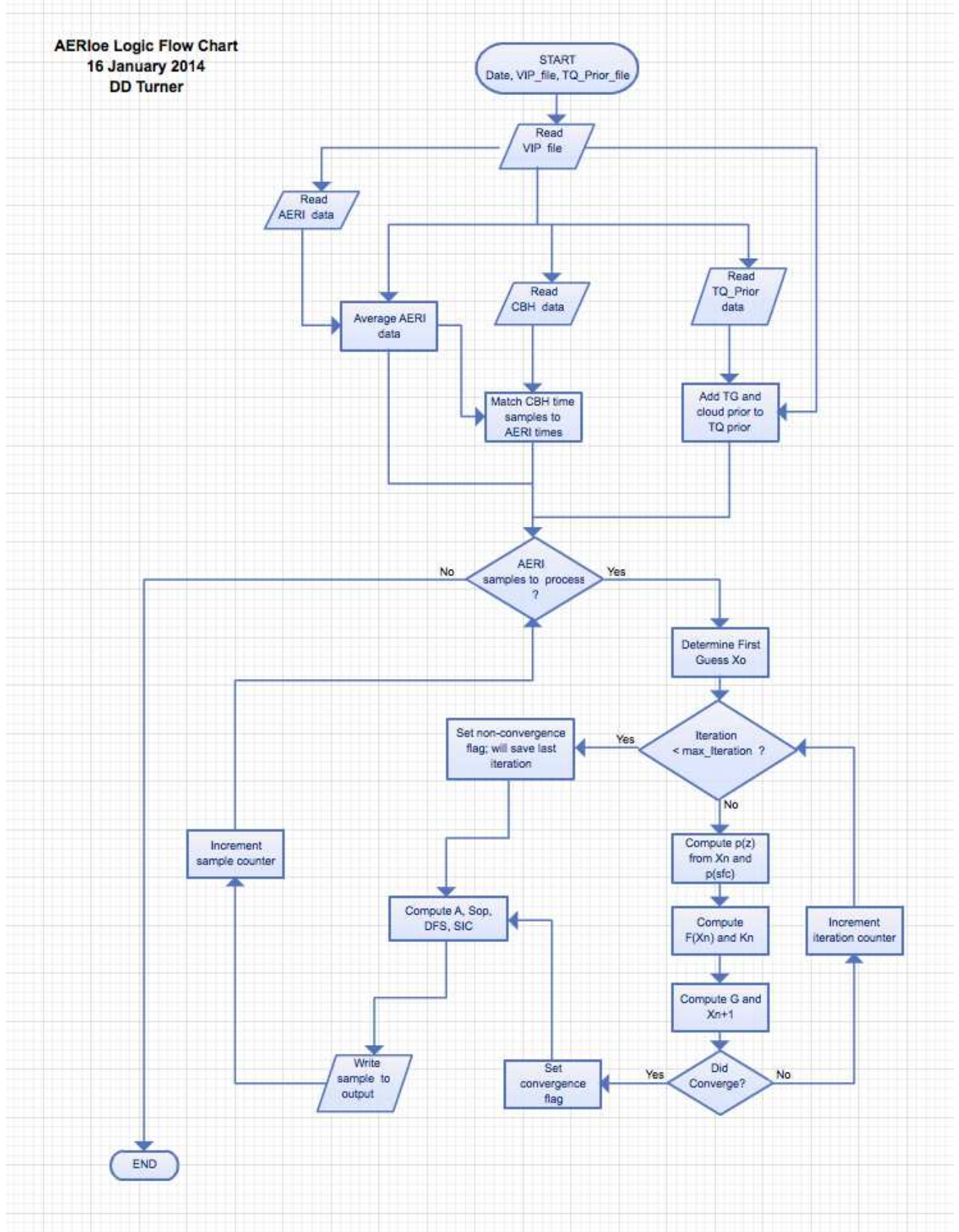


Figure 5.1: The flow chart of the input data streams in the AERIOe. Source: *personal communication with D. D. Turner, 2014*

The measurement error covariance matrix (S_e) should include contributions from the uncertainty in the observations (S_Y), the uncertainties in the forward model (S_F), and the uncertainties of the parameters b (S_b) that are used in the forward model (S_F and S_b can be combined into a single matrix). The S_Y is defined using the noise of the AERI (which is determined from the imaginary component of the complex observed radiances). The noise of the AERI is regarded as random uncorrelated noise, therefore, the measurement covariance matrix is a symmetric matrix with only non-negative diagonal elements where its non-diagonal elements are zero. The forward model error is typically difficult to determine. One way to capture the forward model error is to inflate the S_Y matrix (Masiello et al., 2012). The inflation factor depending on the spectral region can be a factor of 2-4 (Turner and Löhnert, 2014). Note that as it has been mentioned in section 3.1, the principal component noise filtering can be used to reduce the AERI noise; however, even after reducing the noise, the original AERI noise is used in defining the S_Y matrix which is also one way to capture the forward model uncertainty.

The algorithm can be used for both clear sky and cloudy cases. The AERIOe requires a cloud base height estimate to know where to place a cloud vertically. The data of a collocated ceilometer can be the primary input, and this is specified by the VIP file. However, if the ceilometer data is missing or if the ceilometer estimates no cloud, a default cloud base height is assumed, with the default value (often 2 km) that is also specified in the VIP file. This possibility allows the algorithm to overcome any mistake in clear sky prediction and retrieve the cloud properties in any case. If the case is truly clear sky, then a value equal 0 g/m² is expected for LWP within its uncertainties.

The prior information is given to the algorithm in the form of a prior *pdf* with Gaussian distribution. The prior data corresponding to the two different AERIOe applications in the present study, i.e. simulation study (chapter 6) and real data application (chapter 7), are computed from REMO model data (see section 6.2.1) and radiosonde data (see section 7.1). Mean prior profiles of temperature and humidity calculated from either the model or the radiosonde data are interpolated on the defined vertical grid of AERIOe that is a fixed grid spacing with a resolution of 25 m at the surface which reaches to 800 m at 3 km and 2000 m at 6 km. While the prior information of temperature and humidity profiles need to be calculated in advance, the mean value of LWP and Reff and their standard deviation are determined in the VIP file. The prior data are assumed to be 0 ± 50 gm⁻² for LWP and 8 ± 4 for Reff. The cloud properties are considered to be uncorrelated with each other. Besides, no correlation is considered between cloud properties and temperature or humidity profile.

Many inverse problems such as the inverse problem of the present study are ill-determined. Therefore, additional information is often needed to stabilize the retrieval algorithm. In the present work, the additional information (often part of the x -vector) are given in the form of the prior information with very small uncertainty. Small prior uncertainty of a parameter prevents the algorithm to change the parameter in successive iterations, and thus the parameter assumed as a constant parameter in the algorithm. The auxiliary data used in the present work are numerical model profiles of temperature and humidity for upper atmospheric levels (often above 4 km) as well as in-situ observations for the surface temperature, humidity and CO₂.

The forward model in AERIOe includes different steps. First, the LBLRTM (see section 2.4) provides the monochromatic gaseous optical depths at each layer. Then the spectral cloud optical depth is added to the cloud layer, wherein the cloud properties are the same as those used in the LBLRTM-DISORT model (described in Turner (2005)). Then the downwelling

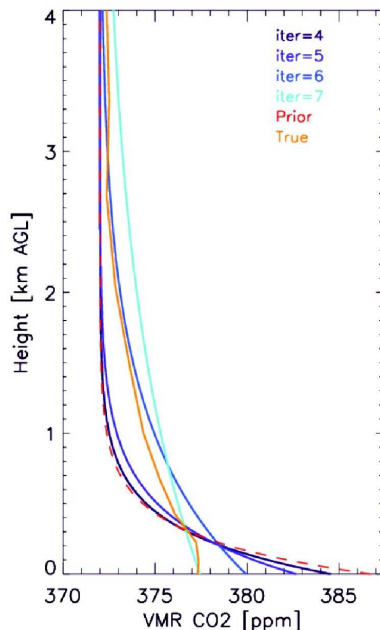


Figure 5.2: An example of AERIOe retrieval using simulated AERI radiances. The blue lines shows the profile in the state vector of different iterations. The orange line shows the true profile (which is used as input data in the simulated radiances) and the red dashed line shows the prior profile.

monochromatic radiance at the surface is computed, and this is convolved with the AERI instrument spectral response function.

An important parameter in Eq. 5.12 that needs to be calculated for each iteration is the Jacobian K_i . In order to calculate the Jacobian in each iteration, first the “base radiance” using X_i as input profiles is calculated. Then each element in the state vector X_i is individually perturbed to provide new input profiles for a new LBLRTM run. Thus the Jacobian for element j in the state vector is calculated as:

$$K_{ij} = \frac{F(X_{ij} + \Delta X_{ij}) - F(X_{ij})}{\Delta X_{ij}}, \quad (5.11)$$

where i shows the iteration number. Note that K_{ij} is a vector with a dimension equal to the measurement vector dimension. Eq. 5.11 is repeated for all state vector elements until K_i which is the Jacobian matrix of iteration i is derived.

In order to find the solution, the AERIOe applies the Gauss-Newton iterations to solve a modified version of Eq. 5.6 as:

$$X_{i+1} = X_i + (\gamma S_a^{-1} + K_i^T S_\epsilon^{-1} K_i)^{-1} K_i^T S_\epsilon^{-1} [y - F(X_i) + K_i(X_i - X_a)] \quad (5.12)$$

The extra parameter in this equation compared to Eq. 5.6 is the γ factor. This equation which has been applied in several studies (*Carissimo et al., 2005; Zhou et al., 2007; Masiello et al., 2012*) is used to change the weight between the prior and the observation vector. In the limit of an infinitely large value of γ , the Eq. 5.12 gives the prior as a solution. On the other hand, when the γ is equal to 1, the explicit form of Eq. 5.6 can be derived. By changing this factor between a large value and 1, the algorithm can move slowly from the information in the prior

data to the information in the observation data, and thus helps the algorithm to be stabilize. This method is particularly useful in cases of a poor first guess. In this case, a large γ in first iterations lets the algorithm adjust the state vector slowly, whereas, with decreasing γ factor in each iteration, more and more information comes from the observation vector. There are different ways for changing the γ value from one iteration to another one such as L-curve method (*Hansen, 1992*). However, in the present version of the AERIOe, the γ values are simply decreased in a fixed sequence as 1000, 300, 100, 30, 10, 3, 1, 1, 1, .. . The algorithm is not considered converged until γ equals 1. This means that the algorithm needs at least 7 iterations before convergence, whereas, the maximum number of iterations is set in the VIP file. Note that, X_0 in Eq. 5.12 is often chosen as the prior, X_a , however, there are different possibilities for selecting the first guess in the AERIOe.

Fig. 5.2 shows different iterations from an example of AERIOe run in order to retrieve the CO₂ profile. In this example simulated AERI radiances (with AERI noise) are used. The true profile which is shown in the plot is used as input profile in the simulated radiances. The prior profile is chosen as a first guess; however, it can be seen that the true profile is significantly different from the prior profile. The γ factor is decreasing with increasing the iteration and reaches to 1 for the iteration 7 that is selected as optimal solution. This example shows that how γ factor helps the algorithm to slowly moves toward the true profile in different iterations and retrieve a profile close to the true profile even with a rather poor first guess.

After convergence the algorithm, the optimal solution as well as other retrieval parameters such as posterior covariance matrix and the number of DFS are saved in a output file for further analysis. In the next sections, the application of the AERIOe for both simulation study and real data in order to retrieve the atmospheric CO₂ profile are presented.

Chapter 6

CO₂ profile retrieval for simulated radiances

In order to assess the ability of the AERIOe to retrieve the atmospheric CO₂, in the first step, a simulation study using the calculated radiances by a radiative transfer model is performed. This step helps to find the strengths and the deficiencies of the algorithm because the simulated radiances have no systematic bias or unexpected issues which can be typically found in the real measurements. These results can show the theoretical potential of the AERI radiances to provide the information about the atmospheric CO₂.

This study is divided into two sections. In the first section, temperature and humidity profiles as well as the mean column amounts of other trace gases are considered as known parameters in the algorithm and the algorithm is performed only for clear sky conditions. Consequently, the only unknown parameter in the algorithm is the CO₂ profile. In this section, first, a simple model is considered for the atmospheric CO₂ profile which is a constant profile with no diurnal change near the surface, meaning that the algorithm only needs to retrieve one value considered as constant mixing ratio of the atmospheric CO₂. These retrieval results are shown in subsection 6.1.1. In the rest of this section, a model to parameterize the atmospheric CO₂ profile is proposed and applied in the algorithm which is presented in subsections 6.1.2 and 6.1.3. The results of running the algorithm with this model are shown in subsections 6.1.4 and 6.1.5.

In the second section the CO₂, temperature, and humidity profiles are all considered as unknown parameters, meaning that the algorithm is performed to retrieve the temperature, humidity and CO₂ profiles simultaneously in clear sky conditions. In this section, first, the prior data of the temperature and humidity profiles are introduced in subsection 6.2.1. The results of simultaneous retrieval of temperature, humidity and CO₂ profiles are shown in subsection 6.2.2. In the rest of this section, two approaches in order to improve the retrieval results are suggested and applied which are shown in subsections 6.2.3 and 6.2.4.

6.1 CO₂ retrieval with fixed temperature and humidity

As it has already explained in section 5.2, the AERIOe can be used to retrieve temperature, humidity, cloud properties and mean column amount of some trace gases such as CO₂, CH₄ and N₂O. In order to evaluate the ability of the AERIOe to retrieve the atmospheric CO₂

concentration, first, a simple step is designed. In this step, temperature and humidity profiles as well as mean column amount of trace gases, CH₄ and N₂O are considered as known parameters in the AERIOe. Then, the AERI radiances are simulated for clear sky conditions and thus cloud properties are considered zero in the algorithm. In this section, the only unknown parameter is atmospheric CO₂ profile.

The AERI radiances are simulated using the LBLRTM. The input temperature and humidity profiles of the LBLRTM are provided by REMO model (see section 3.5). In order to present the realistic random noise of the measurements to the simulated radiances, the noise of the real AERI measurement is added to the simulated radiances. As explained in section 3.1, the standard deviation of the imaginary part of the radiances derived from the radiometric calibration equation over 25 cm⁻¹ spectral band is considered as real AERI noise spectra. These standard deviations are used to compute the random values with normal distribution. They are then added to the simulated radiances. Note that in this step principal component noise filter (see section. 3.1) are not used. The random AERI noise is also used to define the measurement error covariance matrix in the AERIOe. Since the AERI noise is considered as a random uncorrelated matrix, the computed error covariance matrix is a diagonal matrix where its diagonal elements are equal to the square of the random AERI noise.

The spectral bands which are used in this step consist of 612-618, 624-660, 674-713 cm⁻¹. These are the spectral bands which are used in the previous studies to retrieve the temperature profiles from the AERI radiances (*Smith et al., 1999; Turner and Löhnert, 2014*) where the CO₂ spectral band from 713 to 723 cm⁻¹ is also used in the AERIOe run. This extra spectral band which is on the edge of the 15 μm CO₂ line, helps the algorithm to get more sensitivity to the CO₂ mixing ratio in upper atmospheric levels (see section. 2.5). Besides, the spectral band between 538 and 588 cm⁻¹ which has a primary sensitivity to water vapor is removed since the algorithm does not retrieve the humidity profile in this step.

As it is mentioned, in this step, the temperature and humidity profiles are considered as known parameters, meaning that true temperature and humidity profiles in each run should be given to the algorithm and these profiles need to be kept constant in all iterations. The true temperature and humidity profiles are the profiles which are used as input data to provide the simulated radiances. These true profiles are set to equal the prior data. In addition, the 1-σ uncertainty of temperature and humidity profiles in the prior covariance matrix set to very small values. The small variation in the prior uncertainty prevents the algorithm to change the retrieved humidity and temperature profiles in each iteration, so that these profiles are constant in all iterations. Thus, when the retrieval is performed for a daily run, the prior changes at each time step so that it can capture the evolution of the temperature and humidity profiles over the diurnal cycle.

Besides, the spectral bands used in the algorithm were chosen so that there was no sensitivity to other trace gases i.e. CH₄ and N₂O, so that these parameters have no impact on the retrieval result. However, the true values of these trace gases which are used in simulating the radiances are also given to the algorithm as known parameters. In the next subsection, a simple model which is considered for the atmospheric CO₂ profile and the result of running the AERIOe with this simple model is presented.

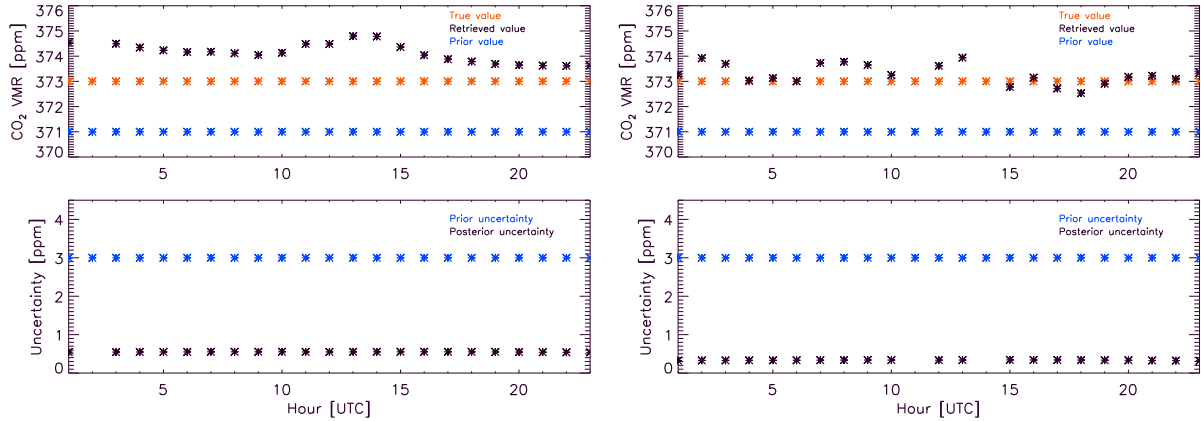


Figure 6.1: The retrieved values of the atmospheric CO₂ mixing ratio using simulated AERI radiances where the original AERI noise is added to the simulated radiances (left panel) and a reduced noise is added to the simulated radiances (right panel). The upper plot shows the retrieved value (in black), true values (in red) which are used as input values in the radiative transfer model to simulate radiances and prior values (in blue) used in the AERIOe algorithm. Lower plot shows 1- σ uncertainty in the prior values (in blue) and 1- σ uncertainty (in black) in the retrieved values.

6.1.1 Retrieve the constant CO₂ mixing ratio

The ability of the AERIOe to retrieve the atmospheric CO₂ is first tested for a simple CO₂ profile model where the CO₂ is considered as a trace gas with a constant atmospheric mixing ratio with height.

The AERI radiances are simulated with the LBLRTM using hourly REMO profiles. The REMO temperature and humidity profiles of 15 January 2002 are used as input profiles to run the LBLRTM. The input of constant CO₂ mixing ratio for this day is equal to 373.0 ppm. The random AERI noise derived from the average noise of measurements during a clear sky day is added to the simulated radiances. These radiances are given to the AERIOe

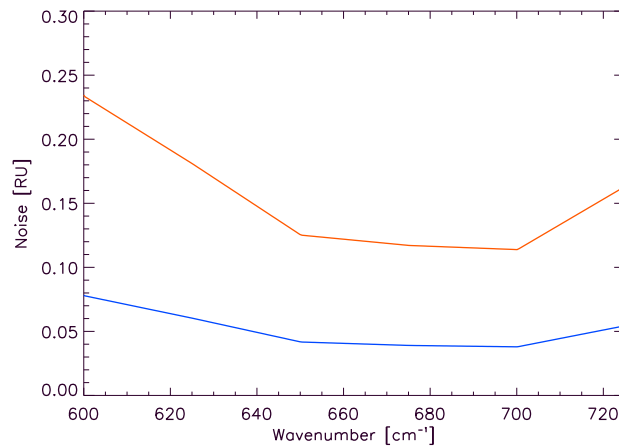


Figure 6.2: The noise spectrum of the AERI in rapid sample mode. The red line shows the original noise and the blue line shows the reduced noise by a factor of 3.

as Y vectors. In this run, the state vector, x is a scalar value, rather than a vector. The prior value of the x is considered 371 ppm with $1\text{-}\sigma$ uncertainty of 3 ppm. The AERIOe is run for the whole day with an hourly temporal resolution. The result is shown in Fig. 6.1.

As the left panel in Fig. 6.1 shows, the retrieved values are around 1 ppm higher than the true values. Besides, the posterior uncertainties are around 0.5 ppm, meaning that the true values can not be captured by the retrieved values within this uncertainty. In this run, the calculated degrees of freedom for signal (DFS) for retrieved values are around 1 and except for the case at 1 UTC, the algorithm converged for all cases.

As explained in section 3.1, the AERI that works in rapid sample mode, provides a sky view approximately every 7 to 12 s. This short time interval for the sky averaging leads to relatively high noise compared to the noise of the AERI that works in the standard mode with 8-min temporal resolution. The high noise in the AERI measurements can have a significant impact on the retrieval result, and thus reduce its accuracy. This problem, particularly in the present study, is significant since the sensitivities of the AERI radiances to the change in the atmospheric CO₂ can be in the same order of the AERI noise, i.e. refer to Fig. 2.4c which shows the sensitivity of the AERI radiances to the change in the CO₂ profile. In addition, the average AERI noise spectra in a clear sky measurements are also shown in Fig. 6.2. Comparison between these two plots shows that the noise spectra is relatively high compared to the AERI sensitivity. One solution can be to take the average radiances to reduce the noise, and thus increase the signal-to-noise ratio. Note that the AERIOe run with the reduced noise simulates the results that might be achieved if the principal component noise filter was applied to the AERI radiance data before the retrieval. This is another way to reduce the noise in the AERI besides averaging it over time.

In order to test the impact of the noise reduction on the retrieval result, the AERIOe is run for the second time where a reduced noise is added to the simulated radiances. The original AERI noise spectra is divided by 3 to get reduced noise spectra. The noise spectra is shown in blue in Fig. 6.2. This noise spectra can be achieved by averaging at least 9 (square of 3) AERI radiances or by averaging the AERI radiances over about 5 min for the AERI radiances with 20 s temporal resolution. Note that, the reduced noise spectra is also used to compute the measurement error covariance matrix in the AERIOe. The right panel in Fig. 6.1 shows new retrieval results. The retrieved values presented in the upper plot show considerable improvement compared to the retrieved values shown in the left panel. The posterior uncertainties are also reduced compared to the left panel and reached around 0.3 ppm. The result shows that about 70% of the true values are captured by the new retrieved values within their uncertainties. The remaining retrieved values have difference less than 1 ppm with the true values. The median retrieved mixing ratio of CO₂ for this day is equal to 373.1 ppm where it is very close to the median true value, 373.0 ppm. The DFS values in this run also increase and reach around 1.3. Besides, the algorithm converged for 21 of 23 cases.

The AERIOe results using the reduced noise spectra in the simulated radiances show good accuracy in capturing the constant atmospheric CO₂ mixing ratio; however, assuming a constant CO₂ profile without any diurnal cycle is a rather simple CO₂ model particularly for the CO₂ profile in the lower atmospheric levels. Due to different interactions in the boundary layer, the CO₂ concentration can have significant diurnal change, especially in lower atmospheric levels. Estimation of this diurnal change is a valuable tool to analyze the land and atmosphere interaction in the carbon cycle study. In the rest of this section, a model to parameterize the diurnal cycle of atmospheric CO₂ is presented in order to use it in the

AERIOe and retrieve the CO₂ profile in the boundary layer.

6.1.2 Parametrization of the CO₂ profile

The CO₂ concentration, particularly near the surface, can increase significantly during nighttime due to soil respiration or it can decrease during daytime due to plant photosynthesis. Measurements of the change in the CO₂ concentration in lower atmospheric levels especially in the boundary layer give a powerful opportunity to the scientist to study the interaction between atmospheric CO₂ and land-vegetation. In order to capture this variation, the AERIOe needs to be modified. However, due to the low sensitivity and small DFS in retrieving the atmospheric CO₂ content which is shown in the previous subsection, the CO₂ profile is not retrieved explicitly the same as temperature or humidity profile. Therefore, a model is used to parametrize the atmospheric CO₂ profile, particularly in the boundary layer. This parametrization simplifies the CO₂ profile, and thus helps the AERIOe provide essential information for capturing the diurnal cycle of the CO₂ profile in the boundary layer.

In order to find an appropriate model to parameterize the CO₂ profile in the boundary layer, the change of the CO₂ concentration in lower atmospheric levels during daytime and nighttime is analyzed. In this analysis, CO₂ profiles provided by REMO model are used. Fig. 6.3 shows the diurnal cycle of CO₂ profiles provided by REMO model for two days with different IWV amounts, a summer day with rather high IWV and a winter day with relatively small IWV. The summer day on 15th of July, 2002 (left plot) shows a difference of about 30 ppm in the CO₂ volume mixing ratio (VMR) in the lower atmosphere near the surface that is mainly due to the plant photosynthesis and respiration of soil and vegetation. During the daytime, the CO₂ uptake by vegetation reduces CO₂ amount near the surface and leaves a rather constant atmospheric CO₂ profile. After sunset and stopping the photosynthesis, the respiration turns into the dominant process which produces a relatively large increment in the CO₂ amount near the surface. Similarly, this process can be seen in the winter day, on 1st of Feb 2002 (right plot). However, the CO₂ difference in lower levels between daytime

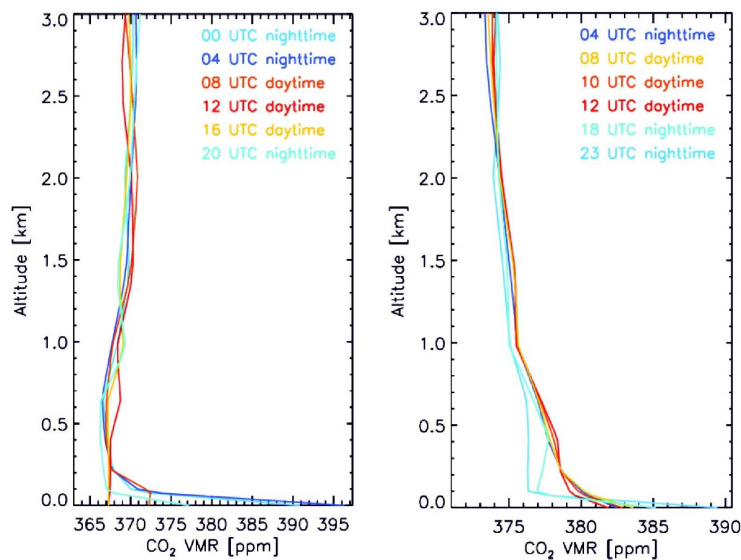


Figure 6.3: The diurnal cycle of atmospheric CO₂ profile on 15th of July (left) and 1st of Feb (right) 2002 at the Hegyhatsal station in Hungary provided by REMO model.

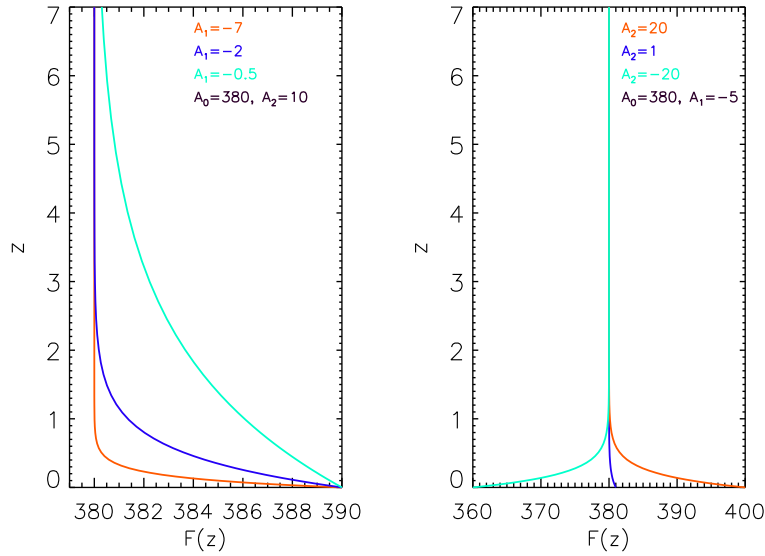


Figure 6.4: The variations of the exponential function defined in Eq. 6.1 in terms of its parameters. The left plot shows the variation in terms of A_1 , while A_0 and A_2 are fixed and the right plot shows the variations in terms of A_2 when the A_0 and A_1 are fixed.

and nighttime for this day is rather lower compared to the summer day. These two examples show that main diurnal changes in the CO₂ VMR are in the lower atmospheric levels and particularly in the CO₂ surface value. In contrast, the CO₂ VMR in upper levels or the levels above the boundary layer shows no considerable diurnal change. The CO₂ amount in these levels usually known as CO₂ background amount. The background CO₂ can change monthly or seasonally, while it also has smooth increases due to the rising of the anthropogenic CO₂ in the atmosphere.

According to the diurnal change and the approximate shape of the CO₂ profile in the boundary layer, an exponential function is used to parametrize the atmospheric CO₂ profile as:

$$F(z) = A_2 \text{EXP}(A_1 z) + A_0, \quad (6.1)$$

where z indicates the atmospheric levels and $F(z)$ gives the CO₂ VMR for each atmospheric level. This exponential function is defined by three parameters, A_0 , A_1 and A_2 , where A_0 indicates the asymptote value of the function when z goes to the quite enough high values; A_1 shows the curvature of the function and A_2 parametrizes the $F(z)$ at $z=0$.

Fig. 6.4 shows variations of this function when these parameters change. As the left plot shows, with changing the A_1 , the curvature of the exponential function changes. This parameter can define the specific height where the CO₂ VMR deviates from the background CO₂ or in another word, it can determine the CO₂ boundary layer. This plot shows that when this parameter goes to high negative values, the height of this layer decreases. Conversely, giving small negative values to this parameter increases the height of this layer. Note that, the values of A_1 are limited between -0.5 and -7.0, because using values out of this range for A_1 gives an unrealistic shape for the CO₂ profile. The right plot of Fig. 6.4 shows the change in the shape of this function due to variations in A_2 . As it can be seen, by changing the A_2 , the surface value of the function can move between negative and positive values, meaning that this parameter can parametrize the surface value of the function. In contrast to A_1 , this parameter has no limitation since both negative and positive values for this parameter can

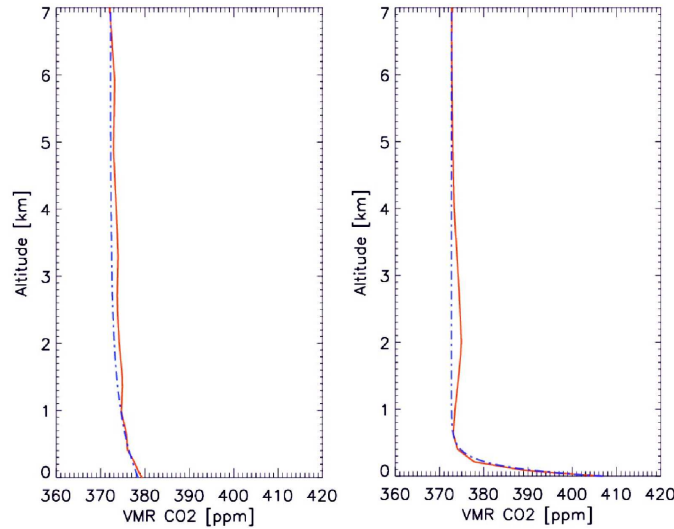


Figure 6.5: Two examples of CO₂ profiles provided by REMO which are also fitted using the defined exponential function in Eq. 6.1. The red curve is the REMO profile, while the dash-dot curve is the fit to the exponential function. The left plot shows a typical daytime profile and the right plot shows a typical nighttime profile.

represent a real CO₂ profile. Based on this analysis, if this function is used to parametrize a CO₂ profile, the A_0 indicate the background CO₂ concentration, whereas A_1 and A_2 can modify the curvature and the surface value of the CO₂ profile respectively.

When using this exponential function to parametrize the CO₂ profile in the AERIOe, the algorithm needs to retrieve only three parameters to determine the CO₂ profile or in other words, the unknown parameters related to the CO₂ profile in the AERIOe state vector consist of three parameters. Besides, the A_0 can be considered as a rather constant parameter in a daily run, so that the algorithm retrieves mainly two parameters which are a reasonable number of parameters to retrieve for the low DFS shown in the previous subsection. In order to run the AERIOe to retrieve these three parameters, a background information or the probability density function for each of these parameters need to be determined. This is explained in the next subsection.

6.1.3 Prior data of the three exponential function parameters

In order to compute the prior data or the probability density function of A_0 , A_1 and A_2 , the defined exponential function in Eq. 6.1 is fit to each of the CO₂ profiles in the REMO dataset. This approach estimates these three parameters for each CO₂ profile. By repeating this process for different CO₂ profiles a dataset is obtained for each parameter which can be used to compute the mean value and its standard deviation. In order to provide these dataset, hourly REMO CO₂ profiles of the Hegyhatsal station in Hungary are used. Note that the CO₂ profiles of this station are also used as input data in the LBLRTM to simulate the AERI radiances. The REMO CO₂ profiles from 2002 and 2003 are utilized which provide more than 1400 profiles to compute monthly prior data.

For estimating the best fit for each CO₂ profile, a retrieval algorithm based on the optimal estimation method is applied. In this algorithm, the Y vector is the CO₂ profile of REMO and the X vector includes A_0 , A_1 and A_2 . The uncertainty in the Y vector to define the

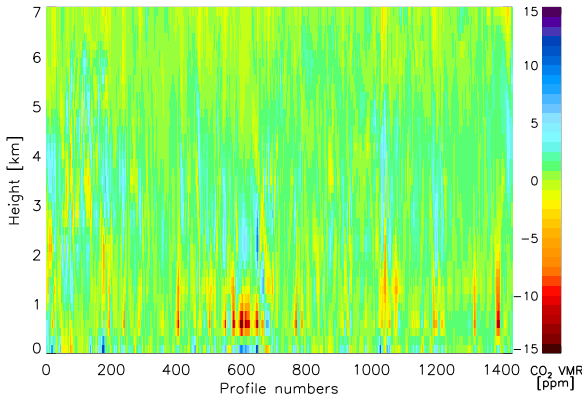


Figure 6.6: The difference between CO₂ profiles of REMO and the fitted profiles using the defined exponential function. This plot shows the difference for the profiles in November of 2002 and 2003.

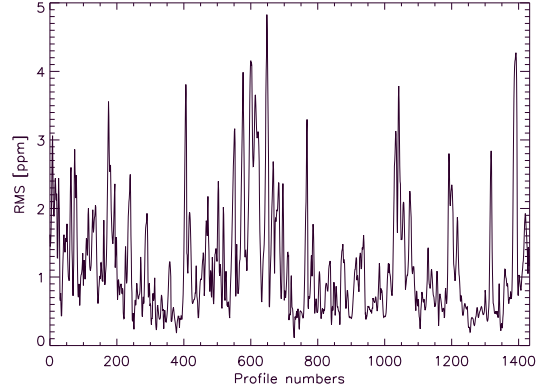


Figure 6.7: The RMS values between CO₂ profiles of REMO and the fitted profiles using the defined exponential function. This plot shows the difference for the profiles in November of 2002 and 2003.

measurement error covariance matrix is taken as 3 ppm in CO₂ VMR from surface to 1 km, 2 ppm for levels between 1 and 5 km and 1 ppm in upper levels with no correlation between different levels. The uncertainty in different layers are selected approximately according to the variations of the CO₂ concentration in the atmosphere which decreases with increasing the height. The forward model of the algorithm is the given exponential function where the Jacobian for each of three parameters is computed as:

$$\frac{\partial F}{A_2} = EXP(A_1 z), \quad (6.2)$$

$$\frac{\partial F}{A_1} = A_2 z EXP(A_1 z), \quad (6.3)$$

$$\frac{\partial F}{A_0} = 1. \quad (6.4)$$

While the Jacobian of A_0 is constant in all iterations, the Jacobian of A_1 and A_2 needs to be calculated in each iteration using updated values of the A_1 and A_2 for the current iteration. The prior values are defined 16 and -7 for A_1 and A_2 respectively while the prior of A_0 is considered between 372 and 377, depending on the month. A small 1- σ uncertainty equal 1 is defined for A_0 in the prior covariance matrix with no correlation with the other two parameters. Besides, the A_1 and the A_2 take 1- σ uncertainty around 10 and 4 respectively. A negative correlation equals 0.5 is defined between these two parameters in the prior covariance matrix. The prior values as well as the uncertainties are determined by giving a small dataset of REMO profiles to a simple code for fitting them to the exponential function. The fitted profiles provides a primary estimation for the parameters and their variations which is in determining the prior data. Note that this simple code is not suitable in order to use for large number of profiles and can not provide accurate estimation for the parameters.

Fig. 6.5 shows typical nighttime and daytime CO₂ profiles of REMO which have been fitted by the exponential function. These two profiles are appropriately captured by the exponential function. However, since the exponential function provides a smooth profile, some small variations in the CO₂ profile can not be seen by fitted profile.

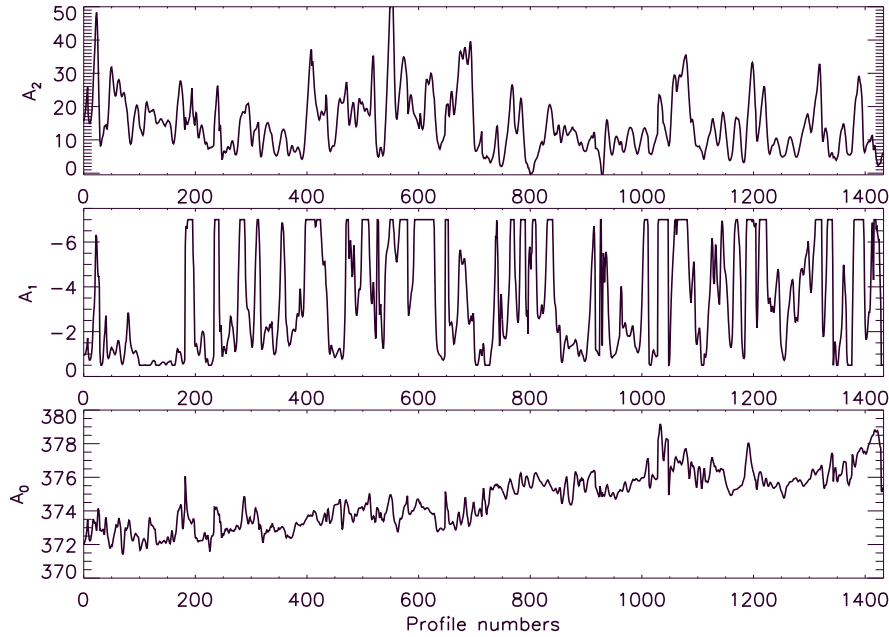


Figure 6.8: Time series of three derived parameters in November 2002 and 2003. The top plot shows the time series of A_2 , the middle plot shows the time series of A_1 and the bottom plot shows the time series of A_0 .

Fig. 6.6 shows the difference between fitted exponential functions provided by this algorithm and REMO profiles in November 2002 and 2003. For this month, the algorithm converged for 1433 profile of 1440 (more than 99%). The differences for each profile are mainly between -3 and 3 ppm, however, for some cases, particularly in the levels between 0.5 and 2 km, some differences higher than 5 ppm can also be seen. Fig. 6.7 shows the root mean square (RMS) values between REMO and fitted profiles which is calculated as:

$$RMS = \sqrt{\frac{\sum (REMO\ profiles - fitted\ profiles)^2}{number\ of\ height\ levels}} \quad (6.5)$$

This plot shows that the RMS values for this months are lower than 4 ppm, while for many cases this value is even smaller. These RMS values are mainly due to the variations in REMO profiles which can not be captured by a smooth exponential function. According to the diurnal variations of the CO₂ concentration in the boundary layer (that is the focus of this study) which can be higher than 20 or 30 ppm, the RMS values lower than 4 ppm shows that the defined exponential function with an acceptable accuracy is appropriate to parametrize the CO₂ profile.

The retrieved values for all three parameters in November are shown in Fig. 6.8. The upper plot shows the values of A_2 changing roughly between 0 and 50. This parameter has the highest variations compared to the two other parameters. The middle plot indicates variations of A_1 , that is limited between -0.5 and -7. The lower plot shows retrieved values of A_0 which is expected to have smallest variations compared to two other parameters. As explained, A_0 defines the background CO₂, and thus has only a slight variation during one month. However, this plot shows a smooth and steady increase in the retrieved A_0 . The main reason of this increase is due to the increase in the background CO₂ in 2003 compared to 2002.

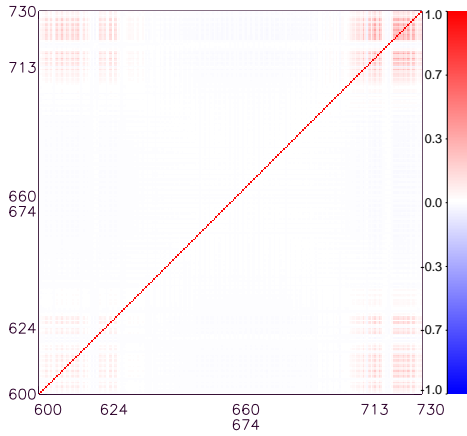


Figure 6.9: The correlation matrix derived from the measurement error covariance matrix. The measurement error covariance matrix is composed of error due to the random AERI noise and forward model error.

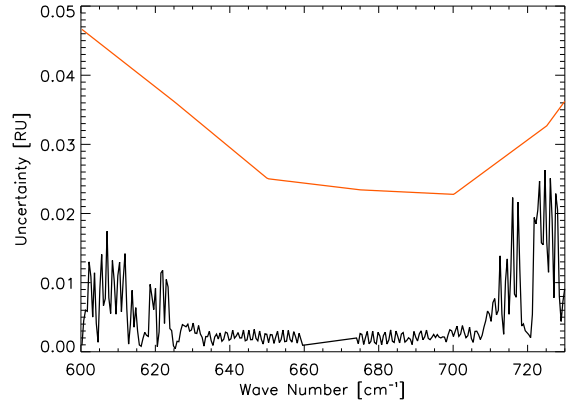


Figure 6.10: The square root of diagonal elements of the forward model error covariance matrix (in black) and the reduced random noise of the AERI (in red). The random noise of the AERI is divided by 5.

For this month, the mean retrieved values are 14.8, -3.6 and 374.6 for A_2 , A_1 and A_0 respectively. The computed $1\text{-}\sigma$ uncertainties are around 8 for A_1 , 2 for A_2 and 1 for A_0 . A negative correlation of about 0.4 is derived between A_1 and A_2 . These values are used as prior values and prior covariance matrix in the AERIOe to run the algorithm. In the next subsection, the result of running the AERIOe for some cases in November of 2002 is presented. This month is chosen rather randomly for running the AERIOe. However, it includes different CO₂ profile shapes which make it useful to evaluate the potential of the AERIOe to retrieve different CO₂ profile shapes.

6.1.4 Case studies

In order to test the strength of the AERIOe to retrieve the defined CO₂ parameters, a new simulation of the AERI radiances is provided. In this simulation, the LBLRTM is used to simulate the AERI radiances with input profiles of temperature, humidity and CO₂ from REMO. As in the previous step, the random noise of the AERI is added to the simulated LBLRTM radiances. In this simulation, a reduced noise by a factor of 5 is used. In the application of real measurements, this noise can be achieved by using averaged radiances over 10 min for AERI measurements with 20 s temporal resolution.

The measurement error covariance matrix is defined using the reduced noise. In addition, in the present run, the error in the forward model is also added to the measurement covariance matrix. The forward model error is caused due to using the smoothed CO₂ profiles computed by the exponential function, rather than true REMO profiles. For estimating this error, the LBLRTM is used to calculate the radiance differences between radiances simulated with true input CO₂ profiles of REMO and radiances simulated with smooth input profiles created from the exponential function. After calculating these radiance differences for all profiles in one month, the corresponding covariance matrix is added to the measurement error covariance matrix created from the random noise of the AERI. The correlation matrix derived from the

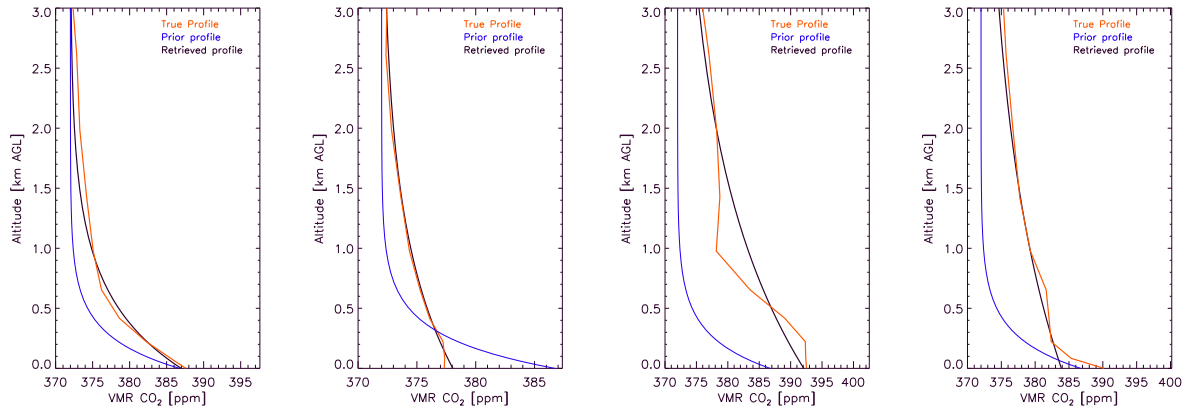


Figure 6.11: The retrieved CO₂ profiles (in black) based on the three retrieved parameters, A_0 , A_1 and A_2 . The prior profiles (in blue) are calculated using three prior values and the true profiles (in red) are provided by REMO model.

covariance matrix of combining these two errors is shown in Fig. 6.9. The forward model error in this plot is calculated using REMO profiles in November 2002 and 2003. As it can be seen, the forward model error adds non-diagonal elements to the measurement error covariance matrix, however, based on Fig. 6.10, which compares the square root of diagonal elements of the forward model covariance matrix and the reduced AERI random noise, the forward model error is about 5 times lower than the AERI noise, and thus this error has a minor effect on the retrieved result.

The X or the unknown parameters in this step includes three CO₂ parameters where the prior data corresponding to these three parameters is provided by the method explained in the previous section.

Fig. 6.11 shows the retrieved results of four different cases which are selected to show the abilities and the deficiencies of the AERIOe to estimate the retrieved CO₂ profile. The retrieved CO₂ profiles (black lines) means the calculated profiles using the retrieved values of three parameters and the exponential function. From the left side, the first and the second plot show a nighttime and a daytime profile respectively. The true profiles are captured rather

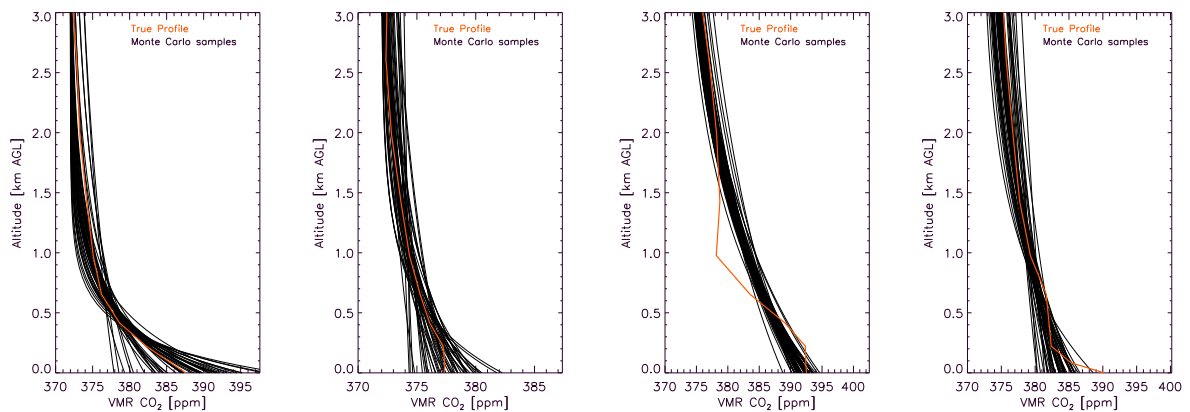


Figure 6.12: The calculated Monte Carlo samples using the uncertainties in the retrieval parameters. The red line shows the true profile.

accurately with the retrieved CO₂ profiles for these two cases. These two profiles show the strength of the AERIOe in retrieving the CO₂ profile when the true profile is rather smooth. On the other hand, when the CO₂ profile is less smooth with altitude, the AERIOe can give only an appropriate estimate of the true profile. The third plot in this panel is one of these examples. Although in this plot, the retrieved CO₂ profile does not fit to all variations of the true profile, the estimated CO₂ profile can give valuable information related to the CO₂ surface value and the rough shape of the true profile. The fourth plot in this panel shows a true CO₂ profile which has deviation around 5 ppm close to the surface. This deviation can not be captured by the retrieved CO₂ profile. The problem can be related to the low sensitivity of the AERI radiances to such a deviation which happens close to the surface or in a low vertical height above the ground.

The posterior uncertainty or the posterior covariance matrix can be calculated for each retrieved vector of the AERIOe. This matrix helps to find the distribution of other CO₂ profiles within the uncertainty of retrieved results. In order to find these CO₂ profiles, Monte Carlo samples, \hat{X} , using the posterior covariance matrix are computed as:

$$\hat{X} = S_{pos}^{1/2}R + X, \quad (6.6)$$

where R is a three elements random vector with a normal distribution, X is the optimal solution of the three parameters and $S_{pos}^{1/2}$ is the square root of the posterior covariance matrix which is calculated using singular value decomposition:

$$S_{pos}^{1/2} = UW^{1/2}V^T, \quad (6.7)$$

where W is a diagonal matrix where its diagonal elements show eigenvalues or singular values of the S_{pos} ; U and V are two identical matrices since the covariance matrix is symmetric and real and their column shows the eigenvectors of S_{pos} . The Monte Carlo samples corresponding to each retrieved profile in Fig. 6.11 are shown in Fig. 6.12.

Each plot shows 50 samples calculated using the method in Eq. 6.6. The calculated samples show about 5 ppm difference with the true profiles close to surface. This difference compared to large variation of the CO₂ concentration in the surface which can be larger than 20 ppm is an acceptable uncertainty. Moreover, the plots show that with increasing the height, the differences between true profiles and calculated samples decrease and reach to less than 3 ppm at 3 km meaning that the uncertainties are rather lower in upper levels compared to the levels close to the surface. This is an expected consequence since the CO₂ concentrations in upper levels are determined using the A_0 parameter which has small prior uncertainty in the AERIOe.

The total DFS of the retrieved parameters are slightly lower than 2 for the profiles shown in Fig. 6.11 which is rather consistent with the number of retrieved parameters in the AERIOe. Although, the AERIOe retrieved three parameters, due to the small prior uncertainty of A_0 , this parameter is relatively constant in the AERIOe meaning that the algorithm retrieves mainly two parameters.

The main purpose of this work is to capture the diurnal cycle of the CO₂ profile in the boundary layer. Consequently, it is important to see the ability of the AERIOe to retrieve the diurnal cycle. Fig. 6.13 shows the diurnal cycle of the CO₂ profile provided by REMO on 4 November 2002 and the retrieved diurnal cycle using the AERIOe for this day as well as the difference between these profiles. The difference plot shows that the differences between true and retrieved profiles are mainly in the order of 3 ppm. However, for some hours the

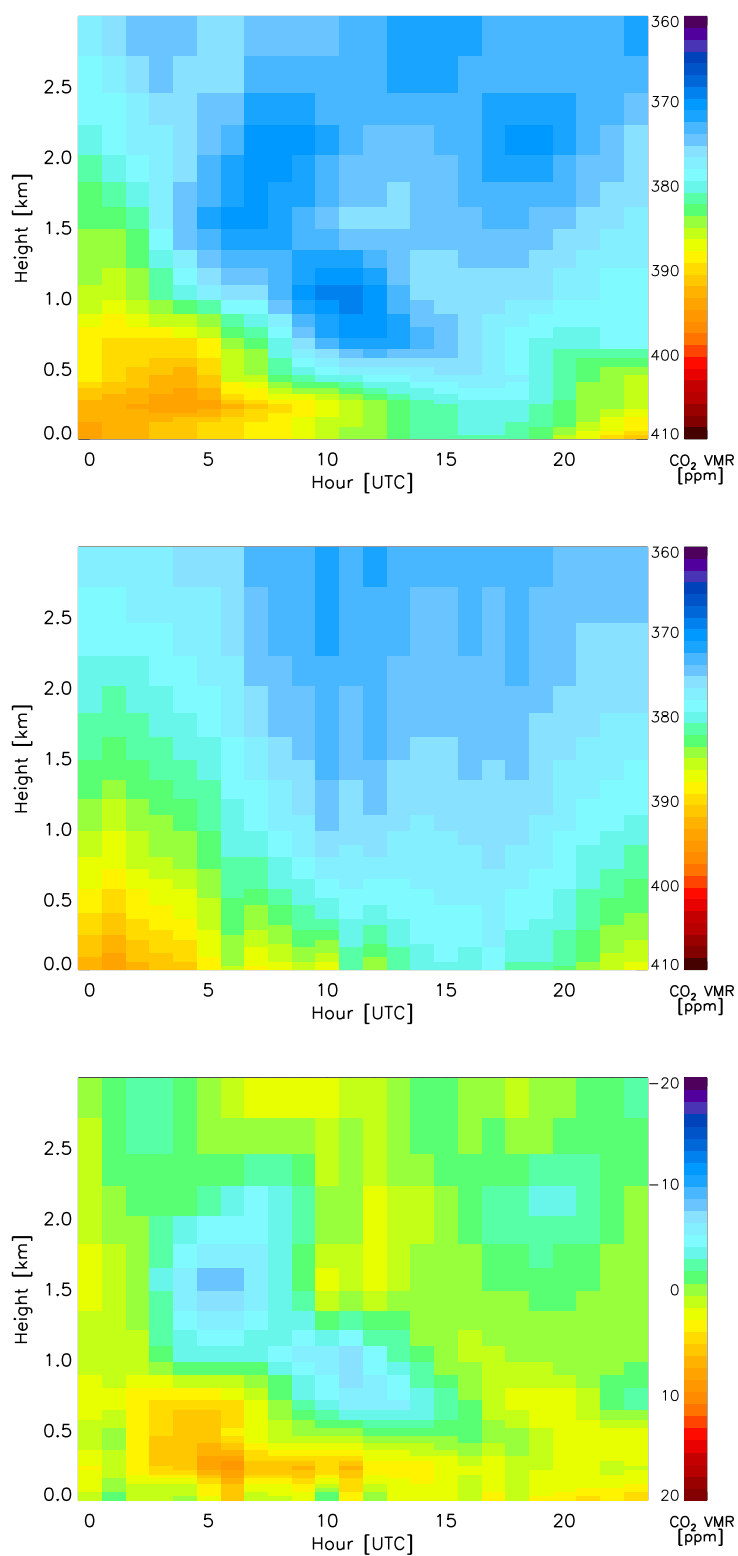


Figure 6.13: The true diurnal cycle of the CO₂ profile in the boundary layer provide by REMO (upper plot), the retrieved diurnal cycle using the AERIOe algorithm (middle plot) and the true minus retrieved profile (lower plot) on 4 of November 2002.

difference around 5 ppm can also be seen between true and retrieved profiles. In addition, the increase of the CO₂ at the midnight and in the early morning, as well as a second increase in the afternoon and after sunset, are retrieved rather accurately by the AERIOe. The retrieved results also capture very accurately the decrease in the CO₂ amount near the surface during the daytime.

These examples show the strength of the AERIOe in estimating the CO₂ profile in the boundary layer, however, in order to have a better assessment, a longer dataset is needed. For this reason, the AERI radiances are simulated with the hourly resolution for November of 2002 using REMO profiles and the AERIOe is run for one month. The statistical analysis of this result is shown in the next subsection.

6.1.5 Statistical assessment

In order to assess the AERIOe ability to retrieve the CO₂ parameters in different cases, the AERIOe is run for one month. The AERI radiances are simulated with the LBLRTM using hourly REMO profiles of temperature, humidity and CO₂ in November 2002. The reduced noise by a factor 5 is added to LBLRTM simulated radiances. The spectral bands which are used in this run are 612-618, 624-660, 674-713 and 713-723 cm⁻¹. The measurement error covariance matrix is calculated by adding the diagonal matrix composed of reduced random noise of the AERI and the forward model error covariance matrix. In this step the temperature and humidity profiles are considered as known profiles in the AERIOe, and thus the unknown vector includes only three CO₂ parameters. The prior values of these three parameters are defined as 14.8, -3.6 for A₁ and A₂. The prior value of A₀, depending on the background CO₂ in each case, is set to 372.0 or 373.0 ppm. A very small value is defined for the uncertainty of the A₀ to make it as a rather fixed parameter in the AERIOe. The 1- σ uncertainty of the A₁ and the A₂ is defined around 8 and 2 ppm respectively, while a negative correlation about 0.4 is considered between these two parameters. In the rest of this subsection, the results of running the AERIOe for November of 2002 is shown and discussed.

The AERIOe run for more than 700 cases where about 98% of these cases converged and fulfilled the convergence criteria. Fig. 6.14 shows the retrieved CO₂ concentration and the true CO₂ concentration at the surface, 90 m, 200 m and 1 km as well as the RMS values between true and retrieved values at each of these levels. Note that, the CO₂ profile is calculated using three retrieved parameters in each case, then the CO₂ concentration at different levels is estimated using the calculated CO₂ profile. This analysis can show the accuracy of the calculated CO₂ profile using this new approach.

These plots show that the variation in the CO₂ concentration decreases with height; this is the expected behavior. While variations at the surface level can be more than 30 ppm, the variations are smaller than 10 ppm at 1 km. Fig. 6.14a shows that the directions of the variations at the surface are captured properly in most of the cases by the AERIOe, however, for some cases, the retrieved values show underestimation compared to the true values. The RMS values between true and retrieved values at the surface level as it is indicated in Fig. 6.14b, is 6.83 ppm which shows a significant reduction compared to the RMS values between true and prior values. The main reason for the difference between true and retrieved values (mainly for the levels in the boundary layer) is due to the limitation of this approach for retrieving the CO₂ profile which gives always a smooth CO₂ profile. Furthermore, the RMS values reduce with increasing the height and reaches to 1.94 at 1 km. This reduction is

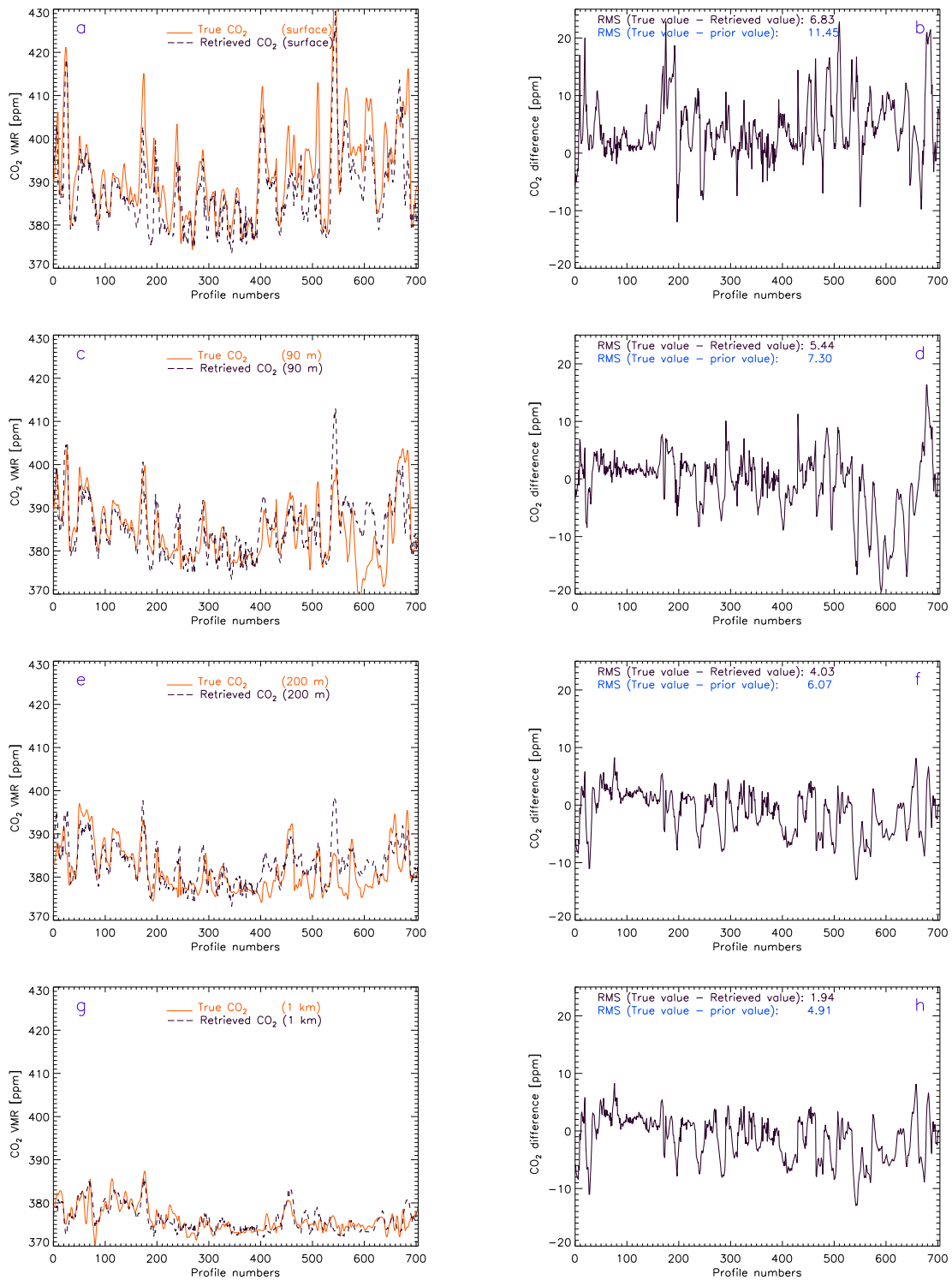


Figure 6.14: The true (in red) and the retrieved (in black) CO₂ concentrations at surface (plot a), 90 m (plot c), 200 m (plot e) and 1 km (plot g) for the AERIOe run in November 2002 using simulated radiances. The right plots show the corresponding RMS values at each level between true and retrieved values as well as the RMS values between true and prior values.

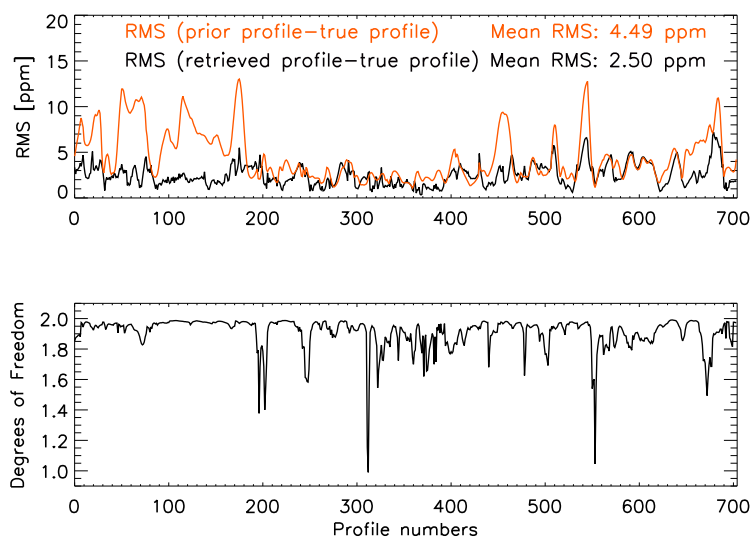


Figure 6.15: The upper plot shows the RMS values between true and retrieved CO₂ profiles (in black) as well as RMS values between prior and true profiles (in red) for the AERIOe run in November 2002 using simulated radiances. The lower plot shows the total DFS for retrieving the CO₂ parameters for the same AERIOe run.

due to the decrease in the variations of the CO₂ VMR in higher altitude which lead to lower underestimation or overestimations in the retrieved CO₂ VMR at these levels. As it is shown in Fig. 6.14h, the AERIOe in this level also shows a significant improvement in the RMS value between true and retrieved values compared to RMS values between true and prior values which is 4.91 ppm.

The RMS values between true CO₂ profiles and retrieved CO₂ profiles (the difference between whole profile) are computed for each case and compared to the RMS values between prior CO₂ profile and true CO₂ profiles. This comparison is shown in the upper plot of Fig. 6.15. This plot shows that for many cases the RMS values between true and retrieved values are significantly reduced compared to the RMS values between true and prior profiles. This reduction occurs mainly for the cases where the prior profile was considerably different than the true profile, and thus the retrieved profile significantly improves the prior profile. On the other hand, for the cases where the prior profile is close to the true profile, the retrieved profile can improve the prior profile only slightly. For these cases, the two RMS values are close to each other. In brief, the mean RMS value between true and retrieved profiles are 2.50 ppm which is about 2 times smaller than the mean RMS values between true and prior profiles that is 4.49 ppm. This can confirm the ability of the AERIOe to improve the knowledge about the CO₂ profile compared to the prior profile.

Another important quantity in the retrieved algorithm is the calculated DFS which is shown in the lower plot of Fig. 6.15. The total DFS for retrieving these three parameters is relatively constant for all cases and is slightly less than 2. Since the A_0 is rather fixed in the algorithm due to its small uncertainty in the prior covariance matrix, the number of retrieved parameters (2) is consistent with the total DFS.

This analysis shows that the AERIOe can provide valuable information related to the CO₂ profile in the boundary layer, if temperature and humidity profiles are considered as known

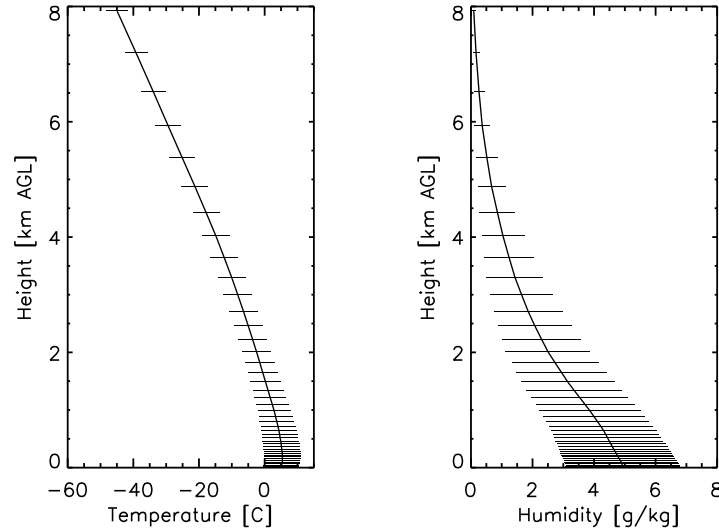


Figure 6.16: The mean temperature profile (left plot) and the mean humidity profile (right plot) as well as their $1\text{-}\sigma$ uncertainties for the prior dataset in November which are derived from REMO data in 2002 and 2003.

parameters. In the next step, it is assumed that the information about the temperature and humidity is limited to only climatological data (prior data) and the AERIOe is run to retrieve the temperature, humidity and CO₂ profile simultaneously to evaluate its potential to retrieve three profiles simultaneously.

6.2 Simultaneous retrieval of CO₂, temperature and humidity profiles

Although the retrieved result in the previous section shows high accuracy to retrieve the CO₂ profile in the boundary layer, it is not totally applicable to the real measurements. The main limitation in the real application is to provide accurate profiles of temperature and humidity. Consequently, these profiles also need to be considered as unknown parameters in the AERIOe. In the present section, the ability of the AERIOe to simultaneously retrieve temperature, humidity and CO₂ profile is tested. In order to run the AERIOe to retrieve the temperature and humidity profiles, first, the prior data of these two profiles need to be determined which is explained in the next subsection.

6.2.1 The prior data of temperature and humidity profile

The prior profiles of temperature and humidity are computed using REMO profiles. For each month, REMO temperature and humidity profiles for the current month as well as immediately preceding and immediately following month from hourly profiles of 2002 and 2003 are used to compute the mean temperature and humidity profiles as well as the covariance matrix. This leads to more than 4000 profiles to compute the prior data for each month.

Fig. 6.16 shows the mean temperature and humidity profile derived for November. The plot also shows the $1\text{-}\sigma$ uncertainty of temperature and humidity at each level. The correlation

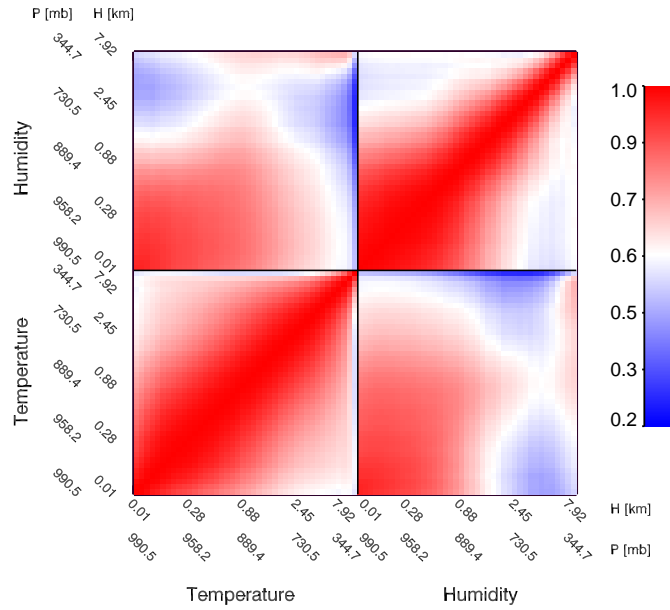


Figure 6.17: The correlation matrix for November derived from REMO data in 2002 and 2003. The plot shows the correlation between T and T (lower left submatrix); T and H (lower right submatrix); H and T (upper left submatrix); and H and H (upper right submatrix).

matrix derived from the calculated covariance matrix for November is shown in Fig. 6.17. The correlation matrix shows the correlation of temperature (T) and humidity (H) in terms of altitude which is considered from the surface up to 17 km. The corresponding pressure levels are also shown in the plot. The correlation matrix is composed of four submatrices to present the correlation of T and T; T and H; H and T; and H and H.

The highest correlation can be seen in the main diagonal elements as it is expected, while it decreases for off-diagonal elements. However, in TT submatrix, the correlation of off-diagonal elements in the boundary layer (lower than 1.5 km) due to the well-mixed condition in the boundary layer are still close to 1. In the tropospheric levels (between 1.5 and 8 km), the correlation of T and T decreases slightly. The behavior of HH submatrices is close to the TT submatrices with slightly lower correlation in the tropospheric levels. The HT and TH submatrices are identical. They show higher correlation in the boundary layer and slightly lower correlation in the upper tropospheric levels.

6.2.2 Case studies

The main settings in the AERIOe run to retrieve temperature, humidity and CO₂ profiles simultaneously are similar to the previous run. The input measurement vector is the LBLRTM simulated radiances where the reduced AERI random noise is added to it. The measurement error covariance matrix is the AERI random uncorrelated noise plus the forward model error. In addition to the spectral bands belonging to the 15 μm CO₂ line which are used in the previous runs, in order to retrieve the humidity profile, the water vapor spectral band between 568 to 588 cm^{-1} is also used in this run. The prior data of the CO₂ parameters are the same as the previous run.

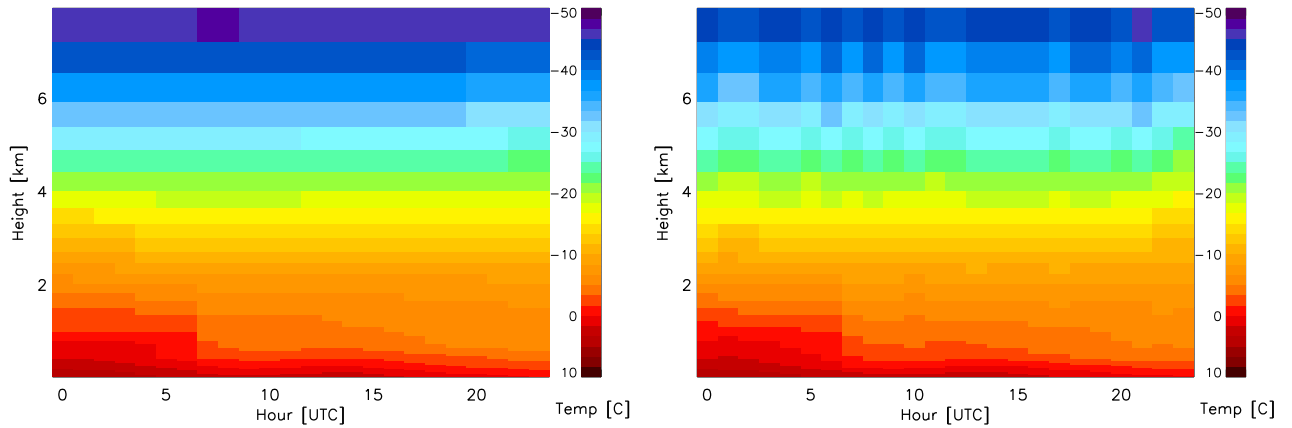


Figure 6.18: The true diurnal cycle of temperature profiles (left plot) provided by REMO and the retrieved diurnal cycle of temperature profiles (right plot) by the AERIOe using the simulated radiances on 5 of November 2002.

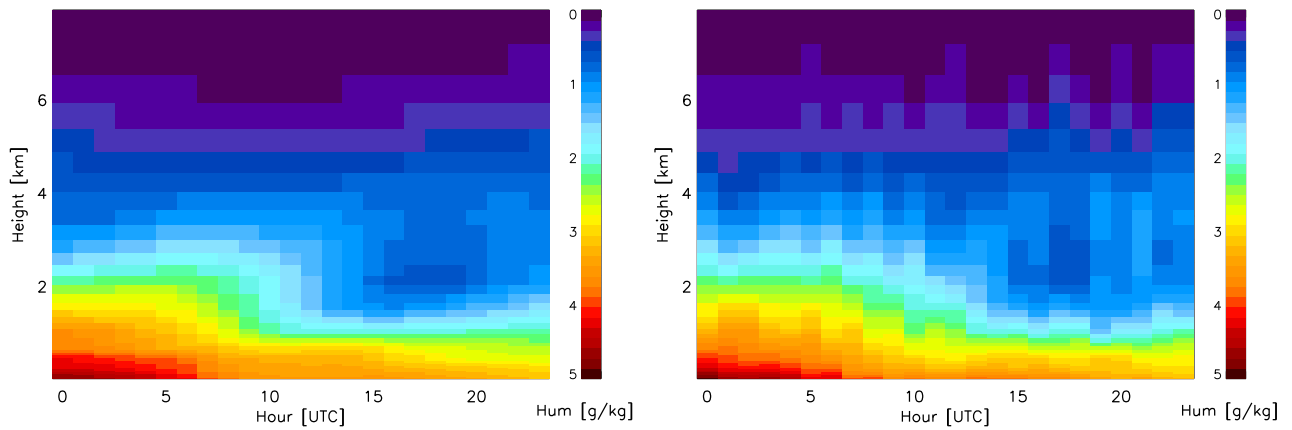


Figure 6.19: The true diurnal cycle of humidity profiles (left plot) provided by REMO and the retrieved diurnal cycle of humidity profiles (right plot) by the AERIOe using the simulated radiances on 5 of November 2002.

Figs. 6.18 and 6.19 show the diurnal cycle of retrieved temperature and humidity profiles (left plots) as well as true profiles (right plots) on 5 of November 2002. The retrieved temperature profiles shows the difference less than 2 °C with the true profiles for the levels below 4 km which increases slightly with height and reaches to around 4 °C for the levels above 6 km. The retrieved humidity profiles shows difference around 1 g/kg with the true humidity profiles for the levels below 4 km which decreases with height and reaches to the values close to zero for the levels above 4 km. This comparison indicates that both temperature and humidity profiles are retrieved rather accurately by the AERIOe. The deficiency in retrieving the temperature profiles is mainly in the upper levels (above 4 km) where the AERIOe retrieved profiles show an overestimation compared to the true profiles.

In contrast to the retrieved temperature and humidity profiles, the AERIOe shows rather poor ability to retrieve the CO₂ profiles shown in Figs. 6.20 and 6.21. In order to analyze the ability of the AERIOe to retrieve the CO₂ profiles in this step, a rather acceptable retrieval case and a poor retrieval case are shown in Figs. 6.20 and 6.21 respectively.

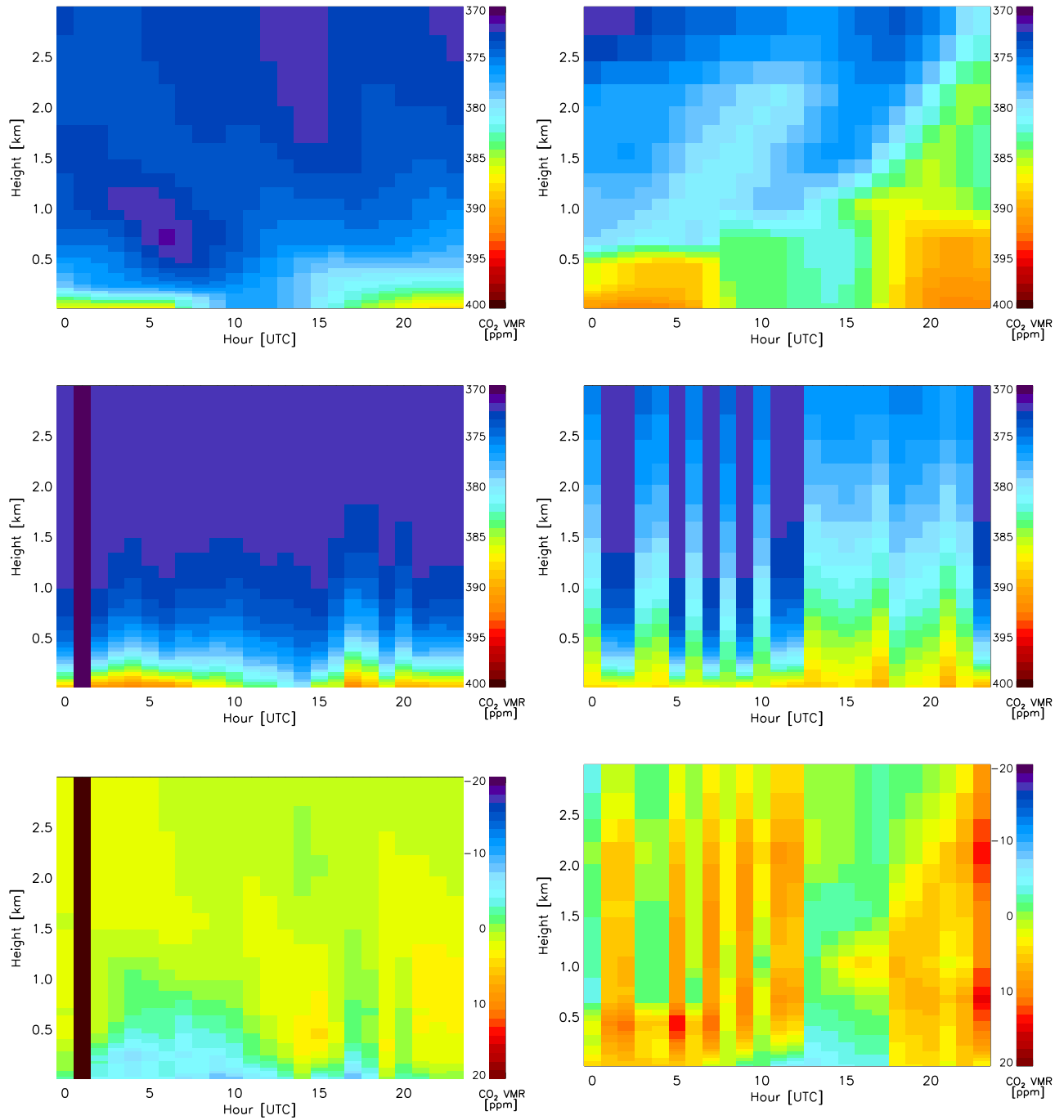


Figure 6.20: The true diurnal cycle of CO₂ profiles (upper plot) provided by REMO and the CO₂ profiles by the AERIOe using the simulated radiances (middle plot) as well as the difference plot (REMO-AERIOe) between these profiles on 14 of November 2002. The retrieved CO₂ profiles belong to the simultaneous retrieval of the temperature, humidity and CO₂ profiles. The black column shows the profile which did not converged.

Figure 6.21: The true diurnal cycle of CO₂ profiles (upper plot) provided by REMO and the CO₂ profiles by the AERIOe using the simulated radiances (middle plot) as well as the difference plot (REMO-AERIOe) between these profiles on 5 of November 2002. The retrieved CO₂ profiles belong to the simultaneous retrieval of the temperature, humidity and CO₂ profiles.

Figs. 6.20 and Fig. 6.21 show the diurnal cycle of the retrieved CO₂ profiles for two sample days on 14 and 5 of November 2002 respectively. In the first case, the retrieved profiles are in an acceptable agreement with the true profiles. The rising of the CO₂ concentrations near the surface in the early morning and during the nighttime as well as the reduction of its concentration during the daytime in lower levels are appropriately captured by the algorithm. The difference plot in this day shows less than 2 ppm difference for the levels above 1 km, however in the lower levels, particularly before the noon time, differences between 5 to 7 ppm can be seen. In contrast, for the second case which is shown in Fig. 6.21, the true CO₂ profiles are poorly captured by the algorithm. Particularly, the increase and the decrease of the CO₂ concentration in lower levels can not be seen in the retrieved result. For more than 50% of the retrieved profiles, differences higher than 10 ppm, approximately in all levels can be seen between true and retrieved profiles. Note that in these two runs, the total DFS of the CO₂ parameters drops compare to the previous run and reaches to around 1.

Further analysis of the CO₂ profiles in these two cases shows that in the first case, the true profiles are rather close to the prior profile, and thus even with a small DFS, the algorithm can provide a rather acceptable result. On the other hand, in the second case, the true profiles have a considerable difference with the prior profile which leads to a poorly retrieved result.

The above analysis shows that the AERIOe with the current settings and with these simulated radiances performs rather poor in retrieving the CO₂ profile when the temperature and humidity profiles are also considered as unknown profiles. In order to improve the AERIOe result in retrieving the CO₂ profiles, two different methods are used which are explained in the next two subsections.

6.2.3 Fixed surface CO₂ concentration

The simultaneous retrieval of temperature, humidity and CO₂ profiles produce a significant drop in the DFS of CO₂ in the AERIOe and the retrieved results show that the AERIOe is not successful in capturing the CO₂ profile. A proper solution for this problem is to provide additional observational information to the algorithm.

As it is explained in section. 3.4, the in-situ tower measurement of the atmospheric CO₂ can provide valuable information about the CO₂ concentration near the surface. This measurement is also available by the tower measurement in Jülich. The CO₂ measurement near the surface can be used as auxiliary data in the AERIOe algorithm to improve the retrieval result. Consequently, this possibility is tested using the simulated radiances to analyze the impact of using the CO₂ surface value as known parameter on the retrieval result of the AERIOe.

In order to give the CO₂ surface value as input data to the AERIOe, the same method which is used to give the true temperature and humidity profile to the AERIOe in section. 6.1 is applied. The prior surface value of the CO₂ is replaced by the true surface CO₂ provided by REMO. In addition, the prior uncertainty of this parameter in the prior covariance matrix is considered very low. The small uncertainty prevents the algorithm from changing this parameter, and thus the algorithm considers this parameter as known or fixed parameter in all iterations. By using this new setting, the AERIOe run is repeated for the previous case with poorly retrieved results shown in Fig. 6.21.

Fig. 6.22 shows the new retrieved CO₂ profiles using the new setting in the AERIOe. As it can be seen, the retrieved result shows significant improvement compared to the previous

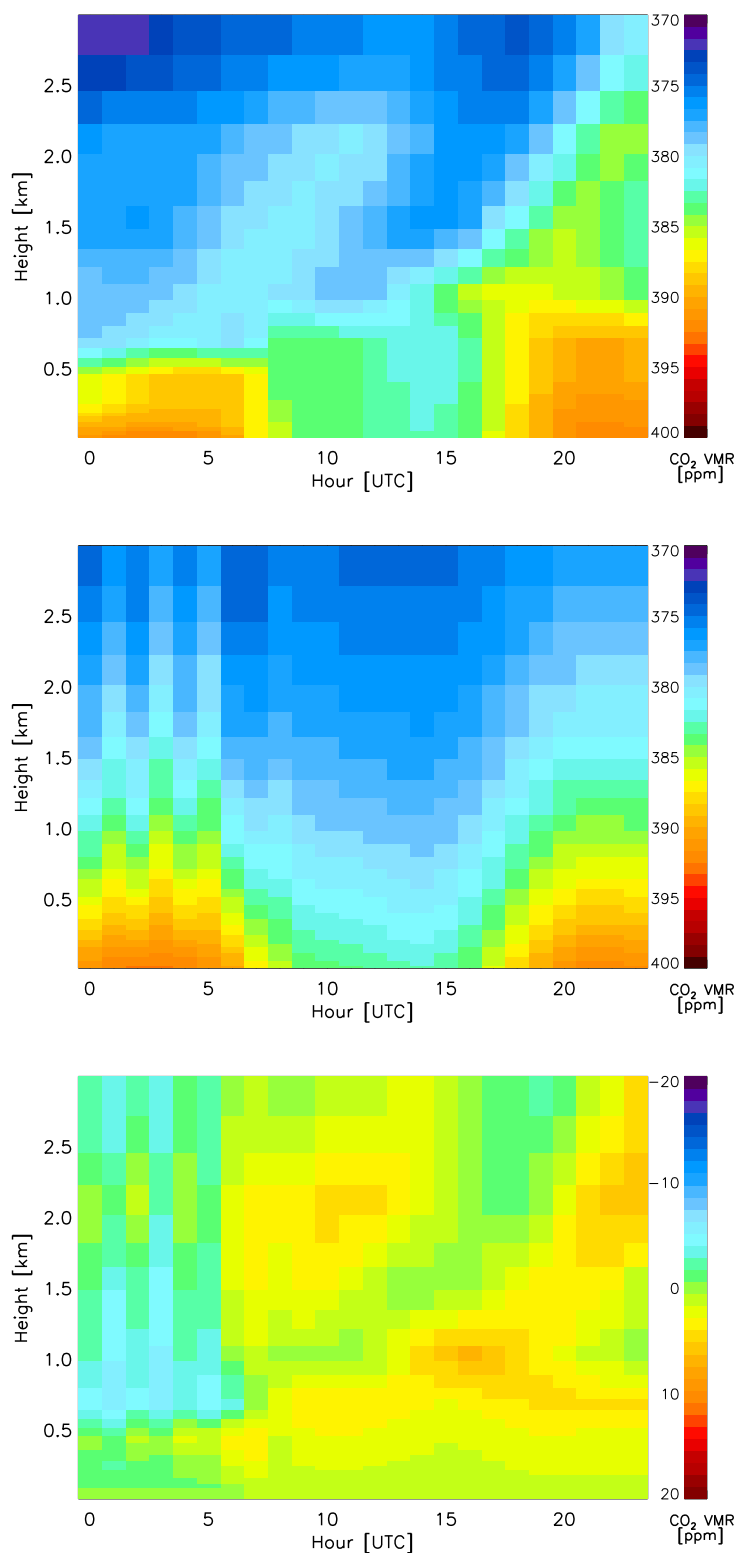


Figure 6.22: The true diurnal cycle of the CO₂ profile in the boundary layer provide by REMO (upper plot), the retrieved diurnal cycle using the AERIOe algorithm (middle plot) and the difference (REMO-AERIOe) between true and retrieved profile (lower plot) on 5 of November 2002. The retrieved CO₂ profiles belong to the simultaneous retrieval of the temperature, humidity and CO₂ profiles when additional information about the CO₂ surface value is also added to the algorithm.

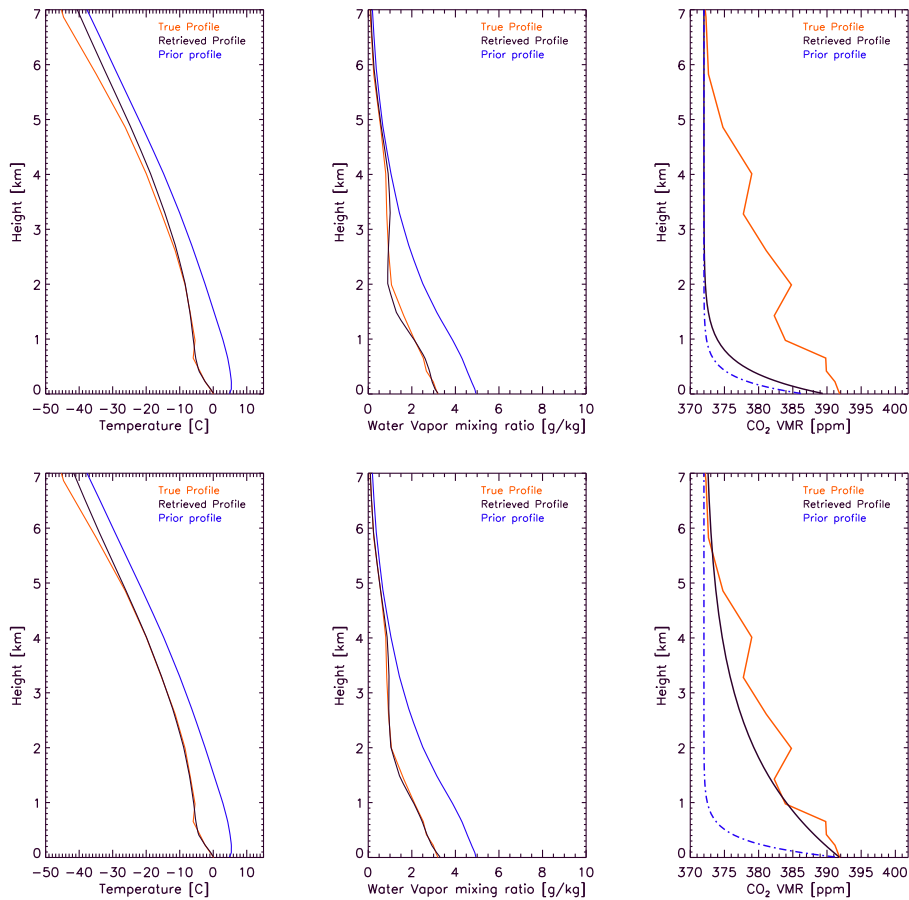


Figure 6.23: The retrieved results of temperature (left plots), humidity (middle plots) and CO₂ profile (right plots) of running the AERIOe with (lower plots) and without (upper plots) CO₂ surface concentration as auxiliary data. Each plot shows retrieved profile (in black), true profile (in red) and prior profile (in blue).

result (shown in Fig. 6.21). The increase in the CO₂ concentration in lower levels in the early morning and after the sunset as well as the decrease in the CO₂ concentration in these levels during the daytime is captured much better by the algorithm. The difference plot shows that the difference between true and retrieved profiles are mainly lower than 3 ppm which slightly increases for the levels between 0.5 and 1 km at the early morning and in the afternoon. This result demonstrates that providing information of the CO₂ concentration at one level close to the surface can improve the retrieved CO₂ profile in the whole boundary layer.

Another valuable improvement that can be seen in the retrieved result after the improvement in the retrieved CO₂ profiles, is the improvement in the retrieved temperature and humidity profiles. In order to show this improvement for a specific hour from the AERIOe run on 5 of November 2002, the retrieved temperature and humidity profiles with and without giving the CO₂ surface concentration as auxiliary data to the AERIOe are shown in Fig. 6.23.

The upper panel in Fig. 6.23 shows the retrieved temperature and humidity profiles while the retrieved CO₂ profile which is shown in the right plot has differences between 5 to 15 ppm with the true profiles in the levels below 5 km. The lower panel shows the same result when the CO₂ surface concentration is given to the AERIOe, and thus the CO₂ profile is

retrieved with higher accuracy which shows less than 5 ppm difference in the same levels (below 5 km). The improvement in both retrieved temperature and humidity profiles in the lower plots compared to the upper plots can be clearly seen. This improvement particularly is considerable for the temperature profile in the upper levels (above 3 km). While in the upper plots, the retrieved temperature profile shows overestimation about 2 to 3 °C above 3 km, in the lower plot, the retrieved temperature profile shows a much improved fit in the levels below 5 km.

6.2.4 Noise filtering

The second approach which is used to improve the retrieved result of the AERIoe is the principal component analysis (PCA) (*Huang and Antonelli, 2001; Antonelli et al., 2004; Turner et al., 2006*). In the previous AERIoe runs, only the averaged radiances are used in order to decrease the noise, and thus increase the signal-to-noise ratio. However, the poor retrieved CO₂ profiles that is shown in section. 6.2.2, may still related to the high noise in the radiances which prevents the algorithm to get the CO₂ signal from the AERI radiances. Consequently, the principal component noise filtering is also used to further reduce the AERI noise. A simulation approach is performed to apply this method on the AERI radiances and to test its impact on retrieval results which is explained in the present subsection.

In the first step, the AERI radiances are simulated with high temporal resolution to provide simulated radiances with temporal resolution identical to the AERI measurements taken in rapid sample mode. The simulation is done using the LBLRTM for two days, 9 and 10 of June 2015. The input profiles of the LBLRTM are provided by model data with hourly temporal resolution. The model profiles are interpolated to compute temperature and humidity profiles with 30 s temporal resolution. The integrated water vapor (IWV) in the first day is rather constant around 20 kg/m^2 and in the second day the IWV gradually increases from 20 to 40 kg/m^2 . This approach allows testing the ability of the AERIoe in both dry and humid conditions. Besides, the CO₂ profiles are made artificially with a diurnal amplitude of about 25 ppm where the CO₂ VMR in the levels lower than 1 km is decreased during daytime and increased after sunset and during nighttime. The original AERI noise is then superimposed to these highly temporally simulated radiances.

The first step in the PCA noise filter algorithm (*Turner et al., 2006*) is to decompose the measurement of radiance to its eigenvectors (principal components) and to find the corresponding eigenvalues. Typically, the decomposition is applied to the covariance matrix C derived from the measurement matrix M composed of measurements samples in a certain time interval. It was shown that the eigenvectors of M are the same as the eigenvectors of C (*Malinowski, 1977*). In addition, the covariance matrix is a symmetric matrix, and thus its decomposition is easier. The PCA consists of different steps where the important ones are decomposition of the covariance matrix to compute eigenvectors and eigenvalues; find the number of eigenvectors which are related to the atmospheric signal, rather than uncorrelated random noise; and reconstruction of the radiances using the selected eigenvectors.

The main challenge in this method is to accurately determine the optimal number of the eigenvectors to reconstruct the radiances. The uncertainty in finding the optimal number of eigenvectors can cause to remove the valuable eigenvectors which carry the atmospheric information. *Turner et al. (2006)* used an objective model to find the optimal number of principal components (PC) for the AERI measurements. The objective method tries to find the eigenvectors that have signal above the noise floor, assuming all noise is uncorrelated.

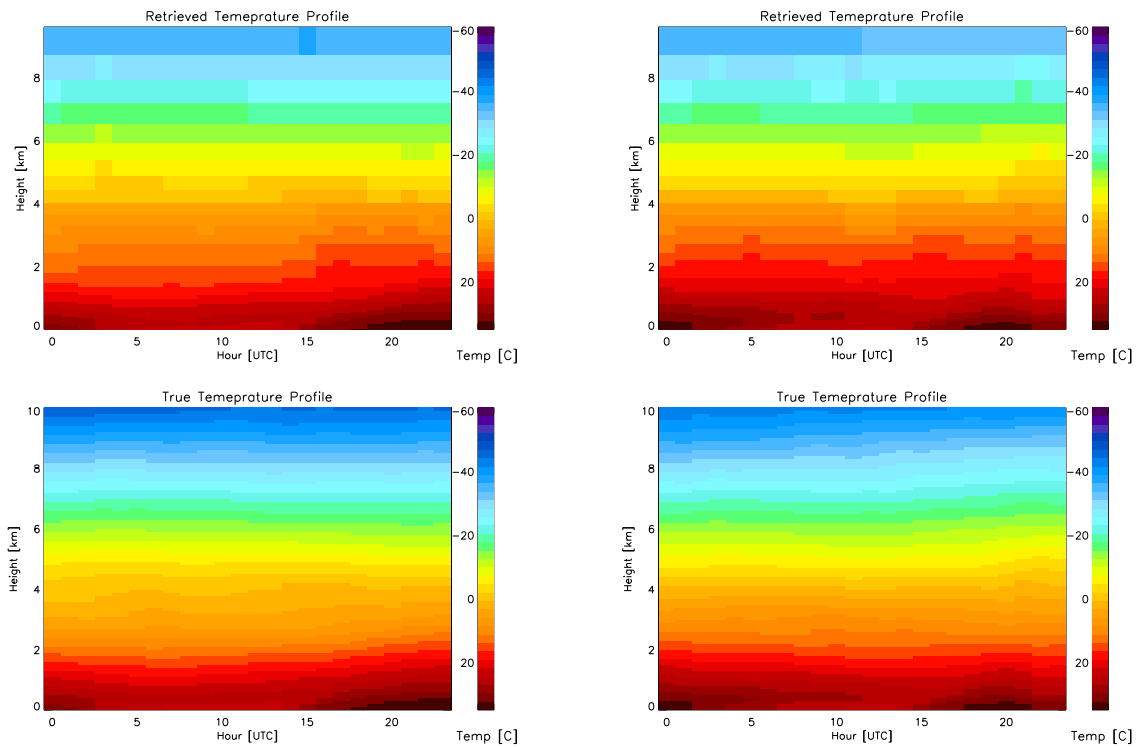


Figure 6.24: The retrieved (upper plots) temperature profiles using the AERIOe with the noise-filtered highly temporally simulated radiances on 9 (left plots) and 10 (right plots) of June 2015. The true profiles are shown in the lower plots.

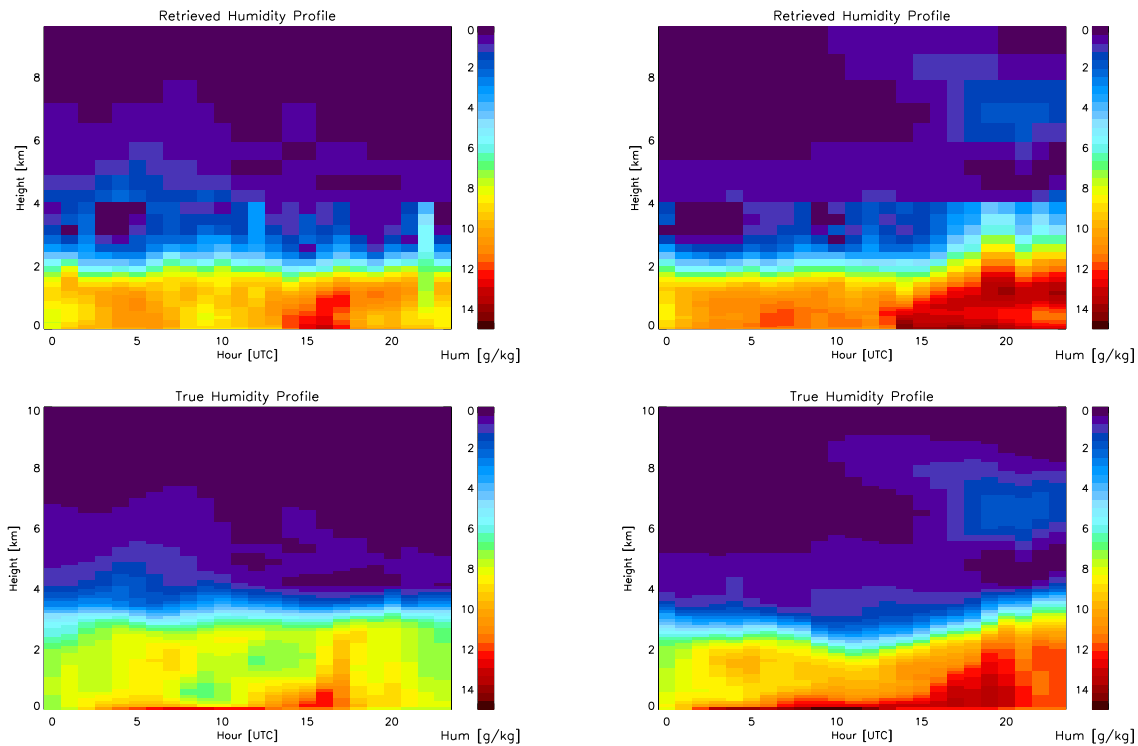


Figure 6.25: The retrieved (upper plots) humidity profiles using the AERIOe with the noise-filtered highly temporally simulated radiances on 9 (left plots) and 10 (right plots) of June 2015. The true profiles are shown in the lower plots.

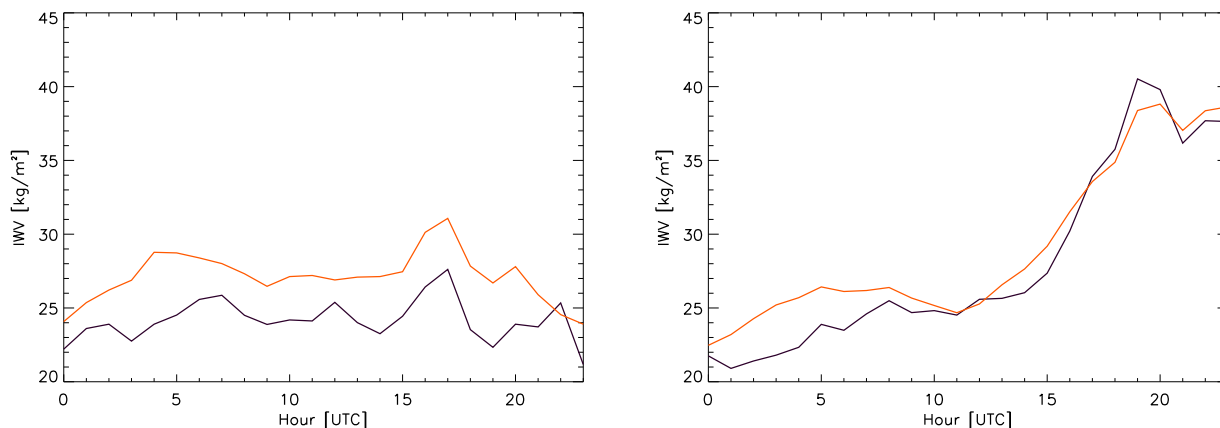


Figure 6.26: The retrieved (in black) IWV using the AERIoe with the noise-filtered highly temporally simulated radiances on 9 (left plots) and 10 (right plots) of June 2015. The true IWV is shown in red.

They showed that the optimal number of eigenvectors that should be used in reconstruction by the noise filter depends on the time of the year and the location of the observation. For example summertime observations require more eigenvectors to capture the atmospheric variability than winter time observations. This method is used in the present study.

In this example, real AERI observations from 8 days centered on the 9-10 June 2015 were used to compute the measurement covariance matrix used in the PCA noise filter. These real observations included a range of different weather conditions, and thus provides a true test of the simultaneous retrieval of temperature, humidity and CO₂ profiles using noise filtered radiance observations. The covariance matrix is then decomposed into its principal components. The optimal algorithm suggested that 284 is the correct number of PCs to use in the noise filter reconstruction of the radiance data. However, using this number to reconstruct the radiances and apply it in the AERIoe algorithm showed the poorly retrieved CO₂ profiles which leads to the fact that the important information related to the atmospheric CO₂ is probably lost with using only 284 principal components. It is found that some of the CO₂ signal is just below the noise level, and by adding the additional 200 eigenvectors to the reconstruction, this information is included in the reconstructed radiance data (*personal communication with D.D.Turner*). Consequently, the radiances are again reconstructed by 484 principal components. The results of using these noise-filtered simulated radiances with 484 principal components in the AERIoe is shown in Figs. 6.24 to 6.28.

Figs. 6.24 show the retrieved and the true temperature profiles. As it can be seen, the retrieved temperature profiles, particularly in the lower levels (below 2 km) shows differences less than 2 °C. In the middle levels (between 2 and 4 km), an overestimations in the order of 3 °C can be seen in retrieved profiles compared to the true profiles. Note that to stabilize the algorithm, both the temperature and humidity values above 4 km are fixed using the true model values.

The retrieved humidity profiles which is shown in Fig. 6.25, indicates an overestimation between 3 to 4 g/kg compared to the true humidity profiles, particularly for the levels below 2 km. Moreover, the retrieved IWV values which are shown in Fig. 6.26 show agreement in terms of variation with the true IWV values. The plot shows that the variations in the IWV values on the first day as well as its significant increase on the second day are captured

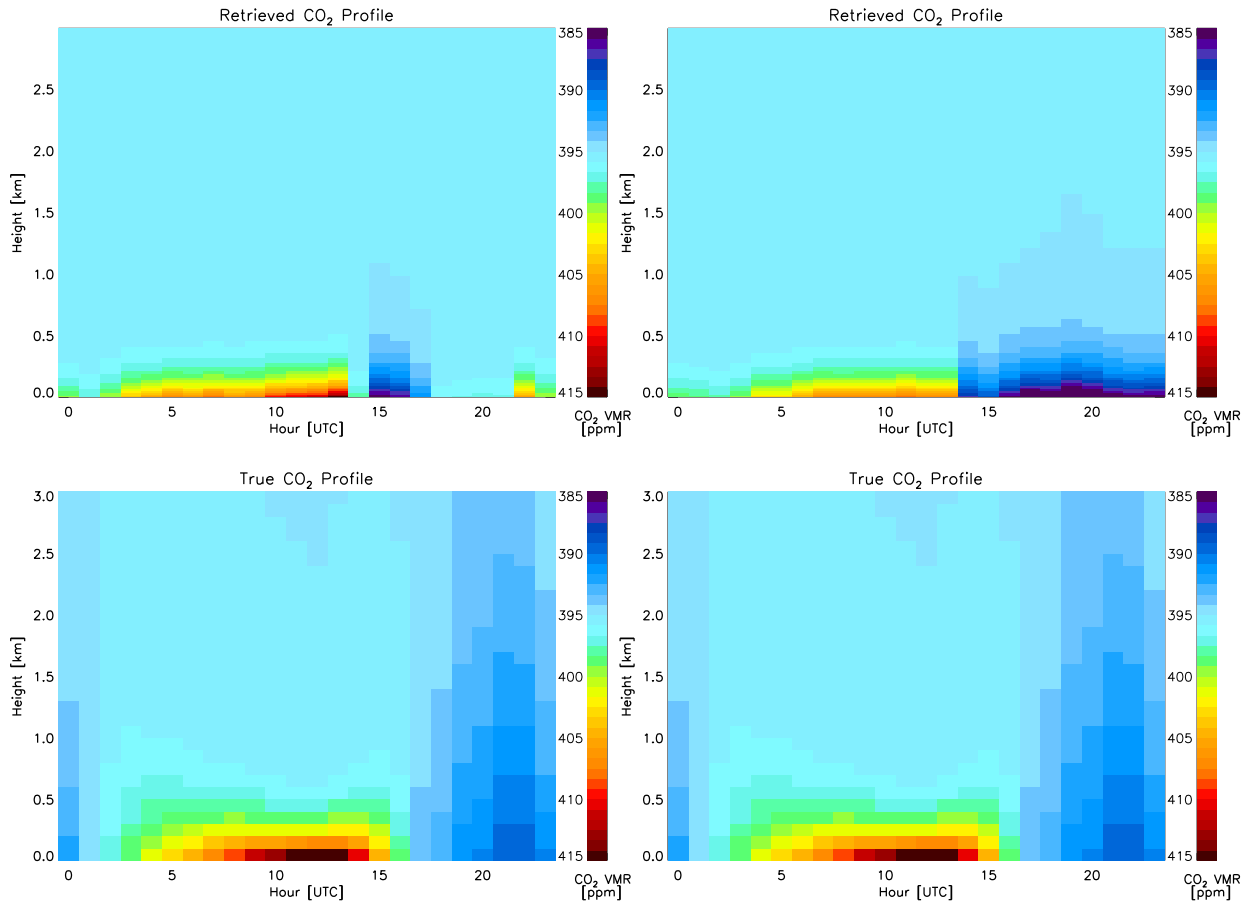


Figure 6.27: The retrieved (upper plots) CO₂ profiles using the AERIOe with the noise-filtered highly temporally simulated radiances on 9 (left plots) and 10 (right plots) of June 2015. The true profiles are shown in the lower plots.

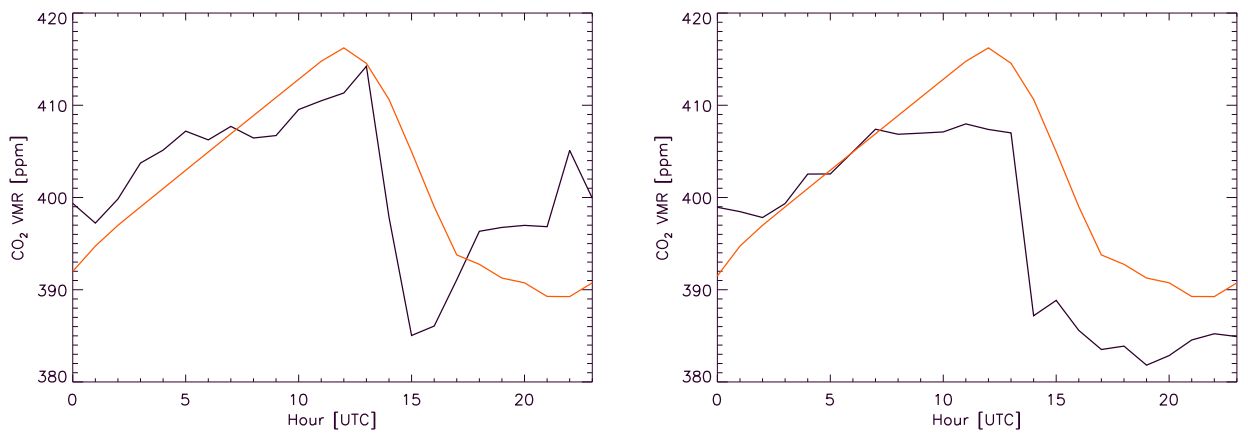


Figure 6.28: The retrieved (in black) CO₂ surface values using the AERIOe with the noise-filtered highly temporally simulated radiances on 9 (left plots) and 10 (right plots) of June 2015. The true CO₂ surface values are shown in red.

appropriately by the algorithm, however, an underestimation less than 4 kg/m^2 can be seen in the retrieved values compared to the true values.

The retrieved and the true CO₂ profiles are shown in Fig. 6.27. The retrieved profiles in both days show clearly the diurnal cycle of the true CO₂ profiles. The retrieved results for the hours before 13 UTC on both days show an overestimation between 5 to 10 ppm compared to the true profiles in the levels below 1 km. On the first days this overestimation can also be seen after 17 UTC, while on the second day, the overestimation turns to an underestimation in the same order after 14 UTC. Fig. 6.28 shows the retrieved CO₂ surface values as well as its true values. In both days, the estimated surface values captured the nighttime increase and the decrease during the daytime. The retrieved maximum value in the first day shows a difference less than 3 ppm with the true maximum value, while, on the second day the true and the retrieved maximum value shows difference around 10 ppm. This result can indicate the higher accuracy of the AERIOe in capturing the high CO₂ values in dry conditions compared to humid conditions.

The simulation study presented in this chapter showed that the AERI radiances can provide valuable information related to the atmospheric CO₂ concentration. However, exploiting this information from the AERI radiances could be rather challenging. This study revealed that for the AERI measurements in rapid sample mode, the noise-filtering using the PCA method is the key point in retrieving the CO₂ profile. This method can remove the main part of the uncorrelated random noise of the measurements and allow the algorithm to retrieve the valuable information. The noise-filtered radiances using the PCA method can capture the diurnal change of the CO₂ concentration near the surface including nighttime increase and daytime decrease while without using this method as it is shown in subsection 6.2.2, the retrieved CO₂ results can not give any appropriate information related to the diurnal change of CO₂ profile. In the next section, applying this method for the real AERI measurements as well as using the real measurements in the AERIOe is presented.

Chapter 7

CO₂ profile retrieval from real AERI measurements

As shown in chapter 6, the simulated AERI radiances show good potential to retrieve the CO₂ profile approximated as an exponential function when the temperature and the humidity profiles are known. However, in case of simultaneous retrieval of temperature, humidity and CO₂ profiles, the accuracy of the retrieved CO₂ profiles are reduced. In order to improve the results, the random AERI noise (which is added to the simulated radiances) needs to be reduced. The main approach that is to use a PCA noise filter. The noise-filtered simulated radiances using the PCA method show a significant improvement in the accuracy of the retrieved CO₂ profiles.

In this section, the PCA method is used to reduce the noise in the real AERI measurements. The noise-filtered radiances are then utilized in the AERIOe algorithm to retrieve the CO₂ profile. The real AERI measurements are selected from two clear sky days in 2012. The tower measurements in Jülich that provide the CO₂ measurements at 100 m are utilized to compare with the CO₂ retrieved results at the surface.

In the first section of this chapter, the prior data of temperature and humidity are introduced. In section 7.2, first an issue in the AERI radiance observations which cause problem in the convergence of the algorithm is presented. The noise-filtered AERI radiances are then utilized to retrieve the temperature, humidity and CO₂ profiles simultaneously. The poor results in the first run are then improved with two approaches which are also explained in this section. In subsection 7.2.1, it is shown that the CO₂ boundary layer can be retrieved when the CO₂ surface measurements used as auxiliary data in the algorithm.

7.1 Prior data of temperature and humidity profiles

The temperature and humidity profiles of radiosondes which are launched at the Essen station in Germany are used to compute the prior data. At this station, the radiosondes are launched at nominally 1045 and 2245 UTC. The prior data are computed using a record of about 8 years of data between 2001 and 2008, meaning that over 3000 profiles are used to make the prior data. The radiosondes that reached at least 15 km above ground and passed the quality control tests are utilized to compute the mean state vector X_a and the covariance matrix S_a . The prior data of a specific month are computed using the radiosondes launched in the

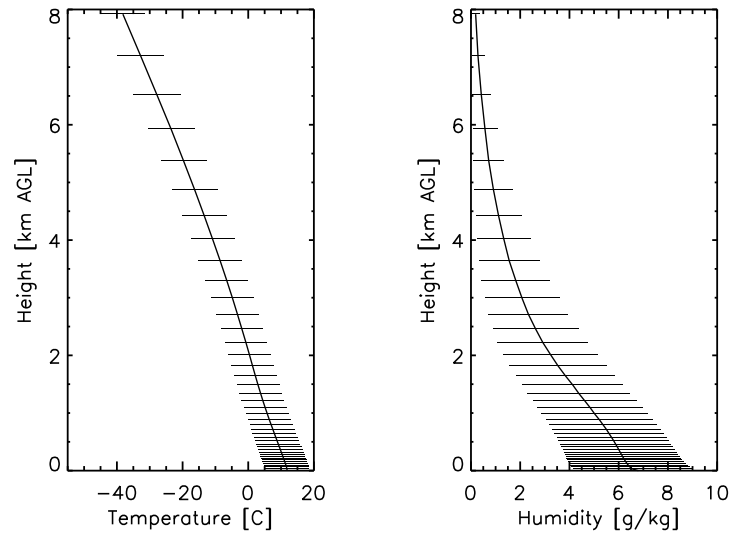


Figure 7.1: The mean temperature profile (left plot) and the mean humidity profile (right plot) as well as their 1- σ uncertainties for the prior dataset in May which are derived from radiosonde data in Essen, Germany.

current month as well as the immediately preceding and the immediately following month. Fig. 7.1 shows the mean prior profile of temperature and humidity.

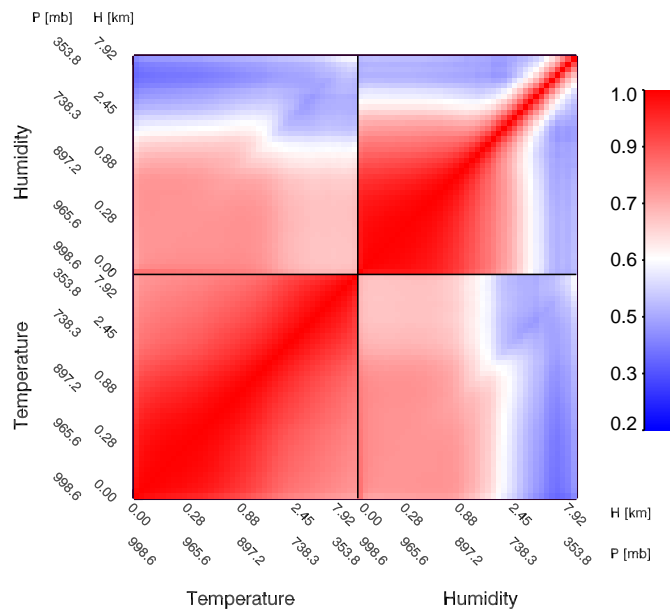


Figure 7.2: The correlation matrix for May derived from radiosonde data in Essen, Germany. The plot shows the correlation between T and T (TT, lower left submatrix); T and H (TH, lower right submatrix); H and T (HT, upper left submatrix); and H and H (HH, upper right submatrix).

The correlation matrix derived from the calculated covariance matrix of the prior data in May is shown in Fig. 7.2. The correlation matrix shows the correlation of temperature (T) and humidity (H) in terms of altitude which is considered from the surface up to 8 km. The corresponding pressure levels are also shown in the plot. The correlation matrix is composed of four submatrices to present the correlation of T and T (TT); T and H (TH); H and T (HT); and H and H (HH).

In both TT and HH submatrices, the correlations in the boundary layer (below 1.5 km) are still close to 1. The correlations in the middle and upper troposphere (between 1.5 and 8 km) in both TT and HH submatrices are lower compared to the correlation in the boundary layer. In addition, the HH submatrix shows lower correlations in the middle and upper troposphere compared to the TT. The HT and TH submatrices are the same, just the HT is the transposed matrix of the TH. In general, the correlations in these two submatrices are lower compared to the TT and HH submatrices.

7.2 Simultaneous retrieval of temperature, humidity and CO₂ profile

Two clear sky days, 25 and 26 of May 2012 are selected in order to apply the AERIoe to the real measurements. These two days are the only clear sky days in 2012 where tower measurements of the atmospheric CO₂ at Jülich are available. In the previous chapter, it was shown that both noise-filtering with the PCA and using the average radiances are needed to increase the signal-to-noise ratio in order to get the CO₂ information from the AERI radiances. Therefore, both of these methods are also used for the real AERI measurements to decrease its noise.

The noise-filtered radiances are computed using 10 days of the AERI measurements which include 25 and 26 of May, i.e. from 21 to 30 of May 2012. These measurements are utilized to calculate the covariance matrix C . The objective algorithm used in the Turner et al. (2006) study is then utilized to estimate the optimal number of PCs to reconstruct the radiance spectra with no uncorrelated noise which is found 321 PCs. As explained in section 6.2.4, since some of the CO₂ signal is below the noise level, 200 additional eigenvectors are added to the reconstruction to include this information (*personal communication with D.D.Turner*). Consequently, the AERI radiances are reconstructed using 521 PCs.

In section 4.5, two different approaches to adjust the radiometric calibration of the AERI radiances have been considered. It was shown that the aft optic correction factor shows a higher impact to correct the 15 μm CO₂ line compared to the obstruction correction factor. However, the results show that using the HATPRO retrieved surface temperature in the LBLRTM run gives an overestimation in calculating this factor. The impact of using the derived f_a factor in section 4.5 on the AERI radiances for these two clear sky days are shown in Fig. 7.3.

Fig. 7.3 shows the mean residual of hourly simulated radiances using the LBLRTM minus the AERI radiances on 25 and 26 of May 2012. The LBLRTM is run using the COSMO_DE profiles of temperature and humidity while the humidity profiles are scaled with the retrieved HATPRO IWV values and the input surface temperatures are replaced by the retrieved surface temperatures of the HATPRO. A constant mixing ratio equal 393.0 ppm is considered as input CO₂ profile in the LBLRTM run. This value is close to the background CO₂ concentration in 2012 (<https://www.esrl.noaa.gov/>). Fig. 7.3 shows the mean residual on

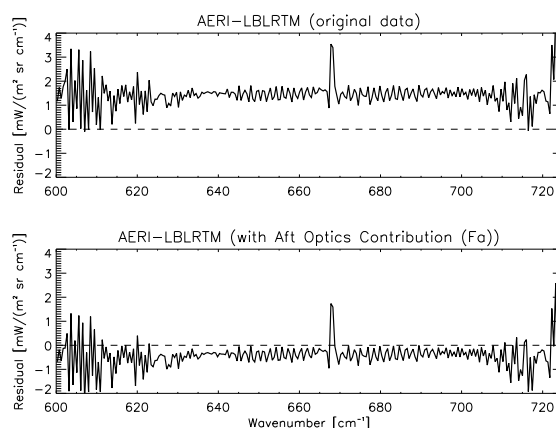


Figure 7.3: The mean residual of AERI minus simulated radiances before (upper plot) and after (lower plot) correction using the aft optic factor, f_a equal 0.010.

these two days before and after radiance correction using the aft optic correction factor, f_a equal 0.010. While the upper plot shows a mean residual around 1.5 RU between AERI and simulated radiances, the lower plot shows a negative residual less than 1 RU. The negative residual clearly indicates that the defined f_a factor is slightly larger than the true correction factor. As it is explained in section 4.5, finding the true or the perfect correction factor needs a quite accurate surface temperature to run the LBLRTM model. Among all available surface temperatures at JOYCE, the one which produced the lowest standard deviation between the calculated and the real AERI radiances is selected to run the LBLRTM. Inherently, even this temperature has uncertainty which leads to an overestimation in computing the correction factor. In order to avoid using a large correction factor to calibrate the AERI radiances, the calculated f_a is slightly reduced based on some correction in the input surface temperature. The new corrected radiances using the new calibration factor equals 0.007 is shown in Fig. 7.4.

The lower plot in Fig. 7.4 shows mean residual around zero for the spectral band between 624 and 710 cm^{-1} . The spectral band between 710 and 720 cm^{-1} shows a residual slightly higher than zero which can be the result of using a constant mixing ratio for the atmospheric CO₂,

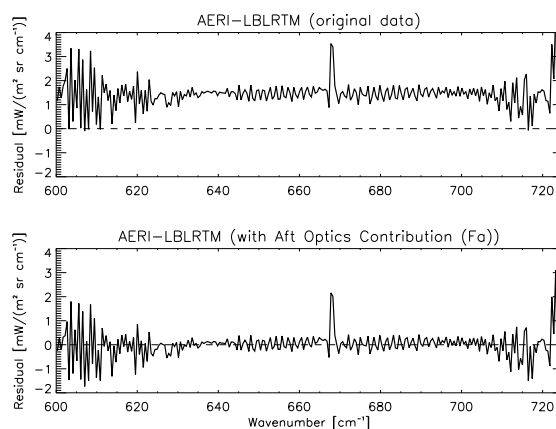


Figure 7.4: The mean residual of AERI minus simulated radiances before (upper plot) and after (lower plot) correction using the aft optic factor, f_a equal 0.007.

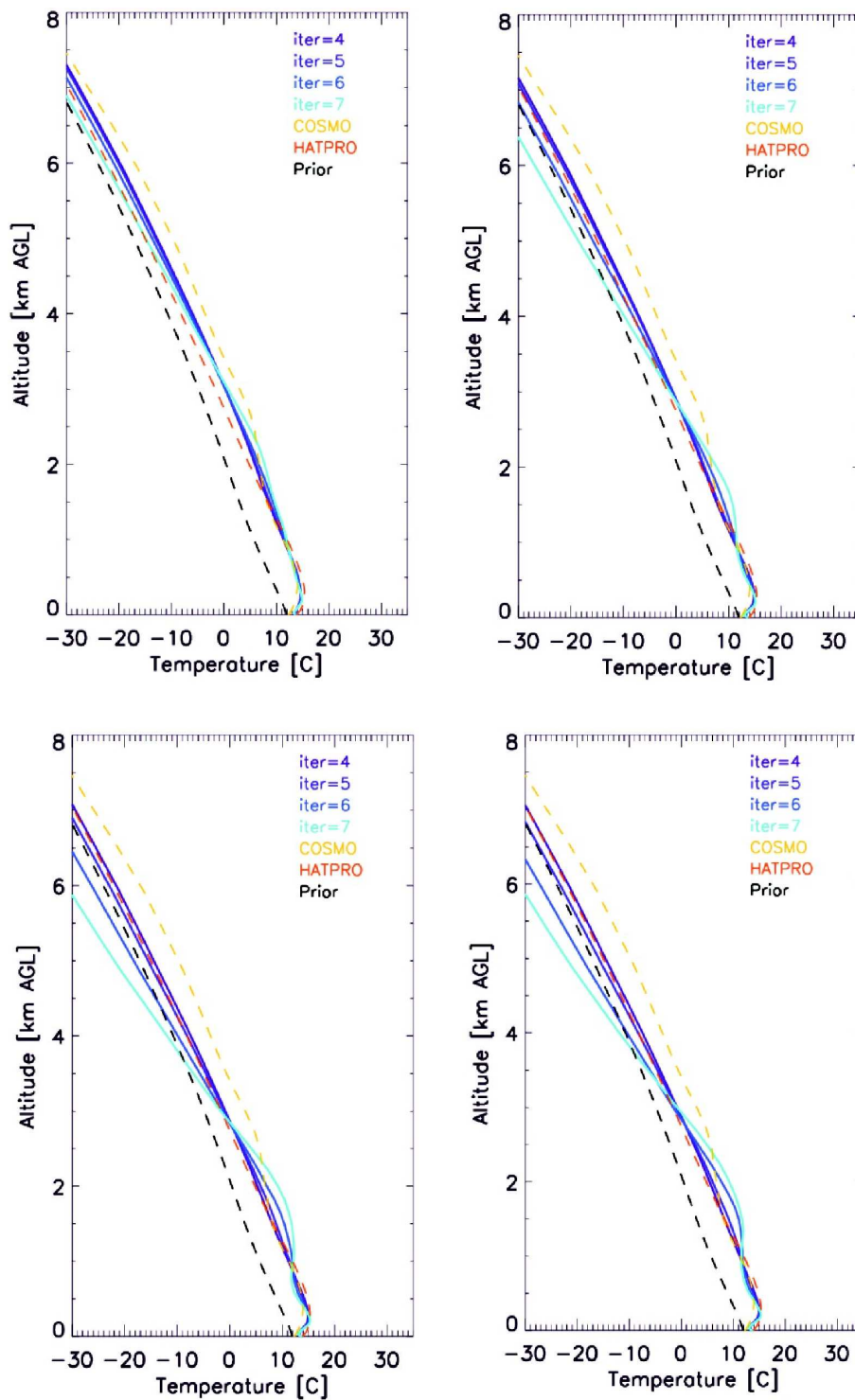


Figure 7.5: The retrieved temperature profile using the original AERI radiances (upper left) as well as using the averaged AERI radiances over 3 (upper right), 30 (lower left) and 60 min (lower right). The dashed black line show the prior profiles, while the COSMO_DE profiles are shown in dashed yellow line and the HATRPO retrieved profiles are shown in dashed red line. The different blue lines show the last four iterations in the AERIOe.

rather than the true profile in the LBLRTM run. In addition, the residual (up to 1 RU) in the

spectral band from 618 to 624 is mainly due to the contribution of the N₂O in this region. Because the true atmospheric N₂O content is not available at JOYCE, an approximation value is used as input profile in the LBLRTM run which leads to the uncertainty in the simulated radiances in this region. The higher residual (up to 2 RU) between 600 and 618 cm⁻¹ are likely due to mismatch in the input humidity profile used in the simulation with true (or what the AERI is observing) humidity profile. Another high residual (up to 3 RU) is a residual in the spectral band between 722 and 725 cm⁻¹. The residual in this part can be due to the spectroscopy issues of this band in the LBLRTM or it can be due to small errors in accounting for the instrument finite-field-of-view correction (*personal communication with D. D. Turner*).

Another issue with the observations from the AERI at Jülich (that is found in the measurements of these two days) which still remains as an open problem is shown in Fig. 7.5. In this plot, the retrieved temperature profiles are shown for the original AERI radiances as well as the averaged radiances over 3, 30 and 60 min. For comparison, the retrieved HATPRO temperatures and the temperature profiles provided by the COSMO_DE are also shown in these plots. Each plot shows four retrieved temperature profiles derived from four last successive iterations of the AERIOe. Although, it is expected that difference in retrieved temperature profiles between two iterations reduces in the last iterations (leading to the convergence of the algorithm), as the plots show, a divergence can be seen in the retrieved profiles of the last iterations. In addition, the divergence in the last iterations is more significant when the averaged radiances are taken over increasing time interval. This problem may be due to the issues in the temperature of the AERI detector (*personal communication with D. D. Turner*). The AERI detector needs to keep an accurately constant temperature during the measurements. This procedure is done using the Sterling cooler which keeps the detector at cryogenic temperatures (~77 K) (see section 3.1). Small variations in the temperature of the detector change the responsivity of the instrument, and thus can lead to minor variations in the observed radiance. If the responsivity is changing and many radiance observations are averaged together, this has non-linear impacts on the mean radiance that can not be well handled by the retrieval. Note that even the original AERI radiance is an average radiance over 12 s, meaning that this issue can be seen even in original AERI radiances, however, it is in a smaller order.

According to these issues with the real AERI radiances, the approach for selecting the optimal solution of the algorithm is slightly changed. As explained in section 5.2, the AERIOe takes an optimal solution when the difference between two iterations fulfills the convergence criteria defined in Eq. 5.6 and the gamma factor reaches 1. According to the plots in Fig. 7.5, the difference between retrieved profiles increases in iteration 6 or 7 where the gamma factor is 1, meaning that these iterations can not typically fulfill the given convergence criteria. Consequently, the algorithm now chooses the iteration with the minimum difference between retrieved profiles of the two iteration which also fulfills the convergence criteria as the optimal solution even if the gamma factor has a value higher than 1. As shown in eq. 5.12, the gamma factor is a multiplier in the optimal estimation equation of the AERIOe which depresses the prior covariance matrix, S_a . Consequently, when the gamma factor is higher than 1, the prior uncertainty is considered lower compared to the true prior uncertainty. Therefore, the calculated DFS is smaller than the true DFS and the calculated posterior covariance matrix which also includes gamma in its calculation become larger (*Turner and Löhnert, 2014*).

In order to retrieve the temperature, humidity and CO₂ profiles simultaneously, the AERIOe is run using the averaged radiances over 1 hour. The prior data of the CO₂ parameters, A_0 , A_1 and A_2 are considered 393., -3 and 5. The prior value of A_0 is selected based on

the background CO₂ concentrations measured in 2012 (<https://www.esrl.noaa.gov/>). The values of A_1 and A_2 are defined according to the prior values derived from two years data of the REMO (see section 6.2.1). The $1-\sigma$ uncertainty of A_2 is defined based on the REMO data and the $1-\sigma$ uncertainty of A_1 which shows the variations in the CO₂ surface value, is defined 15. This value is higher than the provided value by the REMO since the Jülich tower measurements of the CO₂ near the surface shows the diurnal cycle on the order of 20 to 30 ppm in May. A small uncertainty is considered for the A_0 in order to fix it in the algorithm. Furthermore, no correlation is considered between these three parameters.

The spectral bands used in this run are the water vapor band from 550 to 588 cm⁻¹ and two spectral bands, 624-660 and 674-722 cm⁻¹ from the 15 μm CO₂ line. The measurement error covariance matrix needs to include additional sources of uncertainty such as the uncertainty in the spectroscopy of the forward model due to using the real AERI observation radiances. However, calculating the exact value of this uncertainty is quite difficult. Therefore, the error covariance matrix is computed using the original AERI noise and is also inflated in order to capture the forward model error. The inflation factor used in this work is about a factor of 4 which is close to the factor used in the previous AERI studies (*Turner and Löhnert, 2014*).

Figs. 7.6 to 7.10 show the results from the AERIOe retrieval. In order to do the comparison, the retrieved temperature profiles of the HATPRO (see section 3.2) as well as the temperature and humidity profiles provided by the COSMO_DE (see section 3.5) are also shown in Figs. 7.6, 7.7 and 7.8.

Fig. 7.6 shows the AERI and the HATPRO retrieved temperature profiles while the difference between these profiles is also shown in this panel. As the plots show, for the levels below 500 m, the difference between AERI and HATRPO retrieved temperatures is about 1 °C. This difference reaches to 2 °C for the levels from 500 m to 2 km. On the other hand, above 2 km, AERI temperatures are between 2 and 6 °C larger than HATPRO temperatures.

Fig. 7.7 shows the plots for comparison between AERI and COSMO_DE temperature profiles. For the levels near the surface (below 500 m), a difference less than 2 °C can be seen between AERI and COSMO_DE temperatures. For the levels between 0.5 and 1 km, COSMO_DE temperatures are larger, in the order of 2 °C, compared to AERI temperatures. Above 3 km, the same pattern can be seen on both days. Before 11 UTC, AERI profiles are around 3 °C larger than COSMO_DE profiles, while after 11 UTC, COSMO_DE profiles are around 2 °C larger than AERI profiles. At the end of the day, in both plots, AERI profiles become again larger than COSMO_DE profiles.

The water vapor mixing ratio profiles of the AERI and the COSMO_DE are shown in Fig. 7.8. The differences between AERI and COSMO_DE profiles, for the levels above 3 km are mainly lower than 0.5 g/kg, while this difference reaches to 2 g/kg for the levels below 3 km. Furthermore, the derived IWV amounts from the AERI, the HATRPO and the COSMO_DE are shown in Fig. 7.9. In both days, the variations in the AERI retrieved IWV amounts are close to the variations in the HATRPO retrieved values. However, the AERI values are around 2 kg/m² larger than HATRPO values, except for the time interval from 15 UTC on 25 of May until 03 UTC on 26 of May. COSMO_DE IWV values show different pattern compared to AERI and HATRPO values on both days. However, in two time intervals, from 00 UTC to 06 UTC on 25 of May and from 00 UTC to 03 UTC on 26 of May, the AERI retrieved values are very close to COSMO_DE values.

In contrast to the temperature and the humidity profiles which show to some extent good agreement with the model and the other observational data, the retrieved CO₂ surface values

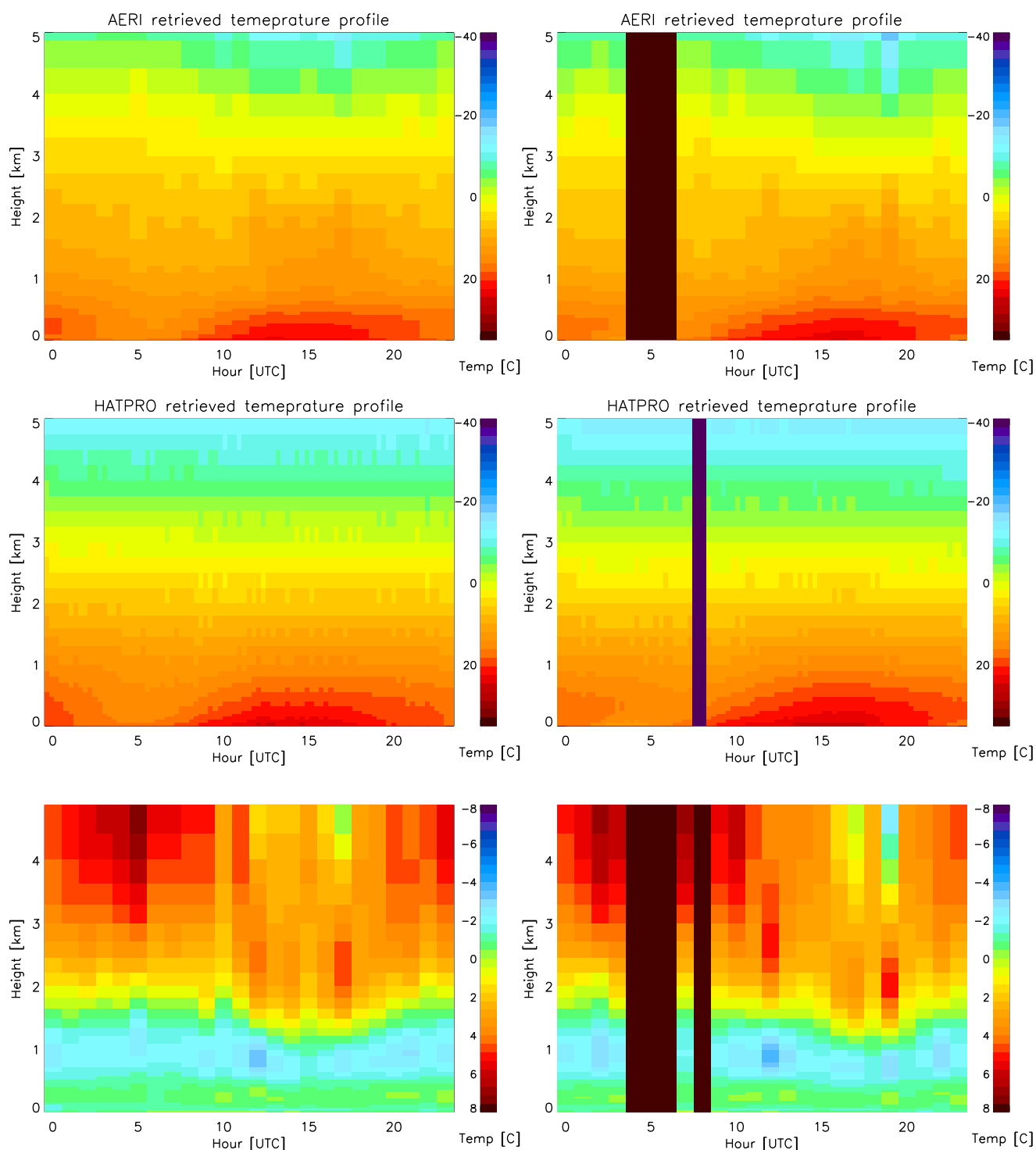


Figure 7.6: The retrieved temperature profiles using the noise-filtered real AERI measurements reconstructed from 521 PCs (upper plots) and the HATPRO retrieved temperature profiles (middle plot) on 25 (left plots) and 26 (right plots) of May 2012. The lower plots show the differences (AERI-HATPRO) between the AERI and the HATRPO temperature profiles. The black columns indicate the non-converged profiles.

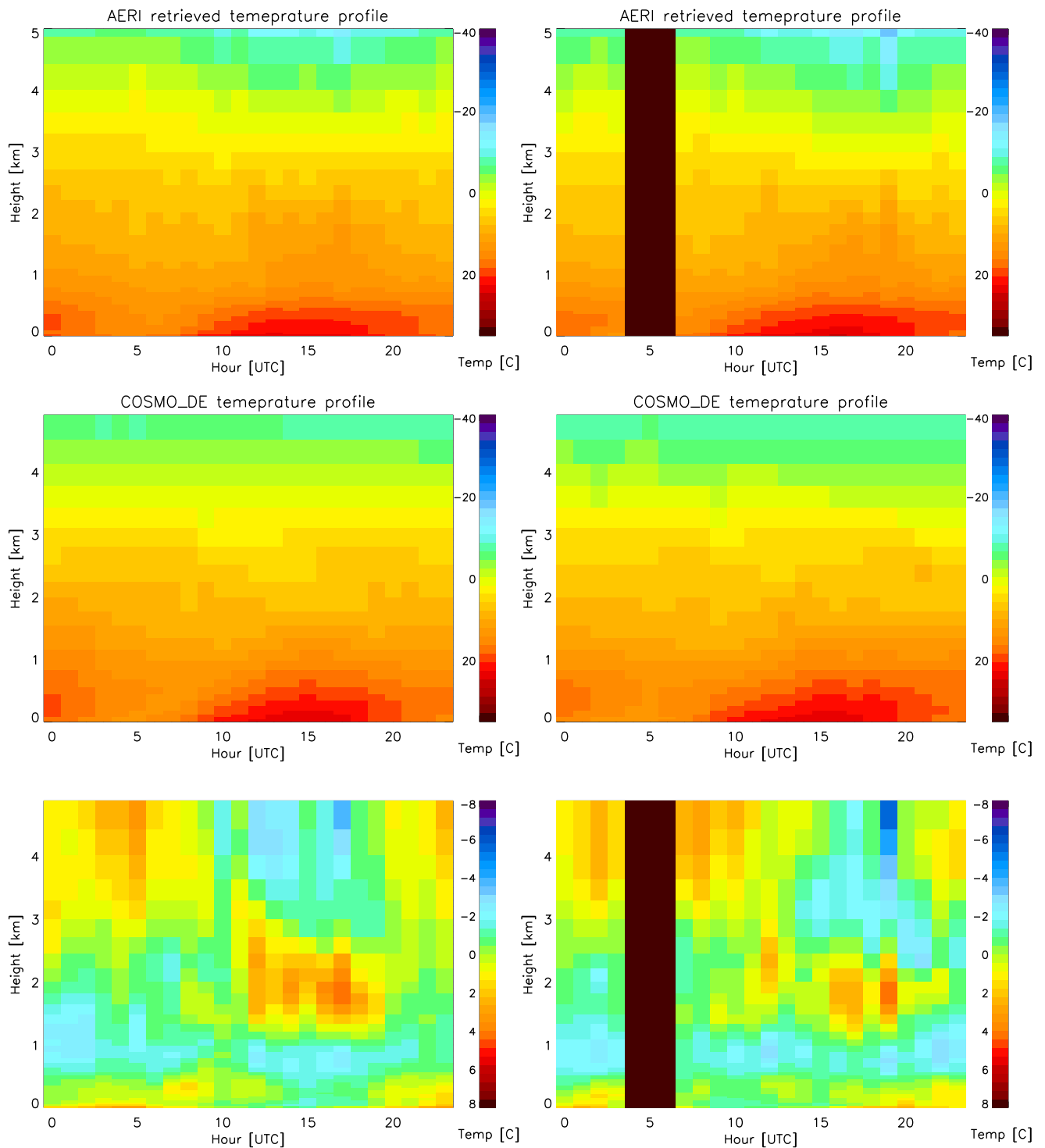


Figure 7.7: The retrieved temperature profiles using the noise-filtered real AERI measurements reconstructed from 521 PCs (upper plots) and the COSMO_DE temperature profiles (middle plot) on 25 (left plots) and 26 (right plots) of May 2012. The lower plots show the differences (AERI-COSMO_DE) between the AERI and the COSMO_DE temperature profiles. The black columns indicate the non-converged profiles.

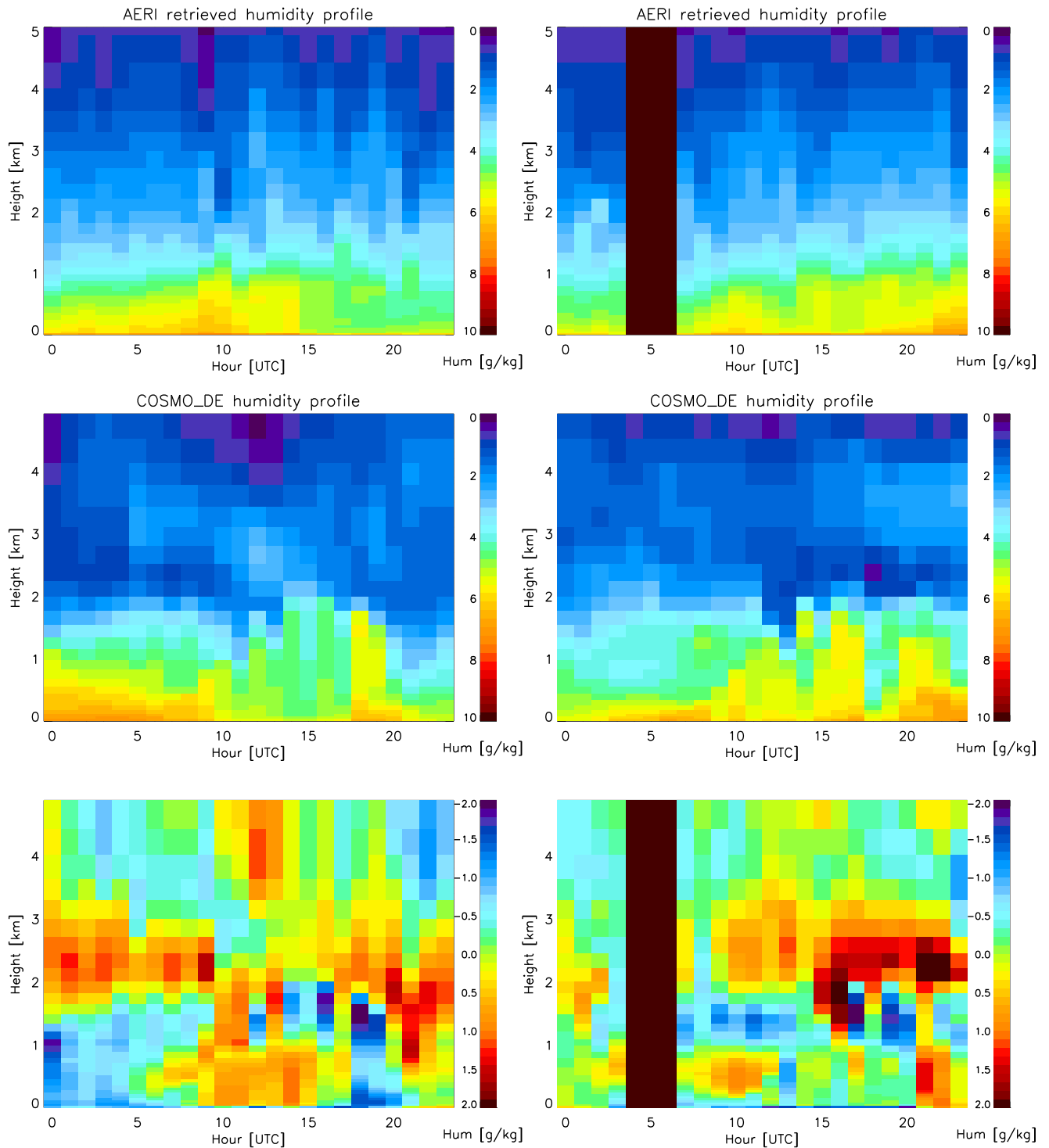


Figure 7.8: The retrieved water vapor mixing ratio using the noise-filtered real AERI measurements reconstructed from 521 PCs (upper plots) and the COSMO_DE water vapor mixing ratio (middle plots) on 25 (left plots) and 26 (right plots) of May 2012. The lower plots show the differences (AERI-COSMO_DE) between the AERI and the COSMO_DE profiles. The black columns indicate the non-converged profiles.

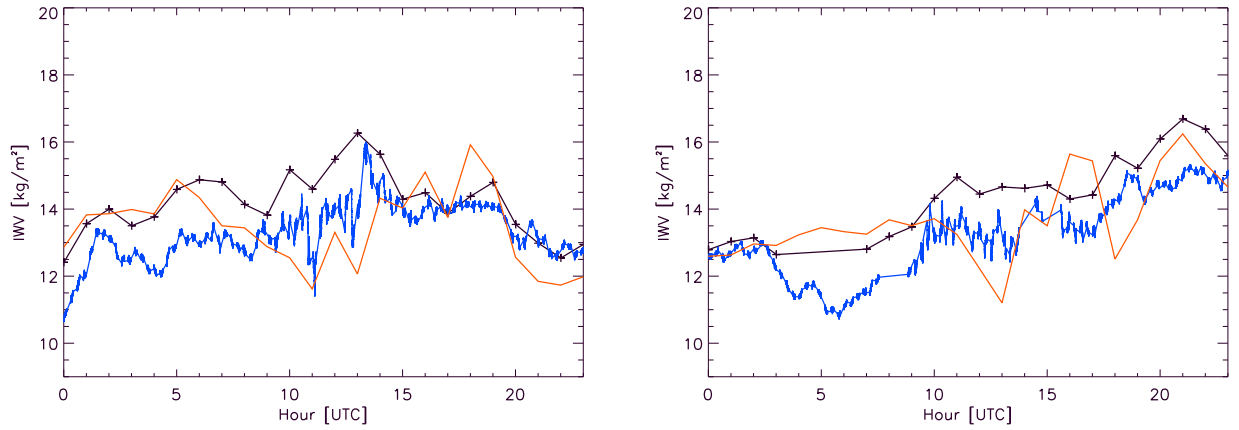


Figure 7.9: The IWV amounts derived from the noise-filtered real AERI measurements reconstructed from 521 PCs (in black), from the HATRPO (in blue) and from the COSMO_DE (in red) on 25 (left plot) and 26 (right plot) of May 2012.

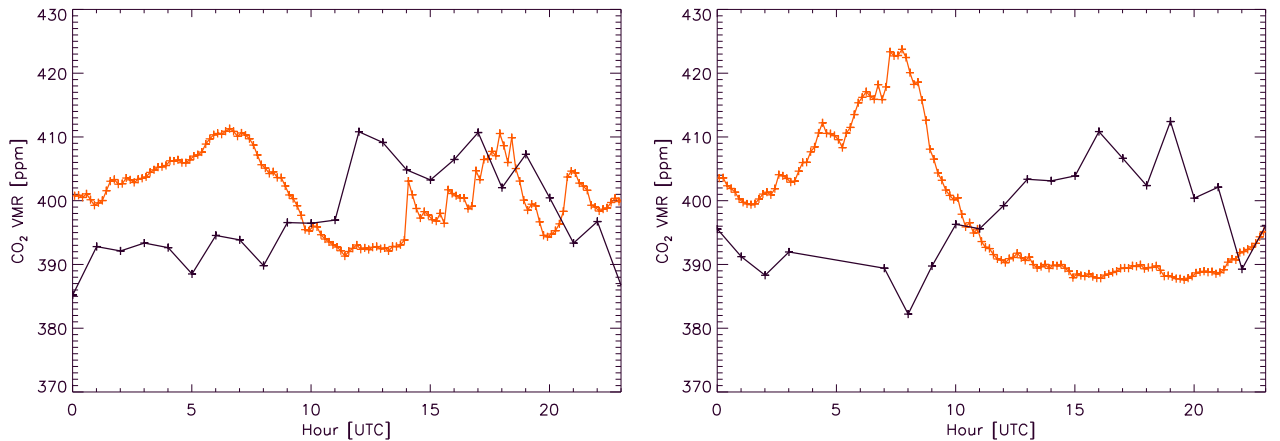


Figure 7.10: The retrieved CO₂ surface values using the noise-filtered real AERI measurements reconstructed from 521 PCs (in black) on 25 (left plot) and 26 (right plot) of May 2012. The red lines show the tower measurements of the atmospheric CO₂ at 100 m in Jülich.

do not show any agreement with the tower measurements. Based on the tower measurements, the CO₂ surface concentration increases during the nighttime and in the early morning and decreases during the daytime. However, on 25 of May, the tower measurements show some peaks and drops in its measurements between 15 and 21 UTC. According to the in-situ wind measurements in Jülich, an increase in the wind (wind-direction cir. 45° north-east) speed from 14 to 20 UTC can be seen where the wind speed increases from 6 to 12 m/s during this time interval. The increase in the tower CO₂ surface measurements may relate to the increase in the wind speed. Note that the accuracy of the tower measurements in 2012 is better than 5 ppm, while the measurements may have an offset which would be constant over several days meaning that the diurnal variation of the tower measurements should be rather accurate (*personal communication with M. V. Hobe*). The diurnal variation captured by the tower measurements can not be seen in the AERI retrieved values. This can be due to low DFS of the CO₂ parameters as it is shown in section 6.2. One solution for this problem is to provide additional information to the algorithm which is explained in the next paragraph.

As shown in section. 6.1, giving the true temperature and humidity profiles to the AERIOe can significantly improve the retrieved CO₂ profiles. Consequently, this approach is used as a first solution to improve the AERI retrieved CO₂ surface values. Since the AERI retrieved profiles show better agreement with the COSMO_DE profiles in the upper levels, the temperature and the humidity profiles of the COSMO_DE are used as true profiles above 4 km in the AERIOe. The COSMO_DE profiles are provided to the algorithm using the prior data, while their uncertainties are set to very small values in order to fix them in the algorithm. The new retrieved profiles are shown in Figs. 7.11 to 7.14.

Fig. 7.11, shows the retrieved AERI temperature profiles. The difference between AERI and HATRPRO profiles as well as the difference between AERI and COSMO_DE profiles are also shown in this panel. For the levels below 2 km, the difference (less than 2 °C) between AERI and HARPRO temperatures as well as between AERI and COSMO_DE temperatures are same as previous run. However, fixing the temperature above 4 km in the AERIOe cause an increase about 2 °C compared to the previous run, in the difference between AERI and HATRPO temperatures, for the layer from 2 to 4 km. Besides, a slight increase about 1 °C can be also seen in the difference between AERI and COSMO_DE temperatures in this layer (from 2 to 4 km).

The AERI retrieved humidity profiles in this run are shown in Fig. 7.12. For the levels below 4 km, same as the previous run, a difference around 2 g/kg can be seen between AERI and COSMO_DE profiles. In addition, Fig. 7.13 shows the retrieved IWV amounts in this run as well as the calculated IWV amounts from the HATRPO and the COSMO_DE. The variations and the amounts of the AERI retrieved IWVs are close to the previous run. However, for the time interval between 15 to 23 UTC on 25 of May, AERI values are around 1 kg/m² larger than HATRPRO values which can not be seen in the results of the previous run shown in Fig. 7.9.

Fig. 7.14 shows the retrieved CO₂ surface values in this run. The plots show that adding extra information of COSMO_DE temperature and the humidity profiles above 4 km does not help the algorithm to capture the diurnal variation of the CO₂ near the surface. However, it should be considered that COSMO_DE profiles above 4 km can be biased and it may also affect on the retrieval results meaning that using perfect temperatures above 4 km (which is not available in this work) may improve the results. Same as the results in the previous run shown in Fig. 7.10, the CO₂ retrieved values show different variations compared to the tower measurements which are not the expected diurnal variation of the CO₂ near the surface. Since the problem in retrieving the CO₂ surface values may still relate to the low DFS, one solution is to give extra information of temperature and humidity profiles below 4 km. However, in the present work, this solution is not used since the available temperature and humidity profiles at the JOYCE are not accurately reliable for the levels below 4 km. Therefore, to solve this problem, an extra spectral band, from 722 to 723 cm⁻¹ is added to the AERIOe spectral bands. As explained in the present section, this spectral band is removed from the AERIOe spectral bands because of the probable spectroscopy issues in this band in the LBLRTM which leads to a high residual between simulated and AERI radiances shown in Fig. 7.4. This small spectral band is added again to see its effect on the AERI retrieved CO₂ surface values. The results of the new run with adding this small spectral band is shown in Figs. 7.15 to 7.18.

The retrieved temperature profiles in this run are shown in Fig. 7.15. The behavior of the AERI retrieved temperatures for the levels below 2 km is nearly close to two previous runs. In contrast, both difference plots (difference between AERI and HATRPRO temperatures as

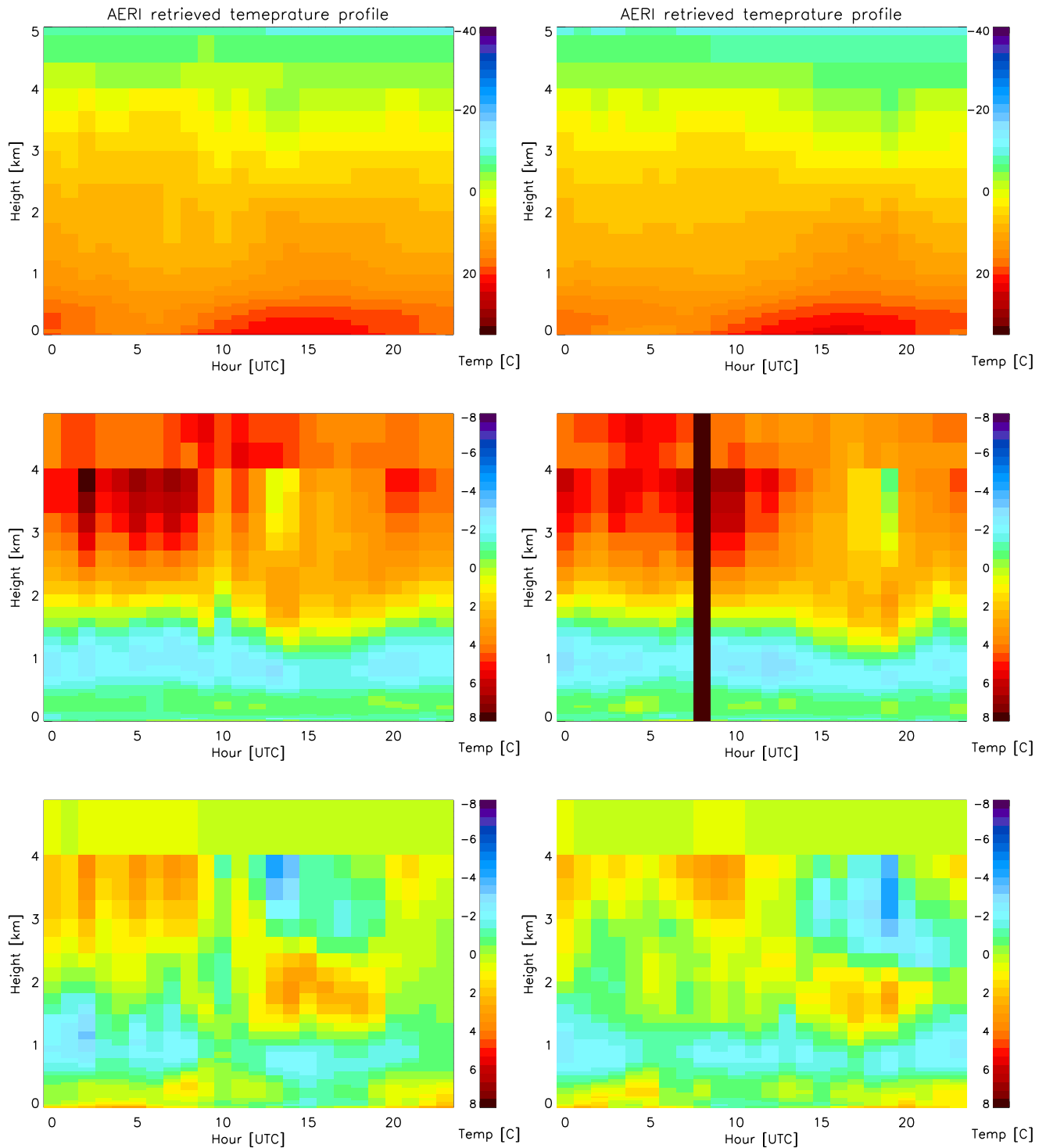


Figure 7.11: The retrieved temperature profiles using the noise-filtered real AERI measurements reconstructed from 521 PCs. COSMO_DE data above 4 km are used to constrain the temperature and humidity in the AERI retrieval. The middle plots show the difference (AERI-HATRPO) between the AERI and the HATRPO temperatures and the lower plots shows the difference (AERI-COSMO_DE) between the AERI and the COSMO_DE temperatures. The left plots belong to 25 and the right plots belong to 26 of May 2012. The black column indicates the non-converged profile.

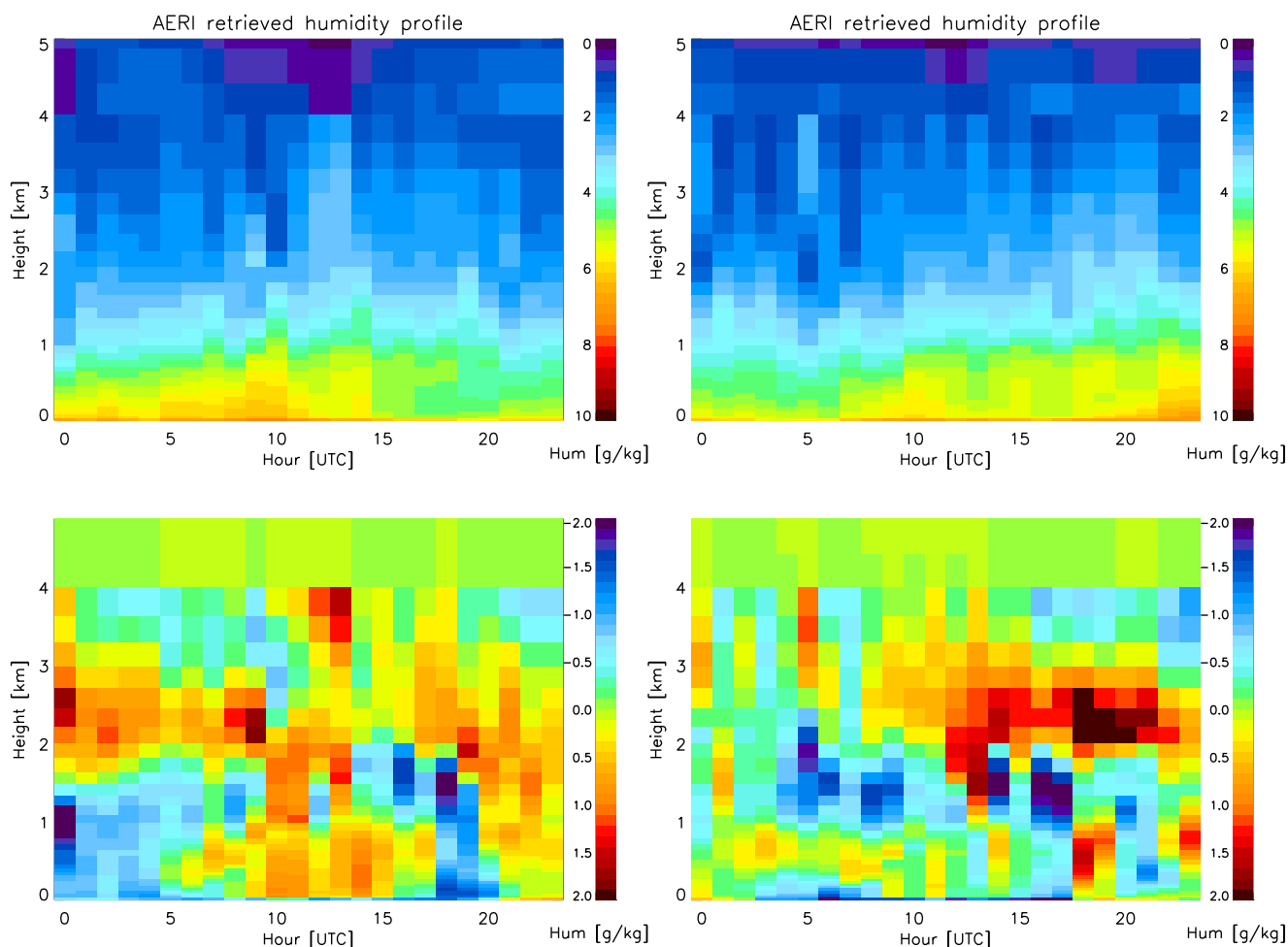


Figure 7.12: The retrieved water vapor mixing ratio profiles using the noise-filtered real AERI measurements reconstructed from 521 PCs. COSMO_DE data above 4 km are used to constrain the temperature and humidity in the AERI retrieval. The lower plots show the difference (AERI-COSMO_DE) between the AERI and the COSMO_DE humidity profiles. The left plots belong to 25 and the right plots belong to 26 of May 2012.

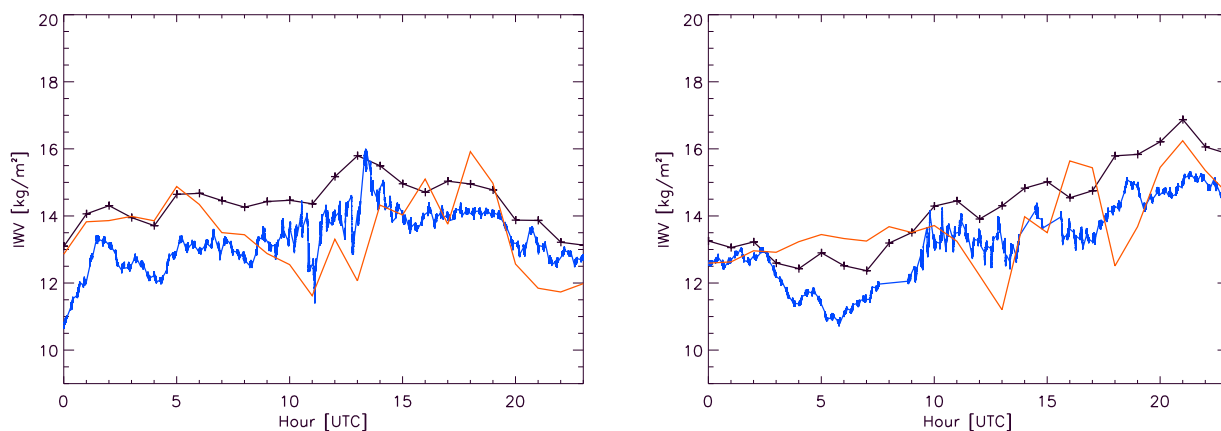


Figure 7.13: The IWV amounts derived from the noise-filtered real AERI measurements reconstructed from 521 PCs. COSMO data above 4 km are used to constrain the temperature and humidity in the AERI retrieval (in black), from the HATRPO (in blue) and from the COSMO_DE (in red) on 25 (left plot) and 26 (right plot) of May 2012.

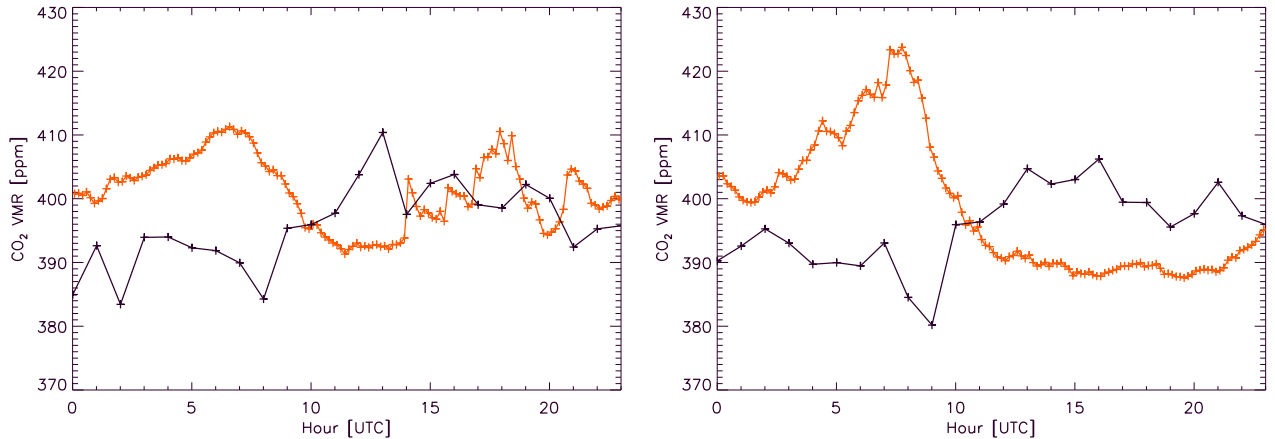


Figure 7.14: The retrieved CO₂ surface values (in black) using the noise-filtered real AERI measurements reconstructed from 521 PCs. COSMO data above 4 km are used to constrain the temperature and humidity in the AERI retrieval on 25 (left plot) and 26 (right plot) of May 2012. The red lines show the tower measurements of atmospheric CO₂ at 100 m in Jülich.

well as difference between AERI and COSMO_DE temperatures) in this panel show that AERI temperatures are significantly larger than HATPRO and COSMO_DE temperatures in the layer between 2 and 4 km. However, an exception can be seen on both days in the time interval approximately between 12 and 19 UTC. The difference between AERI and COSMO_DE temperatures is between 3 to 8 °C while the difference between AERI and HATRPO temperatures is higher than 6 °C. These large differences can be due to the new spectral band and the spectroscopy problem in this band.

The retrieved humidity profiles and the derived IWV amounts are presented in Figs. 7.16 and 7.17. The plot shows similar behavior compared to two previous runs. It is an expected consequence since the water vapor band has no change compared to previous runs.

The retrieved CO₂ surface values in this run are shown in Fig. 7.18. As the plot shows, the AERI values in this run capture the nighttime and the early morning increase as well as the daytime decrease in the CO₂ concentrations near the surface. The second increase after the sunset in the CO₂ surface value can be also seen in the AERI retrieved values. The maximum CO₂ concentrations retrieved by the AERI on 25 of May is about 5 ppm higher than the maximum value of the tower measurements. In addition the AERI maximum occurred 3 hours earlier compared to the maximum of the tower measurements. Furthermore, after 12 UTC, an underestimation higher than 5 ppm can be seen in the AERI retrieved values compared to the tower measurements in this day which turns to an overestimation after 19 UTC.

The tower measurements on the 26 of May show a maximum value around 08 UTC as well as a sudden decrease in its value after this hour. These measurements also show that the CO₂ surface values are nearly constant between 13 and 20 UTC and these values slightly increase after 20 UTC. The AERI retrieved values show nearly the same behavior, while its maximum occurs about 1 hour earlier and it has underestimation about 10 ppm compared to the tower measurements. The decrease in the CO₂ surface values can be also seen in the AERI values for the rest of the day, however, the AERI values show an overestimation from 3 to 10 ppm compared to the tower measurements after 10 UTC.

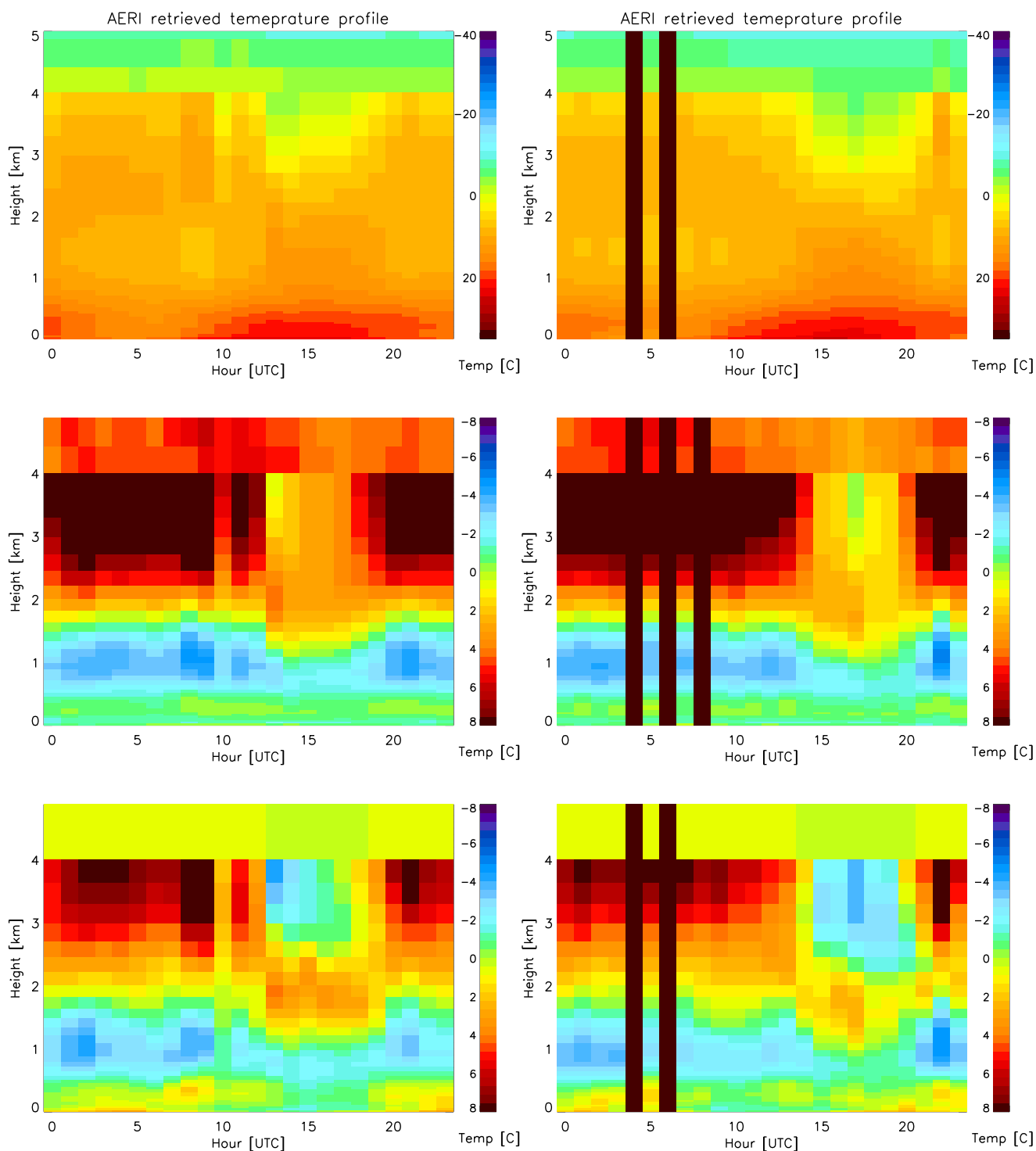


Figure 7.15: The retrieved temperature profiles using the noise-filtered real AERI measurements reconstructed from 521 PCs. COSMO_DE data above 4 km are used to constrain the temperature and humidity in the AERI retrieval. The additional spectral band, $722\text{-}723\text{ cm}^{-1}$ is also used in the AERI retrieval. The middle plots show the difference (AERI-HATRPO) between the AERI and the HATRPO temperatures and the lower plots shows the difference (AERI-COSMO_DE) between the AERI and the COSMO_DE temperatures. The left plots belong to 25 and the right plots belong to 26 of May 2012. The black columns indicate the non-converged profiles.

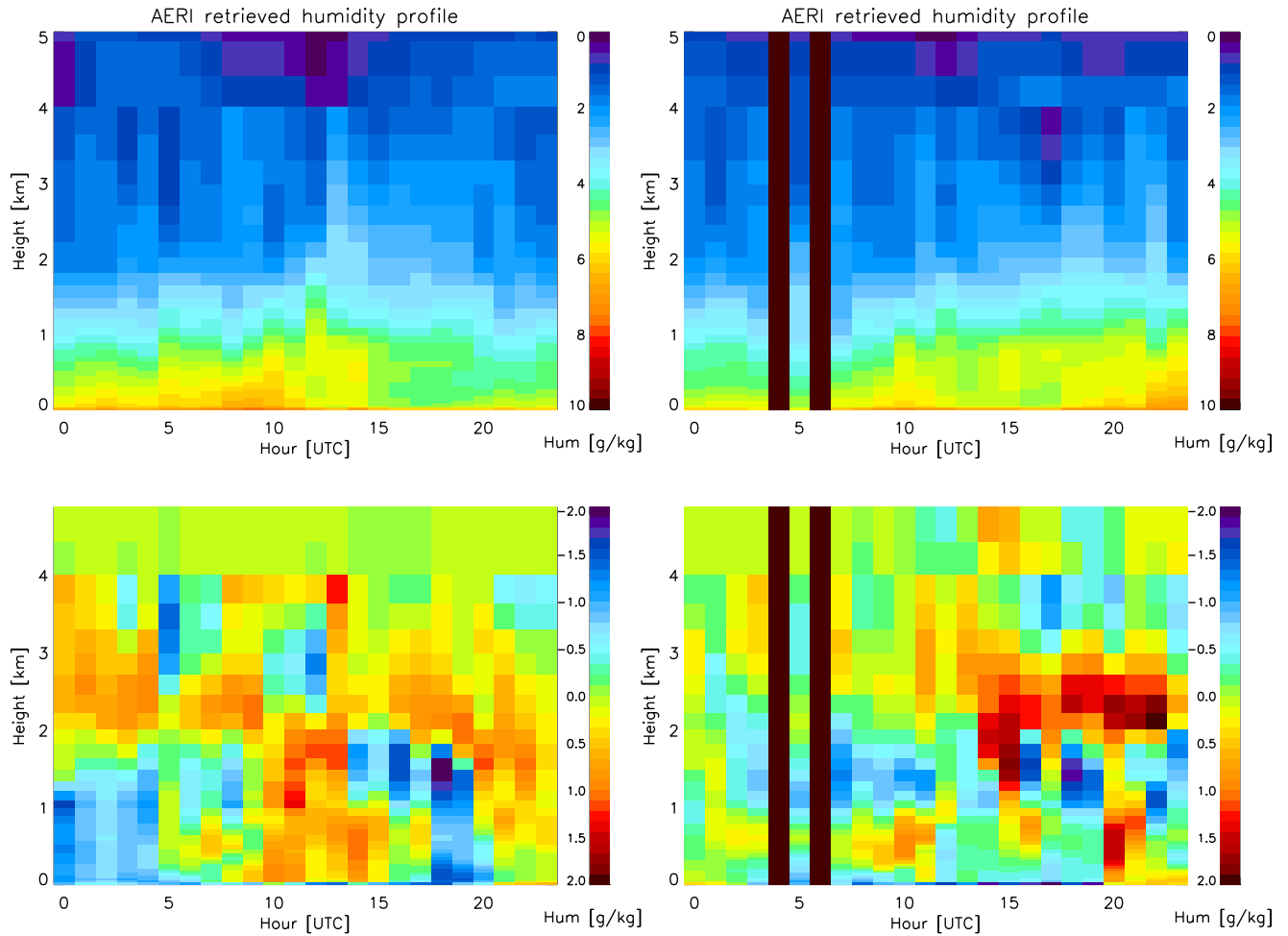


Figure 7.16: The retrieved water vapor mixing ratio profiles using the noise-filtered real AERI measurements reconstructed from 521 PCs on 25 (left plot) and 26 (right plot) of May. COSMO_DE data above 4 km are used to constrain the temperature and humidity in the AERI retrieval. The additional spectral band, $722\text{-}723\text{ cm}^{-1}$ is also used in the AERI retrieval. The lower plots show the difference (AERI-COSMO_DE) between the AERI and the COSMO_DE humidity profiles. The black columns indicate the non-converged profiles.

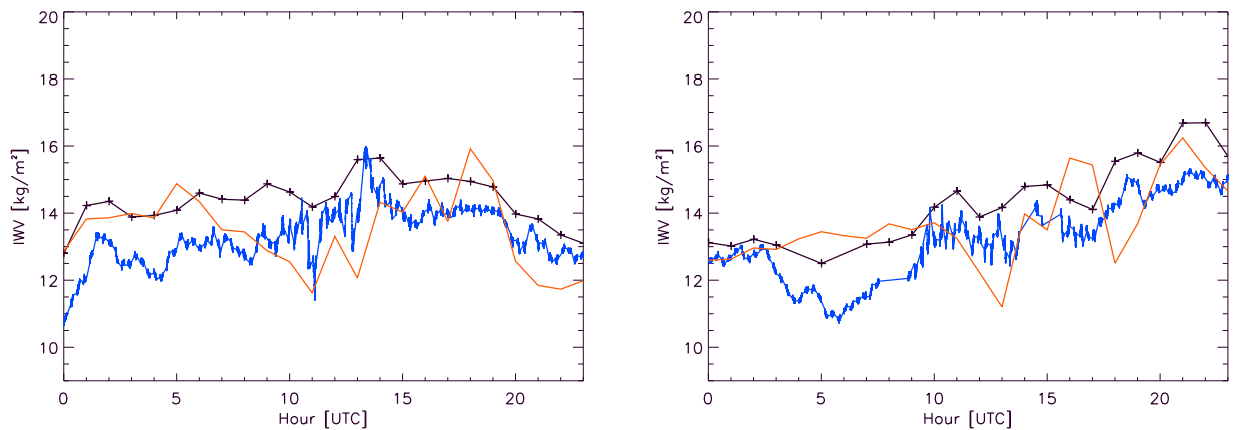


Figure 7.17: The IWV derived from the noise-filtered real AERI measurements (in black) reconstructed from 521 PCs on 25 (left plot) and 26 (right plot) of May. COSMO_DE data above 4 km are used to constrain the temperature and humidity in the AERI retrieval. The additional spectral band, $722\text{-}723\text{ cm}^{-1}$ is also used in this run. The blue lines shows the retrieved IWV from the HATRPO and the red lines shows the IWV from the COSMO_DE.

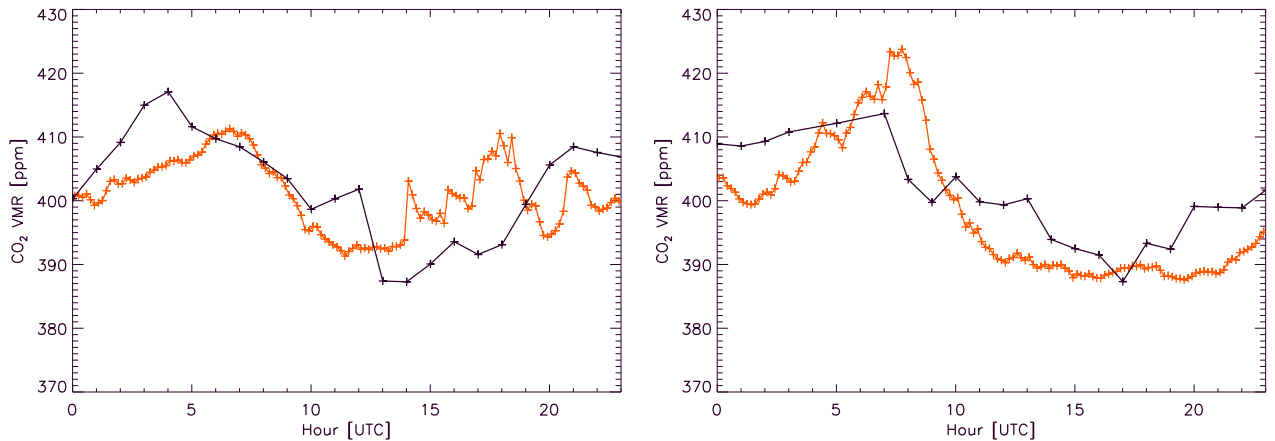


Figure 7.18: The retrieved CO₂ surface values (in black) using the noise-filtered real AERI measurements reconstructed from 521 PCs. COSMO_DE data above 4 km are used to constrain the temperature and humidity in the AERI retrieval. The additional spectral band, 722-723 cm⁻¹ is also used in the AERI retrieval. The left plot belong to 25 and the right plot belong to 26 of May 2012. The red lines show the tower measurements of atmospheric CO₂ at 100 m in Jülich.

In addition, the total DFS of the CO₂ parameters and the 1- σ uncertainty in the retrieved CO₂ surface values as well as the gamma factor of the optimal solution are shown in Fig. 7.19. As expected, the gamma factors except for two profiles are higher than 1. The values of the gamma factor are mainly 3 and 10. The 1- σ uncertainty in the retrieved CO₂ surface values are between 4 and 8 ppm, while for only two profiles the uncertainty reaches to higher than 10 ppm. According to these uncertainties, the retrieved surface CO₂ values are within the uncertainty to the tower measurements. Moreover, the DFS values show two different ranges

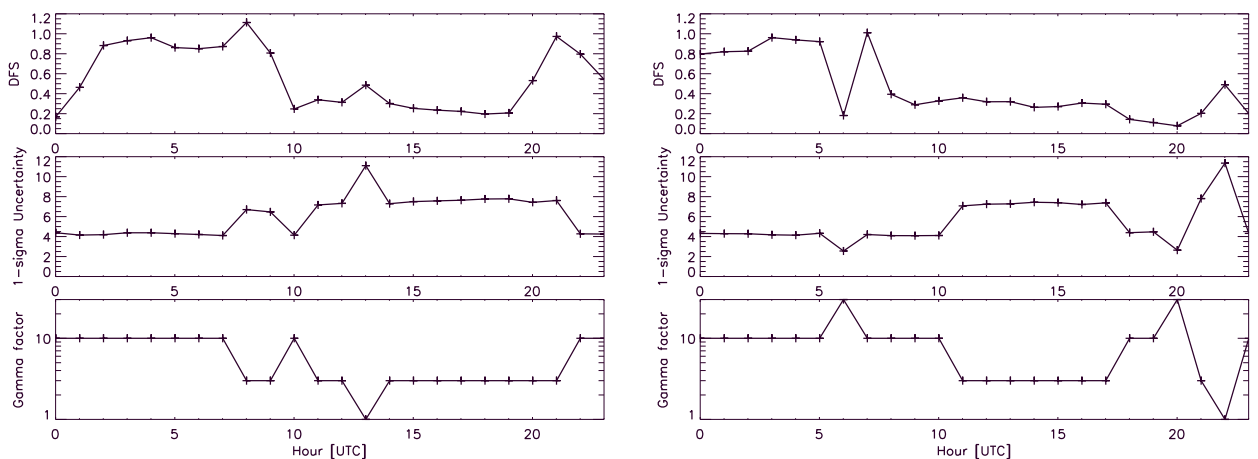


Figure 7.19: The total DFS of CO₂ (upper plot), the 1- σ uncertainty in the surface retrieved CO₂ (middle plot) and the gamma factor derived from AERIOe run using the the noise-filtered real AERI measurements reconstructed from 521 PCs. COSMO_DE data above 4 km are used to constrain the temperature and humidity in the AERI retrieval. The additional spectral band, 722-723 cm⁻¹ is also used in the AERI retrieval. The left plot belongs to 25 and the right plot belongs to 26 of May 2012.

which may relate to the nighttime and daytime profiles. It seems that the DFS values has a decrease for the daytime profiles (between 10 to 19) and its values are roughly between 0.2 and 0.4 while during the nighttime the DFS values increases and reaches the values between 0.8 and 1. Note that due to the gamma factor larger than 1, the derived DFS and 1- σ uncertainty are smaller and larger than the true ones respectively.

The results of the last run show that the AERI has the potential to capture the diurnal change of the CO₂ concentration near the surface when the spectral band from 722 to 723 cm⁻¹ is also used in the AERIOe. However, it seems that the spectroscopy issue in this band causes a significant error in the retrieved temperature profiles. Besides, compared to the tower measurements, the maximum of the AERI retrieved CO₂ surface values, on both days, occurs earlier compared to the tower measurements. Furthermore, the AERI maximum has overestimation or underestimation between 5 and 10 ppm compared to the tower measurements. A difference less than 10 ppm can be also seen between AERI and tower measurements for more than 80% of the AERI retrieved values. Note that in the present work, the possibility to add the extra information of temperature and humidity profiles below 4 km to the algorithm is not tested due to the lack of reliable profiles in this layer.

In addition to retrieving the CO₂ surface value, as shown in section 6.2.3, giving the information of CO₂ concentration near the surface to the AERIOe can help the algorithm to accurately retrieve the CO₂ profile mainly in the boundary layer. This possibility is tested with the real measurements which is explained in the next subsection.

7.2.1 Fixed the CO₂ surface value

In section 6.2.3, it is shown that the A₁ can be retrieved more accurately by the AERIOe if extra information about the CO₂ concentration near the surface is given to the algorithm as auxiliary data. This parameter can give the approximate shape of the CO₂ profile in the boundary layer or in other words, it can provide the information about the height where the CO₂ concentration deviates from the background concentration.

Another test is performed wherein surface in-situ tower observations of CO₂ are included in the AERI retrieval. Because there is no measurement of the CO₂ profile for the whole boundary layer at JOYCE, in order to see the accuracy of the retrieved CO₂ profiles, the retrieved A₁ values are used to estimate the evolution of the CO₂ in the boundary layer over the diurnal cycle. The diurnal variation of the calculated height is then analyzed according to the expected diurnal variation of the boundary layer height for a sunny clear sky day. It is expected that the derived height shows a similar evolution as boundary layer evolution. In a sunny clear sky day, after the sunrise and heating the surface, due to the free convection, the mixing process starts and the well-mixed boundary layer becomes deeper. The mixing layer reaches to its maximum depth around the noon time. In the well-mixed layer, trace gases such as CO₂ are nearly constant with height meaning that a decrease in the CO₂ surface concentration can occur when the CO₂ is mixed over a larger volume of atmosphere as the well-mixed boundary layer becomes deeper. In addition, due to the forest area in Jülich during the daytime, the photosyntheses can also reduce the CO₂ concentration near the surface. Note that the selected cases are in spring time so that the photosynthesis can be significant during this time. On the other hand, after the sunset, the mixing process stops so that the convective mixing layer collapses to a thin layer called stable layer where the trace gases can spread horizontally in this layer which causes an increase in their surface values.

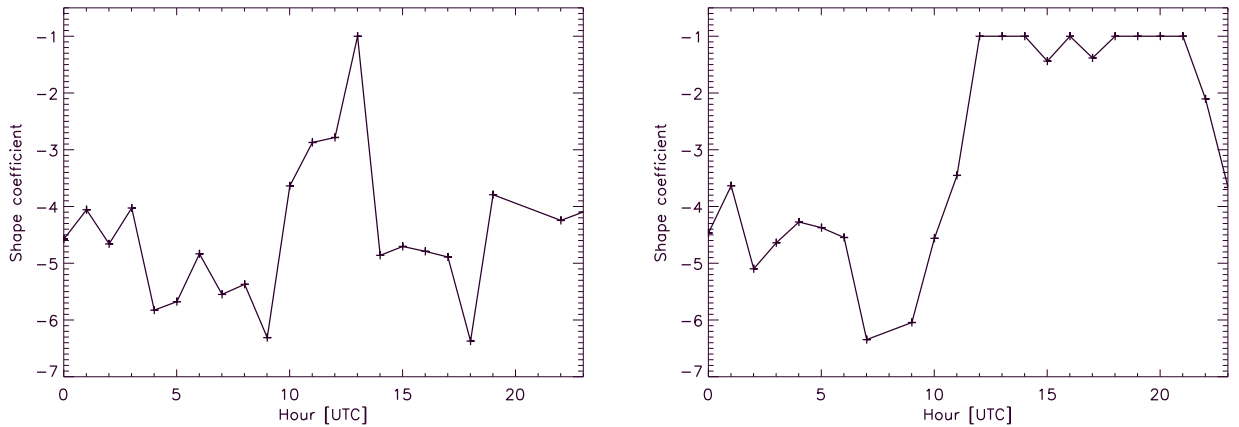


Figure 7.20: The retrieved A_1 (shape coefficient) values using the noise-filtered real AERI measurements reconstructed from 521 PCs. COSMO_DE data above 4 km are used to constrain the temperature and humidity in the AERI retrieval, on 25 (left plot) and 26 (right plot) of May 2012.

Stopping the photosynthesis as well as soil respiration during the nighttime can also help to increase the CO₂ concentration near the surface.

The surface CO₂ values are provided to the algorithm using the prior data with small uncertainties to make the surface CO₂ as a fixed parameter in the algorithm. The prior value for the A_1 is considered -3 with 1- σ uncertainty of 3, same as in previous runs. The desired height is estimated using the retrieved A_1 as:

$$|\text{Exp}(A_1 z)| \leq 0.2. \quad (7.1)$$

The first altitude which fulfills the above condition is considered as the height which shows the evolution of the CO₂ in the boundary layer. This is an estimation which approximately

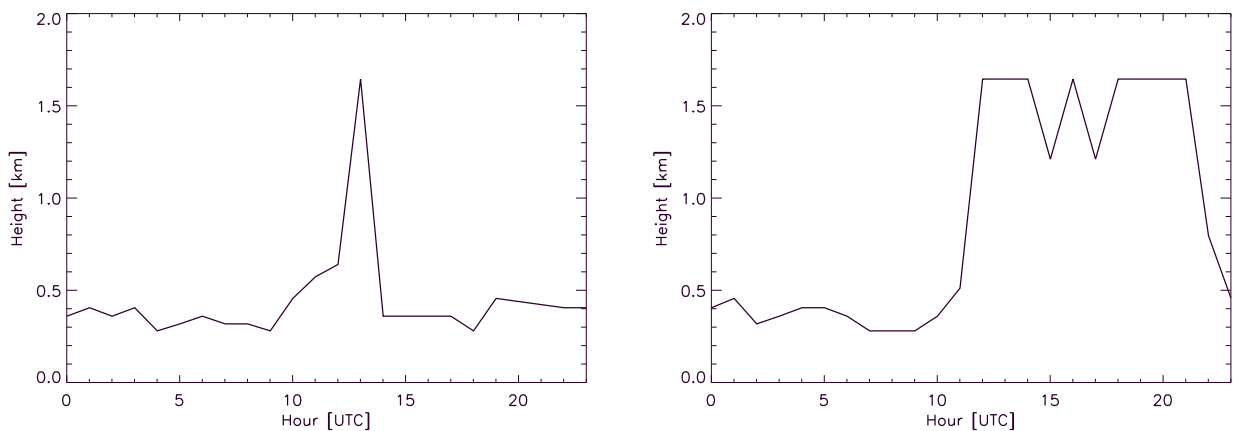


Figure 7.21: The calculated height where CO₂ deviated from its background concentration using the retrieved A_1 values from the noise-filtered real AERI measurements reconstructed from 521 PCs. COSMO_DE data above 4 km are used to constrain the temperature and humidity in the AERI retrieval, on 25 (left plot) and 26 (right plot) of May 2012.

indicates the height where the deviation of the CO₂ concentration from its background concentration reaches less than 20%. The results of the new run are shown in Figs. 7.20 and 7.21.

Fig. 7.20 shows the retrieved A₁ values. The derived height are shown in Fig. 7.21. According to the retrieved temperature profiles, the minimum surface temperature occurs around 07 UTC on both days. An increase in the derived height can be seen with 2 hours delay, around 09 UTC on both days. After that, the calculated height reaches to its maximum value between 12 and 13 UTC on both days. On 25 of May, the altitude of the derived height decreases suddenly after 14 UTC, while on 26 of May, the decrease in the altitude happens after 21 UTC. The sudden decrease on the first day can be related to the unexpected peaks and drops in the tower measurements on this days, for the time interval between 14 and 20 UTC. Note that, the sunset on these two days was around 19:30 UTC. Consequently, the decrease in the altitude of the derived height after 21 UTC on 26 of May is more consistent with this sunset time.

In summary, the temporal evolution of the derived height where the CO₂ deviates from its background concentration for 26 of May corresponds to the temporal evolution of the boundary layer on a sunny clear sky day. However, on 25 of May, the derived height does not show the expected variation of the boundary layer in the afternoon. Therefore, more clear cases are needed to test the algorithm and find the potential of the AERIoe to estimate this height. In addition, accurate CO₂ surface value can help the algorithm to better estimate this height. Note that, the accuracy of the absolute value for the derived height can not be guaranteed. In addition, accurate measurements of the CO₂ near the surface and in upper levels can give the opportunity for comparison of the AERI results and to analyze their accuracy.

Chapter 8

Summary and outlook

Since the industrial revolution, the emission of anthropogenic CO₂ into the atmosphere has resulted in a concentration change from 278 ppm (before 1750) to more than 400 ppm in 2017 (*IPCC*, 2013; *www.esrl.noaa.gov*). As a consequence, many studies have analyzed the effect of the CO₂ increase on the current climate as well as on the future climate (e.g. *IPCC*, 2013; *Martínez-Botí et al.*, 2015). Studying the carbon cycle between three natural reservoirs, land, ocean and atmosphere is an essential path which can help to better analyze and predict current and future climates. The interaction of land-vegetation with the atmosphere can produce large diurnal variation on the order of 20 ppm, but occasionally 50 ppm or more, in the atmospheric CO₂ concentration near the surface. The measurements of this diurnal variation can be helpful in order to study the interaction between the terrestrial ecosystem and the atmosphere as a part of the carbon cycle. However, accurately capturing the diurnal variation of CO₂ mainly in the boundary layer is still a big gap in the CO₂ measurements. Many space-based instruments such as *SCIAMACHY*, *GOSAT* and *OCO-2* (*Bovensmann et al.*, 1999; *Morino et al.*, 2011; *Crisp et al.*, 2017) as well as ground-based instrumentation within the *TCCON* network (*Wunch et al.*, 2011) can provide CO₂ measurements only during daytime. Besides, satellites typically do not have sufficient sensitivity to the CO₂ concentration in the boundary layer which presents another limitation of satellites for providing information about CO₂ variations near the surface.

In the present work, a ground-based infrared spectrometer with high temporal and spectral resolution is used to provide information about the variation of the CO₂ concentration mainly in the boundary layer. The Atmospheric Emitted Radiance Interferometer (AERI) (*Knutson et al.*, 2004a) measures the downwelling infrared radiation at better than 1 cm⁻¹ resolution in the mid-infrared region between 520 cm⁻¹ (19 μm) and 3020 cm⁻¹ (3.3 μm). The AERI was installed at Jülich ObservatorY for Cloud Evolution (JOYCE), Germany in 2011. Although, the AERI is originally designed to provide highly spectrally resolving atmospheric emission for studying spectroscopic issues in the infrared region and for evaluating radiative transfer models (e.g. *Revercomb et al.*, 2003; *Turner et al.*, 2004), its measurements are also utilized to retrieve thermodynamic atmospheric profiles and cloud properties (e.g. *Feltz et al.*, 1998; *Turner et al.*, 2000; *Turner*, 2005; *Löhnert et al.*, 2009; *Turner and Löhnert*, 2014). The mid-infrared region includes several trace gas absorption lines, e.g. CO₂, CH₄ and N₂O which are covered by AERI. These lines can be used to provide information about the atmospheric content of these trace gases if the sensitivity of the AERI radiances to their typical atmospheric change is higher than the noise of the AERI measurements. This possibility has been tested for the 15 μm CO₂ line. It is shown that the typical AERI noise is generally close

to the sensitivity of the AERI radiances to the diurnal change of the CO₂ concentration near the surface. However, applying different methods such as averaging the observed radiances with time and/or reducing the uncorrelated random error using a Principal Component Analysis (PCA) (e.g. *Antonelli et al., 2004; Turner et al., 2006*) can increase the signal-to-noise ratio on appropriate time scale. Therefore, the potential of AERI radiances for retrieving the atmospheric CO₂ is examined in this study. The CO₂ spectral bands used in this study are 624-660 cm⁻¹ and 674-723 cm⁻¹.

The algorithm used in this work called AERIOe (*Turner and Löhnert, 2014*). The AERIOe is a variational retrieval algorithm based on the optimal estimation method which gives the opportunity to calculate the uncertainty in the retrieved result simultaneously. The algorithm shows good ability to retrieve the temperature, humidity and cloud properties according to the previous studies (e.g. *Turner and Löhnert, 2014*). In this work, it is modified in order to retrieve a simplified model of the CO₂ profile. Prior to application of real measurements in the AERIOe, the AERI simulated radiances are used to test the algorithm and evaluate its results. Using the simulated radiances gives the opportunity to work with the radiances without problems of the real measurements. It also gives the opportunity to easily compare the retrieved result with 'truth' which makes the analysis and the evaluation of the retrieved results much simpler. The AERI radiances are simulated using a line-by-line radiative transfer model (LBLRTM). The input profiles of the LBLRTM are provided by the numerical model called REMO which predicts the atmospheric CO₂ profiles as well as temperature and humidity profiles. Furthermore, in order to provide the simulated radiances close to the real measurements, the real noise of the AERI is also added to the simulated radiances.

In the first application of the AERIOe, the atmospheric CO₂ profile is considered as a profile with a constant atmospheric mixing ratio. The primary results using the simulated radiances with the original noise of the AERI show an overestimation higher than 1 ppm compared to the true values, while the uncertainty of the retrieved values is 0.5 ppm. However, the next run with the reduced noise applied to the simulated radiances shows significant improvement in the results where 15 of 22 retrieved values captured the true values within their uncertainty. The rest of retrieved values show a difference of less than 1 ppm compared to the true values.

Although, retrieving a constant CO₂ profile with the AERI shows promising results, CO₂ profile retrieval remains challenging. Due to the low number of degrees of freedom for signal (DFS) in the AERI radiances for CO₂ profiling, the CO₂ profile is parametrized using an exponential function. The exponential function defines the CO₂ profile using 3 parameters while one of them shows the background CO₂ (CO₂ concentration in the levels above boundary layer), one describes the CO₂ variations at the surface and one determines the main curvature of the CO₂ profile. The latter can also be used to derive the height where the CO₂ deviates from its background concentration. These three parameters provide the main information about a CO₂ profile. In addition, since the CO₂ background concentration can be considered with good approximation as a constant value for the diurnal cycle (its variation is typically less than 0.5 ppm for the diurnal cycle), the algorithm needs only to retrieve two parameters to estimate the CO₂ profile. The REMO CO₂ profiles are then approximated by the exponential function to represent the true CO₂ profiles. In addition, the fitted profiles provide a dataset for each of the three parameters which are used as prior data of these parameters in the algorithm. The fitted profiles for more than 1400 profiles (in November) show that the root mean square (RMS) values between true and fitted profiles are less than 4 ppm, while due to the more smooth shape of the CO₂ profiles in the upper levels (above 2 km), the fitted profiles show a better fit behavior at these levels.

The AERIOe is applied using this new modification for retrieving the CO₂ parameters in clear sky conditions, while the temperature and the humidity profiles are considered as known in the algorithm. This ensures that the algorithm uses all measurement information for retrieving only the CO₂ parameters, yielding a maximum possible accuracy. The algorithm is first tested for sample cases with rather different CO₂ profile shapes. It is shown that the algorithm can retrieve the CO₂ profile with high accuracy when the true CO₂ profile has a smooth exponential shape. When the true profiles are less smooth, the algorithm can still provide the main curvature of the true profiles. The diurnal analysis of the AERIOe shows that the estimated CO₂ profiles can capture the main increase and decrease of the CO₂ concentration in the boundary layer. Applying AERIOe to one month of REMO profiles and comparing the retrieved CO₂ concentrations in different levels with the true concentrations gives RMS values of 6.8, 5.4, 4.0 and 1.9 ppm between true and retrieved CO₂ concentrations at the surface, 90 m, 200 m and 1 km respectively. As expected, due to the more smooth shape of the CO₂ profile in the upper levels, the RMS values decrease with increasing the height. However, even for the levels close to the surface, the RMS values are still acceptable compared to the high variation of the CO₂ concentration which can be larger than 20 ppm near the surface. In addition, RMS values between retrieved and true profiles are reduced by about 50% compared to the mean RMS values between prior and true profiles.

Furthermore, the AERIOe is used to retrieve the temperature, humidity and CO₂ profiles simultaneously. Although, the results for the retrieved temperature and humidity profiles show good agreement with the true ones, the retrieved CO₂ profiles have poor accuracy. In order to improve the results, some modification are considered. For example, it is confirmed that providing additional information about the CO₂ surface value (or any level close to the surface), can significantly improve the CO₂ retrieved profiles in the boundary layer. In this case the diurnal increase and decrease of the CO₂ concentration in the boundary layer which is not captured in the original runs, can be determined. In addition, the noise filtering method using the PCA is used in this step. For this, the AERI radiances are simulated for two days with rather low and high integrated water vapor (IWV) and with high temporal resolution. The temporal resolution of the simulated radiances is considered similar to the temporal resolution of the real AERI measurements. The original AERI noise is added to the simulated radiances. Then, the PCA method is applied to these radiances. The noise-filtered radiances are then used in the AERIOe for hourly retrieval of the CO₂ profile, meaning that in this step, both the PCA and the averaged radiances are used to reduce the AERI noise. Besides, additional information about the temperature and humidity profiles above 4 km using the true temperatures and humidity profiles is also provided to the algorithm. It is shown that the retrieved CO₂ surface values capture the nighttime increase and the daytime decrease; however, the retrieved results show between 3 to 10 ppm difference with the true values. Furthermore, the maximum retrieved CO₂ surface concentration indicates less than 3 ppm difference to the true maximum value for the dry day, while, during the humid day a difference on the order of 10 ppm can be seen between true and retrieved maximum CO₂ surface concentration.

Moreover, the AERIOe is applied to the real AERI measurements at JOYCE. Two clear sky days are selected (25 and 26 May 2012), and the AERIOe is run on these days. These days are selected from the AERI measurements on clear sky days in 2012, where the in-situ tower measurements of CO₂ at 100 m in Jülich are available. The real AERI measurements are first corrected with a calculated radiometric calibration factor. In addition, it is shown that due to an unknown issue in the AERI measurements which may relate to small oscillations in the AERI detector temperature, the algorithm can not converge in the last iterations.

Consequently, the approach for selecting the optimal estimation solution in the AERIOe is slightly changed to overcome this problem. This change in the AERIOe causes that the calculated DFS and the estimated uncertainty of the solution to become smaller and larger than the true ones, respectively. It is also shown that due to the spectroscopy problem in the spectral bands from 722 to 723 cm^{-1} , which causes up to 3 RU difference between simulated and real AERI radiances, this band is not used in a first attempt to retrieve the CO_2 profile. Retrieved temperature and humidity profiles of the first run show good agreement with the model data and other JOYCE observation. However, the retrieved CO_2 surface values show large offset as well as different temporal variations compared to the tower measurements. In a next attempt, additional information about the temperature and humidity profiles above 4 km using the model data is provided to the algorithm. The results of the second approach also do not show any considerable agreement in terms of temporal variations and absolute CO_2 values with the tower measurements. Due to the lack of the reliable temperature and humidity profiles below 4 km, AERIOe could not be further constrained. Instead, the spectral band between 722 and 723 cm^{-1} which is removed in the first step is added again. This new spectral band in the AERIOe causes a large overestimation in the order of 4 to 10 $^\circ\text{C}$ in about 70% of the retrieved temperature profiles for the levels above 2 km compared to the retrieved temperature profiles of the previous runs. This overestimation is most probably due to the spectroscopy problem of the new added spectral band; however, it has almost no effect on the retrieved humidity profiles. The retrieved CO_2 surface values of this run show good qualitative agreement with the tower measurements in terms of the temporal variation. The retrieved values on both days show about 5 to 10 ppm difference with the tower measurements where the uncertainties of the retrieved values are between 4 to 7 ppm. Besides, the maximum CO_2 surface value that is captured by the AERIOe on both days occurs 1 to 2 hours earlier compared to the maximum CO_2 surface concentration of tower measurements.

In order to obtain the information about the height where the CO_2 concentration deviates from its background concentration, an extra run for each day is performed while in this run additional information about the CO_2 surface value is provided to the algorithm using the tower measurements. The mentioned height is then calculated using the retrieved parameters of the algorithm. The calculated height particularly for the second day shows an acceptable diurnal variation according to the expected diurnal variation of the boundary layer on a sunny clear sky day. However, due to the lack of the CO_2 measurements in the boundary layer at JOYCE, the absolute value of the calculated height can not be evaluated.

Outlook

As shown, due to the lack of the in-situ tower measurements in 2012, real AERI measurements were tested for only two clear sky days. However, since 2013, CO_2 has been measured continuously and with higher accuracy using in-situ tower measurements in Jülich. This data can be used to evaluate the AERI results for more cases, particularly more clear sky days between 2015 and 2017 where the AERI measurements are also available continuously. In addition, the tower measurements are available for more than one level, since 2014 which can be used to evaluate the AERI retrieved CO_2 concentration in several levels. The results of using noise-filtered AERI simulated radiances with high temporal resolution (chapter 6) revealed that the AERI radiances show different potential for dry and humid days. However, due to the lack of the tower measurements in 2012, the potential of the AERI using the real measurements in different weather conditions, particularly for the days with different water vapor amounts were not tested. The available data of the AERI and tower measurements

from 2015 to 2017 can provide the opportunity to analyze the potential of AERI radiances for different weather conditions with different humidity amounts.

The problem in the real AERI measurements which was indicated in chapter 7 needs to be investigated using more data from different atmospheric conditions. As mentioned, this issue causes problems in the convergence of the AERIOe which also effects the accuracy of the retrieved results. Solving this problem may help the AERIOe to retrieve the result with higher accuracy.

During the recent years, there have been attempts to predict the CO₂ flux near the surface at Jülich using numerical models. Since the in-situ tower measurements provide only the CO₂ concentration near the surface, the model data can be a possibility to evaluate the retrieved CO₂ concentration by the AERIOe at upper levels (0.5 to 1 km). In addition, as shown in chapter 7, the AERIOe results provide an estimation for the height where the CO₂ deviates from its background estimation; however due to the lack of the CO₂ measurements at upper levels, the absolute value of the derived heights have not been evaluated. The model data at Jülich can also give an estimation for this height which can be used to evaluate the derived heights using the AERIOe results.

In chapter 6, it is shown that the simulated AERI radiances can yield the constant CO₂ mixing ratio in clear sky conditions with quite good accuracy. However, this possibility is not applied to the real measurements. The constant mixing ratio can be used to calculate the mean column amount of the CO₂ concentration. This value has been already retrieved by different satellites and ground based instruments mainly as a monthly mean value for clear sky cases. The retrieved value by the AERI can be an additional source for providing this parameter and can be used to compare with other available measurements.

Moreover, the AERI measurements cover two main CO₂ absorption bands, 15 and 4.3 μm . In addition, there are some weaker CO₂ lines at 9.4 and 10.4 μm in the AERI spectra. These lines can also be used in the AERIOe to improve the CO₂ retrievals. Applying the two weak lines in the AERIOe can be simpler compared to the CO₂ line at 4.3 μm because the 4.3 μm line is close to the near-infrared region, meaning that using this line may need more efforts due to scattering of solar radiation into the AERI field of view by clouds and aerosols. However, it would be a good test to see the effect of adding the 4.3 μm band in the algorithm using nighttime data, when the scattering of solar radiation can be ignored.

Bibliography

- Adler, R. F., G. J. Huffman, A. Chang, R. Ferraro, P. Xie, J. Janowiak, B. Rudolf, U. Schneider, D. Curtis, S. and Bolvin, and A. Gruber, The version-2 global precipitation climatology project (GPCP) monthly precipitation analysis (1979–present), *Journal of hydrometeorology*, 4(6), 1147–1167, 2003.
- Alvarado, M. J., V. H. Payne, E. J. Mlawer, G. Uymin, M. W. Shephard, C.-P. K. E., J. S. Delamere, and M. J. L., Performance of the Line-by-Line Radiative Transfer Model (LBLRTM) for temperature, water vapor, and trace gas retrievals: recent updates evaluated with IASI case studies, *Atmospheric Chemistry and Physics*, 13, 6687–6711, 2013.
- Annan, J. D. and J. C. Hargreaves, Using multiple observationally-based constraints to estimate climate sensitivity, *Geophysical Research Letters*, 33(6), 2006.
- Antonelli, P., H. E. Revercomb, L. A. Sromovsky, W. L. Smith, R. O. Knuteson, D. C. Tobin, R. K. Garcia, H. B. Howell, H. L. Huang, and F. A. Best, A principal component noise filter for high spectral resolution infrared measurements, *Journal of Geophysical Research: Atmospheres*, 109(D23), 2004.
- Archer, D. E., H. Kheshgi, and E. Maier-Reimer, Multiple timescales for neutralization of fossil fuel CO₂, *Geophysical Research Letters*, 24, 405–408, 1997.
- Baldauf, M., A. Seifert, F. J., D. Majewski, and M. Raschendorfer, Operational Convective-Scale Numerical Weather Prediction with the COSMO Model: Description and Sensitivities, *Monthly Weather Review*, 139, 3887–3905, 2011.
- Barkley, M. P., P. S. Monks, A. J. Hewitt, T. Machida, A. Desai, N. Vinnichenko, T. Nakazawa, M. Yu Arshinov, N. Fedoseev, and T. Watai, Assessing the near surface sensitivity of SCIAMACHY atmospheric CO₂ retrieved using (FSI) WFM-DOAS, *Atmospheric Chemistry and Physics*, 7(13), 3597–3619, 2007.
- Barnola, J. M., D. Y. S. N. Raynaud, Y. S. Korotkevich, and C. Lorius, Vostok ice core provides 160,000-year record of atmospheric CO₂, *Nature*, 329(6138), 408–414, 1987.
- Bevis, M., S. Businger, T. A. Herring, C. Rocken, R. A. Anthes, and R. H. Ware, GPS meteorology: Remote sensing of atmospheric water vapor using the global positioning system, *Journal of Geophysical Research: Atmospheres*, 97(D14), 15787–15801, 1992.
- Bovensmann, H., J. P. Burrows, M. Buchwitz, J. Frerick, S. Noel, V. Rozanov, K. Chance, and A. Goede, SCIAMACHY–Mission Objectives and Measurement Modes, *Journal of the Atmospheric Sciences*, 56, 127–150, 1999.

- Buchwitz, M. D., R. D. Beek, J. P. Burrows, H. Bovensmann, T. Warneke, J. Notholt, J. F. Meirink, A. P. H. Goede, P. Bergamaschi, S. Körner, and M. Heimann, Atmospheric methane and carbon dioxide from SCIAMACHY satellite data: initial comparison with chemistry and transport models, *Atmospheric Chemistry and Physics*, 5(4), 941–962, 2005.
- Burrows, J. P., E. Hölzle, A. P. H. Goede, H. Visser, and W. Fricke, SCIAMACHY—Scanning imaging absorption spectrometer for atmospheric chartography, *Acta Astronautica*, 35(7), 445–451, 1995.
- Carissimo, A., I. De Feis, and C. Serio, The physical retrieval methodology for IASI: the δ -IASI code, *Environmental Modeling & Software*, 20(9), 1111–1126, 2005.
- Charney, J. G., A. Arakawa, D. J. Baker, B. Bolin, R. E. Dickinson, R. M. Goody, C. E. Leith, H. M. Stommel, and C. I. Wunsch, *Carbon Dioxide and Climate: A Scientific Assessment*, National Academy of Sciences, Washington, DC, 1979.
- Chédin, A., A. Hollingsworth, N. Scott, S. Serrar, C. Crevoisier, and R. Armante, Annual and seasonal variations of atmospheric CO₂, N₂O and CO concentrations retrieved from NOAA/TOVS satellite observations, *Geophysical Research Letters*, 29(8), 2002.
- Chédin, A., S. Serrar, N. A. Scott, C. Crevoisier, and R. Armante, First global measurement of midtropospheric CO₂ from NOAA polar satellites: Tropical zone, *Journal of Geophysical Research: Atmospheres*, 108(D18), 2003.
- Chevallier, F., R. J. Engelen, and P. Peylin, The contribution of AIRS data to the estimation of CO₂ sources and sinks, *Geophysical Research Letters*, 32(23), 2005.
- Chevillard, A., U. Karstens, P. Ciais, S. Lafont, and M. Heimann, Simulation of atmospheric CO₂ over Europe and western Siberia using the regional scale model REMO, *Tellus*, 54B, 872–894, 2002.
- Ciais, P., A. S. Denning, P. P. Tans, J. A. Berry, D. A. Randall, G. J. Collatz, P. Sellers, J. W. White, M. Trolier, H. A. Meijer, and R. J. Francey, A three-dimensional synthesis study of $\delta^{18}\text{O}$ in atmospheric CO₂: 1. Surface fluxes, *Journal of Geophysical Research: Atmospheres*, 102(D5), 5857–5872, 1997.
- Ciattaglia, L., P. Chamard, T. Colombo, and R. Santaguida, *Italian Greenhouse Gas Programs in the Mediterranean Region and in Antarctica*, In Proceedings of the WMO Expert Meeting on Carbon Dioxide Concentration and Isotopic Measurement Technique, 1997.
- Clerbaux, C., A. Boynard, L. Clarisse, M. George, J. Hadji-Lazaro, H. Herbin, D. Hurtmans, M. Pommier, A. Razavi, S. Turquety, and C. Wespes, Monitoring of atmospheric composition using the thermal infrared IASI/MetOp sounder, *Atmospheric Chemistry and Physics*, 9(16), 6041–6054, 2009.
- Clough, S. A., M. J. Iacono, and J. L. Moncet, LBLRTM: Line-By-Line Radiative Transfer Model, *Astrophysics Source Code Library*, 2014.
- Clough, S. A. and I. M. J., Line-by-line calculation of atmospheric fluxes and cooling rates: application to carbon dioxide, ozone, methane, nitrous oxide and the halocarbon, *Journal of Geophysical Research*, 100, 16519–16535, 1995.
- Clough, S. A., I. M. J., and M. J-L., Line-by-line calculation of atmospheric fluxes and cooling rates: application to water vapor, *Journal of Geophysical Research*, 97, 15761–15785, 1992.

- Clough, S. A., F. X. Kneizys, and R. W. Davies, Line shape and the water vapor continuum, *Atmospheric Research*, 23(3-4), 229–241, 1989.
- Clough, S. A., F. X. Kneizys, L. S. Rothman, and W. O. Gallery, Atmospheric spectral transmittance and radiance: FASTCODE1B, *International Society for Optics and Photonics*, 277, 152–166, 1981.
- Clough, S. A., M. W. Shephard, E. J. Mlawer, J. S. Delamere, M. J. Iacono, K. Cady-Pereira, S. Boukabara, and P. D. Brown, Atmospheric radiative transfer modeling: a summary of the AER codes, *Journal of Quantitative Spectroscopy and Radiative Transfer*, 91(2), 233–244, 2005.
- Collard, A. D., S. A. Ackerman, W. L. Smith, H. E. Ma, H. E. Revercomb, R. O. Knuteson, and S. C. Lee, Cirrus cloud properties derived from high spectral resolution infrared spectrometry during FIRE II. part III: Ground-based HIS results, *Journal of the Atmospheric Sciences*, 52, 4264–4275, 1995.
- Comstock, J. M., S. A. McFarlane, R. d’Entremont, D. DeSlover, D. D. Turner, G. G. Mace, S. Y. Matrosov, M. D. Shupe, P. Minnis, D. Mitchell, and K. Sassen, An intercomparison of microphysical retrieval algorithms for upper-tropospheric ice clouds, *Bulletin of the American Meteorological Society*, 88(2), 191–204, 2007.
- Conner, M. D. and G. W. Petty, Validation and intercomparison of SSM/I rain-rate retrieval methods over the continental United States, *Journal of Applied Meteorology*, 37(7), 679–700, 1998.
- Conrath, B. J., R. A. Hanel, V. G. Kunde, and C. Prabhakara, The infrared interferometer experiment on Nimbus 3, *Journal of Geophysical Research*, 75(30), 5831–5857, 1970.
- Crevoisier, C., S. Heilliette, A. Chédin, S. Serrar, R. Armante, and N. A. Scott, Midtropospheric CO₂ concentration retrieval from AIRS observations in the tropics, *Geophysical Research Letters*, 31(17), 2004.
- Crewell, S., H. Czekala, U. Löhnert, T. Rose, C. Simmer, and R. Zimmermann, Microwave radiometer for cloud cartography: A 22-channel ground-based microwave radiometer for atmospheric research, *Radio Science*, 36, 621–638, 2001.
- Crewell, S. and U. Löhnert, Accuracy of boundary layer temperature profiles retrieved with multifrequency multiangle microwave radiometry, *IEEE Transactions on Geoscience and Remote Sensing*, 45(7), 2195–2201, 2007.
- Crisp, D., H. R. Pollock, R. Rosenberg, L. Chapsky, R. A. M. Lee, F. A. Oyafuso, C. Frankenberg, C. O’Dell, C. J. Bruegge, G. B. Doran, A. Eldering, B. M. Fisher, D. Fu, M. R. Gunson, L. Mandrake, G. B. Osterman, F. M. Schwandner, K. Sun, T. E. Taylor, P. O. Wennberg, and D. Wunch, The on-orbit performance of the Orbiting Carbon Observatory-2 (OCO-2) instrument and its radiometrically calibrated products, *Atmospheric Measurement Techniques*, 10(1), 59–81, 2017.
- Delamere, J. S., S. A. Clough, V. H. Payne, E. J. Mlawer, D. D. Turner, and R. R. Gamache, A far-infrared radiative closure study in the Arctic: Application to water vapor, *Journal of Geophysical Research: Atmospheres*, 115(D17), 2010.
- Delmas, R. J., J. M. Ascencio, and M. Legrand, Polar ice evidence that atmospheric CO₂ 20,000 yr BP was 50% of present, *Nature*, 284(5752), 155–157, 1980.

- DeSlover, D. H., S. W. L., P. P. K., and E. E. W., A methodology for measuring cirrus cloud visible-to-infrared spectral optical depth ratios, *Journal of Atmospheric and Oceanic Technology*, 16, 251–262, 1999.
- DOE, *Atmospheric Radiation Measurement Program plan. DOE/ER-0442 and DOE/ER-0441*, U.S. Department of Energy, Washington, DC, 1990, 135 pp.
- Eldering, A., C. O'Dell, P. O. Wennberg, D. Crisp, M. R. Gunson, C. Viatte, C. Avis, A. Braverman, R. Castano, A. Chang, and L. Chapsky, The orbiting carbon observatory-2: first 18 months of science data products, *Atmospheric Measurement Techniques*, 10(2), 549–560, 2017.
- Ellingson, R. E. and Y. Fouquart, The intercomparison of radiation codes in climate model: An overview, *Journal of Geophysical Research*, 96, 8925–8927, 1991.
- Enting, I. G., T. M. L. Wigley, and M. Heimann, *Future Emissions and Concentrations of Carbon Dioxide: key ocean/atmosphere/land analyses*, Technical Paper 31, Division of Atmospheric Research, CSIRO, Melbourne, 1994.
- Feldman, D. R., W. D. Collins, P. Gero, M. S. Torn, E. J. Mlawer, and T. R. Shippert, Observational determination of surface radiative forcing by CO₂ from 2000 to 2010, *Nature*, 519(7543), 339–343, 2015.
- Feltz, W. F., W. L. Smith, H. B. Howell, R. O. Knuteson, H. Woolf, and H. E. Revercomb, Near-continuous profiling of temperature, moisture, and atmospheric stability using the Atmospheric Emitted Radiance Interferometer (AERI), *Journal of Applied Meteorology*, 42(5), 584–597, 2003.
- Feltz, W. F., W. L. Smith, R. O. Knuteson, H. E. Revercomb, H. M. Woolf, and H. B. Howell, Meteorological applications of temperature and water vapor retrievals from the ground-based Atmospheric Emitted Radiance Interferometer (AERI), *Journal of Applied Meteorology*, 37, 857–875, 1998.
- Gaudry, A., J. M. Ascencio, and G. Lambert, Preliminary study of CO₂ variations at Amsterdam Island (Territoire des Terres Australes et Antarctiques Francaises), *Journal of Geophysical Research: Oceans*, 88(C2), 1323–1329, 1983.
- Gaudry, A., P. Monfray, G. Polian, G. Bonsang, B. Ardouin, A. Jegou, and G. Lambert, Non-seasonal variations of atmospheric CO₂ concentrations at Amsterdam Island, *Tellus B*, 43(2), 136–143, 1991.
- Gendt, G., G. Dick, C. Reigber, M. Tomassini, Y. Liu, and M. Ramatschi, Near Real Time GPS Water Vapor Monitoring for Numerical Weather Prediction in Germany, *Journal of the Meteorological Society of Japan*, 82(1B):361–370, 361–370, 2004.
- Han, Y., J. A. Shaw, J. H. Churnside, P. D. Brown, and S. A. Clough, Infrared spectral radiance measurements in the tropical Pacific atmosphere, *Journal of Geophysical Research: Atmospheres*, 102(D4), 4353–4356, 1997.
- Han, Y. and E. R. Westwater, Analysis and improvement of tipping calibration for ground-based microwave radiometers, *IEEE Transactions on Geoscience and Remote Sensing*, 38(3), 1260–1276, 2000.

-
- Hanel, R. A., B. J. Conrath, V. G. Kunde, C. Prabhakara, I. Revah, V. V. Salomonson, and G. Wolford, The Nimbus 4 infrared spectroscopy experiment: 1. Calibrated thermal emission spectra, *Journal of Geophysical Research*, 77(15), 2629–2641, 1972.
- Hansen, P. C., Analysis of discrete ill-posed problems by means of the L-curve, *SIAM review*, 34(4), 561–580, 1992.
- Haszpra, L., Carbon dioxide concentration measurements at a rural site in Hungary, *Tellus B*, 47, 17–22, 1995.
- Hegerl, G. C., T. J. Crowley, W. T. Hyde, and D. J. Frame, Climate sensitivity constrained by temperature reconstructions over the past seven centuries, *Nature*, 440(7087), 1029–1032, 2006.
- Heimann, M., The global tracer model TM2, Technical report, Deutsches Klima Rechenzentrum, Hamburg, No.10, 47 pp, 1995.
- Hönisch, B., N. G. Hemming, D. Archer, M. Siddall, and J. F. McManus, Atmospheric carbon dioxide concentration across the mid-Pleistocene transition, *Science*, 324(5934), 1551–1554, 2009.
- Houghton, J., Global warming, *Reports on Progress in Physics*, 68(6), 1343–1403, 2005.
- Huang, H. L. and P. Antonelli, Application of principal component analysis to high-resolution infrared measurement compression and retrieval, *Journal of Applied Meteorology*, 40(3), 365–388, 2001.
- IPCC, *Climate Change: The Scientific Assessment, Report prepared for Intergovernmental Panel on Climate Change by Working Group I*, Cambridge University Press, Cambridge, Great Britain, New York, NY, USA and Melbourne, Australia, 1990.
- IPCC, *Climate Change: The Scientific Basis, Contribution of working group I to the Third Assessment Report of the Intergovernmental Panel on Climate Change*, Cambridge University Press, Cambridge, United Kingdom and New York, NY, USA, 2001.
- IPCC, *Climate Change: The Physical Science Basis, Contribution of Working Group I to the Fifth Assessment Report of the Intergovernmental Panel on Climate Change*, Cambridge University Press, Cambridge, United Kingdom and New York, NY, USA, 2013.
- Karion, A., C. Sweeney, P. Tans, and T. Newberger, AirCore: An innovative atmospheric sampling system, *Journal of Atmospheric and Oceanic Technology*, 27(11), 1839–1853, 2010.
- Keeling, C. D., R. B. Bacastow, A. E. Bainbridge, C. A. Ekdahl Jr, P. R. Guenther, L. S. Waterman, and J. F. Chin, Atmospheric carbon dioxide variations at Mauna Loa observatory, Hawaii, *Tellus*, 28(6), 538–551, 1976.
- Knuteson, R. O., H. B. Revercomb, F. Best, N. Ciganovich, R. Dedecker, T. Dirks, S. Ellington, W. Feltz, R. Garcia, H. Howell, W. Smith, J. Short, and D. Tobin, Atmospheric Emitted Radiance Interferometer. Part I: Instrument Design, *Journal of Atmospheric and Oceanic Technology*, 21, 1763–1776, 2004a.

- Knuteson, R. O., H. B. Revercomb, F. A. Best, N. C. Ciganovich, R. G. Dedecker, T. P. Dirkx, S. C. Ellington, W. F. Feltz, R. K. Garcia, H. B. Howell, W. L. Smith, J. F. Short, and D. C. Tobin, Atmospheric Emitted Radiance Interferometer. Part II: Instrument Performance, *Journal of Atmospheric and Oceanic Technology*, 21, 1777–1789, 2004b.
- Knutti, R., G. A. Meehl, M. R. Allen, and D. A. Stainforth, Constraining climate sensitivity from the seasonal cycle in surface temperature, *Journal of Climate*, 19(17), 4224–4233, 2006.
- Küchler, N., D. D. Turner, U. Löhnert, and S. Crewell, Calibrating ground-based microwave radiometers: Uncertainty and drifts, *Radio Science*, 51(4), 311–327, 2016.
- Kuze, A., H. Suto, M. Nakajima, and T. Hamazaki, Thermal and near infrared sensor for carbon observation fourier-transform spectrometer on the greenhouse gases observing satellite for greenhouse gases monitoring, *Applied Optics*, 48, 6716–6733, 2009.
- Lafont, S., L. Kergoat, G. Dedieu, A. Chevillard, E. Kjellström, U. Karstens, and O. Kolle, Spatial and temporal variability of land CO₂ fluxes estimated with remote sensing and analysis data over western Eurasia, *Tellus B*, 54(5), 820–833, 2002.
- Lambert, G., P. Monfray, B. Ardouin, G. Bonsang, A. Gaudry, V. Kazan, and G. Polian, Year-to-year changes in atmospheric CO₂, *Tellus B*, 47, 53–55, 1995.
- Lamouroux, J., H. Tran, A. L. Laraia, R. R. Gamache, L. S. Rothman, I. E. Gordon, and J.-M. Hartmann, Updated database plus software for line-mixing in CO₂ infrared spectra and their test using laboratory spectra in the 1.5–2.3 μm region, *Journal of Quantitative Spectroscopy and Radiative Transfer*, 111, 2321, 2010.
- Langmann, B., Numerical modelling of regional scale transport and photochemistry directly together with meteorological processes, *Atmospheric Environment*, 34, 3585–3598, 2000.
- Liou, K. N., *An Introduction to Atmospheric Radiation, International Geographical Series, Second Edition*, Academic Press, 2002, 583 pp.
- Lloyd, J. and G. D. Farquhar, The CO₂ dependence of photosynthesis, plant growth responses to elevated atmospheric CO₂ concentrations and their interaction with soil nutrient status. I. General principles and forest ecosystems, *Functional Ecology*, pages 4–32, 1996.
- Löhnert, U., J. H. Schween, C. Acquistapace, K. Ebell, M. Maahn, M. Barrera-Verdejo, A. Hirsikko, B. Bohn, A. Knaps, E. O’connor, and C. Simmer, JOYCE: Jülich observatory for cloud evolution, *Bulletin of the American Meteorological Society*, 96(7), 1157–1174, 2015.
- Löhnert, U., D. D. Turner, and S. Crewell, Ground-based temperature and humidity profiling using spectral infrared and microwave observations. Part I: Simulated retrieval performance in clear sky conditions, *Journal of Applied Meteorology*, 48, 1017–1032, 2009.
- Lorius, C., J. Jouzel, D. Raynaud, J. Hansen, and H. Le Treut, The ice-core record: climate sensitivity and future greenhouse warming, *Nature*, 347, 139–145, 1990.
- Lubin, D., Infrared radiative properties of the maritime Antarctic atmosphere, *Journal of Climate*, 7(1), 121–140, 1994.

- Lüthi, D., M. Le Floch, B. Bereiter, T. Blunier, J. M. Barnola, U. Siegenthaler, D. Raynaud, J. Jouzel, H. Fischer, K. Kawamura, and T. F. Stocker, High-resolution carbon dioxide concentration record 650,000–800,000 years before present, *Nature*, 453(7193), 379–382, 2008.
- Mace, G. G., T. P. Ackerman, M. P., and Y. D. F., Cirrus layer microphysical properties derived from surface-based millimeter radar and infrared interferometer data, *Journal of Geophysical Research*, 103, 23207–23216, 1998.
- Maier-Reimer, E. and K. Hasselmann, Transport and storage of CO₂ in the ocean - An inorganic ocean-circulation carbon cycle model, *Climate Dynamics*, 2, 63–90, 1987.
- Maier-Reimer, E., U. Mikolajewicz, and A. Winguth, Future ocean uptake of CO₂: interaction between ocean circulation and biology, *Climate Dynamics*, 12(10), 711–722, 1996.
- Majewski, D., D. Liermann, P. Prohl, B. Ritter, M. Buchhold, T. Hanisch, G. Paul, W. Wergen, and J. Baumgardner, The operational global icosahedral-hexagonal gridpoint model GME: Description and high-resolution tests, *Monthly Weather Review*, 130, 319–338, 2002.
- Malinowski, E. R., Theory of error in factor analysis, *Analytical Chemistry*, 49(4), 606–612, 1977.
- Manabe, S. and R. T. Wetherald, Thermal equilibrium of the atmosphere with a given distribution of relative humidity, *Journal of the Atmospheric Sciences*, 24(3), 241–259, 1967.
- Manabe, S. and R. T. Wetherald, The effects of doubling the CO₂ concentration on the climate of a general circulation model, *Journal of the Atmospheric Sciences*, 32, 3–15, 1975.
- Manning, M. R. and K. P. Pohl, *Atmospheric CO₂ monitoring in New Zealand 1971-1985*, DSIR Institute of Nuclear Sciences, Report No. INS-R-350, 1986.
- Martínez-Botí, M., G. L. Foster, T. B. Chalk, E. J. Rohling, P. F. Sexton, D. J. Lunt, R. D. Pancost, M. P. S. Badger, and D. N. Schmidt, Plio-Pleistocene climate sensitivity evaluated using high-resolution CO₂ records, *Nature*, 518(7537), 49–54, 2015.
- Maschwitz, G., U. Löhnert, S. Crewell, T. Rose, and D. D. Turner, Investigation of ground-based microwave radiometer calibration techniques at 530 hPa, *Atmospheric Measurement Techniques*, 6(10), 2641–2658, 2013.
- Masiello, G., C. Serio, and P. Antonelli, Inversion for atmospheric thermodynamical parameters of IASI data in the principal components space, *Quarterly Journal of the Royal Meteorological Society*, 138(662), 103–117, 2012.
- Messerschmidt, J., M. C. Geibel, T. Blumenstock, H. Chen, N. M. Deutscher, A. Engel, D. G. Feist, C. Gerbig, M. Gisi, F. Hase, and K. Katrynski, Calibration of TCCON column-averaged CO₂: the first aircraft campaign over European TCCON sites, *Atmospheric Chemistry and Physics*, 11(21), 10765–10777, 2011.
- Mitchell, J. F., The “greenhouse” effect and climate change, *Reviews of Geophysics*, 27(1), 115–139, 1989.
- Mlawer, E. J., V. H. Payne, J. L. Moncet, J. S. Delamere, M. J. Alvarado, and D. C. Tobin, Development and recent evaluation of the MT_CKD model of continuum absorption, *Phil. Trans. R. Soc.*, 370(1968), 2520–2556, 2012.

- Mlawer, E. J. and D. D. Turner, Spectral radiation measurements and analysis in the arm program, *Meteorological Monographs*, 57, 14.1–14.17, 2016.
- Morino, I., O. Uchino, M. Inoue, Y. Yoshida, T. Yokota, P. O. Wennberg, G. C. Toon, D. Wunch, C. M. Roehl, J. Notholt, T. Warneke, J. Messerschmidt, D. W. T. Griffith, N. M. Deutscher, V. Sherlock, B. Connor, J. Robinson, R. Sussmann, and M. Rettinger, Preliminary validation of column-averaged volume mixing ratios of carbon dioxide and methane retrieved from GOSAT short-wavelength infrared spectra, *Atmospheric Measurement Techniques*, 4(6), 1061–1076, 2011.
- Mudge, F. B., The development of the 'greenhouse' theory of global climate change from Victorian times, *Weather*, 52, 13–17, 1997.
- Nakajima, T. and M. D. King, Determination of the optical thickness and effective particle radius of clouds from reflected solar radiation measurements. Part I: Theory, *Journal of the Atmospheric Sciences*, 47(15), 1878–1893, 1990.
- Neftel, A., H. Oeschger, J. Schwander, B. Stauffer, and R. Zumbunn, Ice core sample measurements give atmospheric CO₂ content during the past 40,000 yr, *Nature*, 295, 220–223, 1982.
- Ning, T. and G. Elgered, Trends in the Atmospheric Water Vapor Content From Ground-Based GPS: The Impact of the Elevation Cutoff Angle., *IEEE Journal of Selected Topics in Applied Earth Observations and Remote Sensing*, 5(3), 744–751, 2012.
- Olivier, J. G. J., A. F. Bouwman, C. W. M. Van der Maas, J. J. M. Berdowski, C. Veldt, J. P. J. Bloos, A. J. H. Visschedijk, P. Y. J. Zandvelt, and J. L. Haverlag, *Description of EDGAR Version 2.0. A set of global emission inventories of greenhouse gases and ozone-depleting substances for all anthropogenic and most natural sources on a per country basis and on 1 × 1 grid*, RIVM/TNO report, December 1996. RIVM, Bilthoven, RIVM report nr. 771060 002, 1996, [TNO MEP report nr. R96/119].
- Petit, J. R., J. Jouzel, D. Raynaud, N. Barkov, J. M. Barnola, I. Basile, M. Bender, J. Chappellaz, M. Davis, G. Delaygue, and M. Delmotte, Climate and atmospheric history of the past 420,000 years from the Vostok ice core, Antarctica, *Nature*, 399(6735), 429–436, 1999.
- Petty, G. W., *A first course in atmospheric radiation, Second Edition*, Sundog Publishing, Madison, Wisconsin, 2006, 458 pp.
- Protat, A., J. Delanoë, D. Bouniol, A. J. Heymsfield, A. Bansemmer, and P. Brown, Evaluation of ice water content retrievals from cloud radar reflectivity and temperature using a large airborne in situ microphysical database, *Journal of applied meteorology and climatology*, 46(5), 557–572, 2007.
- Raven, J. A. and P. G. Falkowski, Oceanic sinks for atmospheric CO₂, *Plant, Cell & Environment*, 22(6), 741–755, 1999.
- Revercomb, H. E., H. Buijs, H. B. Howell, D. D. LaPorte, W. L. Smith, and L. A. Sromovsky, Radiometric calibration of IR Fourier transform spectrometers: solution to a problem with the High-Resolution Interferometer Sounder, *Applied Optics*, 27(15), 3210–3218, 1988.
- Revercomb, H. E., W. L. Smith, R. O. Knuteson, F. A. Best, R. G. Dedecker, T. P. Dirks, R. A. Herbsleb, J. F. Short, H. B. Howell, and D. Murcray, *High Spectral Resolution Fourier*

- Transform Infrared Instruments for the Atmospheric Radiation Measurement Program*, In Proceedings of the Third Atmospheric Radiation Measurement (ARM) Science Team Meeting: March 1-4, 1993, Norman, Oklahoma, (p. 276), 1994.
- Revercomb, H. E., D. D. Turner, D. C. Tobin, R. O. Knuteson, W. F. Feltz, J. Barnard, J. Bösenberg, S. Clough, D. Cook, R. Ferrare, J. Goldsmith, S. Gutman, R. Halthore, B. Lesht, J. Liljegren, H. Linné, J. Michalsky, V. Morris, W. Porch, S. Richardson, B. Schmid, M. Splitt, T. Van Hove, E. Westwater, and D. Whiteman, The ARM program's water vapor intensive periods: Overview, initial accomplishments and future challenges, *Bulletin of the American Meteorological Society*, 84, 217–236, 2003.
- Rodgers, C. D., *Inverse methods for atmospheric sounding: theory and practice*, World Scientific, 2000, 238 pp.
- Rogelj, J., M. Meinshausen, and R. Knutti, Global warming under old and new scenarios using IPCC climate sensitivity range estimates, *Nature climate change*, 2(4), 248–253, 2012.
- Rose, T., S. Crewell, U. Löhnert, and C. Simmer, A network suitable microwave radiometer for operational monitoring of the cloudy atmosphere, *Atmospheric Research*, 75, 183 – 200, 2005.
- Rothman, L. S., R. R. Gamache, R. H. Tipping, C. P. Rinsland, M. A. H. Smith, D. Benner, V. Devi, J. M. Flaud, C. Camy-Peyret, A. Perrin, A. Goldman, S. T. Massie, L. R. Brown, and R. A. Toth, The HITRAN molecular database: Editions of 1991 and 1992, *Journal of Quantitative Spectroscopy and Radiative Transfer*, 48, 469–507, 1992.
- Rothman, L. S., I. E. Gordon, Y. Babikov, A. Barbe, D. Chris Benner, P. F. Bernath, M. Birk, L. Bizzocchi, V. Boudon, L. R. Brown, and A. Campargue, The HITRAN2012 molecular spectroscopic database, *Journal of Quantitative Spectroscopy and Radiative Transfer*, 130, 4–50, 2013.
- Rothman, L. S., I. E. Gordon, A. Barbe, D. C. Benner, P. F. Bernath, M. Birk, V. Boudon, L. R. Brown, A. Campargue, J. P. Champion, and K. Chance, The HITRAN 2008 molecular spectroscopic database, *Journal of Quantitative Spectroscopy and Radiative Transfer*, 110(9-10), 533–572, 2009.
- Ruimy, A., G. Dedieu, and B. Saugier, TURC: a diagnostic model of continental gross primary productivity as net primary productivity, *Global Biogeochemistry*, Cycles 10, 269–285, 1997.
- Saitoh, N., R. Imasu, Y. Ota, and Y. Niwa, CO₂ retrieval algorithm for the thermal infrared spectra of the Greenhouse Gases Observing Satellite: Potential of retrieving CO₂ vertical profile from high-resolution FTS sensor, *Journal of Geophysical Research*, 114(D7), 2009.
- Sarmiento, J. L. and J. R. Toggweiler, A new model for the role of the oceans in determining atmospheric pCO₂, *Nature*, 308, 621–624, 1984.
- Schrade, S., Ground based measurements of Carbon Dioxide and other climatically relevant trace gases using Off-Axis Integrated-Cavity-Output-Spectroscopy (ICOS), Diploma thesis, RWTH Aachen University, Institut für physikalische Chemie, IPC, 2011.

- Schraff, C. and R. Hess, A description of the nonhydrostatic regional cosmo model, part iii: Data assimilation, Technical report, Deutscher Wetterdienst, Offenbach, Germany, 2012, 93 pp.
- Smith, W. L., W. F. Feltz, R. O. Knuteson, H. E. Revercomb, H. M. Woolf, and H. B. Howell, The retrieval of planetary boundary layer structure using ground-based infrared spectral radiance measurements, *Journal of Atmospheric and Oceanic Technology*, 16(3), 323–333, 1999.
- Smith, W. L., H. B. Howell, H. M. Woolf, and H. E. Revercomb, HIS-A satellite instrument to observe temperature and moisture profiles with high vertical resolution, *In 5th Conference on Atmospheric Radiation*, American Meteorological Society, Boston, 1983.
- Smith, W. L., X. L. Ma, S. A. Ackerman, H. E. Revercomb, and R. O. Knuteson, Remote sensing cloud properties from high spectral resolution infrared observations, *Journal of the Atmospheric Sciences*, 50(12), 1708–1720, 1993.
- Smith, W. L., H. E. Revercomb, H. B. Howell, H. L. Huang, R. O. Knuteson, E. W. Koenig, D. D. LaPorte, S. Silverman, L. A. Sromovsky, and H. M. Woolf, GHIS—the GOES high-resolution interferometer sounder, *Journal of Geophysical Research*, 29(12), 1189–1204, 1990a.
- Smith, W. L., H. E. Revercomb, H. B. Howell, H. M. Woolf, R. O. Knuteson, R. G. Decker, M. J. Lynch, E. R. Westwater, R. G. Strauch, K. P. Moran, and B. Stankov, GAPEX: A ground-based atmospheric profiling experiment, *Bulletin of the American Meteorological Society*, 71(3), 310–318, 1990b.
- Solheim, F., J. R. Godwin, E. R. Westwater, Y. Han, S. J. Keihm, K. Marsh, and R. Ware, Radiometric profiling of temperature, water vapor and cloud liquid water using various inversion methods, *Radio Science*, 33, 393–404, 1998.
- Spänkuch, D., W. Döhler, J. Güldner, and A. Keens, Ground-based passive atmospheric remote sounding by FTIR emission spectroscopy: First results with EISAR, *Contributions to atmospheric physics (Beitraege zur Physik der Atmosphaere in German)*, 69(1), 97–111, 1996.
- Steinke, S., S. Eikenberg, U. Löhnert, G. Dick, D. Klocke, P. Di Girolamo, and S. Crewell, Assessment of small-scale integrated water vapour variability during HOPE, *Atmospheric Chemistry and Physics*, 15(5), 2675–2692, 2015.
- Stephan, K., S. Klink, and C. Schraff, Assimilation of radarderived rain rates into the convective-scale model COSMODE at DWD, *Quarterly Journal of the Royal Meteorological Society*, 134, 1315–1326, 2008.
- Takahashi, T., S. C. Sutherland, C. Sweeney, A. Poisson, N. Metzel, B. Tilbrook, N. Bates, R. Wanninkhof, R. A. Feely, C. Sabine, J. Olafsson, and Y. Nojiri, Global sea–air CO₂ flux based on climatological surface ocean pCO₂, and seasonal biological and temperature effects, *Deep-Sea Research II* 49, pages 1601–1622, 2002.
- Thoning, K. W., P. P. Tans, and W. D. Komhyr, Atmospheric carbon dioxide at Mauna Loa Observatory: 2. Analysis of the NOAA GMCC data, 1974–1985, *Journal of Geophysical Research: Atmospheres*, 94(D6), 8549–8565, 1989.

- Thoning, K. W., P. P. Tans, and L. S. Waterman, Atmospheric CO₂ records from sites in the NOAA/CMDL continuous monitoring network, in *Trends: a compendium of data on global change*, Carbon Dioxide Inf. Anal. Cent., Oak Ridge Natl. Lab., U.S. Dep. of Energy, Oak Ridge, Tenn., 2000.
- Tobin, D. C., F. A. Best, P. D. Brown, S. A. Clough, R. G. Dedecker, R. G. Ellingson, R. K. Garcia, H. B. Howell, R. O. Knuteson, E. J. Mlawer, and H. E. Revercomb, Downwelling spectra radiance observations at the SHEBA ice station: Water vapor continuum measurements for 17 to 26 microns, *Journal of Geophysical Research*, 104, 2081–2092, 1999.
- Tolk, L. F., W. Peters, A. G. Meesters, M. Groenendijk, A. T. Vermeulen, G. J. Steeneveld, and A. J. Dolman, Modelling regional scale surface fluxes, meteorology and CO₂ mixing ratios for the Cabauw tower in the Netherlands, *Biogeosciences*, 6(10), 2265–2280, 2009.
- Tranvik, L. J., J. A. Downing, J. B. Cotner, S. A. Loiselle, R. G. Striegl, T. J. Ballatore, P. Dillon, K. Finlay, K. Fortino, L. B. Knoll, and P. L. Kortelainen, Lakes and reservoirs as regulators of carbon cycling and climate, *Limnology and Oceanography*, 54(6part2), 2298–2314, 2009.
- Turner, D. D., *Microphysical properties of single and mixed-phase Arctic clouds derived from ground-based AERI observations*, Ph.D. thesis, University of Wisconsin-Madison, 2003.
- Turner, D. D., Arctic mixed-phase cloud properties from AERI lidar observations: Algorithm and results from SHEBA, *Journal of Applied Meteorology*, 44(4), 427–444, 2005.
- Turner, D. D., S. A. Ackerman, B. A. Baum, H. E. Revercomb, and P. Yang, Cloud phase determination using ground-based AERI observation at SHEBA, *Journal of Applied Meteorology*, 42, 701–715, 2003.
- Turner, D. D., S. A. Clough, J. C. Liljegren, E. E. Clothiaux, K. E. Cady-Pereira, and K. L. Gaustad, Retrieving Liquid Water Path and Precipitable Water Vapor From the Atmospheric Radiation Measurement (ARM) Microwave Radiometers, *IEEE Transactions on Geoscience and Remote Sensing*, 45(11), 3680–3690, 2007.
- Turner, D. D. and R. G. Ellingson, The Atmospheric Radiation Measurement (ARM) Program: The First 20 Years. Meteor. Monogr., *Amer. Meteor. Soc.*, No. 57, 2016.
- Turner, D. D., W. F. Feltz, and R. A. Ferrare, Continuous water profiles from operational ground-based active and passive remote sensors, *Bulletin of the American Meteorological Society*, 81, 1301–1317, 2000.
- Turner, D. D., R. O. Knuteson, H. E. Revercomb, C. Lo, and R. G. Dedecker, Noise reduction of Atmospheric Emitted Radiance Interferometer (AERI) observations using principal component analysis, *Journal of Atmospheric and Oceanic Technology*, 23(9), 1223–1238, 2006.
- Turner, D. D. and U. Löhnert, Information Content and Uncertainties in Thermodynamic Profiles and Liquid Cloud Properties Retrieved from the Ground-Based Atmospheric Emitted Radiance, *Journal of Applied Meteorology and Climatology*, 53, 752–771, 2014.
- Turner, D. D. and E. J. Mlawer, The radiative heating in underexplored bands campaigns, *Bulletin of the American Meteorological Society*, 91(7), 911–923, 2010.

- Turner, D. D., E. J. Mlawer, and H. E. Revercomb, Water vapor observations in the arm program, *Meteorological Monographs*, 57, 13.1–13.18, 2016.
- Turner, D. D., D. C. Tobin, S. A. Clough, P. D. Brown, R. G. Ellingson, E. J. Mlawer, R. O. Knuteson, H. E. Revercomb, T. R. Shippert, W. L. Smith, and M. W. Shephard, The QME AERI LBLRTM: A closure experiment for downwelling high spectral resolution infrared radiance, *Journal of the Atmospheric Sciences*, 61, 2657–2675, 2004.
- Ulaby, F. T., R. K. Moore, and A. K. Fung, *Microwave remote sensing: Active and passive. volume 1-microwave remote sensing fundamentals and radiometry*, Addison-Wesley, Reading, Mass, 1981, 470 pp.
- Uttal, T., J. A. Curry, M. G. McPhee, D. K. Perovich, R. E. Moritz, J. A. Maslanik, P. S. Guest, H. L. Stern, J. A. Moore, R. Turenne, and A. Heiberg, Surface heat budget of the Arctic Ocean, *Bulletin of the American Meteorological Society*, 83(2), 255–275, 2002.
- Wanninkhof, R., Relationship between wind speed and gas exchange, *Journal of Geophysical Research*, 97, 7373–7382, 1992.
- Waring, R. H., J. J. Landsberg, and M. Williams, Net primary production of forests: a constant fraction of gross primary production?, *Tree physiology*, 18(2), 129–134, 1998.
- Westwater, E., The accuracy of water vapor and cloud liquid determination by dual-frequency ground-based microwave radiometry, *Radio Science*, 13, 667–685, 1978.
- Westwater, E. R., Y. Han, V. G. Irisov, V. Leuskiy, E. N. Kadygrov, and S. A. Viazankin, Remote Sensing of boundary-layer temperature profiles by a scanning 5-mm microwave radiometer and RASS: comparison experiment, *Journal of Atmospheric and Oceanic Technology*, 16(7), 805–818, 1999.
- Wunch, D., G. C. Toon, J. F. L. Blavier, R. A. Washenfelder, J. Notholt, B. J. Connor, D. W. Griffith, V. Sherlock, and P. O. Wennberg, The total carbon column observing network, *Philosophical Transactions of the Royal Society of London A: Mathematical, Physical and Engineering Sciences*, 369(1943), 2087–2112, 2011.
- Wunch, D., G. C. Toon, P. O. Wennberg, S. C. Wofsy, R. S. Stephens, M. K. Fischer, O. Uchino, J. Abshire, P. Bernath, S. C. Biraud, and J. F. Blavier, Calibration of the Total Carbon Column Observing Network using aircraft profile data, *Atmospheric Measurement Techniques*, 3, 1351–1362, 2010.
- Zhou, D. K., W. L. Smith Sr, X. Liu, A. M. Larar, S. A. Mango, and H. L. Huang, Physically retrieving cloud and thermodynamic parameters from ultraspectral IR measurements, *Journal of the Atmospheric Sciences*, 64(3), 969–982, 2007.
- Zumberge, J. F., M. B. Hefflin, D. C. Jefferson, M. M. Watkins, and F. H. Webb, Precise point positioning for the efficient and robust analysis of GPS data from large networks, *Journal of Geophysical Research: Solid Earth*, 102(B3), 5005–5017, 1997.

Erklärung

Ich versichere, dass ich die von mir vorgelegte Dissertation selbständig angefertigt, die benutzten Quellen und Hilfsmittel vollständig angegeben und die Stellen der Arbeit - einschließlich Tabellen, Karten und Abbildungen -, die anderen Werken im Wortlaut oder dem Sinn nach entnommen sind, in jedem Einzelfall als Entlehnung kenntlich gemacht habe; dass diese Dissertation noch keiner anderen Fakultät oder Universität zur Prüfung vorgelegen hat; dass sie - abgesehen von unten angegebenen Teilpublikationen - noch nicht veröffentlicht worden ist sowie, dass ich eine solche Veröffentlichung vor Abschluss des Promotionsverfahrens nicht vornehmen werde. Die Bestimmungen dieser Promotionsordnung sind mir bekannt. Die von mir vorgelegte Dissertation ist von PD. Dr. U. Löhnert betreut worden.

Köln, den 13. 08. 2017

Kobra Khosravian

Acknowledgement

I would like to thank all people who contributed directly and indirectly in accomplishment of this dissertation: This work was - to a large extent - supported by graduate school HITEC at the Forschungszentrum Jülich. I gratefully acknowledge use of their courses and services as well as the mentorship program. I would also like to express my deepest appreciation to Dr. Bärbel Köster, the former managing director of HITEC, who supported me since the beginning of this work.

My deepest appreciation goes to my supervisors, Dr. Ulrich Löhnert and Dr. D. D. Turner. Without their continuous support concerning this work, their enthusiasm and encouragement, this study would hardly have been completed. I am also thankful to them for revising the thesis. In addition, I would particularly like to thank Dr. Kerstin Ebell, my scientific mentor, who deeply supported me during this work. Special thanks to Prof. Susanne Crewell, the head of our group, for supporting me to complete this thesis. I would also like to thank Prof. Andreas Wahner for revising this thesis.

I owe my deepest gratitude to my adorable friends, Dr. Farzaneh Taslimi, who encouraged me since the beginning of this study; Zahra Parsakho and Nafise Samiseresht, for all the grateful moments which I had with them as well as Elahe, Mahya, Maryam and all my other friends for their emotional supports.

My deepest heartfelt appreciation goes to my family, my lovely sister and brother, Maedeh and Adel; my brother-in-law, Hozhabr and my cute lovely niece, Rosa who made my world several million times more beautiful. And at the end, I would like to dedicate this thesis to my parents, two angels of my life, for their endless love, supports and encouragements, not only during this work, but also in all seconds of my life.